MODELLING OF PARALLEL BARRIER FOR NOISE CONTROL

WANG ZHIBO

Ph.D

The Hong Kong Polytechnic University

2018

The Hong Kong Polytechnic University

Department of Mechanical Engineering

Modelling of Parallel Barrier for Noise Control

WANG Zhibo

A thesis submitted in partial fulfillment of the requirements for the

Degree of Doctor of Philosophy

Oct, 2017

CERTIFICATE OF ORIGINALITY

I hereby declare that this thesis is my own work and that, to the best of my knowledge and belief, it reproduces no material previously published or written, nor material that has been accepted for the award of any other degree or diploma, except where due acknowledgement has been made in the text.

(Signed)

WANG Zhibo (Name of student)

Department of Mechanical Engineering

The Hong Kong Polytechnic University

Hong Kong, China

Oct, 2017

ABSTRACT

Noise barriers are commonly used to protect the residents from the disturbance of traffic noise. Parallel barriers would also be used in highly populated area but its performance is deteriorated due to the resonances created by the multiple reflections between two parallel walls. To solve this problem, a Helmholtz resonator which acts a sound radiator is mounted on the wall surface to radiate sound and influence the structure of sound reflection waves inside the parallel barriers. Ultimately, the degradation effect due to resonance would be reduced. In order to understand the mechanism and design optimal Helmholtz resonator for controlling noise at wide frequency band, an analytical model for acoustical coupling of the baffled open cavity and the resonator array has been established. The resonators are regarded as the secondary sound sources which interact with multiple acoustic modes inside the cavity. Theoretical study indicates that sound peaks at outside receiver is dominated by one of the cavity modes and contributed from other modes. And the noise reduction inside and outside the cavity can be found at the target frequency when there is an appropriate design of resonators.

The findings from the baffled open cavity in three dimensions is then applied to the noise control of the parallel barriers in two dimensions. There is no analytical expression to describe the acoustics field for open cavity without baffle and a hybrid method alternatively has been established by combining the analytical cavity modes and the numerical radiation modes. In order to suppress the multiple peaks of sound pressure levels at some frequencies, several resonators at different natural frequencies are combined together to obtain a broadband sound abatement. The validated hybrid model indicates that the noise reduction at the receiver can be found at the target

frequency. Through optimal design of the locations of the resonators, the deterioration can be suppressed and a broadband noise reduction can be obtained.

In order to have higher sound suppression especially at low frequency regime, the plate cavity device is installed on the inner walls of parallel barriers. The flexible panel is used to radiate sound to undergo sound cancellation at the region of the barrier top edges to suppress the sound diffractions. A theoretical model which account for the acoustical coupling between the plate vibration and sound radiation of the parallel barriers has been developed. The noise abatement of the parallel barriers after integration with the plate cavity is investigated systematically and optimized on the base of the validated theoretical model. It is found that the several sound peaks can be suppressed when the clamped-clamped plate is properly designed with light mass and high stiffness.

To validate the accuracy of the proposed theoretical model for vibroacoustic coupling of such a complicated system, numerical tool of the fast multipole boundary element method (FMBEM) would also be established. This model can also be adopted to examine the effectiveness of the proposed silencing device in practical use and give the flexibility into the design of complicated structure of the parallel barriers in a three dimensional configuration. The BEM is the ideal solver for sound scattering in infinite space due to the fact that the Sommerfeld radiation condition can be satisfied inherently. The conventional BEM is insufficient for dealing with the sound scattering problem with large scale degree of freedoms and hence the fast multipole algorithm is chosen to accelerate the matrix vectors formulation and computation. Finally, the finite element method (FEM) is coupled to the FMBEM to deal with acoustic-structural interaction. Finally, a series of small scale experiments for open cavity and parallel barriers in anechoic chamber were conducted to valid the analytical and numerical models.

PUBLICATIONS ARISING FROM THE THESIS

Book chapter:

Wang, Zhibo. Choy, Yatsze and Xi, Qiang. Chapter in "Fluid-Structure-Sound Interactions and Control." (pp. 63-68). Springer, Berlin, Heidelberg (ISBN: 978-3-662-48868-3).

Conference paper:

Wang, Zhibo. Choy, Yatsze and Xi, Qiang. "Fan Noise Control by a Flexible Casing." Proceedings of the 3rd Symposium on Fluid-Structure-Sound Interactions and Control, Perth, Australia, 2015.

Wang, Zhibo and Choy, Yatsze. "Environmental noise control by parallel barriers integrated with Helmholtz resonator." INTER-NOISE 2017, Hong Kong, China, 2017

ACKNOWLEDGEMENTS

Foremost, I would like to express my deepest gratitude to my chief supervisor, Dr. Choy Yatsze for who was abundantly helpful and offered invaluable assistance, support and guidance for my Ph.D. study and research. I gratefully acknowledge Dr. Jing Xingjian, my co-supervisor, for giving me the invaluable enlightenment and encouragement.

My sincere thanks are also given to Dr. Liu Yang, Dr. Xi Qiang, Dr. Fei Chengwei, Ms. Chiang Yankei, Mr. Wang Tiangang, Mr. Chen Long and Mr Wei long for their kind assistance and discussions during my study. I must especially thank Dr. Yang Cheng from Shanghai Jiao Tong University who provided me substantial help and illustrative discussion. I wish to thank all the staff and technicians in the laboratories and offices for their support.

The last but not the least, I would like to thank my parents and younger sister and brother for their encouragement and support. Special thanks go to Ms. Zhou Yi, for all of her love, help and understanding during my Ph.D. study.

NOMENCLATURE

Symbol	Description
$\boldsymbol{A}$	The coefficient matrix
a	the sphere radius
a_i	the modal coefficient of the *i*-th eigenmode for cavity
α_E	azimuthal angle in the Euler coordinate
$\boldsymbol{b}$	The coefficient matrix
b_i	the modal coefficient of the *i*-th eigenmode for outside
β_E	polar angle in the Euler coordinate
$\mathbf{C}$	The damping matrix
C_{Sa}	the acoustic pressure on the structural nodal loads
c	the sound speed in the media
$c(\vec{x})$	the constant related to the source point location $\vec{x}$
c_l	the coefficient depending upon the precision of the arithmetic
D	computational domain size
d_l	the size of the cells at level *l*
E	Young's module of the plate
f_{cr}	critical frequency of the resonator
G	Green function
G_H	half space Green function
$h_n^{(1)}$	the first kind spherical Bessel function of *n*-th order
IL	Insertion loss

j_i	the *j*th model index in *i* direction.
j_n	the first kind spherical Hankel function of *n*-th order
$\mathbf{K}$	stiffness matrices
k	the wavenumber
k_j	wave number of the *j*-th eigenmode
$(kd)^*$	threshold value for the wideband multipole expansion
L	the length of the edge of the largest cell
L2L	local to local translation
$\mathbf{M}$	global inertia matrix
M2M	multipole to multipole translation
M2L	multipole to local translation
$\mathbf{N}_a$	the global interpolation functions for the acoustic domain
$\mathbf{N}_S$	the global interpolation functions for the structure domain
N_{dof}	Degree of freedom
N_e	The total boundary element number
Ω_i	The acoustical domain *i*
$\vec{o}$	center of a children box
$\vec{o}'$	center of a parent box
$o(1/r)$	Weak singularity
$o(1/r^2)$	Strong singularity
$o(1/r^3)$	Hyper singularity

$P_n(x)$	Legendre polynomial
p	The sound pressure
$\phi_j(\vec{x})$	*j*th eigenmode
q	the normal velocity
q_s	The sound source strength
q^i	The sound strength by the *i*-th resonator
R_p	the symmetry plane reflection coefficient
r	The distance between two points
ρ_0	The air density
ρ_p	the density of the plate
(r,θ,ϕ)	the spherical coordinates of the vector
S_o	the elements inside the box with centroid *o*
S_c	the coupling face
w	Displacement of the plate
ω	angular frequency
Y_n^m	the spherical harmonics
Z	normal impedance
Z_i	the output impedance at the *i*th resonator's mouth
Δp	acoustic pressure load
μ	Poisson's ratio

TABLE OF CONTENTS

LIST OF FIGURES

LIST OF TABLES

CHAPTER 1

INTRODUCTION AND LITERATURE REVIEW

1.1 Background

The land transportation noise, which is mainly produced by motor vehicles and trains, has seriously reduced the life quality of residents who live in densely populated cities like Hong Kong. Engine operation, tire-road interaction and turbulent air flow around high-speed vehicles are three main causes of land transportation noise. Engine noise is produced by vibrating surfaces and individual sources [1]. It becomes the main noise source when the vehicle moves at low speed. Interactions between tires and road radiate noise when the vehicle moves at high speed. Sound generated by the air turbulence is generally unimportant for land transport. Railway systems are comprised of long-haul freight and passenger trains, a variety of subways, elevated and surface vehicles and so on. Engine noise, rolling noise and aerodynamic noise that are produced by the train become predominant when the train speed is around 50km/h, between 50~300km/h and above 300km/h, respectively. Noise also occurs when train passes through bridges, curves and rail joints as well as brakes [2].

With the number of cars growing continuously and the speed of trains improving gradually, complaints about traffic noise arise frequently from those residents who expose to it excessively. So, how to reduce the noise level near road sides has become an urgent issue for the environmental protection bureau. A variety of measures were developed to solve the problem, among them barrier is one of the most widely used. For the purpose of attenuating the noise level at both sides of the road, two identical barriers are often erected in parallel. However, noise reduction performance of parallel

barrier will decline significantly when they are close to each other.

Many numerical and experimental studies have confirmed that multiple reflections occur in the bounded domain formed by the two parallel reflecting walls and the ground. The reverberation within such a domain degenerates the noise reduction performance of the barriers. Taking the experimental study by Watts [3] as an example, the insertion loss (IL) of the parallel barrier with identical height (2m) reduced 4 dB (A) compared with that of a single barrier. Therefore, reverberation should be considered and its degeneration effect on noise reduction performance should be avoided when the parallel barriers are constructed in close proximity. In addition, the control of low frequency noise still remains a challenge, especially when the noise reduction performance, cost, durability and safety of the barriers are all taken into consideration.

1.2 Literature review on barriers

In general, there are three kinds of noise control elements: (1) controlling noise at the source; (2) modifying the propagation path and (3) reducing the noise level reaching the receiver. The mechanism of the acoustic barrier is based on the second one. Commonly, a noise barrier is placed between the sound source and the receiver to modify the sound propagation, which offers protections of the receiver from the direct sound waves. In this situation only the diffracted wave can reach behind the barrier. Therefore, this region is quiet due to the fact that the diffracted wave is relatively weak when compared with the direct waves and ground reflected waves.

According to whether existing additional sound source, the noise reduction used for barrier can be divided to active and passive noise barrier. The active noise control (ANC), which contains a power and sensor system generally the loudspeaker and microphone, is more effective to reduce the low frequency noise [4-6]. However, the ANC systems developed in the above works generally contain of secondary source

power, error sensors and control circuits, the heavy cost and difficult implementation limit its wide application. The fact is that ANC is not a good option for the outdoor environment. The passive method takes advantage of the sound isolation materials and different barrier shapes to achieve the noise reduction. To the author's best knowledge, most works to optimize the barrier performance is taken passive means. Numerous different types of barrier have been studied and the performance have been evaluated. These studies are mostly based on two ideas. One is to modify the barrier profile shape and the other is to cover the edge of the barrier with absorbent materials. In the earlier attempts, such as T-profiled [7, 8], multiple-edge [9], and novel irregular profile barriers [10, 11] have been studied. Hothersall et al. [12] reviewed the single barrier with different profiles including the T-shaped, Y-shaped and arrow shaped barriers and concluded that the noise reduction performance by T-shaped is better than other types of designs. On the other hand, Li [13] added the absorbent materials on the inner surface of the parallel barriers and evaluated its noise reduction performance in the urban environment. The numerical calculations and scaled experimental measurements indicated that the installation of absorbent materials at the inner surface of barrier could only improve of the noise reduction in the shadow zone. Micro-perforated panel has a good absorption performance in the middle to high frequency range and was adopted by [14] as the absorber on the noise barrier. However, the environmental problem and the durability issue limit the practical use of the absorption materials and the micro-perforated panels. A comprehensive literature review about the noise barrier with different shapes and absorbent materials can be found in Ishizuka and Fujiwara [15].

Of particular interest, the study in this work is focused on the parallel barrier in close proximity. As shown in Fig 1.1, the sound wave approaching the receiver for the single noise barrier and the parallel barrier is compared. The parallel barrier and the ground

forms the bounded domain. It is obvious that the multiple reflections occur within the bounded domain and more sound energy has reached the receiver behind the barriers. This significantly depredates of the acoustic performance of the noise barrier.

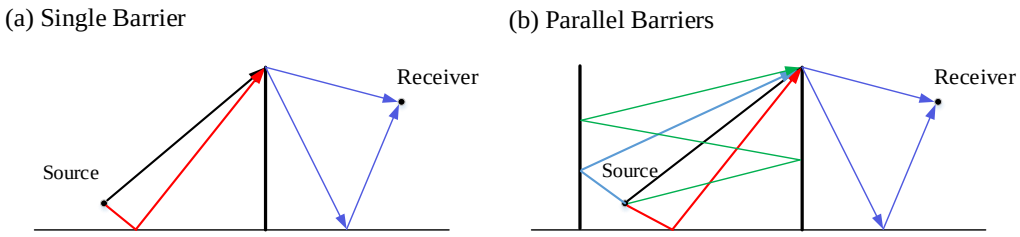

Fig 1.1: The sound propagation over the half-space and diffracted by a thin barrier: (a) Single barrier and (b) Parallel barriers.

1.2.1 Sound propagation in parallel barrier

In order to reduce the noise level on both sides of the roadway, parallel barrier is often used. The sound wave emanated from the vehicles and approaches the receivers after multiple reflections if the parallel barrier are used. The multiple reflections create the reverberant sound field within the bounded domain and can significantly degrade the acoustic performance of the barriers. This phenomenon is well recognized and has been studied by researchers numerically and experimentally. A laser beam had been used by Hutchins and Pitcarn [16] to model the point sound source and examined the propagation paths between parallel barriers. Watts and Godfrey [17] demonstrated experimentally that the insertion loss was significantly reduced for the parallel barrier when compared with the single barrier. In 1996, Watts [3] reported field results for parallel barrier cases to evaluate the degradation effect due to the multiple reflections with the bounded domain by the parallel barrier and the ground. In his work, perfectly reflective barriers of various heights, as well as covered by absorptive conditions and tilted barriers were compared. He reported that the average noise levels behind the single barrier with 2 m in height were increased by 3.1 dB(A) when another barrier with

same height was placed 3.4 m away from this single barrier. When changing the point sound source to a line source, the increase was deteriorated further to 4.4 dB(A). Watts also found that this degradation was greater as the barrier height increased or the separation distance was reduced.

Therefore, in order to eliminate this deterioration, the multiple reflections between the parallel barriers should be reduced. Ways to reduce the deterioration include (1) using the absorption layer on the inner faces which near the sound source, as studied by Watts and Godfrey [17], Li [13] or the far side barrier as pointed out by Watts [3]; (2) tilted the barrier suggested by Watts and Godfrey [17] and Monazzam and Fard [18]; and (3) novel profile such as the wave-trapping barrier by Yang and Pan [10] and subwavelength tube array by Wang [19]. For the barrier with sound absorption material, the thickness of the absorption layer needed increase impractically thick as the frequency decreases. The environmental issue limits the wide application of the absorption material on the outdoor noise barrier.

The titled parallel barrier was designed and compared with other shapes of barrier by Monazzam and Fard [18]. Their numerical results showed that the barrier sloped with 10^{o} had better noise reduction performance.

The wave trapping barrier (WTB) proposed by Pan seems a good choice to improve the noise reduction of the parallel barrier. The typical profile of a WTB has multiple wedges on its inner surface which is near the sound source side. The wedges always redirect reflected waves downwards so that they are trapped within the bounded domain constructed by the two identical barriers and reflecting ground. Additionally, each wedge has a perforated surface, a back cavity, and internal lining to provide appropriate reflection and absorption of incident sound waves. However, as indicated by the numerical results [10], the improvement mainly occurs at frequency above 1000 Hz.

The insertion loss had little difference when compared with that of the parallel reflective barrier for a frequency below 1000 Hz. In the recent work, Wang [19] designed the parallel barrier constructed with hollow narrow tubes to create the inhomogeneous impedance on the inner surface of the parallel barrier. Their analytical model showed that the way of the wave reflection was altered after introducing inhomogeneous impedance on the inside barrier surfaces. The sound energy could be trapped in the semi-enclosed bounded domain and thus improve the noise reduction at the receivers.

1.2.2 Calculation methods

Due to the importance and high construction of the acoustic barrier, its noise reduction should be examined accurately at the design stage. What's more, the exact prediction tool can reveal the noise reduction mechanism and indicate the ways of performance optimization. The full-scale or scaled model experiment is undoubted the most direct way. However, it is hard to distinguish the multiple reflections for parallel barrier and cannot reveal the principles of the noise propagation and reduction, especially in the complex urban sound environment. Moreover, field measurements are time consuming and expensive if a great deal of receiver points are required. For these reasons, these field data are served as the validation tool to examine the accuracy of the proposed calculation models. As the development of the computing techniques and the deeper understanding about the noise propagation and diffracted by the noise barriers, many researchers have conducted various studies to develop the calculation method to predict the noise reduction.

1.2.2.1 Analytical Models

It is hard to derive the exact solution for wave diffraction especially for the

complicated profile of the barrier. Alternatively, the diffracted wave in the shadow zone is represented by the superposition of the scattered wave by the edge and the incident wave. Based on this idea, Sommerfeld [20] obtained the rigorous derivation to diffraction problem above a half plane. In Sommerfeld's solution, the sound field generated due to a plane wave scattered by the thin plane is mainly consist of two terms. One is the direct wave, which can be predicted based on the geometrical acoustic theory and the other contributes from the diffracted wave, which can be expressed by Fresnel integrals. Tolstoy [21] derived waves diffraction solution by wedges in the analytical form. In his method, the sound field by the diffraction was calculated by the superposition of a set of series and their corresponding coefficients. The advantage of this formulation is the diffractions at the edges are calculated exactly, without the approximation for integrals. However, the slow rate in convergence for the series especially at high frequencies limited the application of this method in practice. Another important accurate express of the sound filed diffracted by the screen and wedge was proposed by Hadden [22]. Pierce [23] extended the asymptotic solution to evaluate the sound diffraction by a single wide barrier following the ideas of geometrical theory of diffraction (GTD) developed by Keller [24]. In the recent work, Wei [25] proposed a simplified analytical model for the sound prediction concerning the multiple diffraction and reflection. The used trigonometric functions to approximated the double Fresnel Integral used in Pierce's diffraction theory and hence improve the calculation efficiency. The comprehensive review about the calculation method can be found in Li [26].

1.2.2.2 Empirical Formulas

On the other hand, various empirical formulas have been developed based on extensive experimental measurements, such as the formulas by Redfearn [27],

Maekawa [28], Kurze and Anderson [29] ,and several other empirical models. These empirical formulas are used extensively in engineering areas. Redfearn [27] was among the first researchers to develop graphs, with two known parameters namely the effective barrier height and the diffraction angle. These can be used to determine the noise reduction behind the reflective single barrier radiated by a point source. Subsequently, Maekawa [28] compared experimentally the sound attenuation by a thin rigid barrier when the noise source and reception points located to different positions. The experimental data was presented in a chart and the noise reduction was shown against the Fresnel number. Based on Maekawa's study, several other empirical models were developed to predict the noise reduction in the shadow zone behind the thin barrier wall. Of particular interest, Delany et al. [30] concluded the empirical formula for parallel barrier, which was based on data from over two hundred field measurements. Numerical comparisons have shown that the empirical tools, including formulas, charts and tables, are quite adequate for engineering. However, such methods lost their accuracy and a more elaborate formula is needed when the sound source or the receiver is near to the barrier.

1.2.2.3 Boundary Element Method

However, for the barrier with complex profile or multi-layer materials, analytical and empirical methods may fail. In this regard, the numerical method is always a good choice to predict the noise reduction of the barriers. Among the numerical algorithms, the Boundary Element Method (BEM) is more popular in unbounded domain because of the Sommerfeld radiation condition are satisfied in its formulas. Besides, the Green function used in BEM is obtained analytically and hence improve the accuracy of this method. The third advantage is that the BEM is based on the boundary integral equation

and the discretization is only carried out on the boundary surfaces for a three dimensional domain and edges for a two dimensional domain. This dimension reduction makes the BEM more efficient in meshing and calculation.

Chandler-Wilde and Hothersall [31] applied BEM to the calculation of outdoor sound propagation. Their work described in detail of using the BEM to sound field prediction in air medium over an impedance surface of an arbitrary shape. The predictions were also compared with scale model experiments and good agreements were obtained. Based on the 2D BEM techniques, Seznec [32] studied the parameters affected the noise reduction performance, including barrier profile and absorption boundaries both on the barrier surface and the half ground. The mitigation of noise by single barrier was investigated by Hothersall [8] by mean of the BEM in 2D. The model described in their work can be applied to barriers with arbitrary profile and impedance conditions. Noise reduction performance by single barrier of different height, profile and impedance conditions had been compared. In a similar way, Ishizuka and Fujiwara [15] applied the BEM to study the noise reduction by barriers of different cross-sectional profile and coverings on the surface. Numerical results in their study showed that the top edge covered with absorbent materials and soft conditions can improve the performance of the barrier significantly. As comparison, only a slight enhancement can be obtained when modifying the configuration of the single barrier. In all of the configurations and surface conditions studied in their work, the T-shaped barrier with soft top produces the highest noise reduction. The above predictions of noise reduction for single barrier is based on the two dimensional boundary element analysis, which assumes that the cross section infinitely long and unchanged. However, for barrier that cross section varied, three-dimensional (3D) models need to be developed to consistent with the configuration. In order to speed up the calculation, a quasi-periodic BEM

model was proposed by Fard *et al.* [33] to access the sound field of the barriers in three dimensions. A 2.5D BEM Model was developed by Jean [34] to the study of ground and foundation interaction. Such treatment gives much faster calculations when compared with the fully three-dimensional configuration.

Although the BEM has enjoyed the advantages in modeling the sound radiation by complicated geometries in infinite domains, its low efficiency in solving large-scale problems still restrict its use in industry and scientific calculations. For example, the BEM can only be used to solve the acoustic problems with only a few thousand degree of freedoms on a personal computer for few years. This is because that the matrices produced by the conventional BEM are dense and non-symmetric. The computational time to form such matrices is proportional to $O\left(N_{dof}{}^{2}\right)$ and the solving time is $O\left(N_{dof}{}^{3}\right)$ if the direct solvers are used, in which, N_{dof} is the number for degree of freedom (DOF). Many techniques have been proposed to accelerate the BEM, such as wavelet compression [35], pre-corrected FFT [36], ACA [37] etc. The main idea of these acceleration methods is to speed up the former of the coefficient matrix. Of those acceleration methods, the fast multipole method (FMM) is the most popular. Rokhlin and Greengard [38] pioneered the FMM and used it to accelerate the calculations of conventional BEM. Under the acceleration of the FMM, the calculation time is promisingly reduced to N_{dof} . The main process of the FMBEM is to apply the FMM to accelerate the computing of the system coefficients matrix $\boldsymbol{A}$ and then use the iterative solvers to solve the linear equation of $\boldsymbol{Ax=b}$. It should be noted, the direct calculations of the BEM are still needed for the boundary elements that are near the collection point. The fast multipole algorithm is implemented for boundary elements that are far away from the collection point. Comprehensive review and detailed

comparison about the FMBEM can be found in [39]. When applied the FMBEM to the noise barrier predictions, Bapat [40] developed the adaptive FMBEM to calculate the acoustic wave propagation in three dimensions. The Green function employed explicitly in their work and only the real domain need implementation of the tree structure when considering the semi-infinite problems, which could reduce the CPU time and memory storage. Based on the adaptive tree structure, Zheng [41] obtained the symmetric relationships for the multipole expansion coefficients between the real and the mirror domain which further simplified the multipole/local expansions in the half space. The straight and quasi-circular barriers were served to examine the efficiency and accuracy of their proposed method. Besides, the BEM can be coupled to other numerical method such as the finite element method (FEM) to calculate the acoustic-structure coupling problems. Pates [42] coupled the BEM with the FEM to accurately model acoustic-structural interaction of a composite panel resting on an acoustic cavity. The numerical results was validated with the experimental result for isotropic panels and good agreement was obtained. Fischer [43] conducted the similar acoustic-structure interaction studies by BEM-FEM. Lagrange multipliers approach was used to transfer the data between the non-matched grids on the coupling surface. In the recent work by Isakari et al [44], the fast multipole accelerated BEM-FEM was combined together to conduct the topology optimization for elastic material to reduce the sound response at some fixed receivers.

1.2.2.4 Ray method

Despite the wide interest in using the wave-based BEM, ray based prediction methods have been well developed in the recent years. In 1993, Panneton et al. [45] used a coherent ray model to predict noise reduction of parallel noise barriers. The

authors considered the case of barrier absorption by the modified Delany-Bazley impedance model which proposed by Miki [46]. In their model, multiple reflections by the parallel walls and the ground were modeled by the acoustical imagery method and geometrical theory of diffraction, leading to a complex summation between acoustical waves originating from a single source traveling to the receiver via the top edge of the barriers. In the study, they reported that the ray model gave good precisions for mono-frequency sound that compared reasonably well with theoretical and experimental results for various parallel barrier configurations. Numerical simulations were conducted on a six-lane highway of 36.5 m width. Vehicles were represented by punctual sources placed randomly on the six lanes. 48 sources in total were placed along a distance of 80 m and the receiver were located 15 m behind the near-side barrier. The predicted results reported that the use of hard parallel barrier brings about an insertion loss degradation of 2 to 4 dB in average. By adding absorbent material, this becomes nearly null and brought back to the single barrier case. Unfortunately, they only considered receiver points located within shadow zone very close to the ground. It is also noted that the model proposed by Panneton et al. [45] is limited to access only the total sound field at a particular receiver location below the barrier's top edge. It is thus important to extend the model to calculate the insertion loss provided by a pair of parallel barriers at all possible receiver locations. In 2003, Li and Tang [47] proposed a numerical approach which combined image source theory with the diffraction solution of Hadden and Pierce [22] to predict the IL performance by a single noise barrier which is close to tall buildings. Comparisons with indoor scaled-model experiments and BEM simulations at different receiver locations were made to validate the accuracy of the proposed model.

1.2.2.5 Modal Analysis

Typical parallel barriers consist of a finite confined space bounded by two identical barriers and an infinite half space. Such configuration can be clarified as the acoustic coupling between an open cavity and the unbaffled infinite region.

Of the methods proposed to deal with this phenomenon, the most efficient and widely used being based on modal analysis. The fundamental idea of modal analysis is to express an acoustic field quantity as the summation of a complete set of properly weighted modal functions. The weighting factors are often called the modal amplitudes or modal response coefficients. The summation usually has an infinite number of terms; therefore, the modal analysis does not yield a closed-form solution. However, given that this infinite series converges, one can in practice truncate it to a finite sum and still reach the desired accuracy in the low-frequency regime. The modal analysis theory developed by Dowell, et al. [48] is capable of computing sound fields in damped enclosures. The method used a set of eigenfunctions solved from an eigenvalue problem as the modal functions, which is called the "normal modes." The normal modes and the linear combination of them only satisfy rigid boundary conditions; therefore, large errors are often observed in the regions near damped boundaries. The eigenfunctions that satisfy the complex boundary conditions or irregular shape of the enclosure can be solved numerically from an exact eigenvalue problem [49-51]. The numerically calculated modes are uncoupled and automatically match the boundary conditions, which make them a very good candidate for the modal functions for modal analysis. However, there are several negative properties implicit with them. First of all, the completeness of this set of modal functions is an assumption. Second, the "orthogonality" relationship among these functions is abnormal, which may cause inconvenience for many applications. Finally, solving the exact eigenvalue problem

involves numerical root searching in the complex domain which is complicated and time-consuming [49]. Because of these disadvantages, the modal analysis is not utilized much in the literature. Alternatively, Xu and Sommerfeldt [52] proposed a new set of modal functions called the modified modes. Compared to the normal modes, modified modes are also coupled but can be easily simplified in many cases. Modal analysis based on the modified modes also introduces errors on boundaries but performs faster when compared with the conventional method. Unlike the numerically calculated modes, modified modes are orthogonal and complete. However, the numerical root search is still required. Following the findings for enclosure acoustic systems, numerous efforts have been devoted to the acoustical analysis for open space based on modal analysis. The energy radiated from the outlet of a cylindrical waveguide has been determined for multimode excitation [53]. For the domain-based numerical method, a basic difficulty exists for calculating the sound radiation to the far field reception points. Many treatments have been developed aiming to truncate the infinite domain to a finite one. Of all, the perfectly matched layer (PML) is the most efficient. A PML [54] provides theoretically ideal absorption of outgoing waves without reflection at any incident angle and frequency.

Therefore, the infinity can be truncated to the bounded domain by complex layers of finite thickness. The eigen-problems for such truncated domain can be solved. Koch [55], Hein et al. [56-58] and Duan et al. [59], for example, used PMLs to investigate the acoustic resonance in tunnels, duct-cavity systems and open cavities. All these studies concentrated on the eigenfrequencies of the resonances as well as on the search for real eigenvalues (purely non-dissipated localized modes or trapped modes) and corresponding Fano resonances. Use of leaky modes and modal decomposition have been used to investigate the sound propagation in open street canyons [60]. The analysis

was performed assuming that the source condition is the pressure distribution at the input end of the canyon. Using the hybrid model which combines image source modeling and the ray tracing method, numerical calculations have been conducted to predict the acoustic propagation within an urban canyon [61]. The analytical method based on a 2D image source model has been used to analyze the acoustic propagation for the case of an acoustic canyon with an open roof [62].

While the PML-based numerical method has been used to predict the resonant frequency modes and energy radiation, few studies cover the modal expression for the sound field of an open acoustic cavity. This is because the solution of PML-constructed eigenvalues generates a multitude of spurious eigenvalues which in many cases are very hard to distinguish from the correct ones [63]. This problem, namely a lack of efficient ways to extract the physical eigensolutions, diminishes the practical implementation of using the PML to construct the eigenvalues of the infinite external space.

Alternatively, the non-Hermitian Hamiltonian approach [64-66] can be used to deal with acoustical coupling problems between the finite and infinite physical spaces. The basic principle of this approach is to divide the whole calculated domain into a finite part described by the discrete spectrum and an infinite part described by the continuous spectrum. The governing differential equation is then projected onto the subspace spanned by the wave functions of the discrete spectrum, leading to an effective differential operator, or the effective non-Hermitian Hamiltonian. In the recent work by Maksimov et al. [67]and Lyapina et al. [68], they investigated the acoustical transmission in the duct-cavity system by introducing the non-Hermitian Hamiltonian method. Maksimov et al. [67] demonstrated the coupled mode theory as an effective tool to solve sound transmission problems in 2D and 3D acoustic scatters. Lyapina et al. [68] used the acoustical coupled mode theory to analytically calculate the

eigenfrequencies and their shape functions of the bound states in open acoustic resonators. Xiong [69] derived the sound scattering in a waveguide partly lined with a locally reacting material. After forming the effective matrix, the acoustic resonances of the waveguide lined with impedance boundaries is reduced to the equivalent eigenvalues of the effective matrix. The occurrence of the transmission zero is discussed and linked to the Fano resonance. Tong et al. [70] further extended the non-Hermitian Hamiltonian approach to the open acoustic system in two and three dimensions. They proposed to use the frequency-dependent eigensolutions to construct the sound field of the baffled and unbaffled open cavity and excellent agreement could be found when compared with the sound response results from the numerical solutions. However, as described by the definition, the frequency-dependent eigensolutions are related to the source frequency and hence complicates the problem in practical application. Moreover, the physical eigenvalues and the eigenfunctions used in their method are not clear.

1.3 The Helmholtz resonator for noise control

Various previous works have demonstrated that the degradation of the noise reduction in the diffracted region behind the barrier is due to the multiple reflections within the domain bounded by the parallel barriers and the reflecting ground. In the work by Yang and Pan [10], they showed that sound field of the parallel barriers could be expanded by trapped modes. The problem was solved numerically using FEM combined with perfectly matched layers (PML). The eigenvalues of these trapped modes of such an open domain has also been solved. In fact, the major peaks in the sound spectrum for the receivers behind the barrier are dominated by the (*, 0) modes, in which * are the modal index defined through visual inspection. In the recent work by Tong et al. [70], the sound fields in and outside the parallel barriers are described using

the modal expansion. The sound responses at the receivers are mainly contributed by a set of enclosure and external modes. Therefore, the idea of suppressing these dominated modes to improve the noise reduction at the receivers behind the barrier is proposed. The typical device to reduce the noise level at the resonant frequency especially at low frequency range is Helmholtz resonator. A classical Helmholtz resonator made up of a backing cavity and a narrow neck. It is useful to control noise centralized in a narrow frequency band.

The resonator only works at target frequency and hence leads to a narrow noise reduction spectrum. To broader the frequency band of noise reduction, several resonators with different natural frequencies are needed combining together to form an array of resonators. The studies about resonators array can be found in the control of duct noise by [71, 72]. The duct integrated with multiple similar resonators or with the boundary covered by a perforated backed by the air cavities was discussed [73]. A conclusion was drawn that when resonators tuned with similar natural frequencies are close in spacing, they interact with each other and result in a decrease in the noise control performance compared with that by single resonator [74]. To avoid this degradation, the spacing proximity of the resonators should be considered carefully when applying resonator array to attenuate the sound response. The resonators are also used for the noise abatement in the environmental noise control, such as the periodical single barrier[75] and the sound scatter [76]. Fard et al. [75] studied the IL of single noise barrier whose top embedded with single and multiple Helmholtz resonators. Their numerical results indicated that the increases in IL can be obtained around the natural frequency of the embedded resonator. Three resonators tuned different natural frequencies can achieve an enhancement in noise reduction over the low frequency range of 150 to 300 Hz. However, the interactions among the sound field and the

resonators should be considered carefully. Van der Aa and Forssén [76] investigated the sound field after scattered by cylindrical shell array with perforated holes and the shell core filled with the porous materials. Calculation results of a small array of cylindrical shells are in excellent agreement with measurements from the experiments. The semi-analytical calculations show a strong and narrow insertion loss peak at resonance when the cylindrical shell drilled with perforated holes. When adding the porous materials into the core of the shells, the major change was that the reduction peak was broadened but the amplitude was reduced.

1.4 Vibroacoustic coupling for noise control

It is known that the low frequency noise in the parallel barriers is hard to control. The Helmholtz resonator array can control the noise performance at the low frequency range. The drawback is the narrow reduction spectrum for single resonator when the interest is wide noise abatement. Array resonators combining several resonators at different natural frequencies can achieve a broadband quieting. However, the conflict between effectiveness in performance and compactness in size always persists. The resonator's natural frequency and distance between their apertures governs the noise abatement when using the resonator array to broaden the noise reduction bandwidth.

The conflicting design constraints of broadband effectiveness at low frequencies and volume minimization present a major challenge for existing resonator array and some other reactive devices. Alternatively, the use of flexible boundaries instead of the discontinuity in traditional reactive silencers has been proposed and have attracted a lot of attention. Huang [77] suggested introducing flexible panels for the control of duct noise. The flexible panel is tensioned membrane called the drum-like silencer [78, 79]. The incident sound wave induces the vibration of the tensioned membrane with a low order axial mode, and such vibration reflects the noise at low frequencies very

effectively. Therefore, the drum-like silencer can produce a relatively broad noise reduction in the frequency range from 200 to 1700 Hz. Dynamic motion of the membrane and the interaction pattern is carried out based on the modal analysis [78]. Experimental measurement is conducted to validate the effectiveness without [80] and with flow [81].

Due to the difficulty in finely tuning the membrane and the space occupation of the stretch mechanical system in practical use, Huang [82] proposed to use a flexible plate to replace the tensioned membrane. The theoretical studies show that a wider stopband can be achieved by the plate silencer when compared to the drum-like one. In order for easier implementation in practice, Wang [83] clamped the two ends of the plate instead of the simple support as used in Huang [82]. Their numerical and experimental studies reveal that broadband noise reduction can be obtained when the plate is light in mass and high in bending. Following such requirement, the sandwich plates and PMI foam reinforced by carbon fiber tows have been investigated independently by Wang [84] and Choy [85]. In an attempt to further broaden the noise abatement, micro-perforations were introduced to the light and flexible plate by Wang et al.[86]. The micro-perforations aim to absorb sound waves which cannot be reflected sufficiently by the plate due to the weaker vibroacoustic coupling. Lawrie's group contributed significant insights to the field through theoretical and numerical analysis. For instance, with the aid of a mode-matching method, Lawrie and Guled [87] found that a wider stopband can be achieved through changing the location of the membrane inside the backing cavity.

Their researches show that the coupling between fluid and flexible panels has the potential to reduce the noise level at the low frequency range with an appropriate design. Further, their work indicates that the acoustic-structure interaction slows the acoustic

wave, thereby enabling a more compact device compared to a rigid walled silencer. The main principle of the noise reduction by the plate is to excite the resonances at a low frequency range and probable interactions between these resonances and the incident wave.

For the above-mentioned structural acoustic wave reflector, the broadband performance arises from the fully coupled plate cavity system which has three or four adjacent resonant peaks [78]. Since the properties of the panel play a critical role in regulating the resonances and the modal shapes, the actual performance is sensitive to the change of the panel properties. Hence careful optimization has to be conducted before an actual design can be made [79].

1.5 The motivations of this study

Traffic noise is a particularly acute problem in crowed cities like Hong Kong. Tall buildings are located very close to railway viaducts or road traffic expressways and the noise levels in the adjacent residential areas are significant. In these urban environments, parallel barriers are extensively used to protect residents away from traffic noise on either side of the way. However, the multiple reflections within the bounded domain by the parallel barriers and the rigid ground deteriorate the noise reduction performance. In addition, the low frequency noise control still remains a challenging task for parallel barriers.

Lining a barrier walls with porous sound absorbing materials can attenuate the noise from medium to high frequency range. The durability and environmental problem restrict its wide use in urban cities. The Helmholtz resonators can be employed to control the low frequency noise and enhance the noise reduction at the resonant frequency of the parallel barriers, however, the studies and applications are limited to the enclosed system such the duct or rooms. No literature investigates the acoustical

coupling of resonator on open domain such as the infinite baffled open cavity or the parallel barriers. For duct acoustics, it has been assessed theoretically and experimentally that the plate silencer works well for low frequency range. In this regard, it is proposed to install the plate backed by an acoustic cavity on the inner walls of the parallel barrier to obtain a broadband noise reduction especially at low frequency range.

Therefore, the overall objective in this study is to establish a comprehensive method to predict the sound field of the parallel barriers and develop a broadband passive device that can reduce the low frequency noise effectively. To achieve these objectives, the following three specific tasks are conducted. A first important aspect of the study is to investigate a theoretical model to calculate the sound distribution of the baffled open enclosure. Moreover, the resonator array is integrated to the enclosure walls regarded as the secondary sound sources to reduce the sound radiated from the baffled opening of the enclosure. To simplifying the theoretical model, a single resonator is to be studied in detail and the experimental validation is carried out to evaluate the accuracy of the model and the effectiveness of the resonator on noise reduction of the open enclosure. Secondly, the analysis of acoustical coupling for the infinite baffled open cavity (3D) is extended to the parallel barrier (2D) which the resonator array is installed inside the vertical barrier walls. A thorough hybrid modal combined the numerical and modal superposition method is proposed. Analyses allow the exploration of the working mechanisms and the performance optimization of the resonators on the parallel barriers. The third task of this study is the further noise reduction enhancement for the parallel barriers through the vibroacoustic interaction, in which the plate cavity is proposed to install on the inner side of the barrier walls. The acoustical coupling between the plate cavity and the parallel barrier domain is derived mathematically. A rigorous theoretical study is developed to compare the various design variables on the noise reduction

performance of such device. Moreover, the experimental study is also required to provide validations for the predictions and assessments of effectiveness of the proposed passive noise reduction device.

1.6 Outline of this thesis

The thesis is organized in six chapters. The first chapter presents the background of the land transportation noise to be issued in the work. At the same time, related previous work is reviewed. Motivations and objectives of this study are presented.

In Chapter 2, a numerical method which combined the fast multipole boundary element method (FMBEM) and the finite element method (FEM) is established for the parallel barriers when integrated with the flexible plate cavity system.

In Chapter 3, the first aim is to obtain the analytical rigorous formulas describing the sound field inside as well as outside the infinite baffled open rectangular cavity with a point sound source located at its bottom and coupled with a Helmholtz resonators array. Moreover, the coupled and shifted resonances of the baffled open cavity is derived mathematically. The accuracy of the proposed formulas based on the modal coupling is examined by comparison to the results obtained by BEM simulations. The mechanism and performance of noise reduction by single resonator is studies systematically. The results shows that combination with resonator, the noise level is decreased both inside and outside, which indicates the potential application in the street canyons and parallel barriers.

The acoustical coupling of the parallel barriers and the Helmholtz resonator array is investigated in Chapter 4. The theoretical model developed for infinite baffled open cavity is extended to parallel barriers above semi-infinite rigid ground. The sound field outside the barriers domain is obtained numerically because of the difficulty in finding the Green's function analytically for such an unbaffled cavity. In order to increase the

noise reduction of parallel barrier especially at the deteriorated frequencies, the optimal designed Helmholtz resonator is adopted to vary the acoustic mode. Finally, an experiment in anechoic chamber is carried out, verifying the effectiveness of the noise reduction enhancement by the Helmholtz resonator.

In Chapter 5, aiming for a wideband noise attenuation, the plate cavity is installed on the inside walls of the parallel barriers. A theoretical model is established to account for the vibroacoustic behavior of the parallel barriers after installed with the plate cavity. Following the similar steps, the accuracy of the developed model is first validated through the comparison with commercial software. Various parameters of the plate cavity is compared including the size of the backing cavity, the bending and mass ratio of the flexible plate. Vibroacoustic analysis on the plate shows that the plate plays as a reflector instead of absorber.

The major findings in this study will be summarized in Chapter 6. Recommends for the future work to increase the noise reduction for the parallel barriers will also be discussed briefly.

CHAPTER 2

THE FAST MULTIPOLE BOUNDARY ELEMENT METHOD FOR LARGE SCALE ACOUSTIC PROBLEMS IN THREE-DIMENSIONS

In this chapter, the numerical method for acoustical scattering and vibroacoustic coupling in large scale is introduced. The conventional boundary element method (CBEM) will be discussed first. The CBEM has limited application for acoustical diffraction and radiation problems with large scale elements due to the slow calculation speed. Therefore, the fast multipole boundary element method (FMBEM), which based on the fast multipole algorithm, is developed to accelerate the calculation of the CBEM. Aiming to calculate the vibroacoustic problems, the FMBEM is coupled with the finite element method (FEM). Three cases are presented at the end of this chapter to validate the accuracy and the efficiency of the proposed numerical method.

2.1 Conventional boundary element method (CBEM)

For steady-state acoustic wave problems, the partial differential equation in homogeneous isotropic acoustic media is Helmholtz equation:

$$\nabla^2 p(\vec{x}) + \left(\frac{\omega}{c}\right)^2 p(\vec{x}) = Q_s \delta(\vec{x} - \vec{x}_s) \tag{2.1}$$

where ω and c are the angular frequency and the sound speed in the media, respectively.

The boundary conditions used for BEM can be divided into three types:

- Dirichlet boundary condition, the sound pressure is obtained by:

$$p(\vec{x}) = \bar{p}(\vec{x}) \tag{2.2}$$

- Neumann boundary condition, the normal velocity is defined as:

$$q(\vec{x}) = \frac{\partial}{\partial n} p(\vec{x}) = -i\rho\omega\upsilon_n \tag{2.3}$$

- Robin boundary condition, the normal impedance is given by:

$$p(\vec{x}) = Z\upsilon_n(\vec{x}) \tag{2.4}$$

According to the appropriate boundary conditions, the general solution to Eq.(2.1) in three dimensions is:

$$G(\vec{x},\vec{y}) = \frac{e^{-ikr}}{4\pi r} \tag{2.5}$$

where, *r* represents the distance from the point $\vec{x}$ to $\vec{y}$.

The integral solution to the inhomogeneous Helmholtz equation (Eq.(2.1)) is represented by,

$$p(\vec{x}) = \int_S \left(G(\vec{x},\vec{y}) q(\vec{y}) - p(\vec{y}) \frac{\partial G(\vec{x},\vec{y})}{\partial n} \right) dS + p^I(\vec{x},\vec{y}_s) \tag{2.6}$$

where $\vec{x}$ and $\vec{y}$ are the points in the computational domain and $p^I(\vec{x},\vec{y}_s)$ is the incident wave located at $\vec{y}_s$.

Locating the source point on the boundary, one can obtain the conventional boundary integral equation as,

$$c(\vec{x})\, p(\vec{x}) = \int_S \left(G(\vec{x},\vec{y}) q(\vec{y}) - p(\vec{y}) \frac{\partial G(\vec{x},\vec{y})}{\partial n} \right) dS + p^I(\vec{x},\vec{y}_s) \tag{2.7}$$

where $c(\vec{x})$ is the constant related to the source point location. If the integration part is smooth around $\vec{x}$, $c(\vec{x})$ is set to -0.5. When located at the sharp corners, $c(\vec{x})$ is

determined by the solid angle [88].

Discretizing the boundary surface into N_e elements:

$$\sum_{i=1}^{N_e} S_i \approx S \tag{2.8}$$

Then the integral in Eq.(2.7) can be rewritten in the summation form as:

$$c(\vec{x})\, p(\vec{x}) = \sum_{i=1}^{N_e} \int_{S_i} G(\vec{x},\vec{y})\, q(\vec{y})\, dS_i + \sum_{i=1}^{N_e} \int_{S_i} p(\vec{y}) \frac{\partial G(\vec{x},\vec{y})}{\partial n} dS_i + p^I(\vec{x},\vec{y}_s) \tag{2.9}$$

Setting the points $\vec{x}$ on the boundary surface, and defining:

$$\begin{aligned} p &= \sum_{i=1}^{n} p_i N_i(\xi) \\ v_n &= \sum_{i=1}^{n} v_{ni} N_i(\xi) \end{aligned} \tag{2.10}$$

$$\begin{aligned} G_{ij} &= -i\rho\omega \int_{S_j} G(\vec{x}_j,\vec{y}_i) N_i dS_i \\ H_{ij} &= -i\rho\omega \int_{S_j} \frac{\partial G(\vec{x}_j,\vec{y}_i)}{\partial n} N_i dS_i + c_i \delta_{ij} \end{aligned} \tag{2.11}$$

where p_i and v_{ni} are the sound pressure and the particle normal velocity at the nodes on the boundary surface, and N_i are the shape functions. δ is the Dirac delta function.

Substituting the above Eqs.(2.10) and (2.11) into Eq.(2.9) and yields

$$\sum_{i=1}^{N_e} H_{ij} p_i = \sum_{i=1}^{N_e} G_{ij} v_{ni} + p^I \tag{2.12}$$

The above equation is the general form of the conventional boundary element method and can be expressed as

$$\mathbf{Hp} = \mathbf{Gv_n} + \mathbf{p^I} \tag{2.13}$$

According to the boundary conditions, once we obtain the unknown variables of p and v_n on boundary surface from solving Eq.(2.13), we can evaluate the acoustic pressure within the domain.

2.1.1 The Non-uniqueness solution

When Eq.(2.7) is used to calculate the exterior acoustic problems, non-uniqueness difficulty will occur at certain characteristic frequencies associated with the corresponding interior Dirichlet problem. In the past fifty years, many efforts have been focused to address this non-uniqueness issues [89-91]. Of the developed methods, Combined Helmholtz integral equation formulation (CHIEF) [89] and Burton-Miller formula [90] are the most effective and popular ones.

In 1968, Schenck [89] proposed the CHIEF to handle the non-uniqueness issue in CBEM. The basic idea of CHIEF is as follows. Some points in the interior domain are added to aerate Helmholtz integral equations, resulting an over-determined form for system matrix. The CHIEF is convenient to use but there are two drawbacks that restrict its practical use. The first disadvantage is that the additional interior points are proportional to the wave number. As the wave number increases, more inserting points are needed to maintain accuracy. Large number of interior points increases the dimension of the system matrix and results in the loss of efficiency at high frequency range. More importantly, there are no analytical methods that can be used to determine how many interior elements should be added and where they should be located. These interior points are often introduced on a trial-and error basis.

On the other hand, the Burton-Miller method [90] is alternatively used to deal with the non-uniqueness difficulty concerning the accuracy and convenience for wide frequency range. In this method, the conventional boundary integral equation (Eq.(2.7)) and its normal derivative are proposed to combine together through a constant. As shown in the rigorous derivations, the Burton-Miller formulation proves to be successful to deal with non-uniqueness issue at all frequencies. The negative aspect of this method is that the combination leads to the integration doubles:

$$\left[\int_S \frac{\partial G(\vec{x},\vec{y})}{\partial n(\vec{y})} p(\vec{y}) dS(\vec{y}) + c(\vec{x}) p(\vec{x}) - p^I(\vec{x}) + \alpha \int_S \frac{\partial^2 G(\vec{x},\vec{y})}{\partial n(\vec{y}) \partial n(\vec{x})} p(\vec{y}) dS(\vec{y})\right] \quad (2.14)$$
$$= \int_S G(\vec{x},\vec{y}) q(\vec{y}) dS(\vec{y}) + \alpha \left[\int_S \frac{\partial G(\vec{x},\vec{y})}{\partial n(\vec{y})} q(\vec{y}) dS(\vec{y}) + c(\vec{x}) q(\vec{x}) - q^I(\vec{x})\right]$$

2.1.2 Methods to solve the singularity

As shown in Eq.(2.14), the Green function and its derivatives cause the singularity difficulties. The Green function and its derivatives used in the Burton-Miller method in three dimensions are:

$$G(\vec{x},\vec{y}) = \frac{e^{-ikr}}{4\pi r} \quad (2.15)$$

$$\frac{\partial G(\vec{x},\vec{y})}{\partial n(\vec{y})} = \frac{1}{4\pi r^2}(ikr-1)\frac{\partial r}{\partial y} n(\vec{y}) e^{-ikr}, \quad (2.16)$$

and

$$\frac{\partial^2 G(\vec{x},\vec{y})}{\partial n(\vec{x}) \partial n(\vec{y})} = \frac{1}{4\pi r^3}\left\{(1-ikr) n(\vec{y}) + \left[k^2 r^2 - 3(1-ikr)\right]\frac{\partial r}{\partial y} n(\vec{y})\right\} n(\vec{x}) e^{-ikr} \quad (2.17)$$

which $G(\vec{x},\vec{y})$, $\partial G(\vec{x},\vec{y})/\partial n(\vec{y})$ and $\partial^2 G(\vec{x},\vec{y})/\partial n(\vec{x})\partial n(\vec{y})$ is weakly singular, strongly singular and hyper singular, at $r = 0$, respectively. The weak singularity is easy to tackle and can be evaluated by the Gauss method. Special care should be focused on the strong and hyper singularity. Many methods have been developed to calculate the hyper-singularity and in this study we adopt the method proposed by Silva *et al.* [92] to circumvent this problem. Main steps of this method has been list in the appendix C.

2.2 Fast multipole BEM (FMBEM)

Although the BEM is easy in use for sound scattering problems with complicated

geometries in infinite space, its efficiency in solving large-scale problems still limits its wide application. For example, discretizing parallel barriers into 10000 constant elements, the calculation time is about 3 hours for a single frequencies at a typical personal computer.

As discussed in Chapter 1, the system matrix formed in BEM is dense and nonsymmetrical. The operations to calculate such a matrix is $O\left(N_{dof}{}^{2}\right)$, where N_{dof} is the number of elements if constant element is used. The solution of ***Ax=b*** is another expensive task and the calculations are $O\left(N_{dof}{}^{3}\right)$ if the direct solver is used. Therefore, the calculation efficiency of the BEM is decreased as the increase of the boundary elements and limits the application of this method for acoustic scattering problem in large scale. In the past fewer decades, many methods have been proposed to accelerate the calculation for BEM, A comprehensive review about these methods was discussed in Ref.[93]. In this work, fast multipole method (FMM) is chosen to speed up the calculation for the BEM. The BEM hereafter represents the conventional BEM modified based on the Burton-Miller formula.

The principle for fast multipole algorithm is that the Green's functions can be decomposed into the combination of two parts:

$$G\left(\vec{x},\vec{y}\right)=\sum_{i}G_{x,i}\left(\vec{x},\vec{y}_{c}\right)G_{y,i}\left(\vec{y},\vec{y}_{c}\right) \tag{2.18}$$

where $\vec{y}_c$ is the expansion point which satisfies that condition that $\left|\vec{y}-\vec{y}_{c}\right|<\left|\vec{x}-\vec{y}_{c}\right|$. This procedure can be achieved by means of various expansions methods. In this way, the relationships between $\vec{x}$ and $\vec{y}$ is changed to the combinations of $\vec{x}$ to $\vec{y}_c$ and $\vec{y}$ to $\vec{y}_c$.

Fig 2.1 illustrates the comparison of the computational complexity in the BEM and FMBEM. The solid circle represents the source point and the open circle represents the

field point. The gray dashed circle is the expansion point which satisfying the condition $|\vec{y}-\vec{y}_c|<|\vec{x}-\vec{y}_c|$ and lines represent the computations among the source points, the field points and the expansion points. As shown in Fig 2.1(a), the interactions between the elements $\vec{x}$ and $\vec{y}$ are calculated one by one. When the source element $\vec{x}$ changes, the interactions between $\vec{x}$ and $\vec{y}$ should be calculated again. As compared, when chosen an expansion point $\vec{y}_c$ approximately, the interactions between these elements $\vec{x}$ and $\vec{y}$ are connected through the expansion point and hence the computations among these elements are simplified. More importantly, the operations for the interactions of $\vec{x}$ and $\vec{y}_c$, $\vec{y}$ and $\vec{y}_c$ will be conducted only once when the source point move to others.

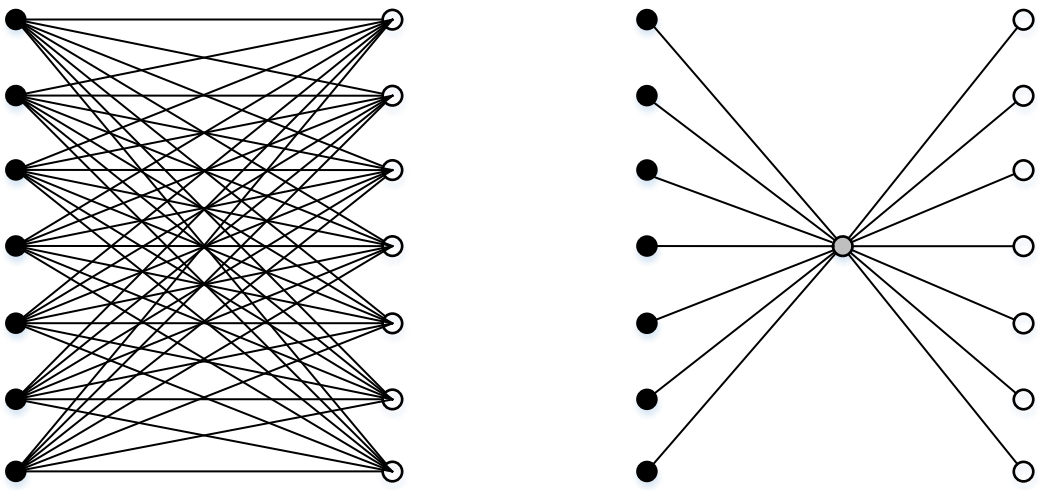

(a) BEM (b) FMBEM

Fig 2.1: The complexity comparison between (a) CBEM and (b) FMBEM.

In other words, in the BEM, any changes in $\vec{x}$ lead to the reevaluation of the entire integral. While in the FMBEM, after the relationships of the source points $\vec{x}$ and the field points $\vec{y}$ satisfying $|\vec{y}-\vec{y}_c|<|\vec{x}-\vec{y}_c|$, the original integral about the Green's function is computed based on the expression as shown in Eq. (2.18). The new integrals need to be evaluated only once even though the $\vec{x}$ moves to other positions. In this

regards, the interactions of $\vec{y}$ and $\vec{y}_c$ are independent of the locations of $\vec{x}$. Therefore, a dramatic decrease of calculations can be obtained as illustrated by the lines shown in Fig 2.1.

At the beginning of section 2.2, the fundamental mechanism of the reduction in calculations of using FMBEM is analyzed. The main procedure of FMBEM is described in the following parts. The wideband expansion algorithm will be presented in the next section.

2.2.1 Methodology and steps

2.2.1.1 Discretization

Firstly, the whole boundary surface is discretized and form a set of boundary elements, which rectangular or triangle elements used in three dimensions. The size of the elements can be referred to the recommendation by Marburg [94]. This step is the same as that adopted by conventional BEM.

2.2.1.2 Tree structure

In three dimensions, the octree is used to divide the domain into sub cubic boxes. Shown in Fig 2.2 is the tree structure for a sphere as an example. Here, the elements generated in the discretization step is represented by the color points.

The details of the division can be described as follows:

(1) First a cubic box that covers all the boundary elements (as shown by the color points in Fig 2.2) and call this box the cell at level 0. Generally the cubic box is a little bigger than the entire boundary that can enclose all the elements.

(2) Divide this parent cell into eight child cells of level 1, as shown in the Fig 2.2 (a). The No. of these child cells is in the sequence from 0 to 7.

(3) Continue dividing the cubic box until the elements number in each cell is less than or equal to a prescribed number. The refined tree structure is shown in Fig 2.2 (b). The number of the boundary elements in a refinement cell varies from 1 to 100. A smaller number need more calculation and therefore suppress the efficiency of the fast multipole method.

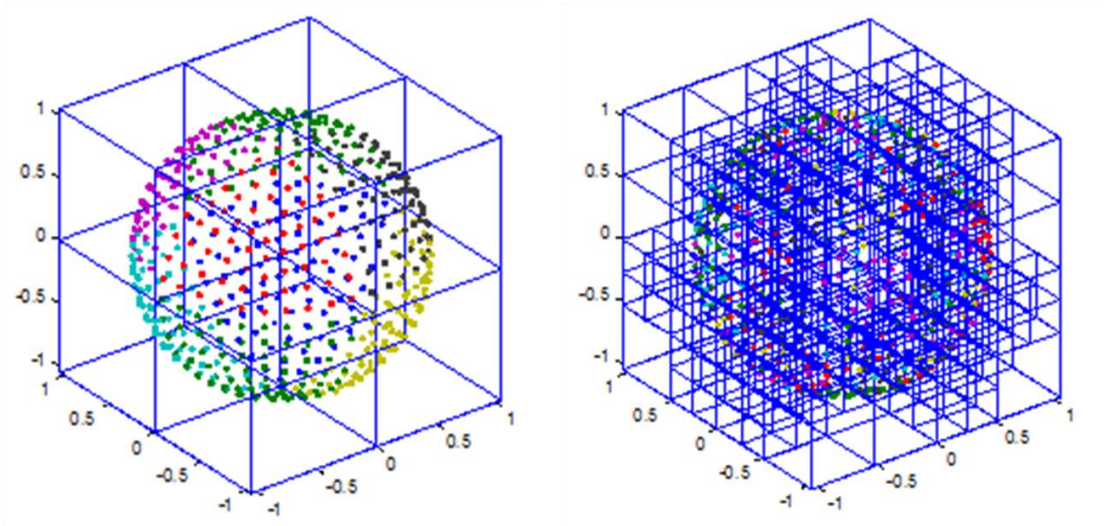

Fig 2.2: The octree structure: (a) eight cells at level 1; (b) the refinement cells.

A childless cell is called a leaf. The size of a cell at level l is given by $L_0 \Big/ \left(2^{i-1}\right)^l$, with L_0 being the size of the largest cell at level 0 and i=3 for the three dimensional problems. In this process, an element can be considered to be within a cell when the element center is inside that cell. An octree structure is thus formed after the above procedures are completed.

After the tree structure process, the cell relationship has been built. The adjacent cells are called for two cells at same level and share at least one common vertex. For two leaf cells at different levels, if the parent cell of one of the leaf cells shares at least

a common vertex with the other leaf cell, they are also said to be adjacent cells. Two cells at same level are called well separated if they are not adjacent at this level but their parent cells are adjacent at their father level. The list of all the well separated cells from the interaction list of cell *C*. The left cells are called far cells of cell *C*. Shown in Fig 2.3 indicates the relations of cell C and its adjacent cells, cells in interaction list and far cells. Their corresponding locations are also shown in this figure.

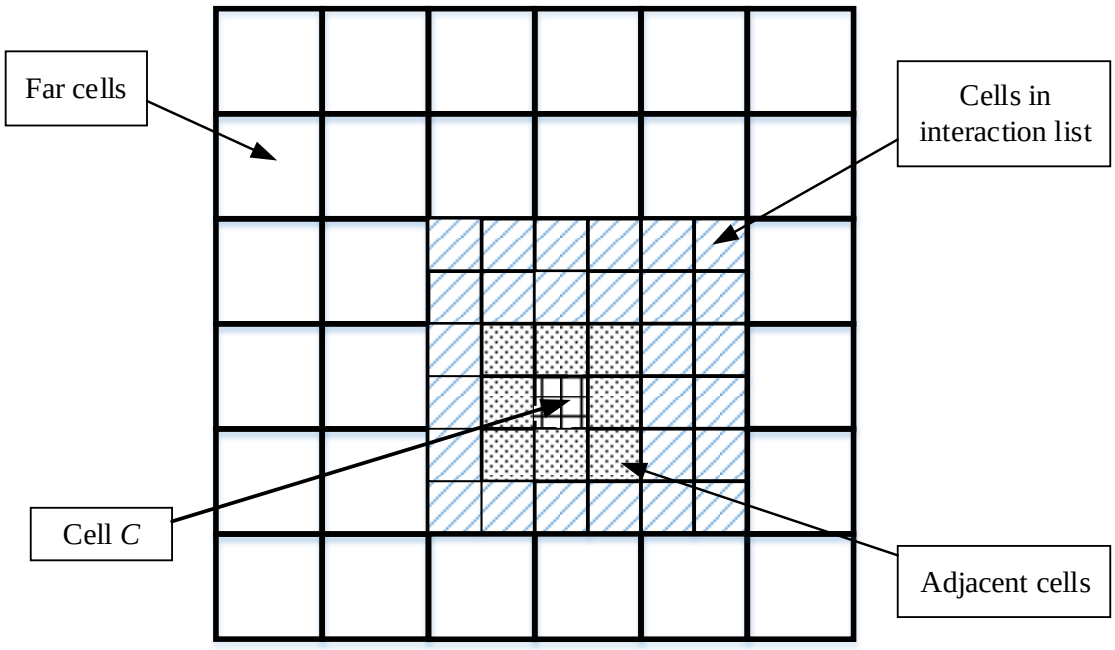

Fig 2.3: The relations for the cell C and other cells.

2.2.1.3 Multipole translation

The main multipole translations in the FMBEM is depicted in Fig 2.4, including the multipole moments expansion, multipole to multipole (M2M) translation, multipole to local (M2L) translation, local to local (L2L) translation and local moments expansion.

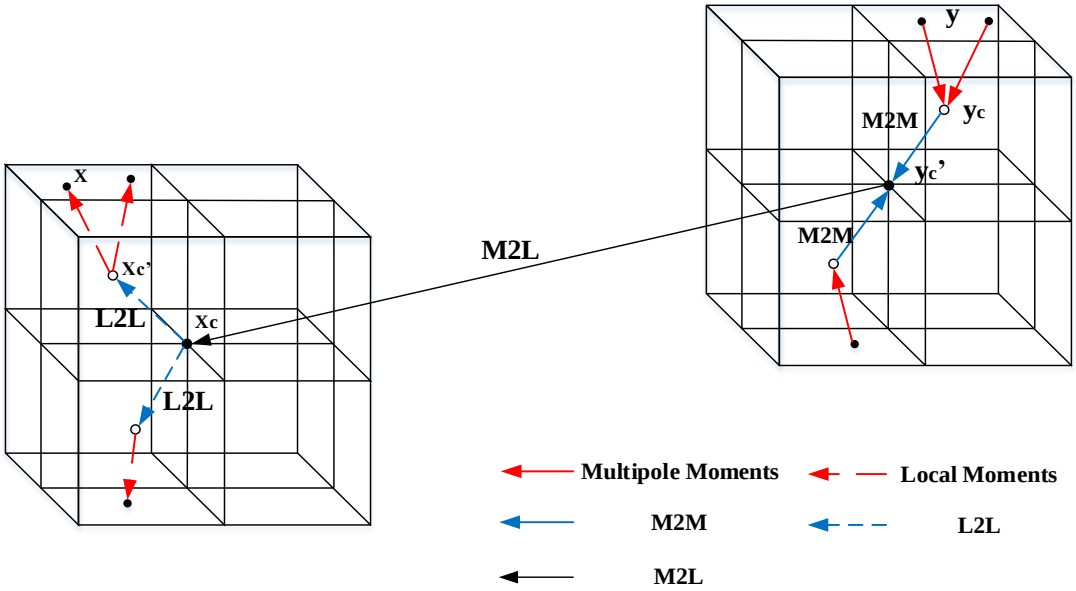

Fig 2.4: The sketch of the multipole expansions and translations.

The first step is to compute the multipole expansions based on the centroids of all childless cells. These multipole expansions hold for $\vec{x}$ and $\vec{y}$. Each element inside the cell is expanded around the centroid $\vec{y}_c$ of the cell which satisfies $|\vec{y}-\vec{y}_c|<|\vec{x}-\vec{y}_c|$. Such expansions is added together forming one set of multipole moments, as illustrated in Eqs.(2.19) and (2.20). This step is called multipole moments expansion which is indicated by the solid red line in Fig 2.4, with the arrow representing the direction of expansion.

$$G(\vec{x},\vec{y})=\sum_{m=-n}^{n} O_n(\vec{x},\vec{y}_c)\,I_n(\vec{y},\vec{y}_c) \tag{2.19}$$

$$M_n(\vec{y}_c)=\sum_j \int_{s_j} I_{n,j}(\vec{y},\vec{y}_c)\,ds_j \tag{2.20}$$

The details about $O_n(\vec{x},\vec{y}_c)$, $I_n(\vec{y},\vec{y}_c)$ and $M_n(\vec{y}_c)$ will be discussed in the following section.

Subsequently, the expansion centroid is moved from the $\vec{y}_c$ of the childless cell to $\vec{y}_c{}'$ of its father cell if satisfying $\left|\vec{y}-\vec{y}_c'\right|<\left|\vec{x}-\vec{y}_c'\right|$. All the moments from the

centroids of the childless cells at all levels are shifted to the centroids of their father cells and this process continues to level 2. Thus, the influence of all the elements inside each cell is translated. The translation of multipole expansions from cell centroids at child level to their parents' centroids at upward level is called multipole to multipole (M2M) translation in the literature, and the solid blue line in Fig 2.4 indicates this process.

$$M2M\left(\vec{y}_c{}'\right)=\sum_{n'}^{\infty}W_{n'}I_{n'}\left(\vec{y}_c{}',\vec{y}_c\right)M_{n'}\left(\vec{y}_c\right) \tag{2.21}$$

In the next step, represented by the solid black line in Fig 2.4, the multipole expansions for the cell *C* at level *l* are converted to local expansions of cells in *C*'s interaction list. These conversions are about the multipole expansions to local representations for the cells in interaction list and are often referred as multipole to local (M2L) expansions.

$$M2L\left(\vec{x}_c\right)=\sum_{n'=0}^{\infty}W_{n'}\tilde{O}_{n'}\left(\vec{x}_c,\vec{y}_c{}'\right)M2M_{n'}\left(\vec{y}_c{}'\right) \tag{2.22}$$

After finish the M2L, all the local representations are then shifted to their children until reaching the childless cell. In Fig 2.4, the dashed blue line represents this operation. This step is defined as local to local (L2L) translation.

$$L2L\left(\vec{x}_c{}'\right)=\sum_{n=0}^{\infty}W_nI_n\left(\vec{x}_c,\vec{y}_c{}'\right)M2L_n\left(\vec{x}_c\right) \tag{2.23}$$

The multipole to multipole (M2M) translation and local to local (L2L) translation are also called respectively as the upward pass and downward pass.

Finally, the calculations for the source point and far away field point can be obtained after the local expansions using the Eq. (2.24).

$$G\left(\vec{x},\vec{y}\right)=\sum_{m=-n}^{n}L2L\left(\vec{x}_c{}'\right)I_n\left(\vec{x},\vec{x}_c{}'\right) \tag{2.24}$$

The above expansions and translations are for the far elements. However, the

influence from the nearby elements should be evaluated in a direct way. The elements in the same cell and its adjacent cells are regarded as the nearby elements and their integrals are calculated directly as in the conventional BEM. These calculations are sketched in Fig 2.5 shows the calculations through the FMBEM and the CBEM.

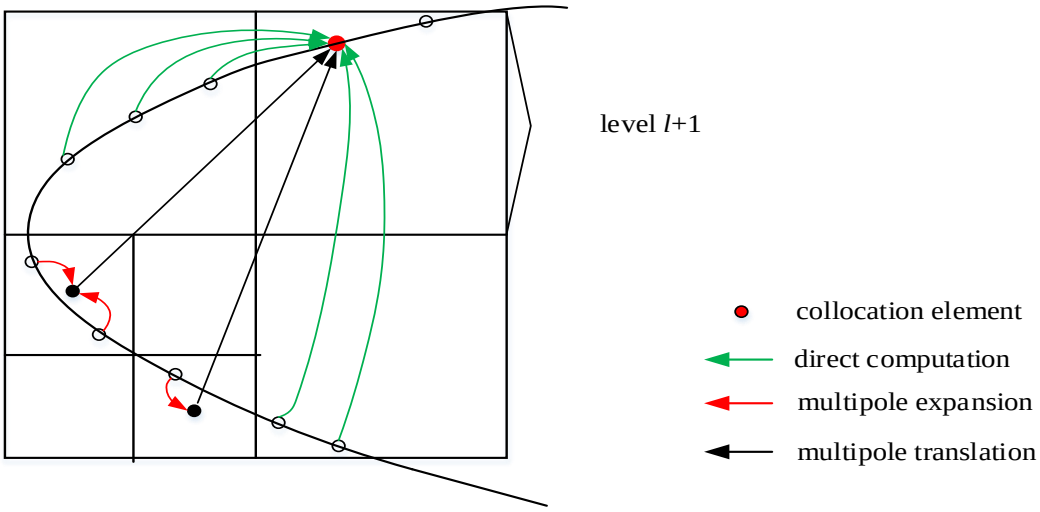

Fig 2.5: The direct and multipole translation step.

Therefore, the integral on the source point $\vec{x}$ can be expressed as:

$$\int_S G(\vec{x},\vec{y})dS = \int_{S_N} G(\vec{x},\vec{y})dS_N + \int_{S_F} G(\vec{x},\vec{y})dS_F \qquad (2.25)$$

where the integral on S_N is done by direct integration as in the BEM, and the integral on S_F is done by the fast multipole algorithm. Then the integrals work together to generate the matrix in the form of $\boldsymbol{A}\lambda = \boldsymbol{b}$ where the field variables are obtained.

Till now, the main procedures for the fast multipole is presented.

2.3 Wideband multipole expansion

To be accurate, any calculation based on the discretization must resolve the smallest wavelengths of interest. Besides, the discretization should accurately represent the boundary surface at low frequencies. Thus, for the acoustic simulations in FMBEM,

there are two basic regimes: the low-frequency and the high-frequency regimes. These regimes can be characterized by the parameter kD, which is in terms of the product by the wavenumber k and the cell size D. The threshold value $(kD)^*$ is often used to recognize these two regimes. The low-frequency regime is set when $kD < (kD)^*$ and the high-frequency regime is set for $kD > (kD)^*$. However, the computational complexity of the FMM for these two regimes is different [39].

(1) Low-frequency regime

In this regime, the computational cost of the FMM is proportional to the degree of freedoms (Dofs) and affected little by the parameter of kd. Here, the most efficient expansion and translation method is based on the spherical multipole wave functions and the rotation-coaxial translation-back-rotation (RCR) decompositions [39, 95].

(2) High-frequency regime

In the high-frequency regime, the parameter of kD heavily affects the computational cost and hence the efficiency. Since the wavenumber k is inversely proportional to wavelength and, in practice, more boundary elements are required for accuracy at high-frequency regime. In this regime, the diagonal FMM translations based on the plane wave expansion is suitable.

Each of these two expansion methods fails in some way outside its preferred regime: the partial wave expansion needs high computational cost in the high-frequency regime; the plane wave expansion result in numerically unstable problems at the low-frequency regime. In each case, the difficulty is fundamental, and cannot be removed by simple expedients. Thus, there exist problems restrict the application in the broadband calculation for either of the two approaches.

Alternatively, the ‘‘hybrid’’ scheme or the wideband fast multipole method is

constructed to deal with the wave problem in wide frequency range. The partial wave expansion is applied on the subwavelength levels of subdivision, and then transitioned to the plane wave expansion once the plane wave expansion are stable. An assessment of these formulations is provided in the work by Cheng et al. [96]. Here, we describe briefly the wideband FMM formulations used for the Helmholtz equation in three dimensions. These include the partial wave expansion method combined with the rotation-coaxial translation method and the plane wave expansion method.

2.3.1 Low-frequency regime

In the low-frequency regime, the partial wave expansion together with rotation-coaxial translation method is used for the multipole expansion and translation.

According to the partial wave expansion method, the Green's function in three dimensions can be expanded as:

$$G(\vec{x},\vec{y}) = \frac{ik}{4\pi}\sum_{n=0}^{\infty}(2n+1)\sum_{m=-n}^{n} O_n^m\left(\overrightarrow{ox}\right)\bar{I}_n^m\left(\overrightarrow{oy}\right) \tag{2.26}$$

in which

$$\begin{aligned} O_n^m\left(\overrightarrow{ox}\right) &= h_n^{(1)}(kr)Y_n^m(\theta,\phi) \\ I_n^m\left(\overrightarrow{oy}\right) &= j_n(kr)Y_n^m(\theta,\phi) \\ Y_n^m(\theta,\phi) &= \sqrt{\frac{(n-m)!}{(n+m)!}}P_n^m(\cos\theta)e^{jm\phi} \\ P_n^m(x) &= (-1)^m\left(1-x^2\right)^{m/2}\frac{d^m}{dx^m}P_m(x) \end{aligned} \tag{2.27}$$

In the above expansions, $\bar{I}_n^m$ is the complex conjugate of I_n^m. (r,θ,ϕ) represent the spherical coordinates of the vectors $\overrightarrow{ox}$ and $\overrightarrow{oy}$. $P_n(x)$ denotes the Legendre polynomial of degree *n*. $h_n^{(1)}$ is the first kind spherical Bessel function of the *n*-th order, and, j_n is the first kind spherical Hankel function of the *n*-th order and Y_n^m the spherical

harmonics.

Substituting above Eq.(2.26) into Eq.(2.14) , the boundary integrals can be written as

$$\begin{aligned}&\int_{So}\left[G(\vec{x},\vec{y})q(\vec{y})-\frac{\partial G(\vec{x},\vec{y})}{\partial n(\vec{y})}p(\vec{y})\right]dS\\&=\frac{ik}{4\pi}\sum_{n=0}^{\infty}(2n+1)\sum_{m=-n}^{n}O_n^m\left(\overrightarrow{ox}\right)M_n^m\left(\vec{o}\right)\end{aligned}\tag{2.28}$$

$$\begin{aligned}&\int_{So}\left[\frac{\partial G(\vec{x},\vec{y})}{\partial n(\vec{y})}q(\vec{y})-\frac{\partial^2 G(\vec{x},\vec{y})}{\partial n(\vec{y})\partial n(\vec{x})}p(\vec{y})\right]dS\\&=\frac{ik}{4\pi}\sum_{n=0}^{\infty}(2n+1)\sum_{m=-n}^{n}\frac{\partial}{\partial n(\vec{x})}O_n^m\left(\overrightarrow{ox}\right)M_n^m\left(\vec{o}\right)\end{aligned}\tag{2.29}$$

where S_O is the discretized elements inside the childless cell whose centroid at $\vec{o}$. Each element inside the cell is expanded around the cell centroid based on the Eqs.(2.28) -(2.29). Then a total multipole moment by the summation of the expansions from each element inside the cell.

Based on the formulas in Eq.(2.26), the multipole moments can be written as

$$M_n^m\left(\vec{o}\right)=\int_{So}\left[\frac{\partial p(\vec{y})}{\partial n(\vec{y})}\bar{I}_n^m\left(\overrightarrow{oy}\right)-\frac{\partial \bar{I}_n^m\left(\overrightarrow{oy}\right)}{\partial n(\vec{y})}p(\vec{y})\right]dS\tag{2.30}$$

The M2M (Eq.(2.31)), M2L (Eq.(2.32)) and L2L (Eq.(2.33)) are given by

$$M_n^m(\vec{o}\,')=\sum_{n'=0}^{\infty}\sum_{m'=-n'}^{n'}\sum_{l=|n-n'|}^{n+n'}(2n'+1)(-1)^{m'}W_{n,n',m,m',l}I_l^{-m-m'}\left(\overrightarrow{o'o}\right)M_{n'}^{-m'}(\vec{o})\tag{2.31}$$

$$L_n^m(\vec{o}\,')=\sum_{n'=0}^{\infty}\sum_{m'=-n'}^{n'}\sum_{l=|n-n'|}^{n+n'}(2n'+1)W_{n',n,m',m,l}\tilde{O}_l^{-m-m'}\left(\overrightarrow{oo'}\right)M_{n'}^{m'}(\vec{o})\tag{2.32}$$

$$L_n^m(\vec{o}\,')=\sum_{n'=0}^{\infty}\sum_{m'=-n'}^{n'}\sum_{l=|n-n'|}^{n+n'}(2n'+1)(-1)^{m}W_{n',n,m',-m,l}I_l^{m-m'}\left(\overrightarrow{oo'}\right)M_{n'}^{m'}(\vec{o})\tag{2.33}$$

In Eq.(2.31), $\vec{o}\,'$ is the centroid of a parent cell at level *l* and $\vec{o}$ is the centroid of one of its children as used on Eq.(2.30) at level *l*+1. In Eq.(2.32), $\vec{o}\,'$ is the centroid of a cell

which located in the interaction list of cell $\vec{o}$. And in Eq.(2.33), the down pass is carried out and $\vec{o}'$ is the centroid of a child cell at level *l*+1 and $\vec{o}$ is the centroid of its father cell at level *l*. As can be found obviously, in the summations of $\sum_{l=|n-n'|}^{n+n'}$, *l* are calculated only for even values of $n+n'-l$. $W_{n,n',m,m',l}$ is computed using the following form as

$$W_{n,n',m,m',l} = (2l+1) i^{n'-n+1} \begin{pmatrix} n & n' & l \\ 0 & 0 & 0 \end{pmatrix} \begin{pmatrix} n & n' & l \\ m & m' & t \end{pmatrix} \tag{2.34}$$

where $\begin{pmatrix} a & b & c \\ d & e & f \end{pmatrix}$ represents the Wigner 3j operator and t equals to $m-m'$.

Finally, the boundary integral equations after the local expansions can be given by the following equation:

$$\begin{aligned} &\int_{So} \left[\frac{\partial p(\vec{y})}{\partial n_y} G(\vec{x},\vec{y}) - \frac{\partial G(\vec{x},\vec{y})}{\partial n_y} p(\vec{y}) \right] dS \\ &= \frac{ik}{4\pi} \sum\nolimits_{n=0}^{\infty} (2n+1) \sum\nolimits_{m=-n}^{n} \bar{I}_n^m \left(\overrightarrow{ox}\right) L_n^m \left(\vec{o}\right) \end{aligned} \tag{2.35}$$

$$\begin{aligned} &\int_{So} \left[\frac{\partial G(\vec{x},\vec{y})}{\partial n_y} q(\vec{y}) - \frac{\partial^2 G(\vec{x},\vec{y})}{\partial n_y \partial n_x} p(\vec{y}) \right] dS \\ &= \frac{ik}{4\pi} \sum\nolimits_{n=0}^{\infty} (2n+1) \sum\nolimits_{m=-n}^{n} \frac{\partial}{\partial n_x} O_n^m \left(\overrightarrow{ox}\right) M_n^m \left(\vec{o}\right) \end{aligned} \tag{2.36}$$

The rotation-coaxial translation method is used to accelerate the translations in M2M, M2L and L2L. The method includes the operations of rotating the z Cartesian axis towards the direction of translation, then executing the translation along the new z axis and, finally, performing another rotation back to the original Cartesian system. The computational complexity of translations in the partial wave expansion method are proportional to $O\left(N_t^5\right)$, with N_t denotes to the maximum truncation terms used in the FMM series, as compared, in the rotation-coaxial translation method the computational

cost is reduced to $O\left(N_t^3\right)$ after the rotations and translations are performed based on the z direction. A comprehensive progress and the computation complexity can be found in the following Fig 2.6.

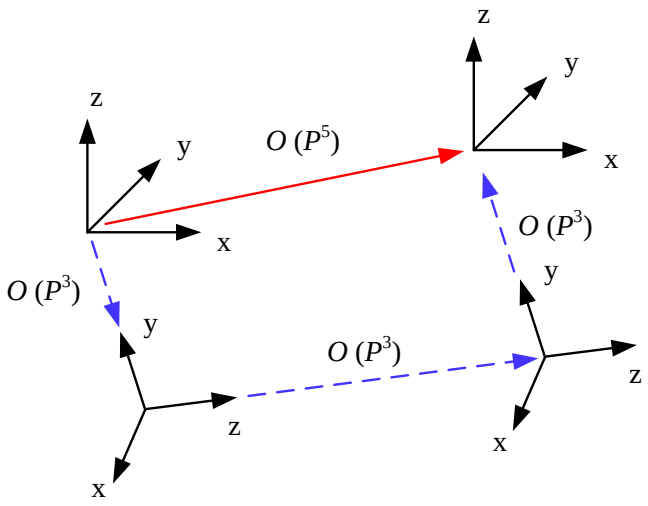

Fig 2.6: Rotation-Coaxial Translation and Computational Complexity.

Before rotation, the Euler angles $\left(\alpha_E,\beta_E,0\right)$ for three dimensions should be defined. Along z axis direction, the forward rotation can be conducted by applying a rotation of $\left(\alpha_E,\beta_E,0\right)$ and the backward rotation can be carried out by applying a rotation of $\left(-\alpha_E,-\beta_E,0\right)$.

The rotation matrices $R_n^{m,m'}\left(\beta_E\right)=R_n^{m',m}\left(-\beta_E\right)$ is given by

$$R_n^{m,m'}\left(\beta_E\right)=\left[\left(n+m'\right)!\left(n-m'\right)!\left(n+m\right)!\left(n+m\right)!\right]^{1/2}$$
$$\times\sum_{s=max(0,m-m')}^{min(n+m,n-m')}\frac{\left(-1\right)^{m'-m+s}\left(\cos\frac{\beta_E}{2}\right)^{2n+m-m'-2s}\left(\sin\frac{\beta_E}{2}\right)^{m'-m+2s}}{\left(n+m-s\right)!\left(m'-m+s\right)!\left(n-m'-s\right)!s!} \tag{2.37}$$

Therefore, the M2M, which based on the partial wave expansion and the rotation-coaxial translation method are carried out by Eqs.(2.38),(2.39) and (2.40).

$$\tilde{M}_n^m\left(\vec{o}\right)=\sum_{m'=-n}^{n}R_n^{m',m}\left(\beta_E\right)e^{im'\alpha_E}M_n^{m'}\left(\vec{o}\right) \tag{2.38}$$

$$\tilde{M}_n^m(\vec{o}') = \sum_{n'=0}^{\infty} T_{n,n'}^m(M2M)\tilde{M}_n^m(\vec{o}) \tag{2.39}$$

$$M_n^m(\vec{o}') = \sum_{m'=-n}^{n} R_n^{m,m'}(\beta_E) e^{-im\alpha_E} \tilde{M}_n^{m'}(\vec{o}') \tag{2.40}$$

$$T_{n,n'}^m(M2M) = \sum_{n'=0}^{\infty} \sum_{l=|n-n'|}^{n+n'} (2n'+1)(-1)^{-m} W_{n,n',m,-m,l}\, j_l\left(k\left|\overrightarrow{o'o}\right|\right) \tag{2.41}$$

in which, angles shown by α_E and β_E are respective equal to the azimuthal and polar angles of $\vec{o}$.

The M2L are carried out by Eqs. (2.42), (2.43) and (2.44).

$$\tilde{M}_n^m(\vec{o}) = \sum_{m'=-n}^{n} R_n^{m',m}(\beta_E) e^{im'\alpha_E} M_n^{m'}(\vec{o}) \tag{2.42}$$

$$\hat{L}_n^m(\vec{o}') = \sum_{n'=0}^{\infty} T_{n,n'}^m(M2L)\tilde{M}_n^{-m}(\vec{o}) \tag{2.43}$$

$$L_n^m(\vec{o}') = \sum_{m'=-n}^{n} R_n^{m,m'}(\beta_E) e^{-im\alpha_E} L_n^{m'}(\vec{o}') \tag{2.44}$$

$$T_{n,n'}^m(M2L) = \sum_{n'=0}^{\infty} \sum_{l=|n-n'|}^{n+n'} (2n'+1)(-1)^{-m} W_{n',n,-m,m,l}\, h_l\left(k\left|\overrightarrow{o'o}\right|\right) \tag{2.45}$$

The L2L are carried out by Eqs.(2.46),(2.47) and (2.48).

$$L_n^m(\vec{o}) = \sum_{m'=-n}^{n} R_n^{m',m}(\beta_E) e^{-im'\alpha_E} L_n^{m'}(\vec{o}) \tag{2.46}$$

$$L_n^m(\vec{o}') = \sum_{n'=0}^{\infty} T_{n,n'}^m(L2L) L_{n'}^m(\vec{o}) \tag{2.47}$$

$$L_n^m(\vec{o}') = \sum_{m'=-n}^{n} R_n^{m,m'}(\beta_E) e^{im\alpha_E} L_n^{m'}(\vec{o}') \tag{2.48}$$

$$T_{n,n'}^m(L2L) = \sum_{n'=0}^{\infty} \sum_{l=|n-n'|}^{n+n'} (2n'+1)(-1)^{m} W_{n',n,m,-m,l}\, j_l\left(k\left|\overrightarrow{o'o}\right|\right) \tag{2.49}$$

Therefore, the boundary integrals modified by the Burton-Miller method can be

solved in the low frequency range.

2.3.2 High-frequency regime

In the high-frequency regime, the FMM is carried out based on the plane wave expansion. According to this method, the Green's function in three dimensions is written as:

$$G(\vec{x},\vec{y}) = \frac{ik}{16\pi^2}\iint e^{-ik\vec{\cdot}\overrightarrow{oy}} D\left(\overrightarrow{ox},\vec{k}\right) d\left(\vec{k}/|\vec{k}|\right) \tag{2.50}$$

$$D\left(\overrightarrow{ox},\vec{k}\right) = \sum_{n=0}^{\infty} i^n (2n+1) h_n^{(1)}\left(k\left|\overrightarrow{ox}\right|\right) P_n\left(\frac{\vec{k}}{|\vec{k}|}\cdot\frac{\overrightarrow{ox}}{\left|\overrightarrow{ox}\right|}\right) \tag{2.51}$$

The boundary integrals and its derivatives can be written in the following form as

$$\begin{aligned}&\int_{So}\left[\frac{\partial p(\vec{y})}{\partial n_y} G(\vec{x},\vec{y}) - \frac{\partial G(\vec{x},\vec{y})}{\partial n_y} p(\vec{y})\right] dS \\ &= \frac{ik}{16\pi^2}\iint D\left(\overrightarrow{ox},\vec{k}\right) M\left(\vec{o},\vec{k}\right) d\left(\vec{k}/|\vec{k}|\right)\end{aligned} \tag{2.52}$$

$$\begin{aligned}&\int_{So}\left[\frac{\partial G(\vec{x},\vec{y})}{\partial n_y} q(\vec{y}) - \frac{\partial^2 G(\vec{x},\vec{y})}{\partial n_y \partial n_x} p(\vec{y})\right] dS \\ &= \frac{ik}{16\pi^2}\iint \frac{\partial D\left(\overrightarrow{ox},\vec{k}\right)}{\partial n_x} M\left(\vec{o},\vec{k}\right) d\left(\vec{k}/|\vec{k}|\right)\end{aligned} \tag{2.53}$$

$M\left(\vec{o},\vec{k}\right)$ is the multipole expansions which are given by

$$M\left(\vec{o},\vec{k}\right) = \int_{So}\left[\frac{\partial p(\vec{y})}{\partial n_y} e^{-ik\vec{\cdot}\overrightarrow{oy}} - ik\left(\vec{n}_y\cdot\vec{k}\right) e^{-ik\vec{\cdot}\overrightarrow{oy}} p(\vec{y})\right] dS \tag{2.54}$$

For the M2M and L2L translations based on the plane wave expansion, the operations are performed based on the unit sphere. The number of wave samples is increased for the upward pass or decreased for the downward pass. Therefore, interpolation and filtering of multipole and local expansions are used for these two

operations. In this study, the spherical truncation method proposed by Ref. [97] is adopted. The operations for M2M are split into interpolation and shifting steps. The interpolation step is performed as:

$$f^n\left(\theta_h^{lv+1}\right)=\frac{2\pi}{J}\sum_{j=1}^{J}M\left(\vec{o},\theta_h^{lv+1},\phi_j^{lv+1}\right)e^{-in\phi_j^{lv+1}} \tag{2.55}$$

$$\begin{aligned}\tilde{f}^n\left(\theta_h^{lv}\right)=&\sum_{h^{lv+1}=1}^{H^{lv+1}}f^n\left(\theta_h^{lv+1}\right)\eta_h^{lv+1}\epsilon_{N+1}^n\\&\times\frac{P_{N+1}^n\left(cos\left(\theta_h^{lv}\right)\right)P_N^n\left(cos\left(\theta_h^{lv+1}\right)\right)-P_N^n\left(cos\left(\theta_h^{lv}\right)\right)P_{N+1}^n\left(cos\left(\theta_h^{lv+1}\right)\right)}{cos\left(\theta_h^{lv}\right)-cos\left(\theta_h^{lv+1}\right)}\end{aligned} \tag{2.56}$$

where: $\epsilon_l^n=\sqrt{l^2-n^2/4l^2-1}$ and η_h represents the Gaussian weighting function. Finally, the shifting from centroids of children cells to their parents' centroids based on the plane wave expansions is performed by:

$$M\left(\overrightarrow{o'},\vec{k}\right)=e^{i\vec{k}\cdot\overrightarrow{oo'}}M\left(\vec{o},\vec{k}\right) \tag{2.57}$$

M2L are performed by the diagonal translation operator:

$$D\left(\overrightarrow{oo'},\vec{k}\right)=\sum_{n=0}^{\infty}i^n\left(2n+1\right)h_n\left(k\left|\overrightarrow{oo'}\right|\right)P_n\left(\frac{\vec{k}}{\left|\vec{k}\right|}\cdot\frac{\overrightarrow{oo'}}{\left|\overrightarrow{oo'}\right|}\right) \tag{2.58}$$

and L2L are performed by a formulation similar to that used in the multipole to multipole expansions. The first step consists of shifting local representations from centroids of parent cells to centroids of children cells using plane waves:

$$L\left(\overrightarrow{o'},\vec{k}\right)=e^{i\vec{k}\cdot\overrightarrow{oo'}}L\left(\vec{o},\vec{k}\right) \tag{2.59}$$

Then, a filtering process is applied using the spectral truncation method:

$$f^n\left(\theta_h^{lv-1}\right)=\frac{2\pi}{J}\sum_{j=1}^{J}L\left(\overrightarrow{o'},\theta_h^{lv-1},\phi_j^{lv-1}\right)e^{-in\phi_j^{lv-1}} \tag{2.60}$$

$$f^n\left(\theta_h^{lv}\right)=\sum_{h^{lv+1}=1}^{H^{lv-1}} f^n\left(\theta_h^{lv-1}\right)\eta_h^{lv-1}\epsilon_{N+1}^n \times\frac{P_{N+1}^n\left(cos\left(\theta_h^{lv}\right)\right)P_N^n\left(cos\left(\theta_h^{lv+1}\right)\right)-P_N^n\left(cos\left(\theta_h^{lv}\right)\right)P_{N+1}^n\left(cos\left(\theta_h^{lv-1}\right)\right)}{cos\left(\theta_h^{lv}\right)-cos\left(\theta_h^{lv-1}\right)} \tag{2.61}$$

$$L\left(\overrightarrow{o'},\theta_h^{lv},\phi_j^{lv}\right)=\frac{1}{2}\sum_{n=-N}^{N} f^n\left(\theta_h^{lv}\right)e^{in\phi_j^{lv}} \tag{2.62}$$

Finally, the boundary integral equations can be written as:

$$\int_{So}\left[\frac{\partial p\left(\vec{y}\right)}{\partial n_y}G\left(\vec{x},\vec{y}\right)-\frac{\partial G\left(\vec{x},\vec{y}\right)}{\partial n_y}p\left(\vec{y}\right)\right]dS =\frac{ik}{16\pi^2}\sum_{s=1}^{S} w_s e^{i\vec{k}\cdot\overrightarrow{oy}}L\left(\vec{o},\vec{k}\right) \tag{2.63}$$

$$\int_{So}\left[\frac{\partial G\left(\vec{x},\vec{y}\right)}{\partial n_y}q\left(\vec{y}\right)-\frac{\partial^2 G\left(\vec{x},\vec{y}\right)}{\partial n_y\partial n_x}p\left(\vec{y}\right)\right]dS =\frac{-k^2}{16\pi^2}\sum_{s=1}^{S} w_s\left(\vec{n}_x,\vec{k}\right)e^{i\vec{k}\cdot\overrightarrow{oy}}L\left(\vec{o},\vec{k}\right) \tag{2.64}$$

2.3.3 Wideband fast multipole method

For the fast multipole algorithm, the low-frequency and high-frequency regime is characterized by a dimensionless parameter kD, i.e., the product of the acoustic wavenumber and the tree structure size. While the frequency is relatively large, the grid size will be small for deep tree structure, resulting in low kD and thus producing the instability issues. As mentioned, low-frequency FMBEM method does not have numerical instability problems, but the computational efficiency of high-frequency is relatively low. Therefore, the wideband FMM is proposed, which uses the partial wave expansion formulation in the low-frequency regime and the plane wave expansion formulation in the high-frequency regime. The rotation-coaxial translation and interpolation and filtering are also implemented during the calculations.

At low-frequency regime, the multipole expansions are based on the partial wave expansions. Then the translations are carried out the rotation-coaxial translation method. For high-frequency regime, the principal expansions are plane wave expansion. In the wideband calculation progress, a switch between the low-frequency and the high-frequency is done through a spherical harmonic translation at the multipole moments and the local moments. Following the results by Cheng et al.[96], the low-frequency formulation is applied when the local cell size d_l becomes $d_l < 0.25\lambda$, in which λ is the acoustic wavelength.

The spherical harmonic function used in the switch from the low-frequency regime to the high-frequency regime is given by

$$M\left(\vec{o},\vec{k}\right)=\sum_{n=0}^{\infty} i^n\left(2n+1\right)\left(-1\right)^{n-1}\sum_{m=-n}^{n}\bar{Y}_n^m\left(\theta,\phi\right)M\left(\vec{o}\right) \tag{2.65}$$

and its inverse operation from the high-frequency regime to the low-frequency regime is given by

$$M\left(\vec{o}\right)=\frac{1}{4\pi}\oint i^{-n}\bar{Y}_n^m\left(\theta,\phi\right)\left(-1\right)^{n-1}M\left(\vec{o},\vec{k}\right)d\left(\vec{k}/\left|\vec{k}\right|\right) \tag{2.66}$$

in which, θ is the polar angle and ϕ is the azimuthal angle from $\vec{k}$.

2.3.4 The truncation terms

In the fast multipole algorithm, the number of terms used in the expansion should to be truncated. The following semi-empirical formula is generally applied to determine the truncation term [93]

$$N_l = kd_l + c_l log\left(kd_l + \pi\right) \tag{2.67}$$

where d_l represents the size of the cells at level *l*, and c_l is the coefficient depending upon the precision of the arithmetic. From the Eq.(2.67), we can get that: the number

of truncation terms at different levels and increases from the bottom to the top level.

Some further methods are made to improve the calculation efficiency of the FMBEM, including the block diagonal preconditioner and the iterative solver (GMRES). These can be found in the work by Chen and Harris [98] and will not discuss in this study.

2.4 Half-space FMBEM

Although the FMBEM algorithm to acoustic propagation and scattering in full-space has been widely studied in Refs. [96, 99-101], the implementations of the FMBEM to evaluate the noise reduction performance acoustic barrier in three dimensions are still quite few [40, 41, 102] and also need further studies. When applying the BEM to predict the acoustic performance of the barrier above the infinite plane ground, the half-space Green's function can be used to remove the discretization of this infinite plane. Therefore, the discretization is only carried out on the barrier boundaries and reduce drastically the number of boundary elements. However, the Green's function for half-space cannot be employed directly in the fast multipole algorithm, as this fundamental solution should be expressed in forms of multipole expansions and translations.

Bapat [40] proposed to employ the half-space Green's function explicitly in the FMEBM. The tree structure used to group the boundary elements is only applied for the structure instead of containing both the real its mirror domain. Only the local expansions are modified and other steps are similar with that for full-space. This procedure simplifies the implementation of the FMBEM for the half-space acoustic problem and reduces the CPU time and memory storage by about a half for these acoustic problems.

Assume the half space general solution is $G_H\left(\vec{x},\vec{y}\right)$, its integral on the infinite plane is zero:

$$\int_S G_H(\vec{x},\vec{y})\frac{\partial p(\vec{y})}{\partial n_y}dS - \int_S \frac{\partial G_H(\vec{x},\vec{y})}{\partial n_y} p(\vec{y})dS = 0 \tag{2.68}$$

The boundary condition for the infinite half plane is

$$ikG_H(\vec{x},\vec{y}) + \frac{Z}{\rho_o c_o}\frac{\partial G_H(\vec{x},\vec{y})}{\partial n_y} = 0 \tag{2.69}$$

So the half-space Green's function for three dimensions is:

$$G_H(\vec{x},\vec{y}) = \frac{1}{4\pi}\left[\frac{e^{ikr}}{r} + R_p\frac{e^{ikr'}}{r'}\right] \tag{2.70}$$

R_p is the symmetry plane reflection coefficient. R_p =1 when the plane is rigid.

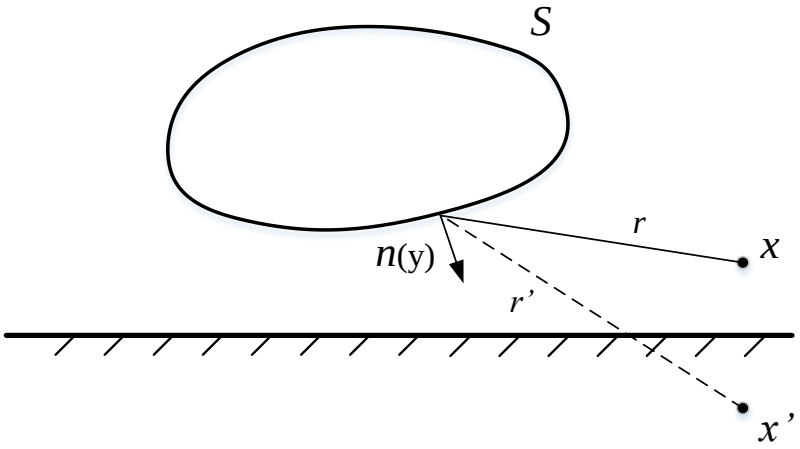

Fig 2.7: Sound scattering at half-space.

Then the Burton-Miller equation can be given by:

$$\begin{aligned}
&\int_{So}\left[p(\vec{y})\frac{\partial G_H(\vec{x},\vec{y})}{\partial n_y} - \frac{\partial p(\vec{y})}{\partial n_y}G_H(\vec{x},\vec{y})\right]dS \\
&+\beta\int_{So}\left[p(\vec{y})\frac{\partial^2 G_H(\vec{x},\vec{y})}{\partial n_y \partial n_x} - \frac{\partial G_H(\vec{x},\vec{y})}{\partial n_x}\frac{\partial p(\vec{y})}{\partial n_y} - \right]dS \\
&= -\frac{1}{2}p(\vec{x}) - \frac{\beta}{2}\frac{\partial p(\vec{x})}{\partial n_x} + p^I + \beta\frac{\partial p^I(\vec{x})}{\partial n_x}
\end{aligned} \tag{2.71}$$

The half-space Green's function G_H represents the interaction for $\vec{x}$ and $\vec{y}$, $\vec{x}'$ and $\vec{y}$, where $\vec{x}'$ is the mirror point corresponding to $\vec{x}$. The multipole expansion for

the half-space Green's function with acoustically rigid ground can be written as:

$$G_H\left(\vec{x},\vec{y}\right)=\frac{ik}{4\pi}\sum_{n=0}^{\infty}\left(2n+1\right)\sum_{m=-n}^{n}\bar{I}_n^m\left(k,\vec{y},\vec{y}_c\right)\left[O_n^m\left(k,\vec{x},\vec{y}_c\right)+O_n^m\left(k,\vec{x}',\vec{y}_c\right)\right] \quad (2.72)$$

Two sets of expansions can be found in the above Eq.(2.72). $O_n^m\left(k,\vec{x},\vec{y}_c\right)$ is for the real domain and $O_n^m\left(k,\vec{x}',\vec{y}_c\right)$ for the image domain. However, there is no necessary to create a tree structure of cells to include the image domain, since $\vec{x}'$ is the mirror point corresponding to $\vec{x}$. Therefore, the tree structure for boundary elements grouping are only implemented for the structure surfaces. The other steps for translations and expansions are similar to that used in full space.

For the impedance plane, the Green's function is given by Ochmann [103].

$$G_Z\left(\vec{x},\vec{y}\right)=\frac{e^{ikr}}{4\pi r}+\frac{e^{ikr'}}{4\pi r'}+2\gamma\int_{-\infty}^{0}e^{-\gamma\eta}\frac{e^{ikr_z}}{4\pi r_z}d\eta \quad (2.73)$$

The expressions for γ, η and r_z can be found in Ref. [103]. And the multipole expansions and the translations of the half-space impedance Green's function as Eq. (2.73) will be conducted in the future study.

2.5 Coupling of FMBEM-FEM

Acoustic-structure interaction problems frequently arise in the aerospace, automotive industries. The sound causes the vibration of the elastic structure and the structural vibration influence the propagation and scattering of the incident wave. In this part, the BEM is coupled with the FEM to accurately model the acoustic-structural interaction. The fast multipole algorithm is used to accelerate the matrix vector computation. The accuracy of the coupled FMBEM-FEM is validated by comparing the numerical solutions with known analytical and experimental results for flexible panels used as silencer in the duct.

The dynamic equation for the sound induced vibration of the plate is given by:

$$D_p \nabla^4 w(x,y,z,t) + \rho_p \frac{\partial^2 w(x,y,z,t)}{\partial t^2} = \Delta p \tag{2.74}$$

in which, w is the displacement, ρ_p the density of the plate and Δp is the acoustic pressure load. D_p is calculated through $D_p = Eh^3 / \left(12\left(1-v^2\right)\right)$, in which E, v and h are the Young's module, Possion's ratio and the thickness of the plate, respectively.

Assume the thickness in z direction is very small compared with the scale in x/y directions. The flexible plate in three dimensions can be treated as a panel vibrating in two dimensions, which is shown as:

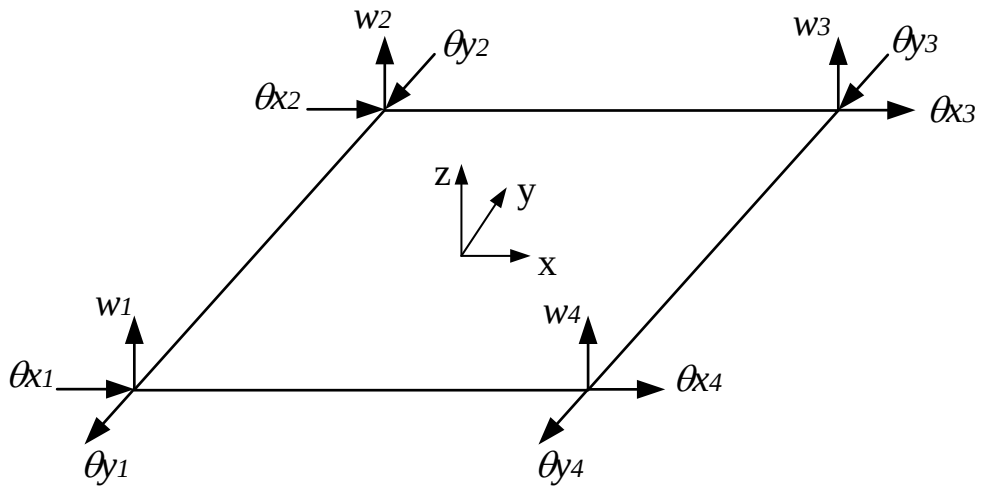

Fig 2.8: late element used for the finite element method.

The harmonic response of the flexible panel induced by the sound is governed by the following dynamic equation:

$$\left(\mathbf{K} + i\omega\mathbf{C} - \omega^2\mathbf{M}\right)\mathbf{w} = \mathbf{f} \tag{2.75}$$

where $\mathbf{M}$, $\mathbf{C}$, $\mathbf{K}$ represent the global inertia, damping and stiffness matrices, $\mathbf{w}$ and $\mathbf{f}$ are the displacement and force acting on the elements.

Dividing the boundary structure into two parts: coupling part and the left one. The BEM equation according to Eq.(2.13) can be rewritten as

$$\begin{bmatrix} \mathbf{H}_{11} & \mathbf{H}_{12} \\ \mathbf{H}_{21} & \mathbf{H}_{22} \end{bmatrix} \begin{Bmatrix} \mathbf{p}_c \\ \mathbf{p}_b \end{Bmatrix} = \begin{bmatrix} \mathbf{G}_{11} & \mathbf{G}_{12} \\ \mathbf{G}_{21} & \mathbf{G}_{22} \end{bmatrix} \begin{Bmatrix} -\rho_0 \omega^2 \mathbf{v}_{\mathbf{n}c} \\ -\rho_0 \omega^2 \mathbf{v}_{\mathbf{n}b} \end{Bmatrix} + \begin{Bmatrix} \mathbf{p}_c^I \\ \mathbf{p}_b^I \end{Bmatrix} \tag{2.76}$$

Then a combined BEM-FEM model can be obtained by considering the compatibility over the vibroacoustic interface:

$$\{\mathbf{f}\} = C_{sa} \{\mathbf{p}_c\} \tag{2.77}$$

in which the coupling matrix C_{sa} represents the acoustic pressure on the structural nodal loads, and it can be expressed as:

$$C_{sa} = \int_{s_c} \mathbf{N}_s^T \mathbf{n} \mathbf{N}_a ds_c \tag{2.78}$$

where S_c denotes the coupling face; $\mathbf{N}_S$ and $\mathbf{N}_a$ are the shape functions for the structural and acoustical domains, respectively; and $\mathbf{n}$ is the surface normal vector.

The normal velocity $\mathbf{v_c}$ of the coupling part can be expressed as a function of displacement $\mathbf{w}$:

$$\mathbf{v}_c = i\omega S^{-1} C_{as} \mathbf{w} \tag{2.79}$$

where $S = \int_{s_c} \mathbf{N}_a^T \mathbf{N}_a ds_c$ and $C_{as} = C_{sa}^T$.

Combining the Eqs.(2.75), (2.76), (2.77) and (2.79) together, we can get the coupled system of equations, as follows:

$$\begin{bmatrix} \left(\mathbf{K} + i\omega\mathbf{C} - \omega^2\mathbf{M}\right) & C_{sa} & 0 \\ \rho_0 \omega^2 \mathbf{G}_{11} S^{-1} C_{as} & \mathbf{H}_{11} & \mathbf{H}_{12} \\ \rho_0 \omega^2 \mathbf{G}_{21} S^{-1} C_{as} & \mathbf{H}_{21} & \mathbf{H}_{22} \end{bmatrix} \begin{Bmatrix} \mathbf{w} \\ \mathbf{p}_c \\ \mathbf{p}_b \end{Bmatrix} = \begin{Bmatrix} 0 \\ i\rho_0 \omega \mathbf{B}_{12} \mathbf{v}_{\mathbf{n}c} \\ i\rho_0 \omega \mathbf{B}_{22} \mathbf{v}_{\mathbf{n}b} \end{Bmatrix} + \{\mathbf{p}^I\} \tag{2.80}$$

The above is the coupling equation for the acoustic-structure interaction generated by the BEM-FEM method.

2.6 Numerical validations

2.6.1 Test case 1: pulsating sphere

The first test case is the sound radiated by a pulsating sphere. The acoustic pressure at any point can be calculated exactly, which are available in textbooks such as [104],

$$p(r)=\left(\frac{a}{r}\right)v_n\frac{i\rho_0\omega a}{1+ika}e^{-ik(r-a)} \tag{2.81}$$

in which, p represents the sound pressure at the receiver with a distance r from the sphere center. The radius of the sphere is indicated by a and v_n the uniform normal velocity.

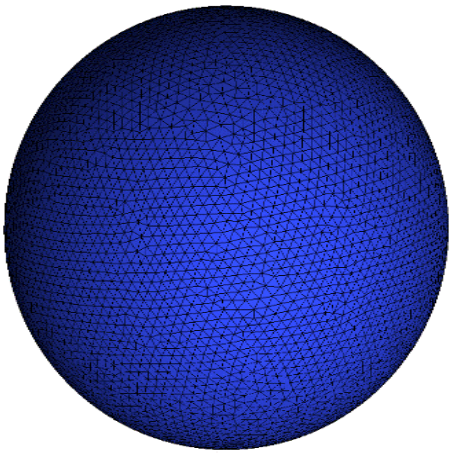

Fig 2.9: Elements for the pulsating sphere.

The radius of sphere a = 1 with pulsating normal velocity equal to unit. The wave number ka calculated in this validation is from 1 to 10, with a step of 0.01. 5400 rectangular elements is meshed by the ANASYS-ICEM, which a commercial grid generator. The acoustic pressure at (5, 0, 0) calculated by the analytical, conventional BEM and the Burton-Miller BEM is plotted in Fig 2.10. As shown by the red dashed line, multiple peaks and dips can be found within the frequency range and the conventional BEM fails to predict the sound pressure at these fictitious frequencies. As compared, the results by BEM modified by the Burton-Miller functions agrees well

with the analytical solutions in the whole frequency range.

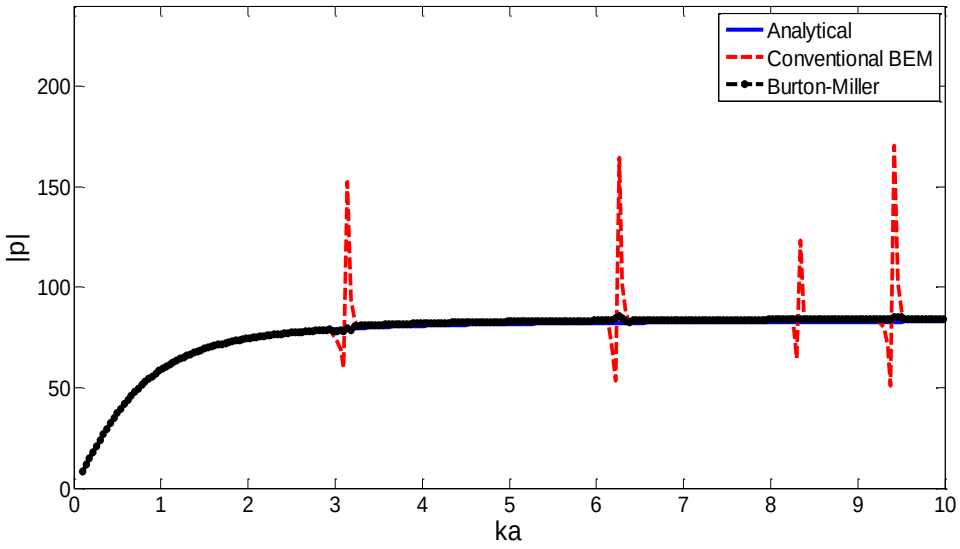

Fig 2.10: The sound pressure calculated by the analytical, conventional BEM and Button-Miller BEM.

This following figure examines the efficiency of the wideband FMBEM by comparison with the conventional BEM. Boundary conditions and geometry parameters are consistent. All these three calculations are implemented on a desktop personal computer with 4 GB in RAM and 2.93 GHz in Core CPU.

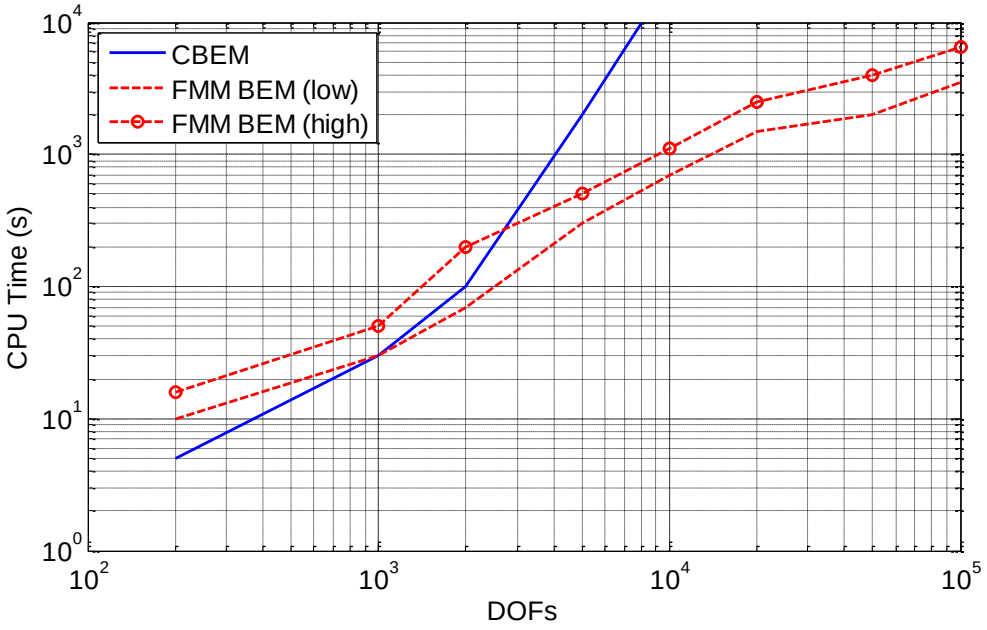

Fig 2.11: The CPU time comparison among the CBEM, FMBEM at low and high frequency for increasing problem scale.

In this test case of the pulsating sphere, the accuracy and the efficiency of the proposed FMBEM has been validated. The results comparison shows that the FMBEM can successfully overcome the non-uniqueness difficulties in wave radiation problems. Accelerated with the fast multipole algorithm, the efficiency of the CBEM for large scale problem is improved obviously.

2.6.2 Test case 2: single acoustic barrier

After validating the accuracy and efficiency of the FMBEM, the proposed FMBEM is verified through the insertion loss prediction of single acoustic barrier in the half space. The geometrical parameters of the single barrier can be referred to Ref [105]. The length of the barrier is 1.22 m and the height is 0.3 m. The ground in the experiment is made by the wooden board and can be assumed acoustically rigid. Therefore, the half-space Green's function used here is the rigid one. The main setup in the FMBEM for the single barrier is similar with that used for the pulsating sphere.

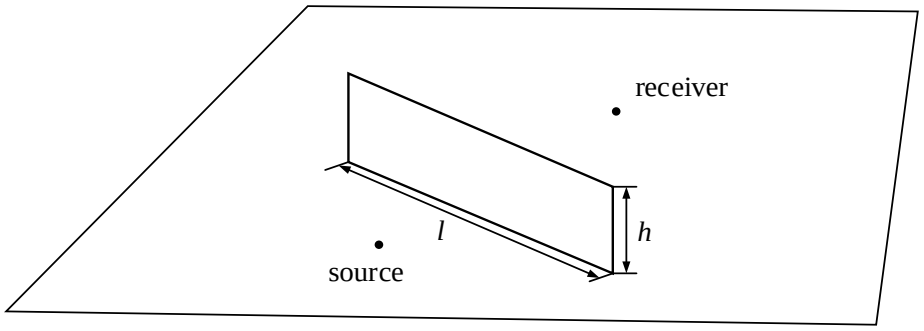

Fig 2.12: The configuration of the single barrier with finite length.

The IL of the single barrier measured in the experiment and compared with that predicted by the proposed half-space FMBEM is shown in the following Fig 2.13. The solid line represents the simulated IL results and the open circles are the experimental ones shown in Ref. [105]. Generally speaking, they agree well and shows the accuracy of the developed half-space FMEBM for acoustic barrier above rigid ground.

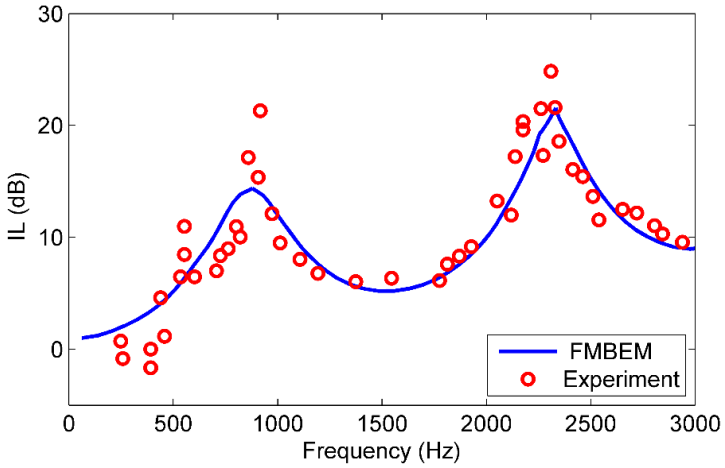

Fig 2.13: The comparison of IL for the single barrier.

The sound pressure level contour at 900 Hz, which around the first IL peak is plotted in Fig 2.14.

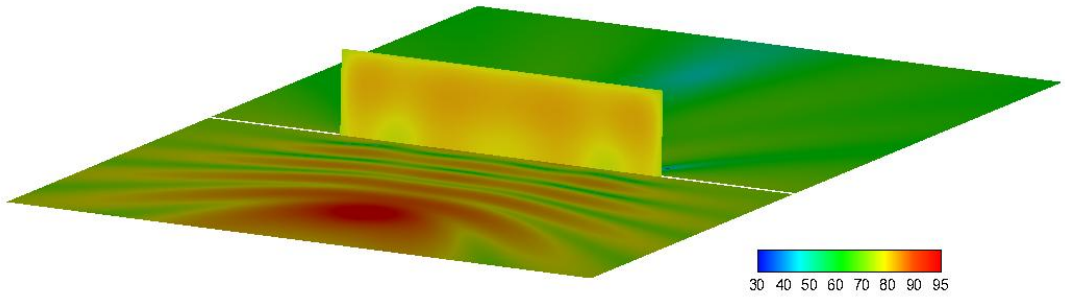

Fig 2.14: The SPL contour for the single barrier.

2.6.3 Test case 3: duct with plate silencer

Finally, the coupling of the FEM and the FMBEM is examined. The following figure sketches the plate silencer which used to control the dipole source in the duct. The details about this device and the experiment setup can be found in Ref.[106]. Two pieces of flexible plate made by the polymethacrylimide were flushed on the wall of the duct together with a backing cavity. The plate had the sizes of 100 mm * 300 mm. Density and elastic modulus for the plate is respectively 32 Kg/m^3 and 36 MPa. The duct wall and the rectangular backing cavity is made by the acrylic plate with a

thickness of 15 mm, which can prevent the sound translated through the duct and cavity walls. Two microphones are located near the outlet of the duct. The flexible plate is designed to control the noise in the low to medium frequency range. Therefore, the experimental measurement and the numerical calculation were only conducted in the frequency range from 100 to 1700 Hz.

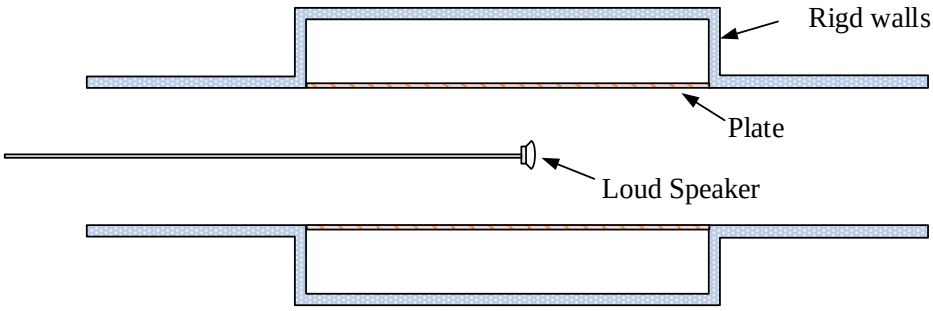

Fig 2.15: The sketch for the plate silencer used in the acoustic duct.

The lines in Fig 2.16 show the comparison of the experimental and numerical results. The dashed red line shows the result by the experiment. The solid blue and solid blank marked with diamond are the results obtained by the proposed FMBEM-FEM and the commercial software COMSOL Multiphysics based on the FEM-FEM. Roughly speaking, they are quite good agreement. The performance by FMBEM-FEM is better than by FEM-FEM.

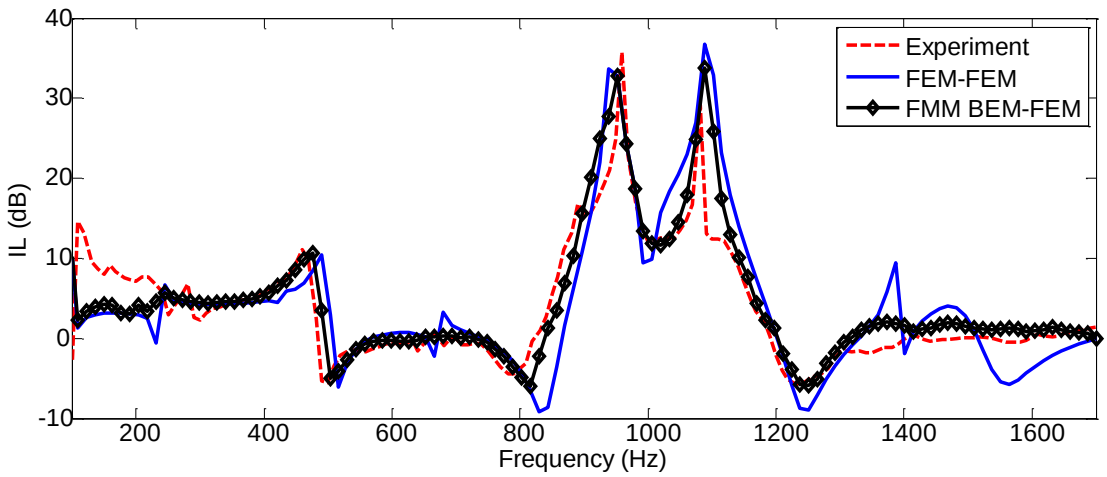

Fig 2.16: The results validation for the proposed FMBEM-FEM through the compared with experiment and FEM-FEM.

2.7 Summary

This chapter concerns the implementation of the FMBEM-FEM for acoustic-structural interaction in three dimensions.

The principle of the BEM is firstly presented. The Burton–Miller BIE formulation is employed to yield unique solutions for sound radiation and diffraction problems.

The wideband fast multipole algorithm used to accelerate the computation of the BEM is then discussed. The partial wave expansion is used in the low-frequency regime and the plane wave expansion formulation is used in the high-frequency regime. The comparison of the sound radiation by a pulsating sphere shows the accuracy and efficiency of the wideband FMBEM.

Subsequently, the wideband FMBEM approach for half-space wave scattering in three dimensions has been presented. The half-space Green's function is used, which the tree structure can be built for the structures in the real domain only.

Finally, the coupled FMBEM-FEM is developed and the accuracy is validated through comparison with the experimental results for the plate cavity system. The results obtained shows a good agreement with these in the literature and demonstrate the accuracy of the proposed wideband FMBEM-FEM method.

CHAPTER 3

ACOUSTICAL COUPLING FOR THE BAFFLED OPEN CAVITY INTEGRATED WITH HELMHOLTZ RESONATORS

3.1 Introduction

Typical parallel barriers consist of a finite confined space bounded by two identical barriers and an infinite half space. Besides, such acoustical system can be found in industry, transport systems and buildings. For example, some openings of ventilation and air-conditioning systems, outlets of different cooling systems and aircraft engines can be considered as open cavities. Moreover, some architectural structures can be modeled by means of open cavities which allow sound propagation to urban areas. These cases can be clarified as the acoustic coupling between an open cavity and the baffled infinite region.

To reduce noise radiation through the cavity opening, both active and passive approaches have been developed. Emms and Fox [107] compared three types of active absorbers to enhance sound transmission loss of a baffled open cavity. Their numerical results found that the combination of a monopole and dipole can provide significant sound transmission loss through the aperture for large wavelengths when compared with the size of the aperture. Recently, Wang et al. [5] developed a the active noise control system called the planar virtual sound barrier. This device consists of microphones, loudspeakers, and control circuits at the opening of the baffled open cavity sound radiation against noise sources inside. Field and Fricke [108] proposed to

use a quarter-wave resonator to reduce noise transmission through openings to the buildings and achieved an extra attenuation of 6–7 dB. Transparent micro-perforated absorbers were used by Kang and Brocklesby to attenuate external noise along the ventilation path [109]. A Helmholtz resonator (HR) is a common resonance control device and has been extensively used in ducts and enclosure systems. Cheng and his co-authors [110-113] established the acoustical coupling of the enclosure and the Helmholtz resonators and investigated the location and internal resistance of the resonators in regard to the noise reduction inside the enclosure. Meanwhile, using a multiple resonator array with different resonance frequencies, a wide band of noise reduction can be obtained. Similar to this idea, a HR array was integrated into structures to improve the transmission loss of a duct [72, 73, 114] and that of an enclosure with a cylindrical shell [115-117]. However, most studies of HR on noise control are focused on the acoustic duct or enclosed systems, while little consider the application in sound reduction in an open system, especially using the HR to attenuate the noise radiation from the baffled open cavity based on modal analysis.

In this chapter, the sound radiation from the baffled open cavity is analyzed based on modal analysis and the Helmholtz resonator is proposed to suppress the noise response outside the cavity. To achieve this, the theoretical model for the acoustical coupling of the baffled open cavity integrated with a Helmholtz resonator array was established. Moreover, the coupled and shifted resonant frequencies of the baffled open cavity was derived mathematically. Finally, the performance of noise reduction by one single resonator is studied systematically at the end of this chapter. The results show that with the combination with the resonator, the noise level is decreased both inside and outside, which indicates the potential application in the street canyons and parallel barriers.

3.2 Description of the model

3.2.1 Acoustical coupling of the baffled open cavity with a resonator array

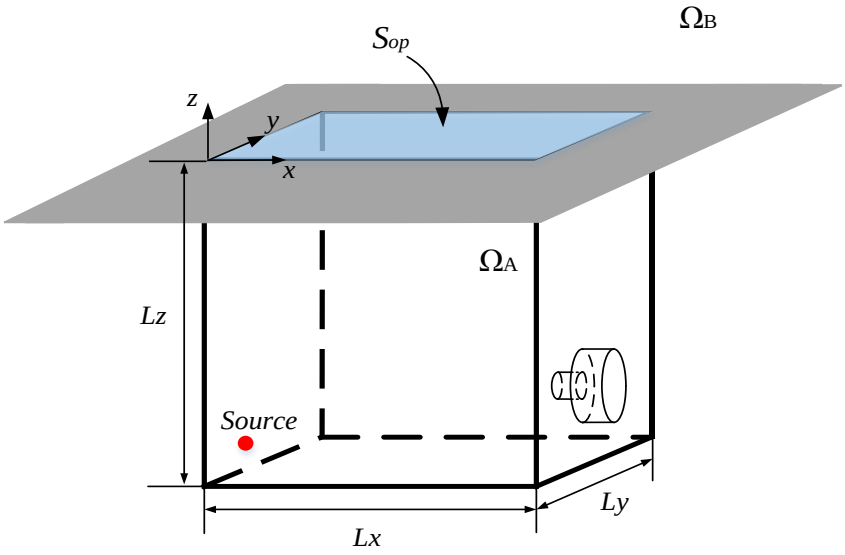

Fig 3.1: The sketch of the baffled open cavity integrated with Helmholtz resonator.

Fig 3.1 shows the sketch to be investigated, comprising the baffled open cavity integrated with the Helmholtz resonator. The cavity has the dimensions of *Lx*Ly*Lz* with five rigid walls. The opening of the cavity, S_{op}, divides the whole domain into two domains, the cavity domain Ω_A and the outside domain Ω_B. Domain Ω_B is semi-infinite and the baffled boundary, for $z = 0$, is assumed to be rigid. The origin of the coordinate is at the upper left corner vertex of the cavity. A classical Helmholtz resonator is made up of a narrow neck and a baking volume. In this study, the aperture of the resonator neck is directed towards the inside domain. The primary point source is located at $\vec{x}_s$, whereas, the *t*-th Helmholtz resonator is regarded as the *t*-th secondary source located at $\vec{x}_t^R$.

Sound pressure p inside and outside the baffled open cavity can be described by the Helmholtz equation in three dimensions:

$$\nabla^2 p\ \vec{x}\ + k^2 p\ \vec{x}\ = -Q_s \delta\ \vec{x} - \vec{x}_s \tag{3.1}$$

where $k = \omega / c_0$ is the wavenumber, c_0 is the speed of sound, and Q_s is the strength of the primary sound source. For the infinite far field, the Sommerfeld radiation condition should be satisfied and all the walls of the cavity are rigid except the opening of resonators.

$$\begin{aligned} \lim_{r\to\infty} r^{1/2}\left(\frac{\partial}{\partial r} - ik\right) p = 0 \\ \left.\frac{\partial p}{\partial n}\right|_{walls} = 0 \end{aligned} \tag{3.2}$$

In the cavity domain Ω_A as shown in Fig 3.1, when regarding the resonator as the secondary sources at $\vec{x}_t^R$, the governing equation for the sound pressure p_A and the boundary conditions are:

$$\nabla^2 p_A\ \vec{x}\ + k^2 p_A\ \vec{x}\ = -Q_s \delta\ \vec{x} - \vec{x}_s \tag{3.3}$$

$$\left.\frac{\partial p_A}{\partial n}\right|_{S_{op}} = -i\rho k c v_n \tag{3.4}$$

$$\left.\frac{\partial p_A}{\partial n}\right|_{\vec{x}_t^R} = -i\rho k c \frac{p_A \delta\left(\vec{x} - \vec{x}_t^R\right)}{Z_t} \tag{3.5}$$

in which, v_n represents the particle velocity at the cavity opening and Z_t is the output impedance at the t^{th} resonator's mouth. In this work, the Helmholtz resonator array is located on the cavity walls and regarded as the secondary sources as described in Eq.(3.5). Note that the sign of volume velocity from the resonators is the same as that of primary source, representing that the sound generated by the resonator is radiated into the cavity.

The sound pressure $p_A(\vec{x})$ for the domain Ω_A can be described by the undamped eigenmodes as:

$$p_A(\vec{x}) = \sum_{j=1}^{N} a_j \phi_j(\vec{x}) \tag{3.6}$$

where, a_j is the modal response of the *j*-th eigenmode $\phi_j(\vec{x})$ and *N* is the maximum number of the truncated mode series.

Combining with the rigid wall conditions, the eigenmodes, $\phi_j(\vec{x})$, for the three dimensional rectangular closed cavity as shown in Fig 3.1 is given by

$$\begin{aligned} \phi_j(\vec{x}) &= \psi_{j_x}(x) \cdot \psi_{j_y}(y) \cdot \psi_{j_z}(z) \\ \psi_{j_\chi}(x) &= \sqrt{\frac{2-\delta_{0,j_\chi}}{L_\chi}} \cos\left(\frac{j_x \pi}{L_x} x\right) \end{aligned} \tag{3.7}$$

The $\phi_j(\vec{x})$ satisfies:

$$\nabla^2 \phi_j(\vec{x}) + k_j^2 \phi_j(\vec{x}) = 0 \tag{3.8}$$

$$k_j^2 = \left(\frac{j_x \pi}{L_x}\right)^2 + \left(\frac{j_y \pi}{L_y}\right)^2 + \left(\frac{j_z \pi}{L_z}\right)^2 \tag{3.9}$$

where k_j is the wave number of the *j*-th eigenfrequency, and j_i is the model index in the *i* direction.

To solve for the coefficient a_j, the second Green identity can be applied:

$$\int_V p \nabla^2 \phi_i dv - \int_V \phi_i \nabla^2 p dv + \int_S \phi_i \frac{\partial p}{\partial n} ds - \int_S p \frac{\partial \phi_i}{\partial n} ds = 0 \tag{3.10}$$

where the volume integral covers the entire enclosure inside the domain Ω_A and the surface integral is evaluated on the entire inside surface of the enclosure, including the openings of the enclosure and the resonators.

Based on the expressions in Eqs.(3.6) and (3.7), Eq.(3.10) can be rewritten as:

$$\begin{aligned}&\sum_{j=1}^{N}\left[a_j\left(k^2-k_i^2\right)\int_V\left(\phi_i\phi_j\right)dv\right]-i\rho kc\int_{S_{op}}\left(\phi_i v_n\right)ds_{op}\\&=-i\rho kcq_s\phi_i\left(\vec{x}_s\right)+\sum_{t=1}^{T}\frac{i\rho kc}{Z_t}\int_{S_R}\left[\phi_i\sum_{h=1}^{N}a_h\phi_h\delta\left(\vec{x}-\vec{x}_t^R\right)\right]ds_R\end{aligned}\tag{3.11}$$

Eq. (3.11) considers the interactions between the open cavity and the multiple resonators, in which the effect of the cavity opening on the acoustical coupling of the cavity-resonator system is indicated by the normal particle velocity v_n.

Using the property of the eigenmodes:

$$\int_V\left(\phi_i\left(\vec{x}\right)\phi_j\left(\vec{x}\right)\right)dv=\begin{cases}1, & i=j\\0, & i\neq j\end{cases}\tag{3.12}$$

Eq.(3.11) can be simplified to:

$$\begin{aligned}&a_i\left(k^2-k_i^2\right)-i\rho kc\int_{S_{op}}\left(\phi_i v_n\right)ds_{op}\\&=-i\rho kcq_s\phi_i\left(\vec{x}_s\right)+\sum_{t=1}^{T}\frac{i\rho kc}{Z_m}\phi_i\left(\vec{x}_t^R\right)\sum_{h=1}^{N}a_h\phi_h\left(\vec{x}_t^R\right)\end{aligned}\tag{3.13}$$

The above equation indicates the effect of the multiple resonators on the modal response of the baffled open cavity.

For outside domain Ω_B, the sound pressure p_B can be expressed by the Kirchhoff-Helmholtz integral equation as:

$$p_B\left(\vec{x}_B\right)=-\int_{-\infty}^{+\infty}\left\{G\left(\vec{x}_B,\vec{x}_{op}\right)\frac{\partial p\left(\vec{x}_B\right)}{\partial\zeta}-p\left(\vec{x}_B\right)\frac{\partial G\left(\vec{x}_B,\vec{x}_{op}\right)}{\partial\zeta}\right\}d\zeta\tag{3.14}$$

in which $\vec{x}_B$ and $\vec{x}_{op}$ are the points in Ω_B and at the opening, respectively. $G\left(\vec{x}_B,\vec{x}_{op}\right)$ is Green's function which satisfies

$$\left(\frac{\partial^2}{\partial x^2}+\frac{\partial^2}{\partial y^2}+k^2\right)G\left(\vec{x}_B,\vec{x}_{op}\right)=-\delta\left(\vec{x}_B-\vec{x}_{op}\right)\tag{3.15}$$

The second term on the right-hand side of Eq. (3.14) vanishes if Green's function is chosen properly and satisfies the boundary conditions at $y=0$, Therefore, Eq.(3.14) can be rewritten as:

$$p_B(\vec{x}) = -\int_{S_{op}} G(\vec{x},\vec{x}_{op}) \frac{\partial p(\vec{x}_{op})}{\partial n} dS_{op} = i\rho kc \int_{S_{op}} G(\vec{x},\vec{x}_{op}) \cdot v_n dS_{op} \tag{3.16}$$

with $G(\vec{x},\vec{x}_{op}) = \frac{1}{2\pi}\frac{e^{-ikr}}{r}$ and $r = |\vec{x} - \vec{x}_{op}|$ being the distance from the field point $\vec{x}$ to the opening point $\vec{x}_{op}$.

Till now, in order to calculate the acoustical coupling of the baffled open cavity with multiple resonators, the coefficient a_j in Eq.(3.6) and the normal particle velocity v_n in Eq.(3.16) should be solved. However, v_n varies as the frequency changes and is hard to calculate due to the integration. Alternatively, a modal based approach is used to describe particle velocity at the opening.

Mathematically, any complete and orthogonal function set can be used to expand the particle velocity at the cavity opening. Considering the boundary conditions at the two ends, the cosine function set, $\chi_m(\vec{x}) = \psi_{m_x}(x) \cdot \psi_{m_y}(y)$, is chosen for the expansion of the normal particle velocity, therefore, v_n can be written as:

$$v_n(\vec{x}_{op}) = \sum_{m=1}^{M} b_m \chi_m(\vec{x}_{op}) \tag{3.17}$$

in which, b_m is the modal response of the *m*-th mode and M is the maximum number of the truncated mode series.

Substituting Eq.(3.17) into Eq.(3.16), the sound pressure p_B in the outside domain Ω_B can be expressed as:

$$p_B(\vec{x}) = \sum_{m=1}^{M} b_m \varphi_m(\vec{x}) \tag{3.18}$$

together with:

$$\varphi_m\left(\vec{x}\right)=j\rho kc\int_{S_{op}}G\left(\vec{x},\vec{x}_{op}\right)\cdot\chi_m\left(\vec{x}_{op}\right)dS_{op} \tag{3.19}$$

Now, as shown in Eq. (3.6) and Eq.(3.18), we have obtained the expressions describing the sound field of the baffled open cavity integrated with multiple resonators. According to the boundary conditions, the unknown coefficients of a_j and b_m can be determined. The solving procedures are presented in the following.

Substituting Eq.(3.17), Eq.(3.13) can also be simplified based on the modal expression equation of v_n at the opening,

$$\begin{aligned}&a_i\left(k^2-k_i^2\right)-i\rho kc\int_{S_{op}}\left(\phi_i\sum_{m=1}^{M}b_m\chi_m\right)ds_{op}\\&=-i\rho kcq_s\phi_i\left(\vec{x}_s\right)+\sum_{t=1}^{T}\frac{i\rho kc}{Z_t}\phi_i\left(\vec{x}_t^R\right)\sum_{h=1}^{N}a_h\phi_h\left(\vec{x}_t^R\right)\end{aligned} \tag{3.20}$$

Another requirement is that the sound pressure continuity at the opening should be satisfied, i.e.

$$p_A\left(\vec{x}\right)\big|_{Sop}=p_B\left(\vec{x}\right)\big|_{Sop} \tag{3.21}$$

Substituting Eqs.(3.6) and (3.18) into Eq.(3.21), we can obtain

$$\sum_{j=1}^{N}a_j\phi_j\left(\vec{x}\right)=\sum_{m=1}^{M}V_m\varphi_m\left(\vec{x}\right) \tag{3.22}$$

Multiplying $\tau_\mu\left(\vec{x}\right)$ on both sides of Eq.(3.22) and integrating over the opening leads to:

$$\begin{aligned}&\sum_{j=1}^{N}a_j\delta_{j_x,\mu_x}\delta_{j_y,\mu_y}\psi_{j_z}\left(0\right)\\&=i\rho kc\sum_{m=1}^{M}b_m\int_{S_{op}}\int_{S_{op'}}\chi_\mu\left(\vec{x}\right)G\left(\vec{x},\vec{x}'\right)\chi_m\left(\vec{x}'\right)d_{S_{op}}d_{S_{op'}}\end{aligned} \tag{3.23}$$

When defining $Z_{\mu,m}=i\rho kc\int_{S_{op}}\int_{S_{op'}}\chi_\mu\left(\vec{x}\right)G\left(\vec{x},\vec{x}'\right)\chi_m\left(\vec{x}'\right)d_{S_{op}}d_{S_{op'}}$ as the (modal) radiation impedance of the opening [118], Eq.(3.23) can be rewritten as:

$$\sum_{j=1}^{N}a_j\delta_{j_x,\mu_x}\delta_{j_y,\mu_y}\psi_{j_z}\left(0\right)=\sum_{m=1}^{M}V_mZ_{\mu,m} \tag{3.24}$$

Eqs. (3.20) and (3.24) form two equations for the two unknown coefficients a_j and

V_m. After solving the coefficients, the acoustical coupling of the baffled open cavity with the Helmholtz resonator array can be analyzed.

3.2.2 Analytical solution with one single resonator

As observed from the last item of Eq. (3.20), when multiple resonators are used, complex acoustic interactions among the cavity and the resonators occurs. Each resonator couples with not only multiple cavity modes, but also with other resonators. Such interactions make the analysis of the acoustical coupling of the cavity and the resonators complex. In fact, the coupling of one single resonator and the open cavity shows a very representative feature. Therefore, multiple resonators are reduced to one single resonator in the proposed theoretical model and will be discussed in detail.

For one single resonator, Eq. (3.20) can be simplified to:

$$\begin{aligned} &a_i\left(k^2-k_i^2\right)-i\rho kc\sum_{m=1}^{M}b_m\int_{S_{op}}\left(\phi_i\chi_m\right)ds_{op} \\ &=-i\rho kcq_s\phi_i\left(\vec{x}_s\right)+\frac{i\rho kc}{Z}\phi_i\left(\vec{x}^R\right)\sum_{h=1}^{N}a_h\phi_h\left(\vec{x}^R\right) \end{aligned} \tag{3.25}$$

Dividing both sides of Eq.(3.25) by $\left(k^2-k_i^2\right)$ yields:

$$\begin{aligned} &a_i-\frac{i\rho kc\sum_{m=1}^{M}b_m\int_{S_{op}}\left(\phi_i\chi_m\right)ds_{op}}{\left(k^2-k_i^2\right)} \\ &=-\frac{i\rho kcq_s\phi_i\left(\vec{x}_s\right)}{\left(k^2-k_i^2\right)}+\frac{i\rho kc\phi_i\left(\vec{x}^R\right)}{Z\left(k^2-k_i^2\right)}\sum_{h=1}^{N}a_h\phi_h\left(\vec{x}^R\right) \end{aligned} \tag{3.26}$$

By multiplying the two sides of Eq.(3.25) by $\sum_{i=1}^{N}\phi_i\left(\vec{x}^R\right)$, one can obtain:

$$\begin{aligned} &\sum_{i=1}^{N}a_i\phi_i\left(\vec{x}^R\right)-i\rho kc\sum_{i=1}^{N}\phi_i\left(\vec{x}^R\right)\frac{\sum_{m=1}^{M}b_m\int_{S_{op}}\left(\phi_i\chi_m\right)ds_{op}}{\left(k^2-k_i^2\right)} \\ &=-i\rho kc\sum_{i=1}^{N}\phi_i\left(\vec{x}^R\right)\frac{q_s\phi_i\left(\vec{x}_s\right)}{\left(k^2-k_i^2\right)}+i\rho kc\sum_{i=1}^{N}\frac{\left[\phi_i\left(\vec{x}^R\right)\right]^2}{Z\left(k^2-k_i^2\right)}\sum_{h=1}^{N}a_h\phi_h\left(\vec{x}^R\right) \end{aligned} \tag{3.27}$$

Then the summation $\sum_{h=1}^{N} a_h \phi_h \left(\vec{x}^R \right)$ can be solved by:

$$\begin{aligned} \sum_{h=1}^{N} a_h \phi_h \left(\vec{x}^R \right) = & -i\rho kc \frac{\sum_{h=1}^{N} \phi_h \left(\vec{x}^R \right) \dfrac{q_s \phi_h \left(\vec{x}_s \right)}{\left(k^2 - k_h^2 \right)}}{1 - i\rho kc \sum_{h=1}^{N} \dfrac{\left[\phi_h \left(\vec{x}^R \right) \right]^2}{Z \left(k^2 - k_h^2 \right)}} \\ & + i\rho kc \frac{\sum_{h=1}^{N} \phi_h \left(\vec{x}^R \right) \dfrac{\sum_{m=1}^{M} b_m \int_{S_{op}} \left(\phi_h \chi_m \right) ds_{op}}{\left(k^2 - k_h^2 \right)}}{1 - i\rho kc \sum_{h=1}^{N} \dfrac{\left[\phi_h \left(\vec{x}^R \right) \right]^2}{Z \left(k^2 - k_h^2 \right)}} \end{aligned} \tag{3.28}$$

Substituting Eq.(3.28) into Eq.(3.25), the modal response a_i with one single resonator gives:

$$\begin{aligned} & a_i \frac{\left(k^2 - k_i^2 \right)}{i\rho kc} \\ & - \sum_{m=1}^{M} b_m \int_{S_{op}} \left(\phi_i \chi_m \right) ds_{op} - i\rho kc \phi_i \left(\vec{x}^R \right) \frac{\sum_{h=1}^{N} \phi_h \left(\vec{x}^R \right) \dfrac{\sum_{m=1}^{M} b_m \int_{S_{op}} \left(\phi_h \chi_m \right) ds_{op}}{\left(k^2 - k_h^2 \right)}}{Z - i\rho kc \sum_{h=1}^{N} \dfrac{\left[\phi_h \left(\vec{x}^R \right) \right]^2}{\left(k^2 - k_h^2 \right)}} \\ & = -q_s \phi_i \left(\vec{x}_s \right) - q_s \phi_i \left(\vec{x}^R \right) \frac{i\rho kc \sum_{h=1}^{N} \phi_h \left(\vec{x}^R \right) \dfrac{\phi_h \left(\vec{x}_s \right)}{\left(k^2 - k_h^2 \right)}}{Z - i\rho kc \sum_{h=1}^{N} \dfrac{\left[\phi_h \left(\vec{x}^R \right) \right]^2}{\left(k^2 - k_h^2 \right)}} \end{aligned} \tag{3.29}$$

When defining:

$$\begin{aligned} \mathbf{A} &= \left[a_1, a_2, \cdots, a_N \right]^T \\ \mathbf{B} &= \left[b_1, b_2, \cdots, b_M \right]^T \end{aligned} \tag{3.30}$$

$$m_{n,m}=\frac{-i\rho kc}{\left(k^2-k_n^2\right)}\left[\psi_{n_z}(0)\delta_{n_{xy},m}+\frac{i\rho kc\phi_n\left(\vec{x}^R\right)\sum_{h=1}^{N}\phi_h\left(\vec{x}^R\right)\psi_{h_z}(0)\delta_{h_{xy},m}\Big/\left(k^2-k_h^2\right)}{Z-i\rho kc\sum_{h=1}^{N}\left[\phi_h\left(\vec{x}^R\right)\right]^2\Big/\left(k^2-k_h^2\right)}\right]$$

$$\mathbf{M}=\begin{Bmatrix} m_{1,1},m_{1,2},\cdots,m_{1,M} \\ m_{2,1},m_{2,2},\cdots,m_{2,M} \\ \vdots \\ m_{N,1},m_{N,2},\cdots,m_{N,M} \end{Bmatrix} \tag{3.31}$$

$$\mathbf{\Phi}=\begin{bmatrix} \delta_{1x,1}\psi_{1y}(0), & \delta_{2x,1}\psi_{2y}(0), & \cdots, & \delta_{Nx,1}\psi_{Ny}(0) \\ \delta_{1x,2}\psi_{1y}(0), & \delta_{2x,2}\psi_{2y}(0), & \cdots, & \delta_{Nx,2}\psi_{Ny}(0) \\ & \vdots & & \\ \delta_{1x,NX}\psi_{1y}(0), & \delta_{2x,NX}\psi_{2y}(0), & \cdots, & \delta_{Nx,NX}\psi_{Ny}(0) \end{bmatrix} \tag{3.32}$$

$$\mathbf{Z}=\begin{bmatrix} Z_{1,1}, & Z_{1,2}, & \cdots, & Z_{1,M} \\ Z_{2,1}, & Z_{2,2}, & \cdots, & Z_{2,M} \\ & & \vdots & \\ Z_{N_{XY},1}, & Z_{N_{XY},2}, & \cdots, & Z_{N_{XY},M} \end{bmatrix} \tag{3.33}$$

$$\mathbf{S}=-j\rho kcq_s\begin{bmatrix} \dfrac{\phi_1\left(\vec{x}_s\right)}{\left(k^2-k_1^2\right)}+\dfrac{\phi_1\left(\vec{x}^R\right)}{\left(k^2-k_1^2\right)}\dfrac{i\rho kc\sum_{h=1}^{N}\phi_h\left(\vec{x}^R\right)\phi_h\left(\vec{x}_s\right)\Big/\left(k^2-k_h^2\right)}{Z-i\rho kc\sum_{h=1}^{N}\left[\phi_h\left(\vec{x}^R\right)\right]^2\Big/\left(k^2-k_h^2\right)} \\ \dfrac{\phi_2\left(\vec{x}_s\right)}{\left(k^2-k_2^2\right)}+\dfrac{\phi_2\left(\vec{x}^R\right)}{\left(k^2-k_2^2\right)}\dfrac{i\rho kc\sum_{h=1}^{N}\phi_h\left(\vec{x}^R\right)\phi_h\left(\vec{x}_s\right)\Big/\left(k^2-k_h^2\right)}{Z-i\rho kc\sum_{h=1}^{N}\left[\phi_h\left(\vec{x}^R\right)\right]^2\Big/\left(k^2-k_h^2\right)} \\ \vdots \\ \dfrac{\phi_N\left(\vec{x}_s\right)}{\left(k^2-k_N^2\right)}+\dfrac{\phi_N\left(\vec{x}^R\right)}{\left(k^2-k_N^2\right)}\dfrac{i\rho kc\sum_{h=1}^{N}\phi_h\left(\vec{x}^R\right)\phi_h\left(\vec{x}_s\right)\Big/\left(k^2-k_h^2\right)}{Z-i\rho kc\sum_{h=1}^{N}\left[\phi_h\left(\vec{x}^R\right)\right]^2\Big/\left(k^2-k_h^2\right)} \end{bmatrix} \tag{3.34}$$

Eqs. (3.24) and (3.29) can be rewritten as:

$$\mathbf{A}+\mathbf{MB}=\mathbf{S} \tag{3.35}$$

$$\mathbf{\Phi A}=\mathbf{ZB} \tag{3.36}$$

The coefficient matrix $\mathbf{A}$ and $\mathbf{B}$ can be obtained after solving Eqs.(3.35) and (3.36). With the analytical model proposed above, the sound field in and outside the baffled open cavity integrated with a Helmholtz resonator can be calculated.

3.3 Numerical results and discussions

The configuration of the rectangular open cavity and the properties of the air media are listed in Table 3.1. The geometrical parameters of the baffled open cavity used in this study are 0.45 m long (L_x), 0.17 m high (L_y) and 0.54 deep (L_z). The source is located at (0.05, 0.085, -0.49) m while the evaluation receivers are randomly chosen at (0.45, 0.085, -0.05) and (0, -0.2, 0.5) m. The preliminary study has shown that these two locations can represent the sound field inside and outside the open cavity.

Table 3.1, Air properties, cavity size, sound source and receiver locations.

Air property		**Sound Source**	
Density: ρ_0 [kg/m^3]	1.225	Location: (x_s,y_s,z_s) [m]	(0.05,0.085, -0.49)
Sound speed: c [m/s]	340	Strength: Q_s [kg/s^2]	0.0001
Baffled Open Cavity		**Receiver Locations**	
Width: L_x [m]	0.45	R1[m]	(0.4, 0.085,-0.54)
Height: L_y [m]	0.17	R2[m]	(0.65, 0, 0.2)
Depth: L_z [m]	0.54		

3.3.1 Modal truncation and convergence

Theoretically an enclosed cavity has infinite degrees of freedom, i.e. an infinite number of cavity modes. In the numerical implementation, however, the mode series has to be truncated to form a finite number in Eqs.(3.6) and (3.17). The accuracy increases as the number of the truncated modes is large enough, however, the convergence will slow. Because this work is concentrated on controlling the low-frequency noise, it is possible to only use a limited number of lower-order modes to obtain reasonably accurate results [119].

A convergence study was conducted first by comparison of the calculated results at different modal numbers in the frequencies from 30 to 1000 Hz with a step of 1 Hz. The frequency band of [30, 1000] covers the major low-frequency resonance peaks for

the present baffled open cavity. Two arbitrary locations inside and outside the cavity were selected to compute the SPLs. Their locations are listed in Table 3.1.For the acoustic modes $\phi_n(\vec{x})$ used in the calculation, the total number *N* ranges from 5 to 500. The finite cosine series in Eq.(3.17) is truncated to *Nx*, accordingly. The amplitude and phase of the sound pressure at the randomly selected receivers have been evaluated as the modal number increases. The calculated results are shown in Fig 3.2 for the baffled open cavity without the acoustic resonator and Fig 3.3 for the baffled open cavity integrated with one single resonator, respectively. As shown in these two figures, the amplitude and phase of the sound pressure at the random inside and outside receivers converge as the number of modes increase.

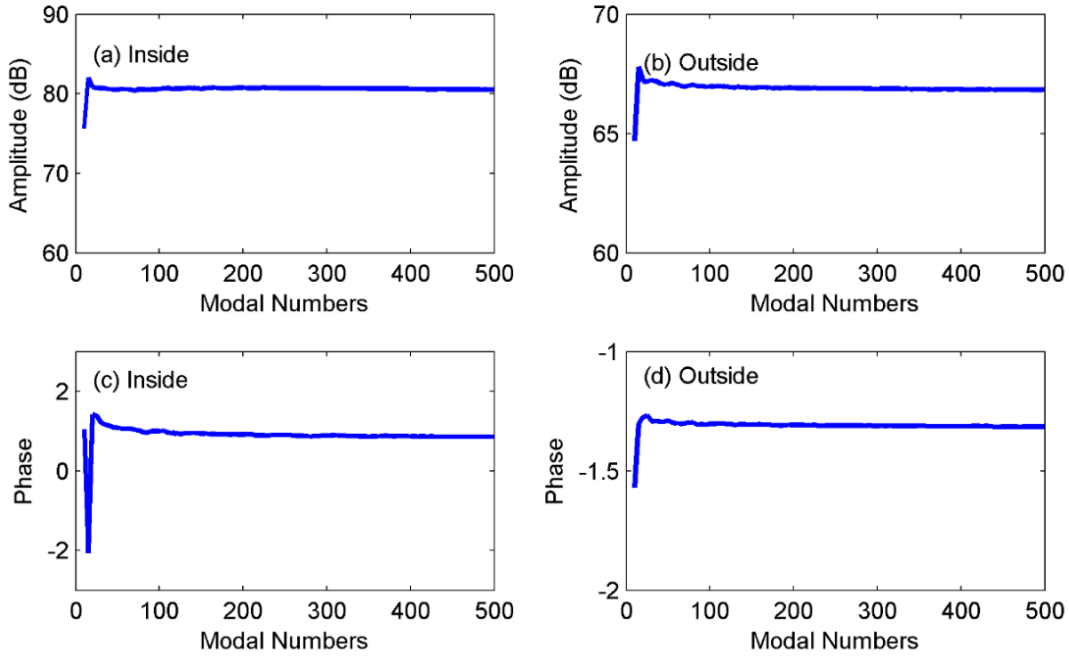

Fig 3.2: Model number used for calculation for baffled open cavity without resonator.

Subsequently, an acoustic resonator is designed to target the cavity mode at 381 Hz. A similar conclusion can be obtained from Fig 3.3 when the acoustic resonator is coupled to the cavity system. When comparing these two figures, we can find that the sound pressure converge slower for the baffled open cavity coupled with an acoustic

resonator than that with no resonator. That is to say, more modes should be used when calculating the acoustic coupling of the baffled open cavity with the acoustic resonator, which indicates that the acoustic resonator interacts with multiple cavity modes instead of only the target mode.

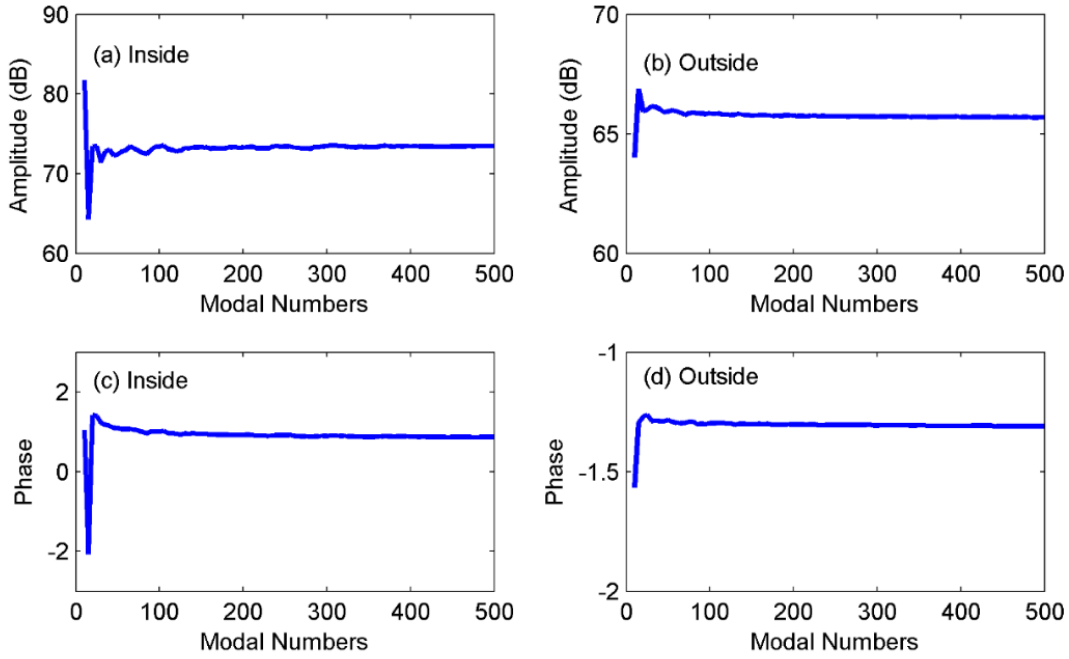

Fig 3.3: Model numbers used for calculation for baffled open cavity with single HR.

Generally speaking, the calculated results in the above two figures show that the number of cavity modes of 500 is normally enough. Further increasing the modal number does not make significant difference in the frequency range of interest below 1000 Hz. Therefore, 500 cavity modes in total will be used in the following simulations and results analysis for frequencies of interest below 1000 Hz.

To validate the proposed theoretical model, the sound fields inside and outside the open cavity are compared with the results calculated by using the BEM modified with the Burton-Miller formulation. The frequency range from 30 up to 1000 Hz at a step of 1 Hz. The maximum size of constant elements used in the BEM simulation is 0.02m, which is almost 1/17 of the wavelength of 1000 Hz.

Fig 3.4 shows the comparison of the theoretical and simulated sound pressure levels at R1 inside the cavity and R2 outside the cavity. In the calculations, the number of cavity modes is 500 and the external modes is 34. The blue lines show the results at R1 obtained by the two methods and the red lines show the results at R2. It is known that the sound field at the cavity opening is hard to calculate accurately. However, a good agreement can be found at R1, which is near the open cavity. It is shown in the figure that the results obtained by the proposed theoretical model agree well with the numerical results, so the accuracy of the theoretical model is validated.

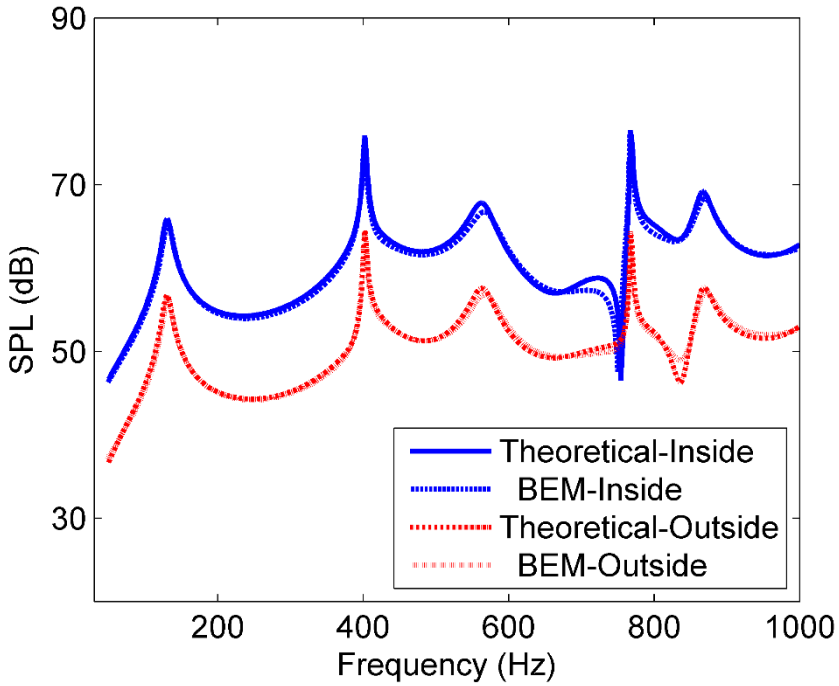

Fig 3.4: Comparison between the sound fields obtained by the proposed method and the BEM simulations.

Fig 3.5 compares the sound pressure contour in the x-z plane for 404 Hz obtained by the proposed model and the BEM method. The color legend for these two figures are set to the same. The sound pattern inside the cavity seems almost the same and excellent agreement can be found.

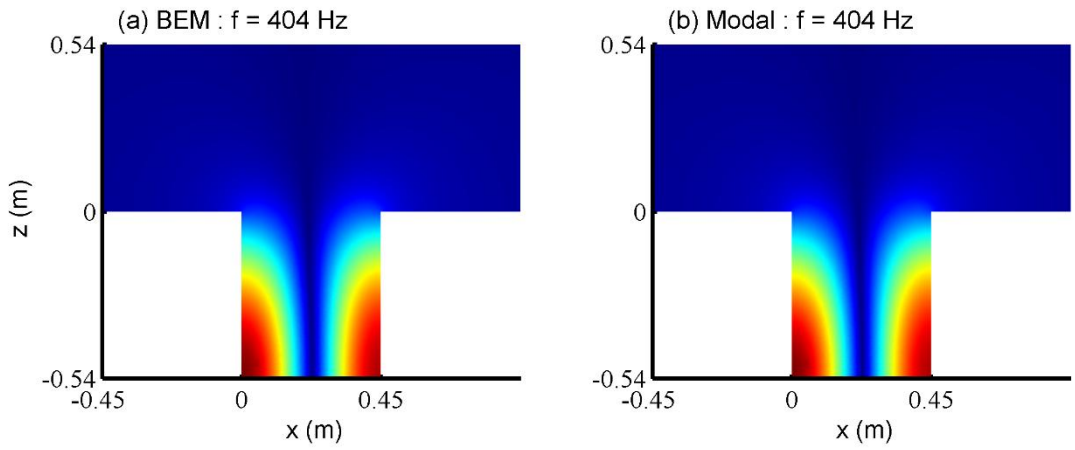

Fig 3.5: The comparison of sound pressure distribution calculated by the BEM and the proposed method: (a) BEM; (b) Modal.

3.3.2 Acoustical resonances of the baffled open cavity with one single acoustic resonator

When compared with the eigenfrequencies of the enclosed cavity, the peaks of sound pressure level shift to higher frequency, which is due to the infinite baffled opening. In order to suppress the sound radiation from the cavity opening, more efforts should be devoted to the sound pressure peaks at receivers outside the cavity. Knowing the frequencies of these resonances at the design phase is crucial for implementing appropriate passive noise control techniques. The second point is that, optimizing the resonator design requires the knowledge of the nodal lines for the corresponding acoustic modes. This can avoid positioning the resonators too close to them. Last but not least, the insertion of the resonator can suppress the noise response well at the target resonances; however, the noise level at off-target frequencies may be improved. Therefore, in order to achieve broadband noise reduction, it would greatly benefit from an early knowledge of the acoustic eigenvalues and eigenmodes of the cavity with and without the resonator. In this section, using the established theoretical model accounting for the acoustical coupling, the variation of the baffled open cavity resonant frequencies

after one single resonator mounted on the cavity wall is investigated.

3.3.2.1 The coupling and shifting due to the cavity opening

Neglecting the sound source and covering the resonator aperture with a rigid stopper, the free vibration behavior of the baffled open cavity can be described by the following equation, which is the simplified form of Eq.(3.25):

$$a_i\left(k^2-k_i^2\right)-i\rho kc\int_{S_{op}}\left(\phi_i v_n\right)ds_{op}=0 \tag{3.37}$$

Substituting the modal expression for v_n into Eq.(3.37), we can obtain,

$$a_i\left(k^2-k_i^2\right)-i\rho kc\sum_{m=1}^{M}b_m\int_{S_{op}}\left(\phi_i\chi_m\right)ds_{op}=0 \tag{3.38}$$

Using the orthogonal property of the eigenmodes, the characteristic matrix equation of the baffled open cavity is then given from Eq.(3.38) as:

$$\begin{aligned}
&a_1\left(k^2-k_1^2\right)-i\rho kc\psi_{1_z}(0)\sum_{m=1}^{M}b_m\int_{S_{op}}\left(\psi_{1_x}\psi_{1_y}\chi_m\right)ds_{op}=0\\
&a_2\left(k^2-k_2^2\right)-i\rho kc\psi_{2_z}(0)\sum_{m=1}^{M}b_m\int_{S_{op}}\left(\psi_{2_x}\psi_{2_y}\chi_m\right)ds_{op}=0\\
&\qquad\vdots\\
&a_N\left(k^2-k_N^2\right)-i\rho kc\psi_{N_z}(0)\sum_{m=1}^{M}b_m\int_{S_{op}}\left(\psi_{N_x}\psi_{N_y}\chi_m\right)ds_{op}=0
\end{aligned} \tag{3.39}$$

Combining Eqs. (3.24) and (3.39) together, these two set of equations can be written in matrix form as:

$$\begin{bmatrix}\mathbf{I} & \mathbf{M}\\ \mathbf{\Phi} & -\mathbf{Z}\end{bmatrix}\begin{bmatrix}\mathbf{A}\\ \mathbf{B}\end{bmatrix}=0 \tag{3.40}$$

in which $\mathbf{I}$ denotes the identity matrix. The expressions about $\mathbf{M}$, $\mathbf{\Phi}$ and $\mathbf{Z}$ are similar to that used in Eqs.(3.31)-(3.33). $\mathbf{A}$ and $\mathbf{B}$ represent that modal coefficients as used in Eq.(3.30).

Note that the frequency nullifying the determinant of the matrix $\begin{bmatrix}\mathbf{I} & \mathbf{M}\\ \mathbf{\Phi} & -\mathbf{Z}\end{bmatrix}$ in Eq.(3.40) yields the eigenvalues of the baffled open cavity system. Therefore, the

eigenfrequencies of this open acoustic system can be solved.

The obtained eigensolutions from Eq.(3.40) are shown plotted by the solid blue circle in Fig 3.6. In contrast to its closed counterpart, characterized by real spectra, open systems have complex spectra which permits external radiation. For example, the eigenfrequency corresponding to the (1,0,0) mode is 381.1 Hz for the enclosed cavity with the six rigid walls, whereas, the eigenvalue for the baffled open cavity is (402.3+1.5i). The imaginary part in the eigenvalue represents the radiation losses in the infinite space. Furthermore, the eigensolutions are shifted to larger ones.

3.3.2.2 The coupling and shifting due to the resonator

When removing the rigid stopper at the resonator aperture and neglecting the primary sound source, we can obtain the following equation accounting for the open cavity and the single resonator as:

$$a_i\left(k^2-k_i^2\right)-i\rho kc\int_{S_{op}}\left(\phi_i v_n\right)ds_{op}=\frac{i\rho\omega}{Z}\phi_i\left(\vec{x}^R\right)\sum_{h=1}^{N}a_h\phi_h\left(\vec{x}^R\right) \quad (3.41)$$

Especially when the baffled cavity opening is closed as $v_n=0$, the above Eq.(3.41) is the acoustically coupled model for the enclosure with one single HR as that in Li and Cheng [110].

Dividing $\left(k^2-k_i^2\right)$ on both sides of Eq.(3.41) yields:

$$a_i=\frac{i\rho kc\int_{S_{op}}\left(\phi_i v_n\right)ds_{op}}{\left(k^2-k_i^2\right)}+\frac{i\rho kc}{Z\left(k^2-k_i^2\right)}\phi_i\left(\vec{x}^R\right)\sum_{h=1}^{N}a_h\phi_h\left(\vec{x}^R\right) \quad (3.42)$$

Then multiplying these two sides by $\sum_{i=1}^{N}\phi_i\left(\vec{x}^R\right)$, one can obtain:

$$\begin{aligned}\sum_{i=1}^{N}a_i\phi_i\left(\vec{x}^R\right)=&\sum_{i=1}^{N}\frac{i\rho kc\int_{S_{op}}\left(\phi_i v_n\right)ds_{op}}{\left(k^2-k_i^2\right)}\phi_i\left(\vec{x}^R\right)\\&+\sum_{i=1}^{N}\frac{i\rho kc}{Z\left(k^2-k_i^2\right)}\left[\phi_i\left(\vec{x}^R\right)\right]^2\sum_{h=1}^{N}a_h\phi_h\left(\vec{x}^R\right)\end{aligned} \quad (3.43)$$

Therefore, the summation $\sum_{h=1}^{N} a_h \phi_h\left(\vec{x}^R\right)$ can be expressed as:

$$\sum_{h=1}^{N} a_h \phi_h\left(\vec{x}^R\right) = \frac{\sum_{i=1}^{N} i\rho kc\phi_i\left(\vec{x}^R\right)\int_{S_{op}}\left(\phi_i v_n\right)ds_{op} \Big/ \left(k^2 - k_i^2\right)}{1 - \sum_{i=1}^{N} i\rho kc\left[\phi_i\left(\vec{x}^R\right)\right]^2 \Big/ \left[Z\left(k^2 - k_i^2\right)\right]} \tag{3.44}$$

Substituting Eq.(3.44) into Eq.(3.41) yields:

$$\begin{aligned} & a_i\left(k^2 - k_i^2\right) - i\rho kc\int_{S_{op}}\left(\phi_i v_n\right)ds_{op} \\ & = \frac{i\rho kc}{Z}\phi_i\left(\vec{x}^R\right)\left\{\frac{i\rho kc\sum_{h=1}^{N}\phi_h\left(\vec{x}^R\right)\int_{S_{op}}\left(\phi_h v_n\right)ds_{op} \Big/ \left(k^2 - k_h^2\right)}{1 - \sum_{h=1}^{N} i\rho kc\left[\phi_h\left(\vec{x}^R\right)\right]^2 \Big/ \left[Z\left(k^2 - k_h^2\right)\right]}\right\} \end{aligned} \tag{3.45}$$

The above equation can be further simplified after substituting the expression for v_n:

$$\begin{aligned} & a_i\left(k^2 - k_i^2\right) - i\rho kc\sum_{m=1}^{M} b_m\int_{S_{op}}\left(\phi_i \chi_m\right)ds_{op} \\ & = i\rho kc\phi_i\left(\vec{x}^R\right)\left\{\frac{i\rho kc\sum_{h=1}^{N}\phi_h\left(\vec{x}^R\right)\sum_{m=1}^{M} b_m\int_{S_{op}}\left(\phi_h \chi_m\right)ds_{op} \Big/ \left(k^2 - k_h^2\right)}{Z - \sum_{h=1}^{N} i\rho kc\left[\phi_h\left(\vec{x}^R\right)\right]^2 \Big/ \left(k^2 - k_h^2\right)}\right\} \end{aligned} \tag{3.46}$$

This leads to a similar matrix form as Eq.(3.40) expressed as:

$$\begin{bmatrix} \mathbf{I} & \mathbf{M}^R \\ \mathbf{\Phi}^R & \mathbf{-Z} \end{bmatrix}\begin{bmatrix} \mathbf{A}^R \\ \mathbf{B}^R \end{bmatrix} = 0 \tag{3.47}$$

where the superscript ‘R’ represents the variables for the system at the presence of the resonator. The above matrix can be used to solve the resonances of the baffled open cavity integrated with one single resonator. The calculated results are shown by asterisk in Fig 3.6, in which the open circles represent the resonance of the baffled open cavity without resonator.

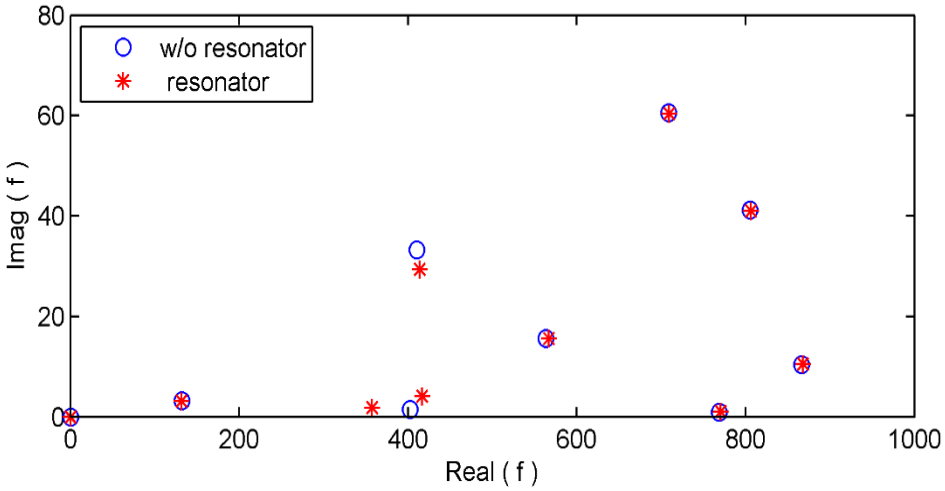

Fig 3.6: The eigenfrequencies of the baffled open cavity without and with one single resonator.

Similar to the baffled open cavity with rigid walls, the eigenfrequencies after integrated with a resonator consist of real part and imaginary parts. The imaginary parts represent the radiation loss to the infinite space and are relatively small when compared with their real part. Therefore, the high Q-factor can be observed at these frequencies. Furthermore, as indicated by Fig 3.6, when inserting the acoustic resonator whose natural frequency is f=381.1 Hz, two new frequencies of 357.4+1.8i and 416.5+4.1i are produced normally lying on either side of the original frequency of 402.3+1.5i. A little shift can be observed for other resonant frequencies. In other words, after inserting one resonator, one additional resonance emerges and little changes at other resonances. The results are consistent with the studies for the acoustical coupling of the enclosure and the resonator by Fahy and Schofield [120]. The separation between the new frequencies is dominated by the target modal property and the characteristics of the resonator compared with the cavity. The comparison of modal pattern for the above eigenfrequencies is plotted in the following Fig 3.7.

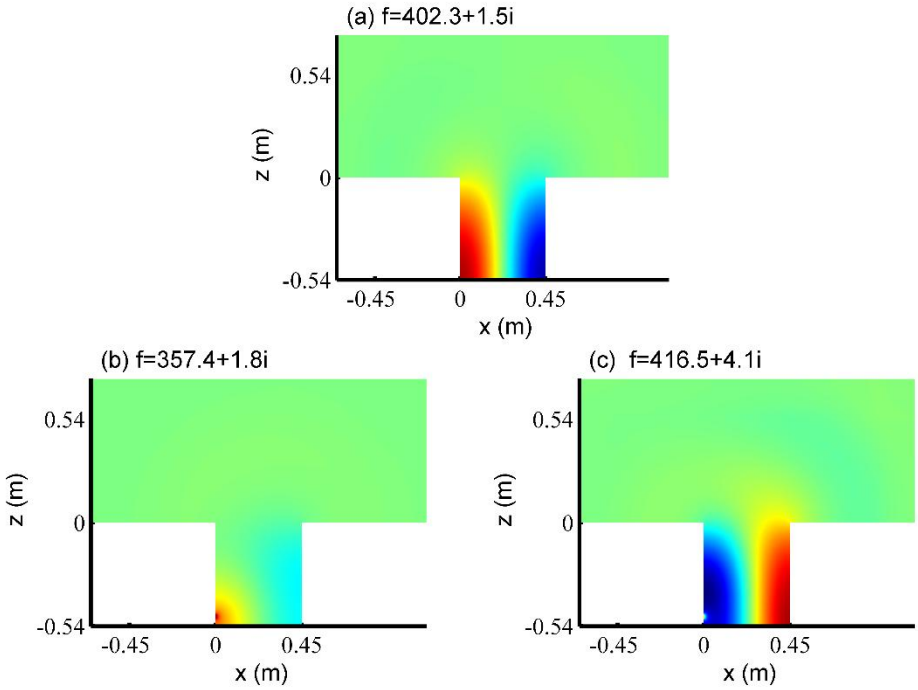

Fig 3.7: Normalized modal pattern for the open cavity before and after integrated with the resonator: (a) Original pattern at f=402.3+1.5i without resonator; (b) and (c) the newly coupled patterns after inserting the resonator at f=357.4+1.8i and f=416.5+4.1i.

Fig 3.7 (a) presents the sound pressure distribution at 402.3+1.5i Hz for the baffled open cavity without resonator. Fig 3.7 (b) and (c) illustrate the sound fields at the newly emerged frequencies of 357.4+1.8i and 416.5+4.1i Hz after being coupled with one single acoustic resonator. The natural frequency of the resonator is 381 Hz and target for the enclosed-cavity mode of (1, 0, 0). The geometrical parameters and the location of the resonator will be investigated in detail in the next section.

3.4 The noise reduction by one single Helmholtz resonator

3.4.1 Sound response inside and outside the baffled open cavity

In order to control the noise level of the baffled open cavity system, the sound field of such open system should be analyzed in detail first. The frequencies of sound

pressure level peaks as shown in Fig 3.4 appear at 134, 404 and 769 Hz, below 1000 Hz. Except for the first peak at 134 Hz, the other peak frequencies are close to the resonant frequencies of the enclosed cavity. It is obvious that the opening increases the values of the resonances for the enclosed cavity, and the formation mechanism of the sound pressure distribution at 134 Hz is different from others.

Fig 3.8 show the sound pressure level distribution on the cross plane when the source is located at (0.05, 0.085, -0.49) and the frequencies are (a) 134, (b) 404 and (c) 769 Hz respectively. It can be found that sound pressure distribution at the last two frequencies appears almost as the mode patterns caused by the two rigid walls of the rectangular cavity. While at 134 Hz, the sound pressure level remains almost the same within the open cavity except at the cavity opening. This means that the sound pressure distribution at 134 Hz is mainly due to the reflection of the bottom plane and the open cavity behaves like a quarter wavelength resonator, a similar pattern can be found in the study by Ref.[5].

For the (2a) and (3a) figures in Fig 3.8, the sound pressure distributions are similar to their enclosure modal pattern. At each frequency, a clear modal feature can be identified within the cavity domain. Within the cavity formed by four vertical rigid walls and the reflective bottom, multiple reflections occur. These reflecting waves superimpose with each other and with the direct waves generated by the noise source. In fact, the sound pressure level at each of the above frequencies is dominated by one associated mode of the enclosed cavity, as shown by Fig 3.8 (2b) and (3b). Take the sound peak at 404 Hz as the example, the sound field within the cavity is dominated by the enclosed-cavity mode of (1, 0, 0) and the sound field outside the cavity is mainly contributed by the second external mode. Therefore, the direct and effective noise reduction enhancement at these frequencies aims to suppress the corresponding

resonances, the Helmholtz resonator device is hereafter introduced.

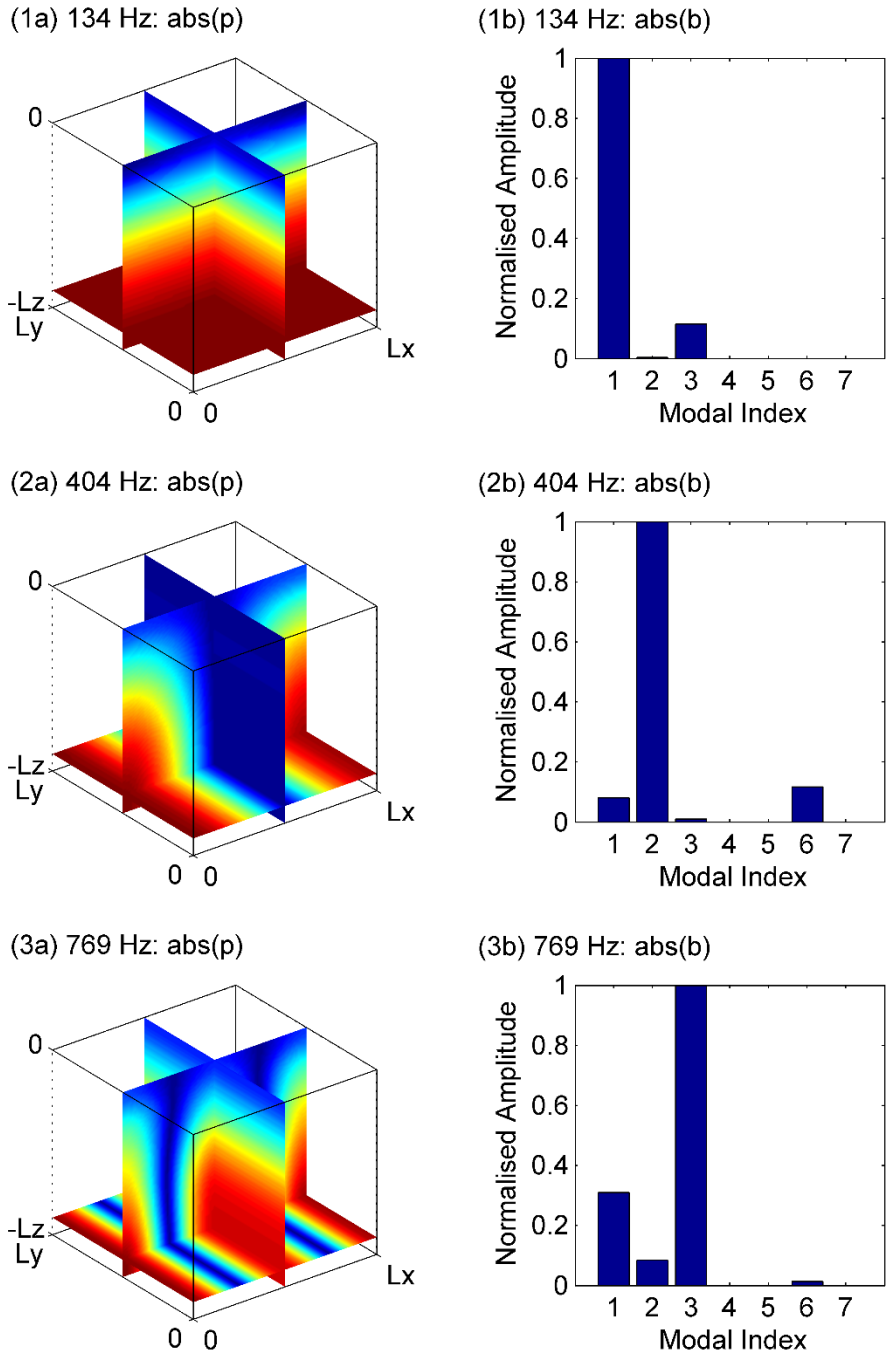

Fig 3.8: Sound slice within the rectangular open cavity: (a) f=134Hz; (b) f=404Hz; (c) f=571Hz and (d) f=769Hz.

3.4.2 The mechanism of HR on noise control

When mounting a resonator on the cavity wall, resonators interact with the cavity

through a dual process: (1) the vibration of the lumped mass inside the resonator neck reflects part of acoustic energy from the incident wave back to the cavity, resulting in an acoustic interaction with the open cavity. (2) Meanwhile, part of the incident acoustic energy passing to resonators is trapped inside the resonator cavity as kinetic and potential fluid energies, part of them being dissipated through energy loss mechanisms. It is also known that insertions of acoustic resonators can control the target mode well, however, other off-target modes may be improved, which in turn deteriorates the noise control performance if the frequency range of interest is broadband [110].

Eq.(3.29) provides analytical expressions in terms of the modal coefficients inside the cavity under the effect of one single Helmholtz resonator. As shown on the right-hand side of Eq.(3.29), the first term is the effect of the primary sound source, the second term characterizes the radiation opening and the last term indicates the resonator contributions after being coupled with the original sound field. As expected, the single resonator interacts with all of the acoustical modes of the cavity. If a targeted cavity mode is well separated from other modes, the interaction among these modes and the resonator can be neglected. On the contrary, high modal density or a larger frequency band may necessitate the consideration of the interaction among the resonator and multiple cavity modes. The same applies if the control performance of the resonator should be evaluated in a broad band.

Especially, when the cavity opening is covered with a rigid wall, the problem degenerates to the acoustical coupling of the enclosure with one single resonator, as studied by Cheng's group [110, 112, 113]. Though the expression by Eq. (3.29) is not as straight as that by Li and Cheng [110], Eq. (3.29) still shows two important factors which dominate the noise control performance: location and internal resistance of the resonator. The value of $\phi_h\left(\vec{x}^R\right)$ is location dependent and hence the noise reduction is

sensitive to the resonator locations. Traditionally, the resonator is set at the anti-nodal surfaces where the strongest coupling happens and the most effective noise control undergoes. The sound response at the target frequency can be suppressed well in this case; however, the noise response in the vicinity may be improved. Aiming to achieve noise reduction within a frequency band instead of a narrow band around the peak, acoustical coupling of the single resonator and the multiple enclosed-cavity modes should be considered [112]. Therefore, the optimal location for the single resonator used for the open cavity may not be consistent with the traditional one used for the enclosure. Besides, due to the space limitation, the resonator in this study was limited to being mounted on the vertical walls of the cavity.

On the other hand, when the resonator location is fixed, the output impedance of *Z* at the resonator aperture, is very important in determining the noise reduction performance within the chosen frequency band. The output impedance of the resonator is mainly dependent on its internal resistance and the physical parameters in geometry. An excessively high internal resistance renders *Z* approach to infinity, thereby annulling the effect of the resonator. On the contrary, if the internal resistance is too low, Z tends towards zero at the resonance frequency, which causes an unacceptably high amplitude a_i at the two newly emerged frequencies (coupled peaks) after the resonator is installed [113]. Neither of the two above scenarios are desirable. Therefore, the location of the resonator and its internal resistance need to be investigated and properly chosen.

If the aperture of the resonator is covered with rigid stoppers, then *Z* goes to infinity. In this circumstance, i.e., neglecting the effect of the resonator, the modal coefficient a_i can be determined based on Eq. (3.29)

$$a_i = -\frac{i\rho kc}{\left(k^2 - k_i^2\right)} q_s \phi_i\left(\vec{x}_s\right) + \frac{i\rho kc}{\left(k^2 - k_i^2\right)} \sum_{m=1}^{M} b_m \int_{S_{op}} \left(\phi_i \chi_m\right) ds_{op} \qquad (3.48)$$

As expected, the model coefficient is determined by the primary sound source and the cavity opening, as indicated by the first and second term on the right-hand side of Eq. (3.48), respectively. From this expression, the effect of the opening on the sound distribution inside the cavity is obvious, i.e., the influence of the opening is selective to the cavity modes ($\int_{S_{op}} \left(\phi_i v_n\right) ds_{op}$). In other words, the opening only contributes to a_i when $i_{xy} = m$ due to the orthogonal property. This can be used to explain the high sound level inside and outside the baffled open cavity mainly existing around frequencies associated with $\left(i_x, i_y, 0\right)$ modes.

When considering the resonator as the secondary sound source mounted on the wall, the volume velocity source strength q^R directed outwards from the aperture into the cavity is given by:

$$q^R = \frac{p\left(\vec{x}^R\right)}{Z} = -\frac{i\rho kc\sum_{h=1}^{N}\phi_h\left(\vec{x}^R\right)\dfrac{\phi_h\left(\vec{x}_s\right)}{\left(k^2-k_h^2\right)}}{Z - i\rho kc\sum_{h=1}^{N}\dfrac{\left[\phi_h\left(\vec{x}^R\right)\right]^2}{\left(k^2-k_h^2\right)}} q_s + \frac{i\rho kc\sum_{h=1}^{N}\phi_h\left(\vec{x}^R\right)\dfrac{\sum_{m=1}^{M} b_m \int_{S_{op}} \phi_h\left(\vec{x}\right)\chi_m\left(\vec{x}\right) dS_{op}}{\left(k^2-k_h^2\right)}}{Z - i\rho kc\sum_{h=1}^{N}\dfrac{\left[\phi_h\left(\vec{x}^R\right)\right]^2}{\left(k^2-k_h^2\right)}} \tag{3.49}$$

It is observed from Eq.(3.49) that the location and internal resistance of the resonator have a strong effect on q^R through the items $\phi_h\left(\vec{x}^R\right)$ and Z . A low internal resistance results in high values of q^R in the vicinity of the resonance of the resonator, which promotes strong re-radiation from the resonator. With the increase of the resonator resistance, q^R decreases and approaches to zero eventually, thereby disabling the

resonator's radiation.

If further assuming that the multiple mode interactions can be ignored, the relationship between the secondary source from the resonator and the primary sound source can be obtained from Eq.(3.49),

$$q^R/q_s = -i\rho kc\phi_h\left(\vec{x}^R\right)\frac{\phi_h\left(\vec{x}_s\right)-b_{h_{xy}}\psi_{h_z}\left(0\right)}{Z\left(k^2-k_h^2\right)-i\rho kc\left[\phi_h\left(\vec{x}^R\right)\right]^2} \tag{3.50}$$

For appropriate designs of the resonator, the ratio of the resonator source to the primary source can approach -1 at the resonant frequency, i.e. $q^R/q_s \to -1$. In this way, the sounds generated by the two sources are of the same amplitude but out of phase. The noise reaching the receivers at proper locations is canceled.

3.4.2.1 The output impedance of the HR

The acoustic resonator used in this study was referred to the T-shaped acoustic resonator designed and developed by Li *et al.* [111] due to its compactness in size. Such typical resonator consists of two branches, a short circular neck tube and a long rectangular volume tube perpendicular to the short one. The radius of the circular neck is α and the area of the cross-sectional area for the rectangular tube is S2. The physical lengths of the neck branch is LB1 and the volume branch is divided into LB2 and LB3, respectively. The plane wave propagation inside the resonator is assumed when deriving the resonant frequency and output impedance at the aperture. In this study, the crucial frequency of the resonator was 4096 Hz, which is far greater than the frequency of interest and validates the satisfaction of the plane wave assumption.

As derived by Ref. [111], the acoustic output impedance, Z, at the external aperture of the resonator can be calculated from

$$Z = iz_0 \frac{1-\frac{S_2}{S_1}\tan(\mathbf{k}_1 L_1)\tan(\mathbf{k}_2 L_2)-\frac{S_3}{S_1}\tan(\mathbf{k}_1 L_1)\tan(\mathbf{k}_3 L_3)}{S_1\tan(\mathbf{k}_1 L_1)+S_2\tan(\mathbf{k}_2 L_2)+S_3\tan(\mathbf{k}_3 L_3)} \tag{3.51}$$

where $\mathbf{k}_1$, $\mathbf{k}_2$ and $\mathbf{k}_3$ are the complex propagation constant of three branches considering the absorption process, and L_i is the effective lengths of the relative branch i, which is the summation of the physical lengths and its end correction [121],

$$\begin{aligned} L_1 &= LB_1 + 1.7a \\ L_2 &= LB_2 + 1.5\frac{8}{3\pi}a \\ L_3 &= LB_3 + 1.5\frac{8}{3\pi}a \end{aligned} \tag{3.52}$$

Notice that the L_1 in this study is a little different from that presented in Ref [111], because the resonator aperture in their study was unflanged. Li *et al.* [111] validated the proposed impedance model and generally speaking, the calculation accuracy of acoustic impedance by Eq.(3.51) is satisfactory.

3.4.2.2 The noise control by the single HR

Three resonators, consist of a circular short neck tube and rectangular backing volume, were designed in this study. Their geometry parameters are indicated in the following Table 3.2. In order to facilitate the analysis, the resonator is named using a 'HR' together with an integer indicating the natural frequency of the resonator. The 'S', 'M' and 'L' represent their volume size are small, medium and large.

Table 3.2 Geometry parameters for three resonators

Resonator	Resonant frequency [Hz]	Neck Branch Diameter [m]	Volume Branch width [m]	LB1 [m]	LB2 [m]	LB3 [m]
HR381S	381	0.021	0.037	0.04	0.03	0.04
HR381M	381	0.021	0.049	0.021	0.03	0.036
HR381L	381	0.03	0.05	0.03	0.042	0.041

It is known that noise abatement by resonators is sensitive to their location and internal resistance [112]. Therefore, three resonators were fabricated whose natural frequencies were tuned to the same value of 381 Hz. The neck branches of these two resonators are identical while the volume branches were different. We named the resonator in small volume branch HR381S and the larger one HR381M and the largest one HR381L. Comparison of the sound response when these two resonators were installed at the same position can roughly validate the relative size effect of the resonator on the noise radiation reduction of the open cavity. When considering the internal resistance effect, three values of Ri from the Ref. [113] have been investigated. The location effect can be examined by changing the resonator location. Due to the space limitation and the practical application in the noise barrier studied in the next chapter, the resonators were only mounted on the vertical walls of the cavity. The locations of these two resonators are list in Table 3.3 and the sound attenuation performance is compared through the sound pressure level at the inside and outside receivers.

Table 3.3 Resonator locations for three resonators.

	Helmholtz resonator	Location		
		x	y	z
HR381-S1	HR381S	0	0.085	-0.49
HR381-M1	HR381M	0	0. 085	-0.49
HR381-M2	HR381M	0.45	0. 085	-0.49
HR381-M3	HR381M	0	0.085	-0.29
HR381-L1	HR381L	0	0.085	-0.049

In this section, the enclosure mode (2, 0) which dominants the second sound perk at 404 Hz was chosen as the target mode. The locations of the HR381 were shown in Table 3.3.

3.4.2.2.1 Location effect

The first comparison was to investigate the location effect of the resonator on the noise abatement at receivers inside and outside the cavity.

Fig 3.9 (a) and (b) illustrates the SPL changes after inserting the resonator. Fig 3.9 (a) presents the receiver inside the cavity and (b) the receiver outside the cavity. A similar SPL variation tendency could be obtained at the two receivers. The locations of the resonators can be found in Table 3.3. When the resonator is nearest the sound source, the maximum noise reduction can be observed around the target frequency. For a longer distance of the resonator from the primary sound source, weaker coupling between the cavity and resonator resulted less noise reduction. Fig 3.9 (c) and (d) present the source strength generated at the resonator aperture compared with the primary sound source based on Eq.(3.49). The solid line in these two sub-figures is the amplitude and phase of the primary sound source. As can be observed, the variation of the amplitude $\left|q^R/q_s\right|$ in Fig 3.9 (c) is consistent with the changes of the sound pressure level in Fig 3.9 (a) and Fig 3.9 (b). Taking the dashed green line as the example, two SPL peaks in the vicinity of the original one are caused by the strong sound reflection at the resonator aperture. When the primary source frequency approached the tuned natural frequency of the resonator HR381-M1, the relative amplitude generated by the resonator was almost equal to the primary sound source, while the phase difference in radians was π. In other words, the sound response at the receiver generated by the primary sound source and the resonator was identical but out of phase, resulting in the noise cancellation. A similar observation was made for HR381-M2 and HR381-M3. While the enclosure modal functions were the same at these resonators, the acoustical coupling of the resonators and the cavity varied due to the baffled opening.

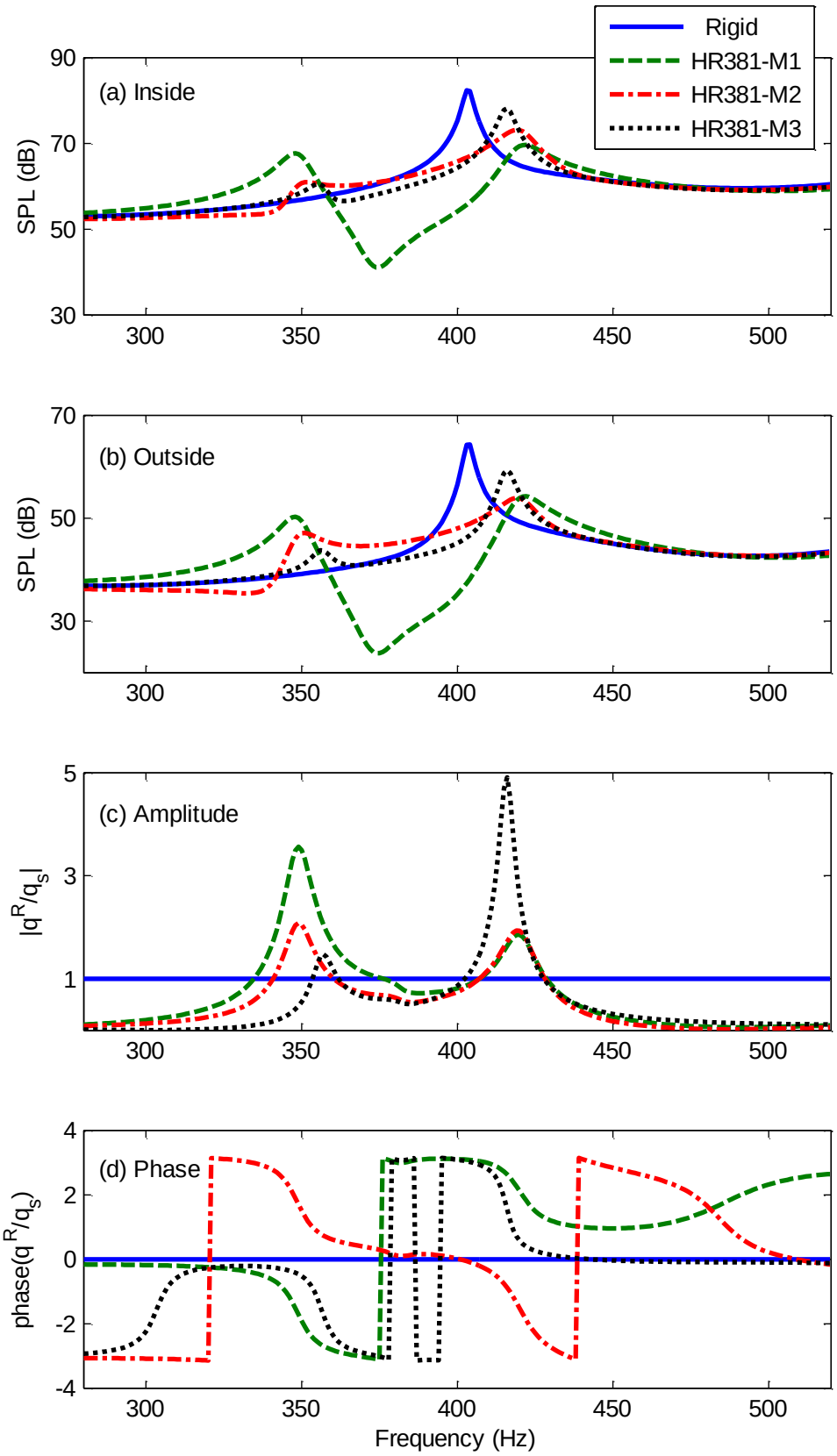

Fig 3.9: Predicted SPL comparison at inside and outside receivers when the same resonator located at different positions.

Fig 3.10 presents the sound field variation at 402 Hz when the resonator was in the above locations.

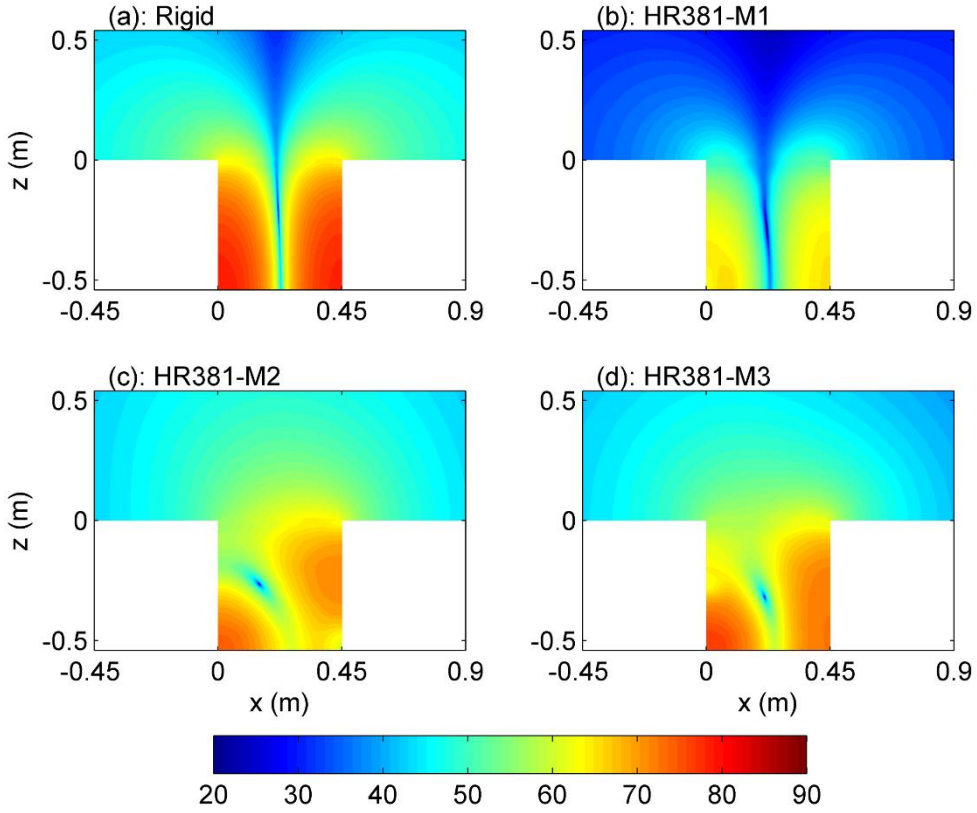

Fig 3.10: The sound field at 402Hz: (a) without resonator; (b) with HR381-M1; (c) HR381-M1 and (d) HR381-M3.

3.4.2.2.2 Internal resistance

Subsequently, the internal resistance of the resonator was investigated. The internal resistance Ri on the noise control of the baffled open cavity can be explained as follows with the help of Fig 3.11. A large internal resistance in resonators can definitely increase the dissipation ability, but reduce the radiation from resonators. However, the energy dissipation in resonators also depends on the vibration of the lumped mass in the resonator neck. The high internal-resistance constrains the vibrating level of the lumped mass, and consequently weakens the interaction between resonators and the cavity. Therefore, an excessive internal resistance can only bring about a moderate SPL reduction in the vicinity of the original peak, as shown in Fig 3.11 by a dashed line. On

the contrary, a low internal resistance in resonators leads to a drastic SPL peak reduction at the targeted frequency at the expense of creating two pronounced peaks as shown by a dot-dashed line in Fig 3.11. Resonators thus radiate sound back into the enclosure efficiently and only dissipate a small amount of energy in the frequency band. The resonator in this condition works as a reflector with little dissipation. None of the above scenarios is desirable. The energy dissipation and radiation in Ref.[113] has also been used to confirm the above analysis.

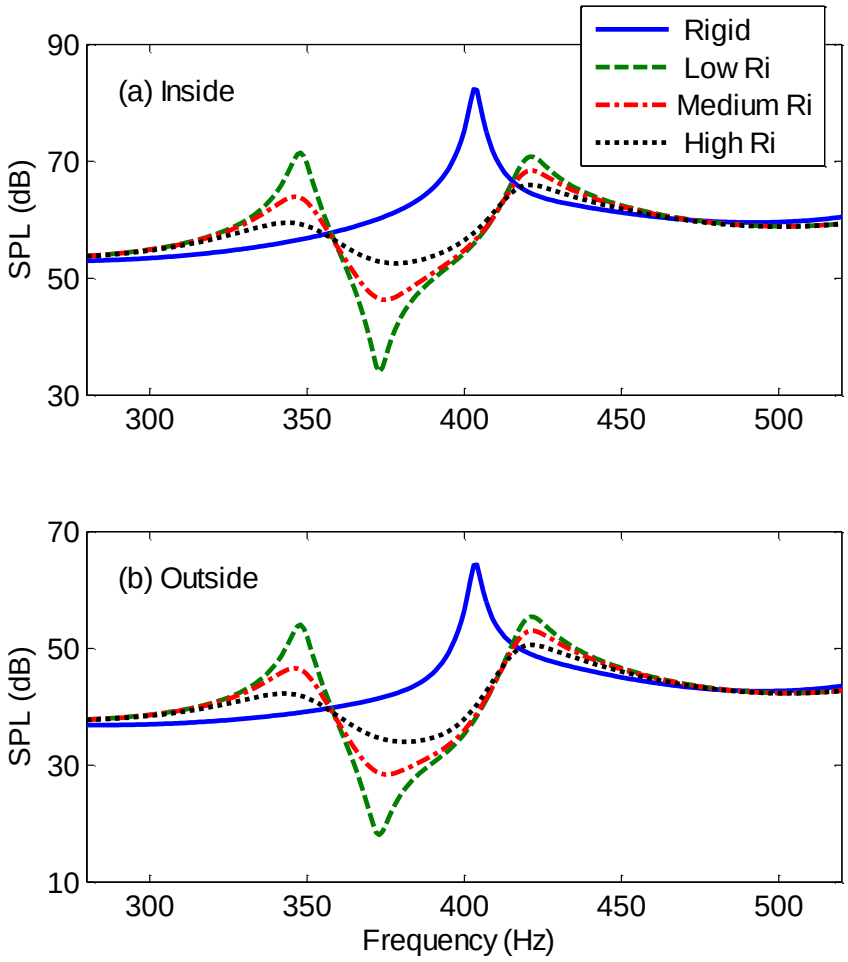

Fig 3.11: Predicted SPL comparison at inside and outside receivers when three different resonators located at same position.

As obtained from Fig 3.11, when the resistance of the resonator is at optimal value or approximates to the optimal value, the noise reduction is maximum and the peaks at the coupled frequencies are relatively flat, resulting in overall sound reduction within

the frequency band. When the internal resistance of the resonator is much lower than the optimal value, the insertion of the resonator produces two pronounced peaks, thereby affecting the sound attenuation ability of the resonator within the chosen band. In this case, most of the energy is radiated back to the cavity with little amount of energy dissipated by the resonator. This is attributed to the low mobility of the resonator aperture so that the resonator and the enclosure cannot be effectively coupled.

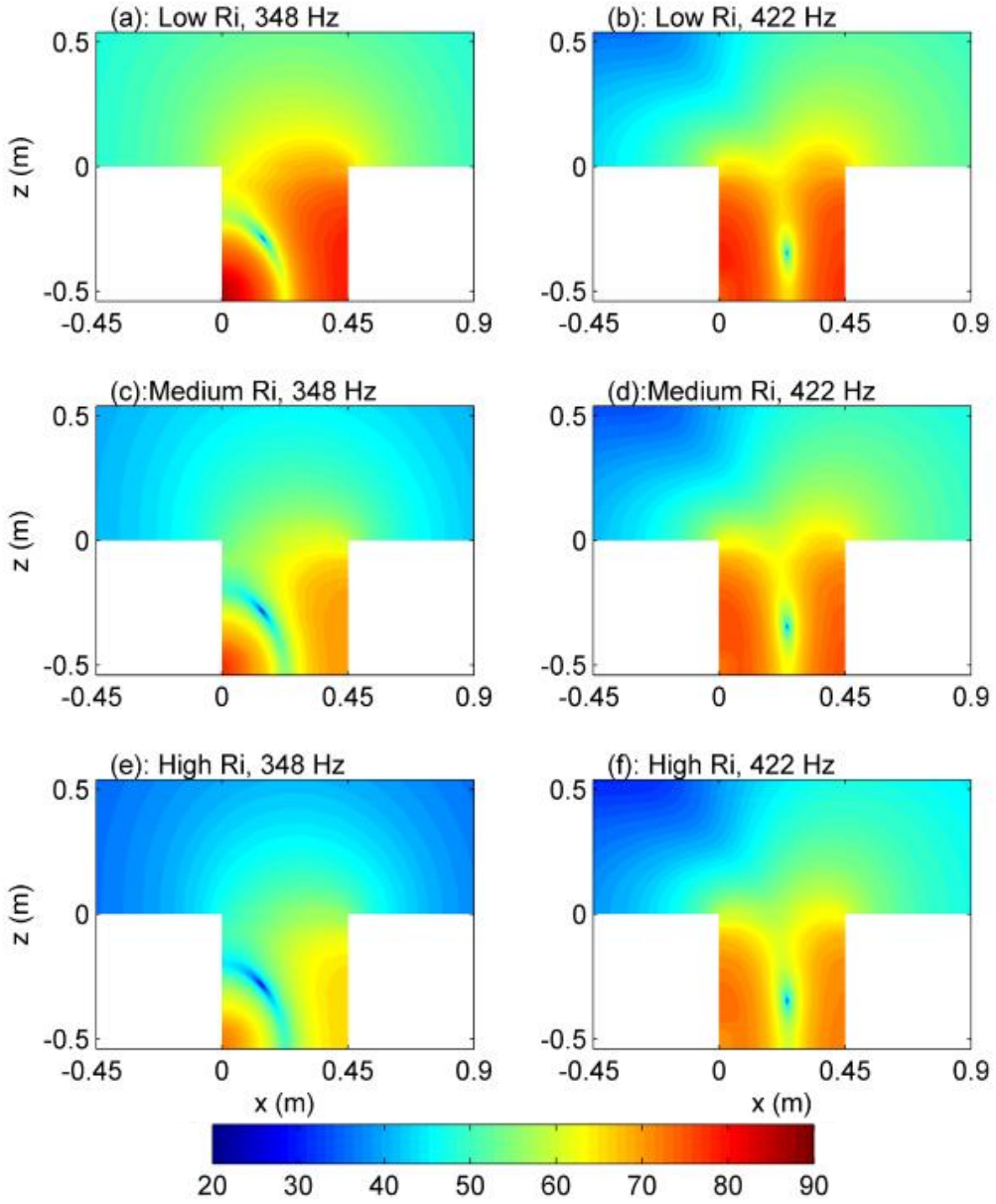

Fig 3.12: The sound field at the emerged new peaks for resonator with different internal resistance.

3.4.2.2.3 Relative resonator size

This section investigates the effect of resonator size on the sound field inside and outside the cavity. Three resonators were designed to have the same natural frequency of 381 Hz, while the neck and volume branches were different. HR381-S1 and HR381-M1 have an identical neck branch but the volume size of HR381-M1 is larger than that of HR381-S1. For the third resonator, HR381-L1, it had either the largest diameter of aperture or volume of backing cavity. The relative volume ratios of these three resonators were 3.4%, 5.2% and 7.4% when compared to the open cavity, respectively.

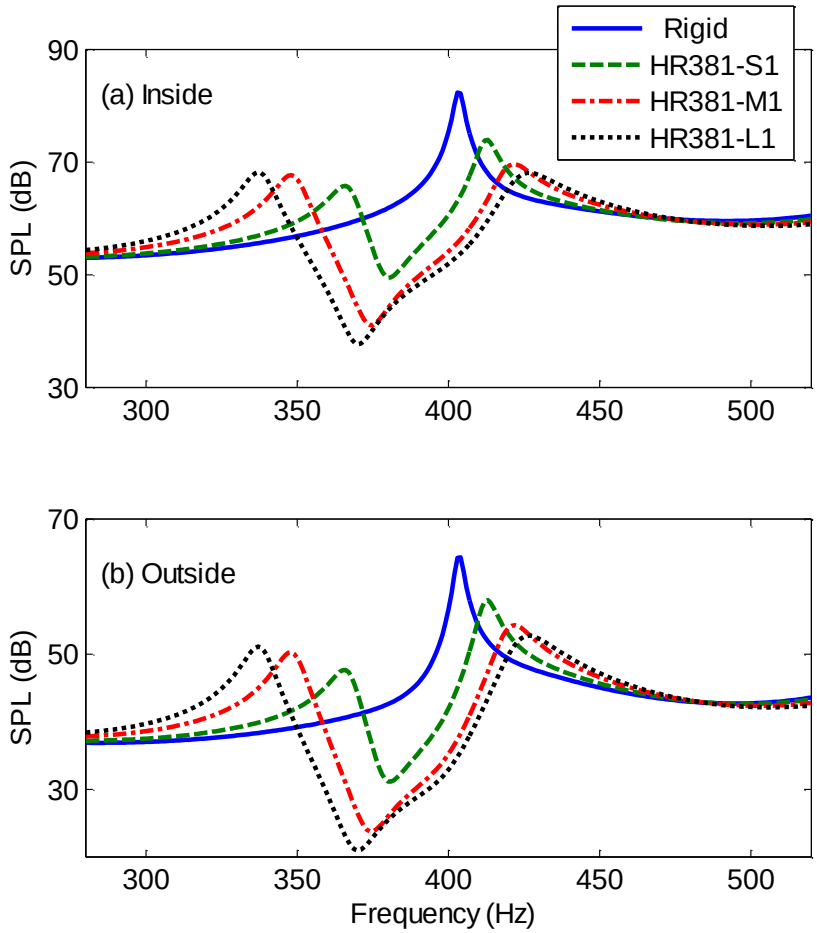

Fig 3.13: the SPL variation when installed with same resonator of different relative size.

Fig 3.13 presents the SPL changes at receivers R1 and R2 when installed with one single resonator of a different size. These resonators were tuned to the same natural frequency and located at the same location at (0, 0.085, -0.49). For a Helmholtz

resonator with a small cavity/long neck, the dip of SPL occurs exactly at the tuned frequency in a narrow frequency range (green dashed line). For a large cavity/short neck, there is a slight shift in the dip SPL from the tuned frequency to a lower frequency (dot-dashed and dotted lines). As the resonator size increases, the broader the noise reduction frequency range that can be obtained. The following contours indicate the sound field at 402 Hz before and after being embedded with a different sized resonator.

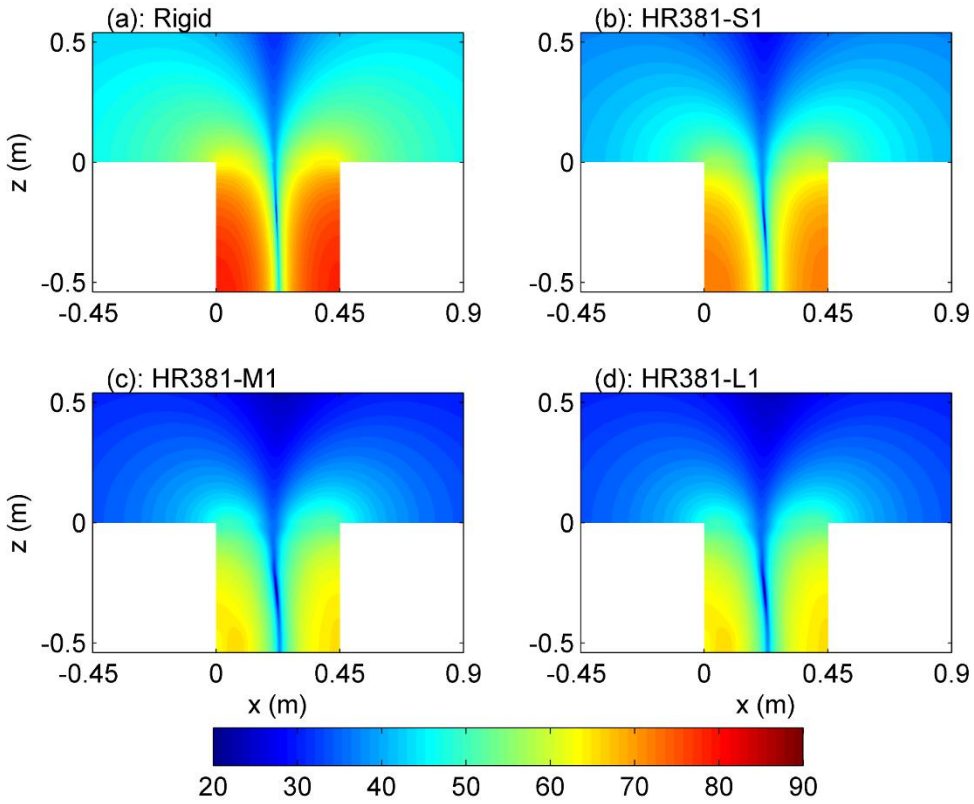

Fig 3.14: The sound field at 402 Hz for resonator with different relative size.

As indicated by the calculated results, when using a resonator to suppress the sound radiation from the open cavity, the noise reduction performance is mainly determined by the acoustical coupling of the resonator and the cavity mode. With proper design and careful location, the resonator can attenuate effectively the sound radiation at the target frequency. Besides, a broad noise reduction range can be obtained. However, two new peaks emerged around the original resonant frequency and the sound response

maybe enhanced. Therefore, when using the resonator (array) to reduce the sound radiation from the open cavity in the wide frequency regime, the induced additional resonant frequencies have to be considered carefully.

3.5 Experimental validation

Experiments were carried out to validate the aforementioned results. Fig 3.15 is the sketch of the experimental setup. Two B&K microphones were positioned at R1 and R2, respectively. One was installed flush with the cavity walls and the other was supported by the tripod. Both the AD (BNC 2120) and the DA (NI. 9234) convectors were controlled by a LABVIEW program, which is made to run from 200 to 1000 Hz. The output noise signal from the DA converter was passed firstly via a power amplifier (LA 1201) and then to the loudspeaker.

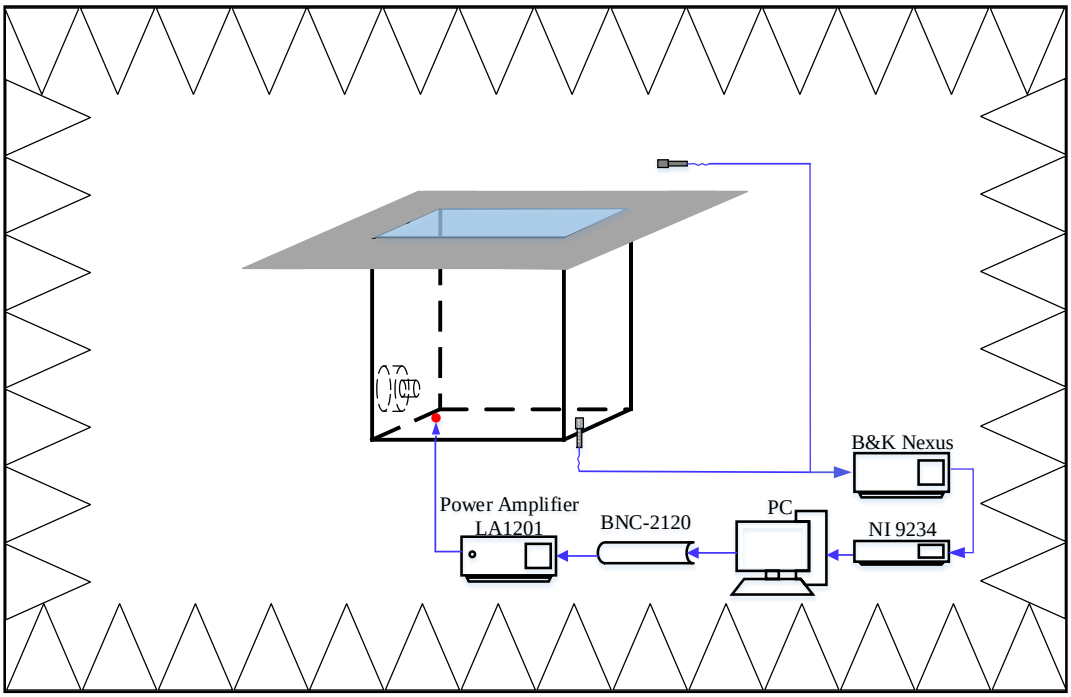

Fig 3.15: The sketch of the experimental setup.

An acoustic resonator was used in the experiment is shown in Fig 3.16. The resonator was fabricated using a circular PVC tube and rectangular aluminum tube. The physical

length of the circular branch was 21.0 mm and that for rectangular branch is 71.5 mm. The area of cross section for the rectangular branch were 29.5 mm*29.5 mm. Fig 3.17 indicates the rectangular open cavity and the baffled panel. The open cavity was constructed from acrylic plates which were 20 mm in thickness to prevent sound transmission through the side walls. The size of the cavity was the same as that in calculations. The opening of the cavity was located at the center of the baffled panel and the size of the baffle was 2.4m*2.4m. The primary source, generated by a 20-cm diameter loudspeaker, was located at (0.05, 0.085, -0.49) m near the cavity bottom and generated tonal or broadband sound. The resonator was mounted on the cavity wall and was used to control the noise level in the above baffled open cavity in the validation experiments.

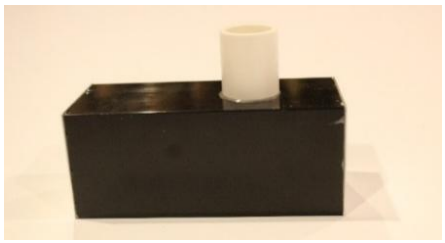

Fig 3.16: A typical T-shaped Helmholtz resonator.

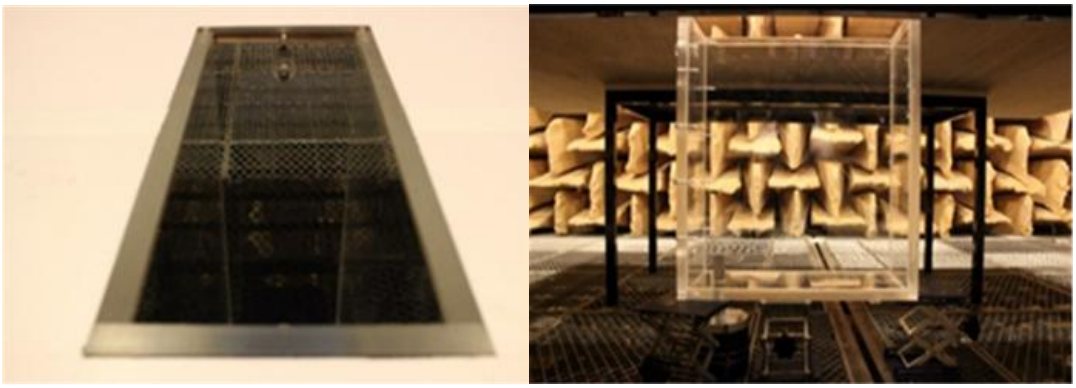

Fig 3.17: Experimental setup for the baffled open cavity in anechoic chamber.

Practically, the frequency response of the loud speaker is not always flat as indicated by the solid blue curve in Fig 3.18. The acoustical resonances of the cavity might be

misinterpreted. Therefore, the loud speaker was regulated to equalization first by inverse filtering. A loud speaker with a short rigid tube was used in the equalization process and the microphone was placed 20 mm in front of the tube aperture. The measured white noise response was used to construct an inverse filter. Fig 3.18 shows the loud speaker frequency response before and after equalization. As expected, the sound amplitude emitted from the loud speaker had almost the same level (±0.3 dB) from 200 to 1000 Hz with a step of 1 Hz [122].

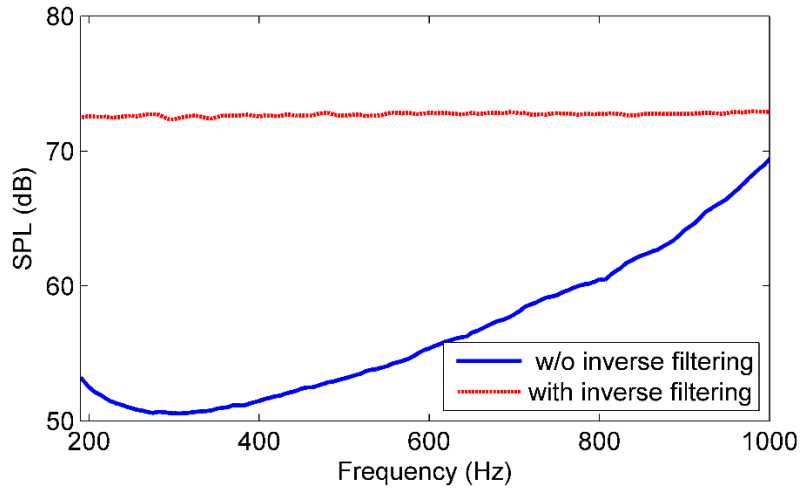

Fig 3.18: The sound amplitude emitted from the loud speaker before and after equalization.

To examine the accuracy of the proposed theoretical model, a comparison of the SPL at the same receivers was made. The SPL predicted by the proposed theoretical method and measured in the experiment was compared firstly for the baffled open cavity without the resonator. Fig 3.19 (a) shows the SPLs at (0.45 m, 0.085 m, -0.49 m) inside the open cavity while Fig 3.19 (b) shows those at (0.65 m, 0. m, 0.2 m). The solid lines shows the results predicted by the theoretical model and the dashed line for the results measured in the experiments. Well agreement can be found for the solid and dashed lines in these two figures, which shows that the proposed model could be used to accurately predict sound pressure inside and outside the baffled open cavity.

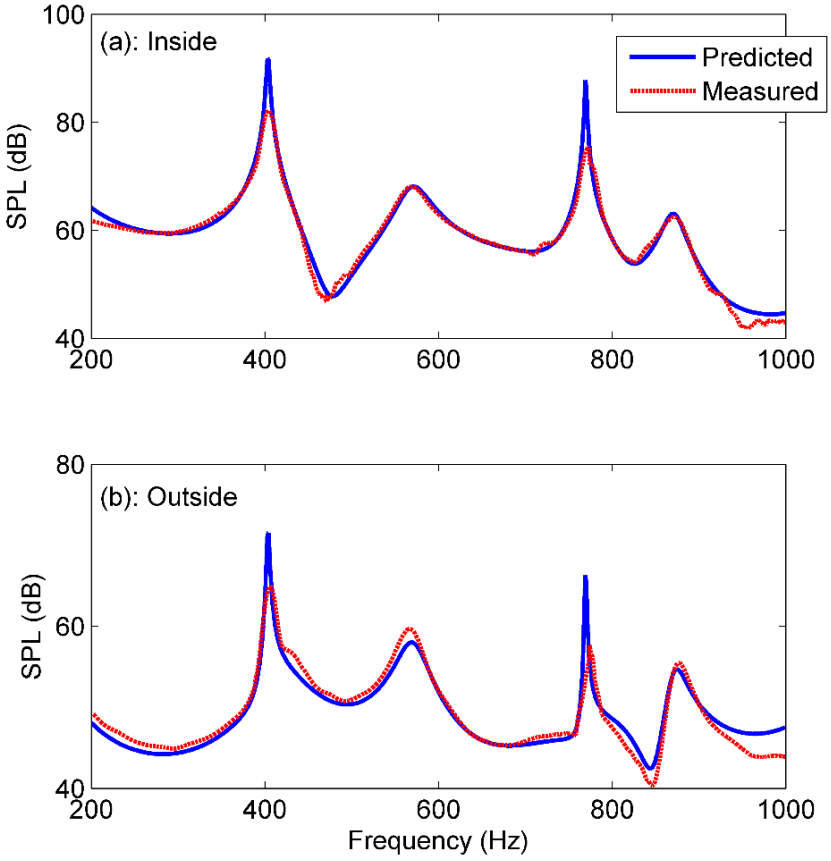

Fig 3.19: Measured and predicted SPL comparison at inside and outside receiver without acoustic resonator.

Subsequently, a comparison of SPL was made for the baffled open cavity with one single resonator. The resonator was located at (0.0 m, 0.085 m, -0.49 m), at the same vertical level as the sound source. The aperture of the resonator was toward the cavity side. Fig 3.20 shows the SPLs at the same two receivers as used in Fig 3.19. After inserting the resonator, the noise reduction can be found at the two receivers either in the experiment or the calculation. Two new peaks emerged in the vicinity of the original one. Generally speaking, the results obtained by the proposed model agree well with the experimental results, which shows that the proposed method could be used to accurately predict sound pressure response for the cavity with a partial opening.

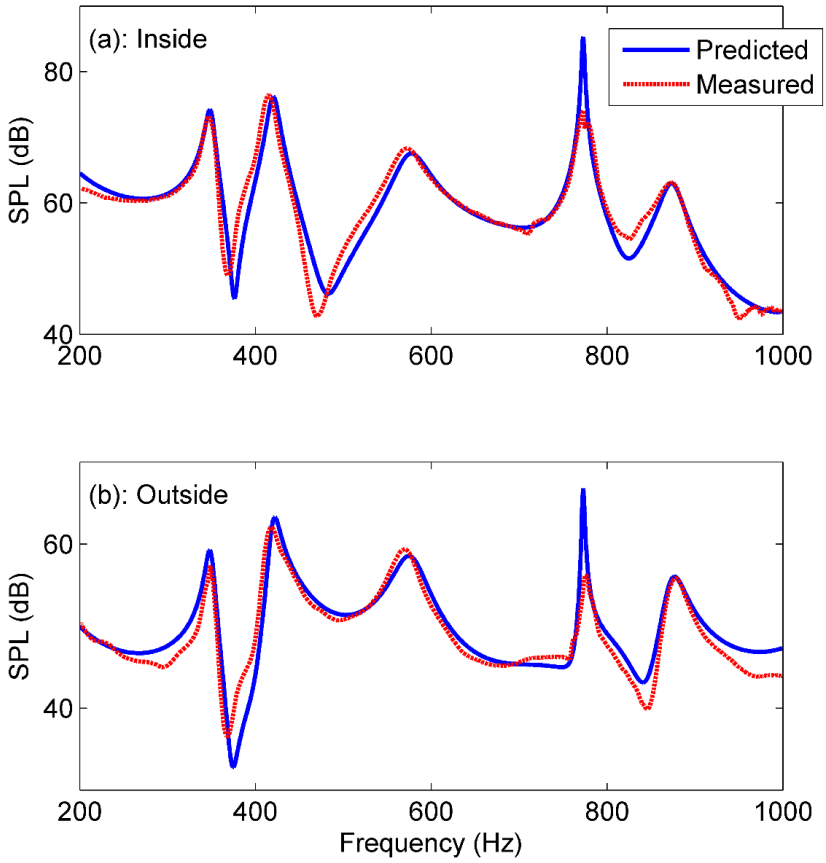

Fig 3.20: Measured and predicted SPL comparison at inside and outside receiver with single one acoustic resonator which natural frequency is 381 Hz.

3.6 Summary

The aim of this chapter has been to establish a theoretical model for the acoustical coupling between a baffled open cavity and a Helmholtz resonator array based on the modal coupling method. For the convenience of the analysis, the resonator array was simplified to one single resonator. The accuracy of the theoretical method was validated by comparison with the numerical method BEM programs and good agreement was found.

Combining the dominant equations of the sound field inside and outside, the characteristic matrix equation was produced and the eigenvalues of the open space determined. Due to the radiation loss, the eigenfrequencies is complex and shifted to

higher values compared with those for the enclosed cavity. The theoretical analysis indicates that the sound peaks inside and outside the baffled open cavity are dominated by one cavity mode whilst being contributed from other modes. After inserting the resonator whose natural frequency was equal to the dominant one, the noise reduction inside and outside the cavity could be found obviously at the target frequency. Besides, two new resonances emerged around the original eigenfrequency. The location, internal resistance and the relative size of the resonator, which determine the noise abatement performance were investigated. The longer the distance of the resonator from the primary sound source, the weaker the coupling between the cavity and resonator resulting in less noise reduction. When the resistance of the resonator is at the optimal value or approximates to the optimal value, the noise reduction is maximum and the peaks at the coupled frequencies are relatively flat, thus resulting in overall sound reduction within the frequency band. As the resonator size increases, a broader noise reduction frequency range can be obtained.

Finally, experiments at the same receivers for the baffled open cavity without and with single one resonator was performed in an anechoic chamber. The measured results demonstrate the accuracy of the proposed theoretical model and the effectiveness of using the Helmholtz resonator to reduce the noise radiation from the opening of the cavity. The proposed model provides a useful tool to analyze the sound radiation from the opening of the baffled open cavity and noise reduction device based on the modal control.

CHAPTER 4

NOISE REDUCTION FOR PARALLEL BARRIERS BY INTEGRATION WITH HELMHOLTZ RESONATORS

4.1 Introduction

As discussed in Chapter 1, the multiple reflections between the barriers create a reverberant sound field within the bounded domain and deteriorate the performance at some discrete frequencies [10, 123]. These frequencies correspond to the resonances in such an unbaffled open cavity system and their SPLs at receivers are higher than at other frequencies. When analyzing the sound response at these resonances, a strong oscillation with a high pressure amplitude can be found within the bounded domain by the two vertical barriers and the reflective ground. In this regards, a modal insight can help to gain a deeper understanding of wave propagation in parallel barriers but not much literature exists on this issue. Essentially, the degradation in the performance is due to the resonance in the bounded domain, so the effective and direct way to improve the degradation is to suppress the resonance within the two vertical parallel barriers. The Helmholtz resonator (HR) is the common resonance control device and has been extensively used in ducts and enclosure systems. A series of work by Li and Cheng [110-113] systematically investigated the acoustical coupling of an enclosure and Helmholtz resonators. The theoretical model and the optimization strategy were established and investigated effect of the physical characteristics and the locations of the resonators. Meanwhile, by using a resonator array with different resonance

frequencies, a wide band noise reduction can be achieved. Similar to this idea, a HR array was integrated into structures to improve the transmission loss of a duct [72, 73, 114] and that of an enclosure cylindrical shell [115-117]. However, most of the work focused on the acoustic duct or enclosed systems, little concerns the HR application on the sound reduction in the open system such as parallel barriers.

Therefore, the objective of this chapter is to study the sound propagation in parallel barriers from a modal view and use the Helmholtz resonator to enhance the noise reduction.

4.2 Numerical modeling of the parallel barriers

The following Fig 4.1 shows the schematic diagram of the parallel barriers.

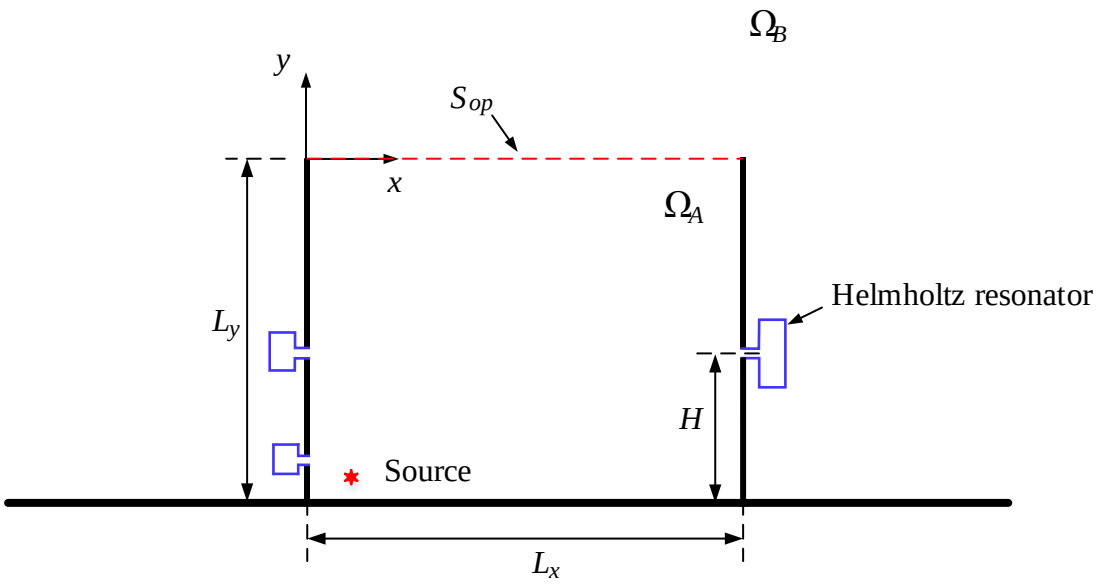

Fig 4.1: The parallel barriers integrated with multiple resonators.

The height of the two barriers is the same as L_y and the distance between these two barriers is L_x. It is assumed that the cross sections are unchanged in the *z*-direction. A primary sound source marked by the asterisk is fixed near the left barrier. The origin of

the coordinate is at the left top vertex of the barrier. All the walls of the barrier are assumed to be acoustically rigid. The ground is considered perfectly reflecting in this chapter. Multiple Helmholtz resonators are embedded in the walls of the parallel barriers.

When a harmonic time dependence sound pressure field is generated by a point source at $\vec{x}_s = (x_s, y_s)$ in the cross-section plane, the sound field $p(\vec{x})$ can then be described by a two-dimensional inhomogeneous Helmholtz equation:

$$\nabla^2 p\ \vec{x}\ + k^2 p\ \vec{x}\ = -Q_s \delta\ \vec{x} - \vec{x}_s \tag{4.1}$$

where $k = \omega / c_0$ is the wavenumber, c_0 is the speed of sound in the air, and Q_s and $\vec{x}_s$ are the source strength and location, respectively.

For convenience, the whole acoustic domain of the parallel barriers together with the semi-infinite half space is divided into two parts: (1) the bounded rectangular cavity domain Ω_A, which is enclosed by the parallel barriers, the reflecting ground and the opening and (2) the outside domain Ω_B. The two domains are shown in Fig 4.1. They are connected through the cavity opening S_{op} (red dashed line).

For the infinite far field, the Sommerfeld radiation condition should be satisfied and all the walls of the barrier are acoustically rigid except the opening of resonators,

$$\begin{gathered} \lim_{x\to\infty} r^{1/2}\left(\frac{\partial}{\partial r} - ik\right) p = 0 \\ \frac{\partial p}{\partial n} = 0 \end{gathered} \tag{4.2}$$

In the bounded cavity domain Ω_A as shown in Fig 4.1, when regarding the resonator as the secondary sources at $\vec{x}_t^{\,R}$, the governing equation for the sound pressure p_A and the boundary conditions is:

$$\nabla^2 p_A\ \vec{x}\ + k^2 p_A\ \vec{x}\ = -i\rho kcq_s \delta\ \vec{x} - \vec{x}_s \tag{4.3}$$

together with the boundary conditions for the opening of the cavity and the acoustic resonator, i.e.,

$$\left.\frac{\partial p_A}{\partial n}\right|_{S_{op}} = -i\rho kcv_n \tag{4.4}$$

$$\left.\frac{\partial p_A}{\partial n}\right|_{\vec{x}_t^R} = -i\rho kc\frac{p_A}{Z_t} \tag{4.5}$$

in which v_n is the particle velocity at the cavity opening and Z_t is the output impedance at the aperture of the *t*-th resonator. Multiple resonators are mounted on the cavity walls and regarded as the secondary sources as described in Eq.(4.5) by means of the Robin boundary condition. The aperture of these resonators is towards the inner side of the bounded domain. Note that the sign of volume velocity from the resonators is the same as the primary sound source, which represents that the sound is radiated into the cavity.

The sound pressure $p_A(\vec{x})$ inside the domain Ω_A can be described by the undamped eigenmodes as:

$$p_A(\vec{x}) = \sum_{j=1}^{N} a_j \phi_j(\vec{x}) \tag{4.6}$$

where, a_j is the modal response of the *j*th eigenmode $\phi_j(\vec{x})$, and *N* is the maximum number of the truncated mode series.

Combining with the rigid wall conditions, the eigenmodes, $\phi_j(\vec{x})$, for the two dimensional rectangular closed cavity is given by

$$\phi_j(\vec{x}) = \psi_{j_x}(x)\cdot\psi_{j_y}(y) \tag{4.7}$$

where $\psi_{j_s}(s) = \sqrt{\frac{2-\delta_{0,j_s}}{L_s}}\cos\left(\frac{j_s\pi}{L_s}s\right)$ and j_s is the model number in the s direction.

The $\phi_j(\vec{x})$ satisfies:

$$\nabla^2\phi_j\ \vec{x}\ + k_j^2\phi_j\ \vec{x}\ = 0 \tag{4.8}$$

$$k_j^2 = \left(\frac{j_x\pi}{L_x}\right)^2 + \left(\frac{j_y\pi}{L_y}\right)^2 \tag{4.9}$$

where k_j is the wave number of the *j*-th eigenfrequency, and j_x and j_y are the model index in the *x* and *y* directions, respectively.

In the outside domain Ω_B, the sound pressure $p_B(\vec{x})$ is dominated by the sound radiation from the opening. When employing the plane wave to expand the field in the outside infinite space, traveling wave solution would create complexity. Alternatively, in this chapter, an expansion by an incomplete basis set is proposed based on the normal velocity distribution at the opening.

The sound pressure in the outside domain Ω_B and the particle normal velocity v_n at the opening can be expressed as used in Chapter 3.

$$v_n(\vec{x})\big|_{S_{op}} = \sum_{m=1}^{M} b_m\psi_m(\vec{x}) \tag{4.10}$$

$$p_B(\vec{x}) = \sum_{m=1}^{M} b_m\varphi_m(\vec{x}) \tag{4.11}$$

where M is the maximum modal number to be truncated. However, for the outer domain Ω_B of the parallel barriers (Fig 4.1), it is hard to express in the analytical way as used in Chapter 3 due to the difficulty in finding the Green function. Alternatively, the numerical method based on the finite element or boundary element analysis is used to obtain the $\varphi_m(\vec{x})$. The details about using a numerical tool to obtain the $\varphi_m(\vec{x})$ will be discussed in Section 4.2.1.

Based on the second Green identity and the sound pressure continuity at the opening, the following two equations can be obtained, the detailed derivation of which can be

found in Chapter 3 and will not be discussed here.

$$\begin{aligned} & a_i\left(k^2-k_i^2\right)-i\rho kc\sum_{m=1}^{M} b_m\delta_{i_x,m}\psi_{i_y}\left(0\right) \\ & =-i\rho kcq_s\phi_i\left(\vec{x}_s\right)+\sum_{t=1}^{T}\frac{i\rho kc}{Z_t}\int_{S_R}\left[\phi_i\sum_{h=1}^{N}a_h\phi_h\delta\left(\vec{x}-\vec{x}_t^R\right)\right]ds_R \end{aligned} \tag{4.12}$$

$$\sum_{i=1}^{N} a_i\delta_{i_x,\mu}\psi_{i_y}\left(0\right)=\sum_{m=1}^{M} b_m\left[\int_0^{L_x}\psi_\mu\left(x\right)\varphi_m\left(\vec{x}\right)dx\right] \tag{4.13}$$

Similarly, when defining $Z_{\mu,m}=\int_0^{L_x}\psi_\mu\left(x\right)\varphi_m\left(x,0\right)dx$ as the radiation impedance of the opening [118], Eq.(4.13) can be rewritten as:

$$\sum_{i=1}^{N} a_i\delta_{\mu,i_x}\psi_{i_y}\left(0\right)=\sum_{m=1}^{M} b_m Z_{\mu,m} \tag{4.14}$$

When we set:

$$\begin{aligned} \mathbf{A} &= \left\{a_1,a_2,\cdots,a_N\right\}^T \\ \mathbf{B} &= \left\{b_1,b_2,\cdots,b_M\right\}^T \end{aligned} \tag{4.15}$$

$$\mathbf{K}=\begin{bmatrix} k^2-k_1^2,0,0,\cdots,0 \\ 0,k^2-k_2^2,0,\cdots,0 \\ \ddots \\ 0,0,\cdots,k^2-k_N^2 \end{bmatrix} \tag{4.16}$$

$$\begin{aligned} \mathbf{Z^R} = i\rho kc & \left[\frac{1}{Z_1}\begin{Bmatrix}\phi_1\left(\vec{x}_1^R\right)\\ \phi_2\left(\vec{x}_1^R\right)\\ \vdots \\ \phi_N\left(\vec{x}_1^R\right)\end{Bmatrix},\frac{1}{Z_2}\begin{Bmatrix}\phi_1\left(\vec{x}_2^R\right)\\ \phi_2\left(\vec{x}_2^R\right)\\ \vdots \\ \phi_N\left(\vec{x}_2^R\right)\end{Bmatrix},\cdots,\frac{1}{Z_T}\begin{Bmatrix}\phi_1\left(\vec{x}_T^R\right)\\ \phi_2\left(\vec{x}_T^R\right)\\ \vdots \\ \phi_N\left(\vec{x}_T^R\right)\end{Bmatrix}\right] \\ & \times\begin{bmatrix}\left\{\phi_1\left(\vec{x}_1^R\right),\phi_2\left(\vec{x}_1^R\right),\cdots,\phi_N\left(\vec{x}_1^R\right)\right\}\\ \left\{\phi_1\left(\vec{x}_2^R\right),\phi_2\left(\vec{x}_2^R\right),\cdots,\phi_N\left(\vec{x}_2^R\right)\right\}\\ \ddots \\ \left\{\phi_1\left(\vec{x}_T^R\right),\phi_2\left(\vec{x}_T^R\right),\cdots,\phi_N\left(\vec{x}_T^R\right)\right\}\end{bmatrix} \end{aligned} \tag{4.17}$$

$$\mathbf{M} = i\rho kc\begin{bmatrix} \delta_{1_x,1}\psi_{1_y}(0), \delta_{1_x,2}\psi_{1_y}(0), \cdots, \delta_{1_x,M}\psi_{1_y}(0) \\ \delta_{2_x,1}\psi_{2_y}(0), \delta_{2_x,2}\psi_{2_y}(0), \cdots, \delta_{2_x,M}\psi_{2_y}(0) \\ \ddots \\ \delta_{N_x,1}\psi_{N_y}(0), \delta_{N_x,2}\psi_{N_y}(0), \cdots, \delta_{N_x,M}\psi_{N_y}(0) \end{bmatrix} \tag{4.18}$$

$$\mathbf{S} = -i\rho kcq_s\begin{Bmatrix} \phi_1(\vec{x}_s) \\ \phi_2(\vec{x}_s) \\ \vdots \\ \phi_N(\vec{x}_s) \end{Bmatrix} \tag{4.19}$$

$$\mathbf{\Phi} = \begin{bmatrix} \delta_{1_x,1}\psi_{1_y}(0), \delta_{2_x,1}\psi_{2_y}(0), \cdots, \delta_{N_x,1}\psi_{N_y}(0) \\ \delta_{1_x,2}\psi_{1_y}(0), \delta_{2_x,2}\psi_{2_y}(0), \cdots, \delta_{N_x,2}\psi_{N_y}(0) \\ \ddots \\ \delta_{1_x,M}\psi_{1_y}(0), \delta_{2_x,M}\psi_{2_y}(0), \cdots, \delta_{N_x,M}\psi_{N_y}(0) \end{bmatrix} \tag{4.20}$$

$$\mathbf{Z} = \begin{bmatrix} \int_0^{L_x}\psi_1(x)\varphi_1(x,0)dx, \int_0^{L_x}\psi_1(x)\varphi_2(x,0)dx, \ldots, \int_0^{L_x}\psi_1(x)\varphi_M(x,0)dx \\ \int_0^{L_x}\psi_2(x)\varphi_1(x,0)dx, \int_0^{L_x}\psi_2(x)\varphi_2(x,0)dx, \ldots, \int_0^{L_x}\psi_2(x)\varphi_M(x,0)dx \\ \ddots \\ \int_0^{L_x}\psi_{N_x}(x)\varphi_1(x,0)dx, \int_0^{L_x}\psi_{N_x}(x)\varphi_2(x,0)dx, \ldots, \int_0^{L_x}\psi_{N_x}(x)\varphi_M(x,0)dx \end{bmatrix}$$

(4.21)

Eqs.(4.12) and (4.14) can be simplified to:

$$\left(\mathbf{K} - \mathbf{Z}^{\mathbf{R}}\right)\mathbf{A} - \mathbf{MB} = \mathbf{S} \tag{4.22}$$

$$\mathbf{\Phi A} = \mathbf{ZB} \tag{4.23}$$

The coefficient matrix $\mathbf{A}$ and $\mathbf{B}$ can be obtained after solving the above equations. After these two coefficient are obtained, the sound pressure in cavity domain Ω_A governed by Eq.(4.6) and the sound pressure of outside domain Ω_B governed by Eq.(4.11). can be solved.

4.2.1 Numerical validation

This part conducts the computational investigation to examine the accuracy of the theoretical method proposed above. The configuration of the acoustical domain and the properties of air are listed in Table 4.1.

Table 4.1: The air properties, configurations of the parallel barriers, sound source and the receiver locations used in the calculations.

Air properties	
Density: ρ_0 [kg/m^3]	1.225
Sound speed: c [m/s]	343
Parallel Barriers	
Width: Lx [m]	1.83
Height: Ly [m]	1
Sound Source	
Location: (x_s,y_s) [m]	(0.1, -0.9)
Strength: Qs[kg/s^2]	$4\pi \times 10^{-4}$
Receiver Locations	
R1[m]	(1.7, -0.1)
R2[m]	(5, -0.9)

The parallel barriers used in this study are similar to configuration in [10] and have the size of 1.83 m long (Lx) and 1 m high (Ly). It should be noted that, in order for comparison to be made with the parallel barriers installed with the Helmholtz resonator studied in the following section, the thickness of the barrier walls is expanded to 0.1 m. Preliminary study indicates little change in the frequency range of interest for the sound response at the receivers, when changing the thickness from 0 to 0.1 m. The source is located at (0.1, −0.9) m while the evaluation receivers are randomly chosen at (1.7, -0.1) and (5, -0.9) m, representing the sound field in the domain Ω_A and Ω_B, respectively.

Due to the difficulty in describing the sound field in the outside domain Ω_B

analytically, the numerical software COMSOL based on the finite element method is an alternative to be utilized to calculate the sound response due to the normal vibration velocity at the cavity opening. The commercial FEM solver is chosen instead of the BEM tool developed in Chapter 2 due to the fact that the FEM is more efficient in the calculation in 2D within the confined domain. Moreover, the post package of the COMSOL offers another advantage to analyze the calculated results. The calculated frequency range is from 30 to 1000 Hz with a step size of 1 Hz. The maximum triangle mesh sizes are 1/12 the wavelength of 1000 Hz.

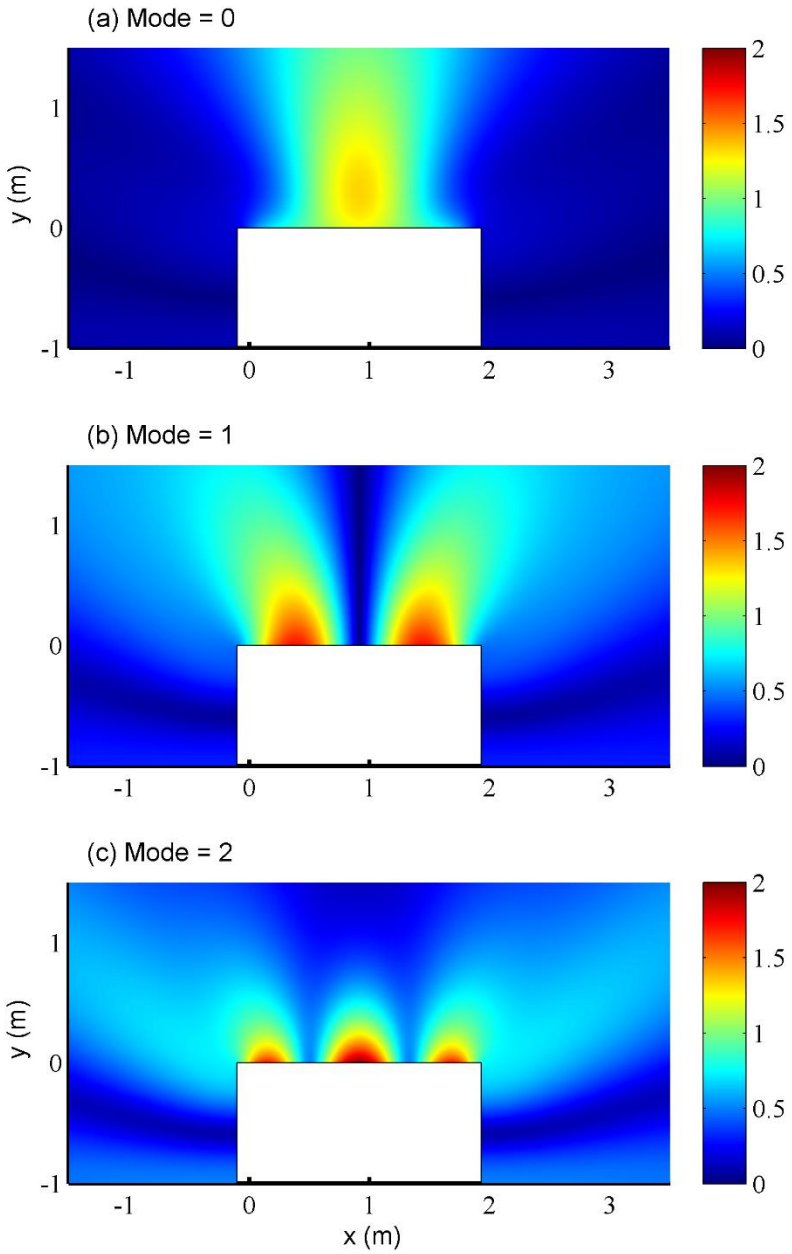

Fig 4.2: The absolute sound pressure distribution of first three modes at f=200 Hz: (a) mode=0; (b) mode=1 and (c) mode=2.

In order to simulate the Sommerfeld radiation condition in the semi-infinite space, the artificial absorbing layers -- Perfectly Matched Layer (PML) is employed, which enables minimal reflections and promises the least influence on the domain of interest from the reflections. Note that only frequencies above 30 Hz are treated in COMSOL, as at very low frequencies, the PMLs needed for calculation become very thick in order

to prevent spurious wave reflection. The Fig 4.2 presents the modulus values of the first three base functions in $\{\varphi_m(\vec{x})\}$ at the frequency of 200 Hz, which is obtained from the numerical software COMSOL.

Convergence study for the modal number was carried out as the steps in Chapter 3. For the acoustic modes $\phi_n(\vec{x})$ in Eq.(4.6), the total number ranges from 0 to 400. The finite cosine series in Eq.(4.10) is truncated to m=30. The amplitude and phase of the sound pressure at the randomly selected receivers have been evaluated as the increasing of the modal number. Numerical results show that 400 enclosed-cavity modes are normally enough in the frequency range below 1000 Hz. This will be used in the following simulations and results analysis.

The performance of the proposed method is verified by calculating the sound pressure at field points R2 for multiple frequencies below 1000 Hz, as shown in Fig 4.3. The sound source strength is taken as $q_s=4\pi\times10^{-4}$ kg/s^2 for all frequencies. Fig 4.3 compares the results obtained by the analytical model and the COMSOL. The solid line shows the SPL at R2 calculated by the COMSOL and the dashed line represents the results by the proposed theoretical model. The excellent agreement can be found for the results by the two methods and verifies the accuracy of the proposed method.

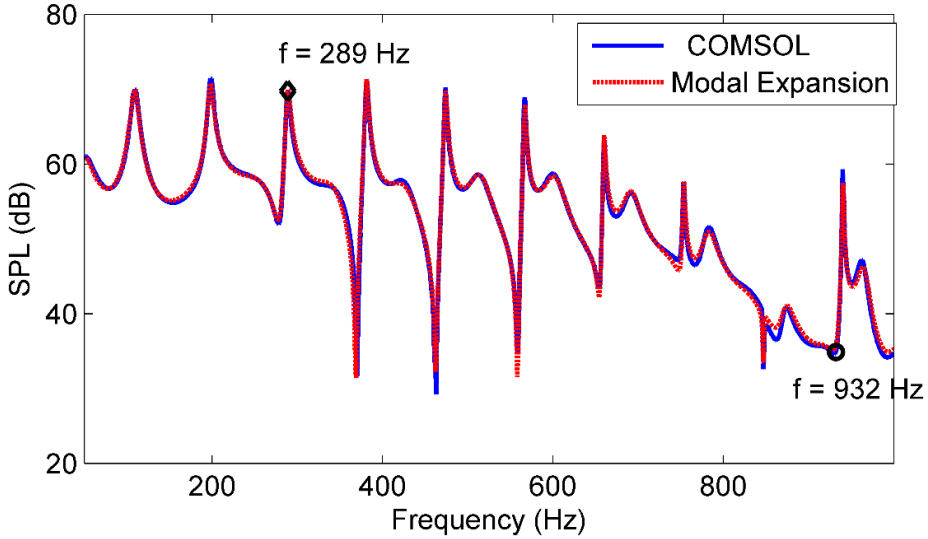

Fig 4.3: The sound pressure level for parallel barrier comparison by COMSOL and modal expansion.

Fig 4.4 provides a comparison of the reference sound field via COMSOL and the predicted sound pressure distribution based on the coupled enclosure modes and the radiation modes. Two frequencies are chosen, one is the f=289 Hz, representing one of the sound level peak; the other is f=932 Hz, the dip point in the sound pressure level curve as shown in Fig 4.3. The contours in Fig 4.4 (a) and (b) shows the sound field of the parallel barriers at 289 Hz, calculated by the COMSOL and the theoretical model. The color legend are the same and shown in the right side of the figures. Generally speaking, the sound field calculated by these two methods seem almost the same at this peak frequency. The similar conclusion can be obtained for the contours in Fig 4.4 (c) and (d) which show the sound field at 932 Hz. Therefore, excellent agreement between the results of the proposed method and the reference method is observed. Based on the results comparison in Fig 4.3 and Fig 4.4, the accuracy of the proposed theoretical model based on the mode coupling method has been validated and the analysis in the following studies are based on this method except as otherwise defined. The modal number for the enclosed cavity is 400 and for the external space is 30.

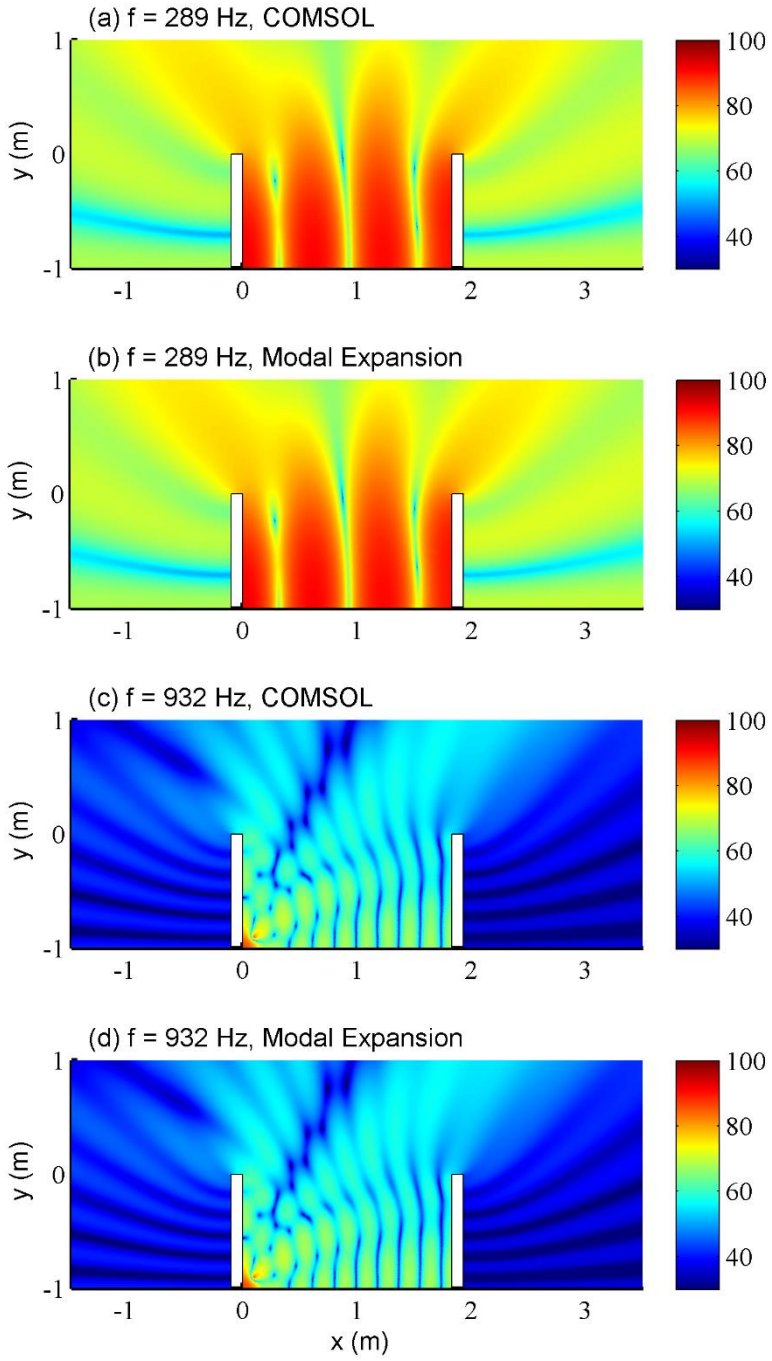

Fig 4.4: Sound pressure distribution of the parallel barrier at two selected frequencies: (a) reference sound pressure field obtained using COMSOL at f=289 Hz; (b) reconstructed field using mode coupling at f=289 Hz; (c) reference sound pressure field obtained using COMSOL at *f*=932 Hz and (d) reconstructed field using mode coupling at *f*=932 Hz.

4.3 Numerical results and analysis

Following the steps for baffled open cavity, to understand the noise control mechanism of the parallel barriers, the sound field of such an open system is analyzed in detail below by referring to Fig 4.3. The frequencies of sound pressure level which peak below 1000 Hz appear at 51, 109, 198 etc., as listed in Table 4.2. Except for the first peak of 51 Hz, the other peak frequencies are related to the second to the ninth frequencies listed in third column in Table 4.2. It is obvious that the opening increases the values of the modal frequencies of the enclosed rigid cavity, and the formation mechanism of the sound pressure distribution at 51 Hz is different from others. The following Fig 4.5 distinguishes sound response at 51 Hz and the other five peaks.

Table 4.2, The comparison of the eigenvalues of first ten (*m*, 0) enclosed cavity modes and the frequencies of the sound pressure level for parallel barrier.

Enclosed-cavity			Parallel Barriers	
Mode number	Modal indices	Frequency	Peaks	Frequency
	(i_x, i_y)	Hz		Hz
1	(0,0)	0	1	51
2	(1,0)	93.72	2	109
3	(2,0)	187.43	3	198
4	(3,0)	281.15	4	289
5	(4,0)	374.86	5	381
6	(5,0)	468.58	6	474
7	(6,0)	562.3	7	567
8	(7,0)	656.01	8	660
9	(8,0)	749.73	9	753
10	(9,0)	843.44	10	849

Fig 4.5 (a)–(f) show the sound pressure level on the cross plane when the source is located at (0.1, -0.9) and the frequency is 51, 109, 198, 289, 381, 474 Hz, respectively. It can be observed that sound pressure distribution at the last five frequencies appear almost as the mode patterns caused by the two rigid walls of the parallel barriers, while the sound pressure level at 51 Hz remains almost the same within the domain bounded

by the parallel reflecting barriers and ground (this domain is called bounded domain hereafter). This means that the sound pressure distribution at 51 Hz is mainly due to the reflection of the bottom plane and the bounded domain behaves like a 1/4 wavelength resonator at 51.0 Hz.

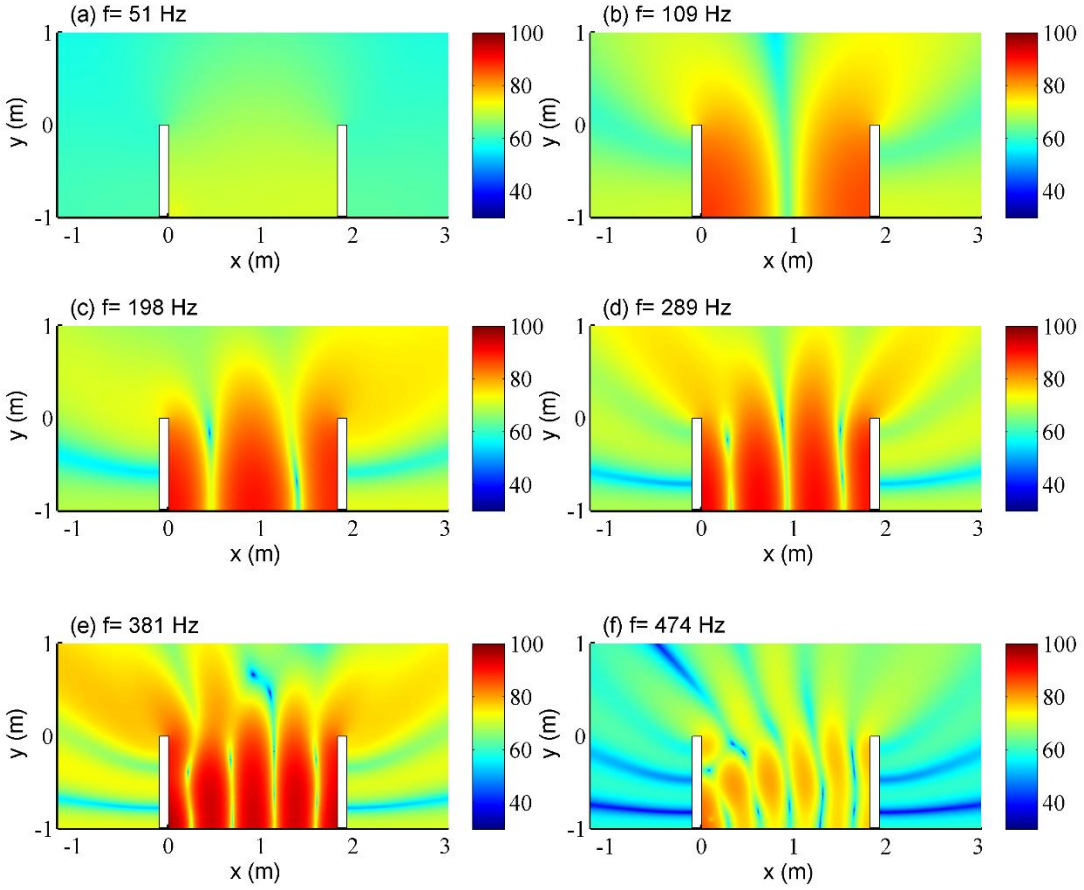

Fig 4.5: The sound perssure level field in the parallel barriers excited by a source at (0.1, -0.9) m: (a) f=51 Hz; (b) f=109 Hz; (c) f=198 Hz; (d) f=289 Hz; (e) f=381 Hz; (f) f=474 Hz.

In Fig 4.5(b)-(f), the sound pressure distribution is similar to their enclosure modal pattern. At each frequency, a clear resonance feature can be identified within the bounded domain. Within this domain, multiple reflections occur, and these reflecting waves superimpose with each other and with the direct waves generated by the noise source. In a harmonic steady state, the superposition of these waves forms a resonance response. In fact, the sound pressure level at each of the above frequencies is dominated by one associated radiation mode with its natural frequency closely coinciding with the

frequency. Therefore, the noise reduction enhancement at these frequencies for the parallel barriers is to suppress the corresponding resonances.

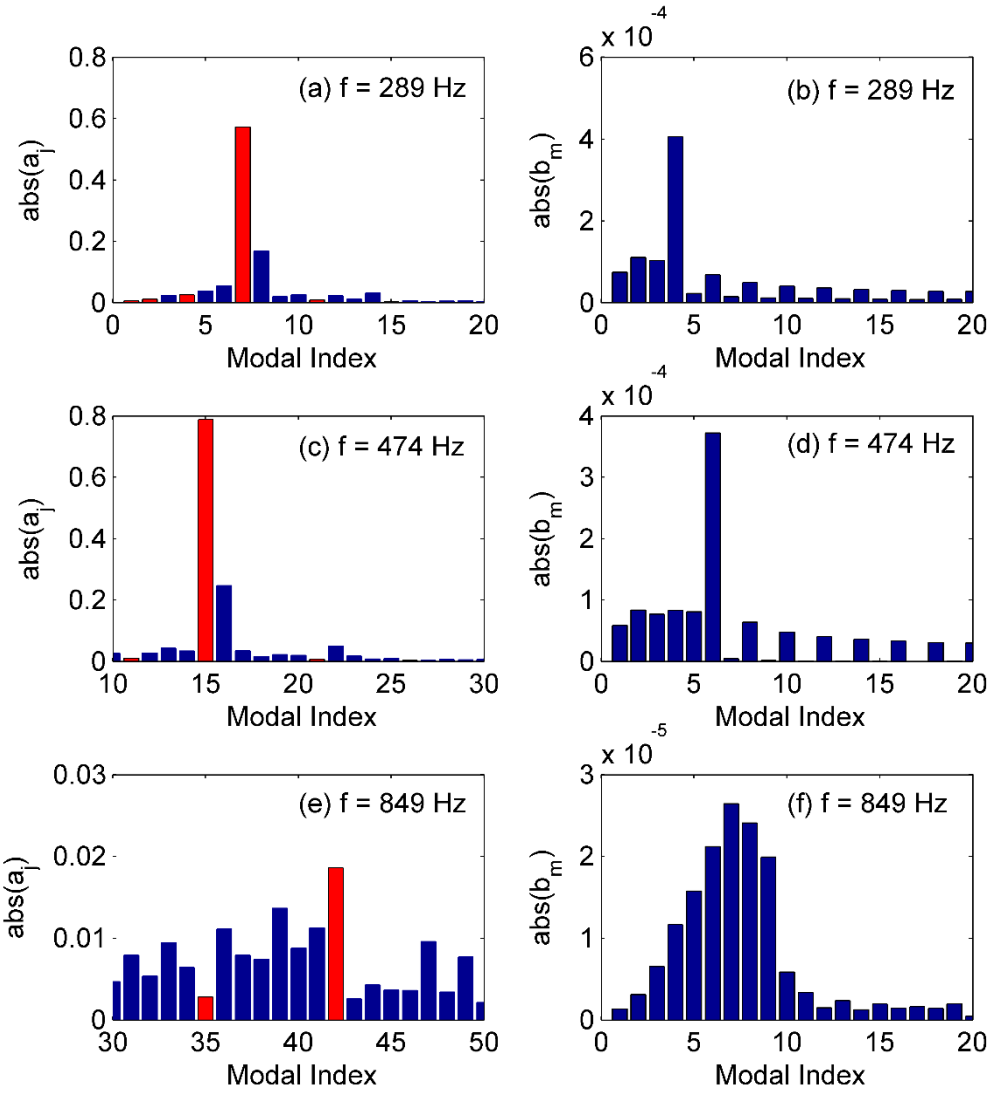

Fig 4.6: Modal amplitude at two different frequencies: (a) and (b) for 289 Hz, (c) and (d) for 474 Hz and (e) and (f) for 849 Hz.

Fig 4.6 shows the modal coefficients $|a_j|$ and $|b_m|$ for the sound pressure at the receiver R2, the two selected freqeuencies are f=289 Hz and f=474 Hz. Fig 4.6 (a) and (b) indicate the modal coefficients at 289 Hz and (c) and (d) for 474 Hz. Shown by red in Fig 4.6 (a) and (c) are the (m,0) modes as listed in Table 4.2. It can be observed obviously that the sound pressure at these two frequencies are dominated by the (3,0)

mode and (5,0) mode respectively.

When concerning the sound pressure level curve as shown in Fig 4.3, it is found that some peaks emerged together with dips. For example, Fig 4.3 has a peak close to f=474 Hz and a dip around f=463 Hz. This phenomenon is referred as the Fano resonances, a feature can be found in the open acoustic system when a high Q-factor resonance interact with the continuous spectrum.

Although not having a standard Fano lineshape, this phenomenon is a type of Fano resonance in that the asymmetric lineshape can be explained in terms of the interferences between resonant eigenmodes and non-resonant eigenmodes. Fano resonance occurs where there is a quasi-trapped mode (of high quality factor and sharp narrow resonance). When the source frequency sweeps from below to above the resonance frequency of the quasi-trapped mode, a sharp phase change occurs for the response of this quasi-trapped eigenmode while the modal coefficients of the other non-resonant eigenmodes remain almost the same within the narrow frequency band. A similar phenomenon was observed in the scattering coefficients of acoustic resonators, although the spectrum there displayed a standard Fano lineshape [69, 124].

4.4 Helmholtz resonator integrated with parallel barriers

As illustrated in Section 4.3, the sound response peaks at the receiving point are related to the resonances in the bounded cavity domain. The assumption is proposed that if the resonances inside the bounded cavity domain is suppressed, the sound response corresponding to this mode can be abated. In order to control these resonances and then enhance the noise reduction performance of the parallel barriers, the Helmholtz resonator (HR) is chosen and applied in such artificial enclosure acoustic system. The previous studies in Chapter 3 have validated the effectiveness of the

Helmholtz resonator on the noise radiation from the baffled open cavity in three dimensions. The studies in this chapter mainly focus on applying the Helmholtz resonator array to obtain a broadband noise reduction for parallel barriers. Several resonators with different natural frequencies are proposed to increase the noise reduction of parallel barriers at low frequencies.

Fig 4.1 shows the sketch to be investigated, comprising the parallel barriers integrated with multiple Helmholtz resonators. As above, both the parallel barriers and resonators are treated to have rigid walls. In this design, the aperture of the resonator neck is directed towards the inside of the bounded domain. In order to facilitate the analysis and comparison, the resonator is named using a 'HR' together with an integer indicating the resonator's natural frequency.

In this chapter, the two-dimensional Helmholtz resonator is presented, in which the traditional concentric hole is replaced by an infinite slit. The geometrical parameters of the HR are carefully designed and their resonance frequencies are validated by numerical calculations. As we known, the natural frequency calculation of the HR is on the base of the plane wave assumption. Thus, the frequency range covered by the model must always be below the internal critical frequency of the acoustic resonator [104, 125]. If the maximum radius of a circular resonator is $\alpha_{\max}$ = 21mm, the critical frequency of the resonator is $f_{cr} = 1.84c_0/(2\pi\alpha_{\max})$ Hz, below which the plane-wave assumption is still valid. This is a rather high frequency, whose value would increase further as the radius decreases meaning that the plane wave assumption is valid in the frequency range of interest. Due to the space limitation and the practical installation, the T-shaped acoustic resonators as used in Chapter 3 are used for noise enhancement of parallel barriers at low frequencies (f <1000 Hz) [125].

We study firstly the location effect of a single Helmholtz resonator on the

degradation when integrated at different vertical height on the parallel walls. A Helmholtz resonator with a resonant frequency of 281 Hz, represented as 'HR281', is designed for the fourth peak in the sound pressure level curve. Following the findings about the baffled open cavity and the resonators, the closer spacing between the resonator and the sound source could result in a good noise reduction around the target frequency. Therefore, one single HR281 is installed at the left side of the parallel barriers and 0.1 m above the ground, the same height as the sound source from the ground. Sound pressure level at the receiver R2 (5m, -0.9m) for the perfect reflecting walls is shown with the solid blue line in Fig 4.7, named 'Rigid Wall'. As compared, the dashed red line shows the sound pressure level change at the same receiver after being integrated with the single HR281 whose aperture center is 0.1 m above the ground.

It can be obviously found that after integration with the HR281, the sound pressure levels around the original peak are suppressed. Good noise reduction enhancement is available at the degradation frequency 289 Hz. As shown by the diamond and circle, the sound pressure level is reduced from 68.93 dB to 51.79 dB, and a 17.14 dB noise reduction is obtained. Besides, the noise performance within the frequency range [198,381] has also been improved. This is because, the enclosure mode (3, 0) not only dominates the sound response at 289 Hz, but also mainly contributes to the noise level in the vicinity frequency range. However, at higher frequencies, the sound pressure level is increased after intruding the HR281, thereby deteriorating the noise reduction performance within this frequency range. The low sound pressure level by the rigid parallel barriers is due to the fact that their dominant modes cannot be excited well. After being fully coupled with the resonator HR281, the modal response at these frequencies is enhanced. Such findings are different from those in Chapter 3, where noise reduction could only be found around the target frequency and vanished at high

frequencies. As compared, the SPL variations at the same receiver after the parallel barriers are integrated with the three dimensional resonator are plotted by the dot-dashed line. The noise response is suppressed in the vicinity of the target frequency and little difference can be observed at other frequencies. Therefore, the two-dimensional resonator in this study acts like the acoustical coupling between the small cavity (resonator cavity) and the unbaffled open domain through a narrow tube (resonator neck). Such an acoustic resonator not only abates the target mode, but also influences the resting modes.

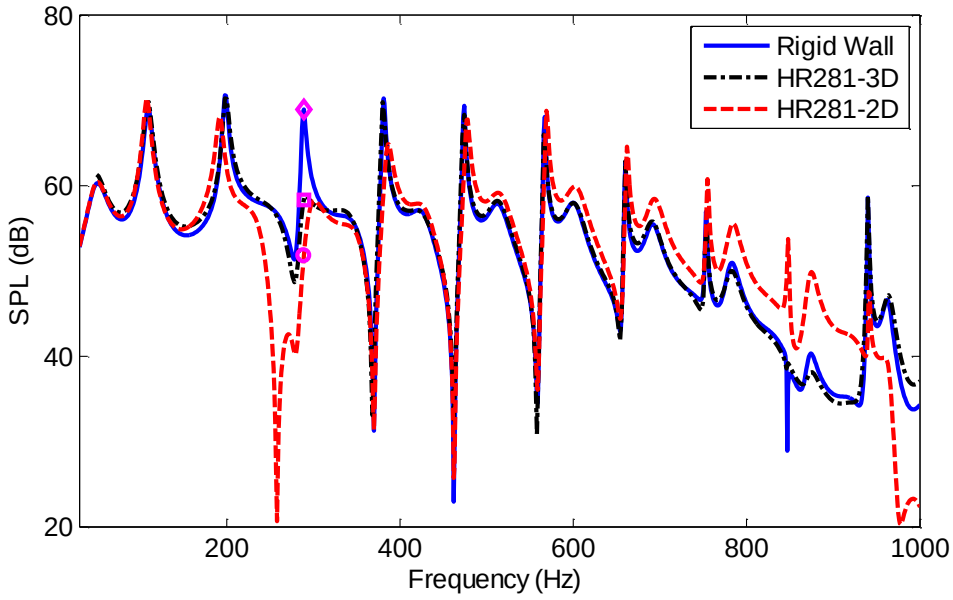

Fig 4.7: SPL changes when the parallel barriers integrated with HR281 in 2D and 3D.

The following figure shows the modal coefficients $|a_j|$ and $|b_m|$ before and after resonator HR281 is installed at 0.1m above the ground. The first row shows the modal coefficients $|a_j|$ and $|b_m|$ at 289 Hz and the second row at 849 Hz. For the parallel barriers with rigid wall, the sound wave has a strong oscillation inside the bounded domain Ω_A around 289 Hz, the corresponding modal coefficients are high and result in a peak for the sound response at the outside receiver. When the frequency increases

to 849 Hz, the mode (9, 0) is not excited well, the sound pressure levels dominated by this mode is relative low. After installed with the HR281 at the left wall, the SPL at the outside receiver is suppressed around 289 Hz. The modal amplitude for the cavity mode (4, 0) and the fourth radiation mode is reduced, as shown by the red bars in Fig 4.8(a) and (b). However, due to the modal coupling, the original weak excitation cavity mode (9, 0) has been enhanced, which results in an increase in noise level at the outside receivers. The modal amplitudes for this mode and the corresponding radiation mode have been increased obviously, which can be found in Fig 4.8(c) and (d).

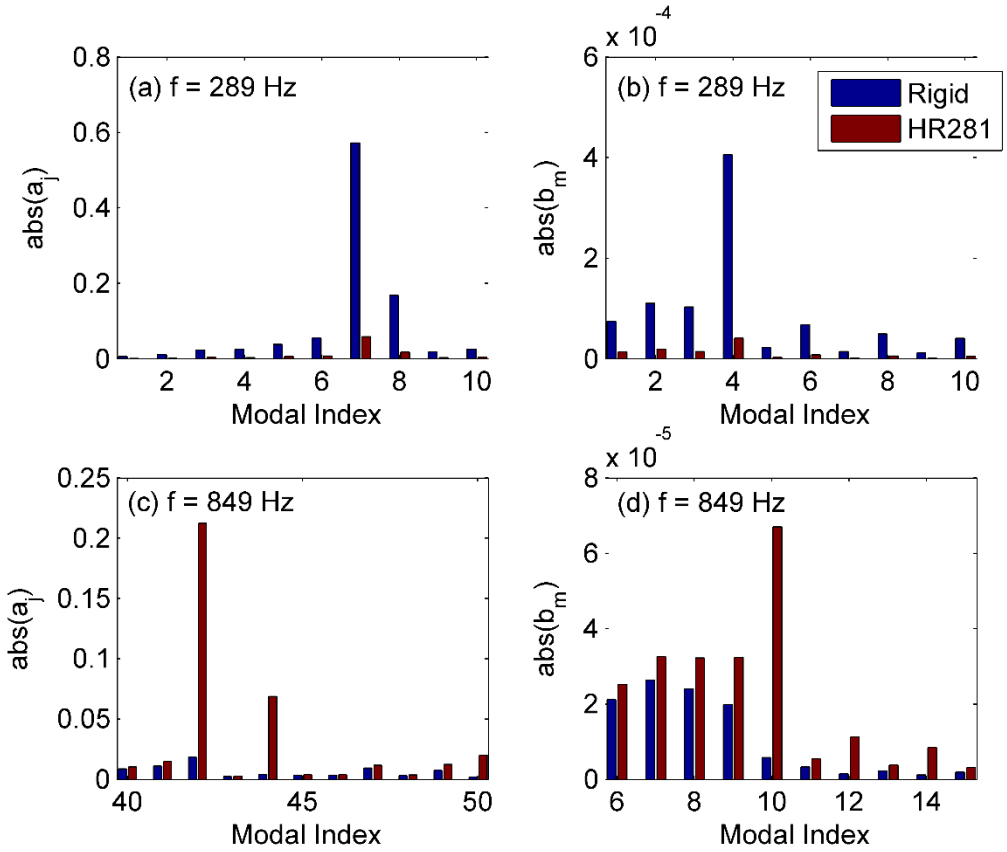

Fig 4.8: The modal coefficients at two selected frequencies before and after installed with HR281.

Fig 4.9 illustrates the comparison of sound pressure distributions for the 289 Hz before and after the single HR281 is installed. The sound field pattern still remains almost the same. However, the sound field distribution at the corresponding frequencies

has a distinctive signature, with the sound pressure substantially reduced. The advantage of the proposed barriers is more obvious in the shadow zone outside the two parallel barriers: the sound energy is less than 55 dB for the proposed barriers and above 65 dB for the rigid wall units. Besides, as shown clearly in Fig 4.9, after being integrated with HR281, the sound response reduction is not only achieved at the shadow zone, but also can be obtained in the whole illustrated domain.

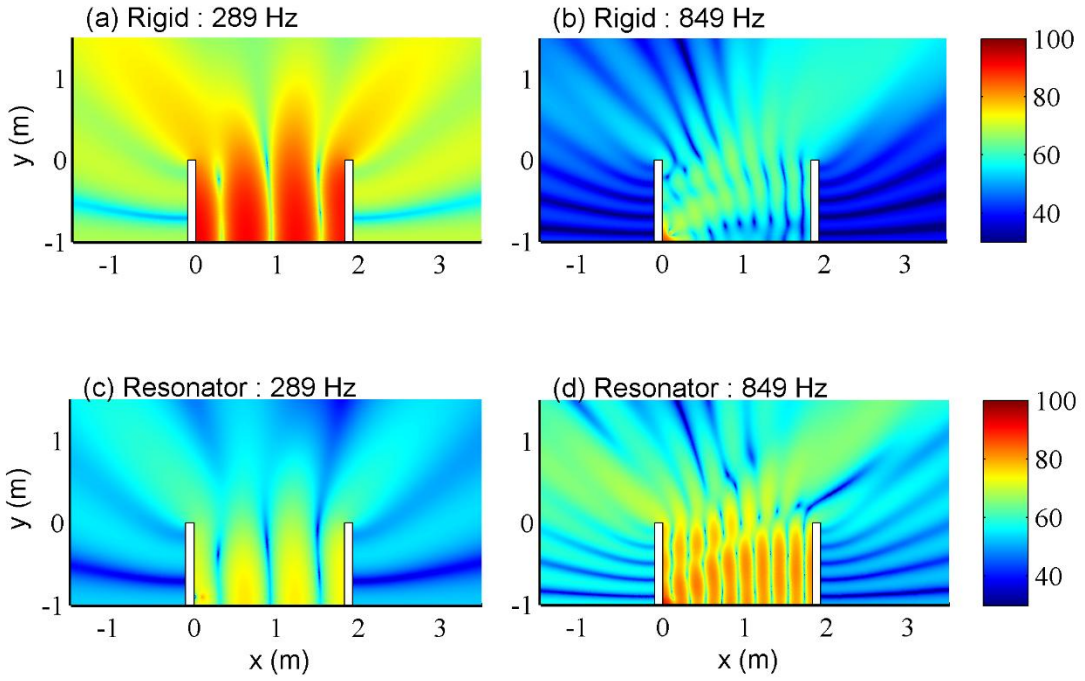

Fig 4.9: The sound pressure distribution at the 289 Hz before and after installed with the HR281: (a) and (b) rigid wall without resonator; (c) and (d) with single resonator whose natural frequency is 281 Hz.

It is known that modal response control and modal rearrangement are the two general control strategies to suppress associated with different types of acoustical mode [126]. Previous studies in the duct noise control show that the aperture of the two identical resonators should not too close. When their center distance is greater than a quarter wavelength of the resonators' natural frequency, the sound transmission loss is larger than that of a single resonator. However, when these two same resonators are in close proximity, they interact and lead to a decrease in the overall performance. In this

study, the center distance among the resonators is larger than 0.1 m. The first study was to investigate the noise reduction performance when a resonator is installed at different locations. Three locations were tested and their corresponding positions are listed in Table 4.3. The calculated SPL changes are shown in Fig 4.10.

Table 4.3: Resonator locations for HR281.

		Helmholtz resonator	Location	
			x	y
Same-Frequency	Case-1a	HR281	0	0.1-Ly
	Case-1b	HR281	0	0.2-Ly
	Case-1c	HR281	1.83	0.1-Ly

Similar to the conclusion in Chapter 3, the closer the resonator from the primary sound source, the stronger the acoustical coupling that occurs and the higher the noise reduction can be achieved in the vicinity of the target frequency. Shown in Fig 4.10 is the SPL changes when the same HR281 is located at three different locations. These lines shows that the sound responses around the third peak are suppressed. However, the sound pressure level is enhanced in the high frequency range where the resonances have not been excited well. This result is consistent with that for a single resonator.

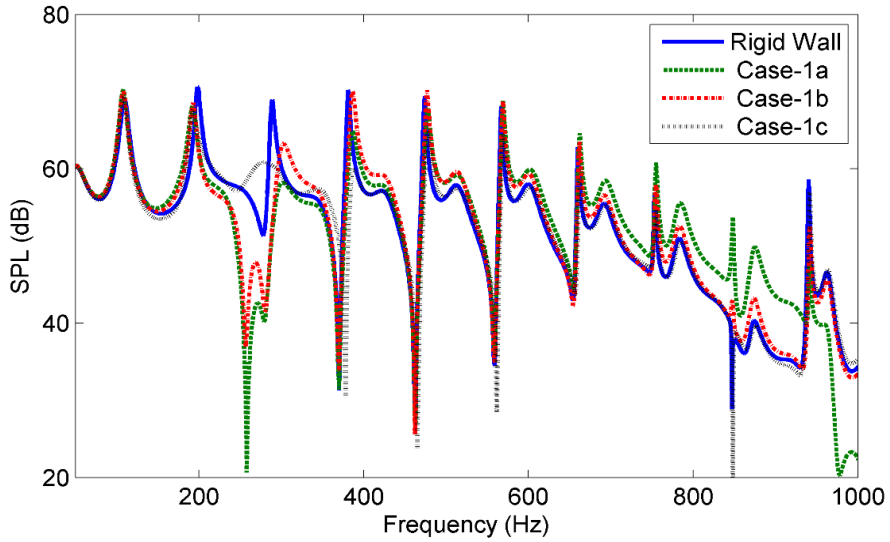

Fig 4.10: SPL changes after installed with single resonator at different locations.

Therefore, in order to lower the noise response around the sound peaks and maintain the original weak resonances, the resonator should be properly located, as indicated by Case-1b.

Then, two resonators (referred to as HR281-1 and HR281-2) with the same natural frequency were designed to study the arrangement of two identical resonators for the noise reduction in frequency range of interest. Their positions are listed in Table 4.4.

Table 4.4 Resonator locations for HR281.

		Helmholtz resonator	Location	
			x	y
Same-Frequency	Case-2a	HR281-1 HR281-2	0 0	0.1-Ly 0.3-Ly
	Case-2b	HR281-1 HR281-2	0 1.83	0.2-Ly 0.1-Ly
	Case-2c	HR281-1 HR281-2	1.83 1.83	0.1-Ly 0.3-Ly

In order to avoid the interaction between the two resonators, their center distance is larger than 0.1 m. the locations of these two identical resonators are referred the findings from the single one HR281.

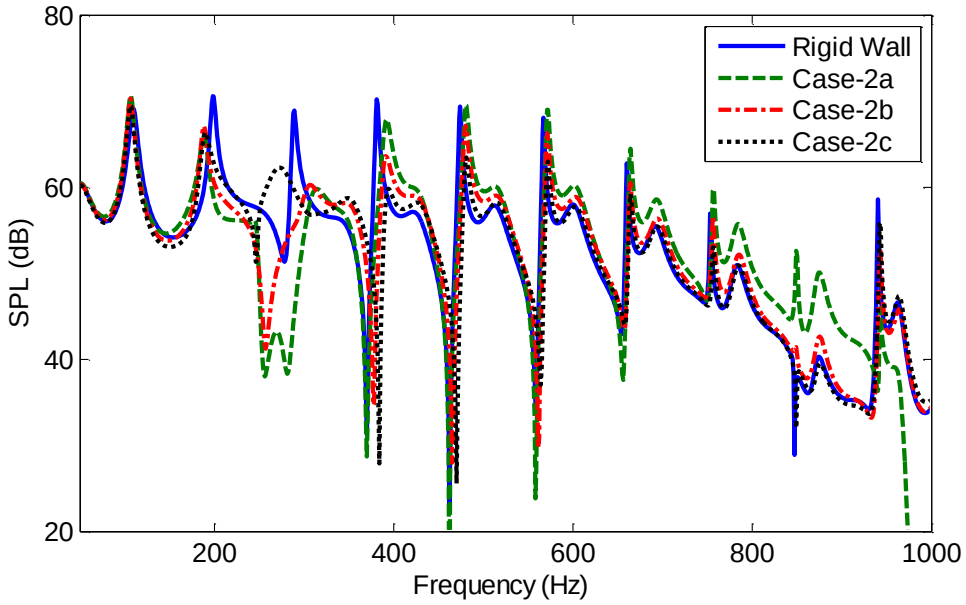

Fig 4.11: The SPL of the parallel barrier with the rigid wall compared to the Helmholtz resonator at 281 Hz.

Fig 4.11 indicates that sound response changes after being integrated with the same two resonators at different positions. These two resonators were installed in the left barrier, as indicated by Case-2a, and the sound response is shown by the dashed line with a reduction of 8.54 dB at its corresponding resonant frequency compared with the rigid wall result. However, similar to the predictions in Case-1a, the sound response at the higher frequencies is shifted and enhanced. The dot-dashed line shows the SPL changes at the same receiver when the same two resonators were installed at each side of the barrier. The sound response of the two resonators installed at the far barrier side is shown by the dotted line. When compared with the results from a single resonator, it is found that the noise reduction is mainly determined by the near resonator. The addition of the same resonator has little effect on the total noise abatement if the resonator is embedded on the far side wall. In this study, the primary sound source was located at (0.1,-0.9), near the left barrier. When moving the source towards to the far side, a similar conclusion can be obtained.

The following contours in Fig 4.12 are the sound field at 289 Hz and 849 Hz in the above three cases. The first column illustrates the sound distribution at 289 Hz after the two same resonators are installed at different positions and the other column is for that at 849 Hz. As can be found for 289 Hz when compared with Fig 4.9 (a), the modal pattern at this frequency is suppressed and modified. When HR281 is located at the positions according to Case-2a, the noise response around the primary sound source is reduced drastically. As indicated by the modal control theory, when the sound source is moved to the anti-nodal line, the noise response dominated by this mode is relatively low due to the weak excitation. When moving the resonators to the far side, the acoustical coupling of the resonator and the (4, 0) mode is decreased, and the noise abatement is thereby reduced. However, the strong acoustical coupling instead leads to

an increase in sound response at 849 Hz. As shown in Fig 4.12(b), the original weak modal excitation has been enhanced and resulted in the higher sound level around this frequency.

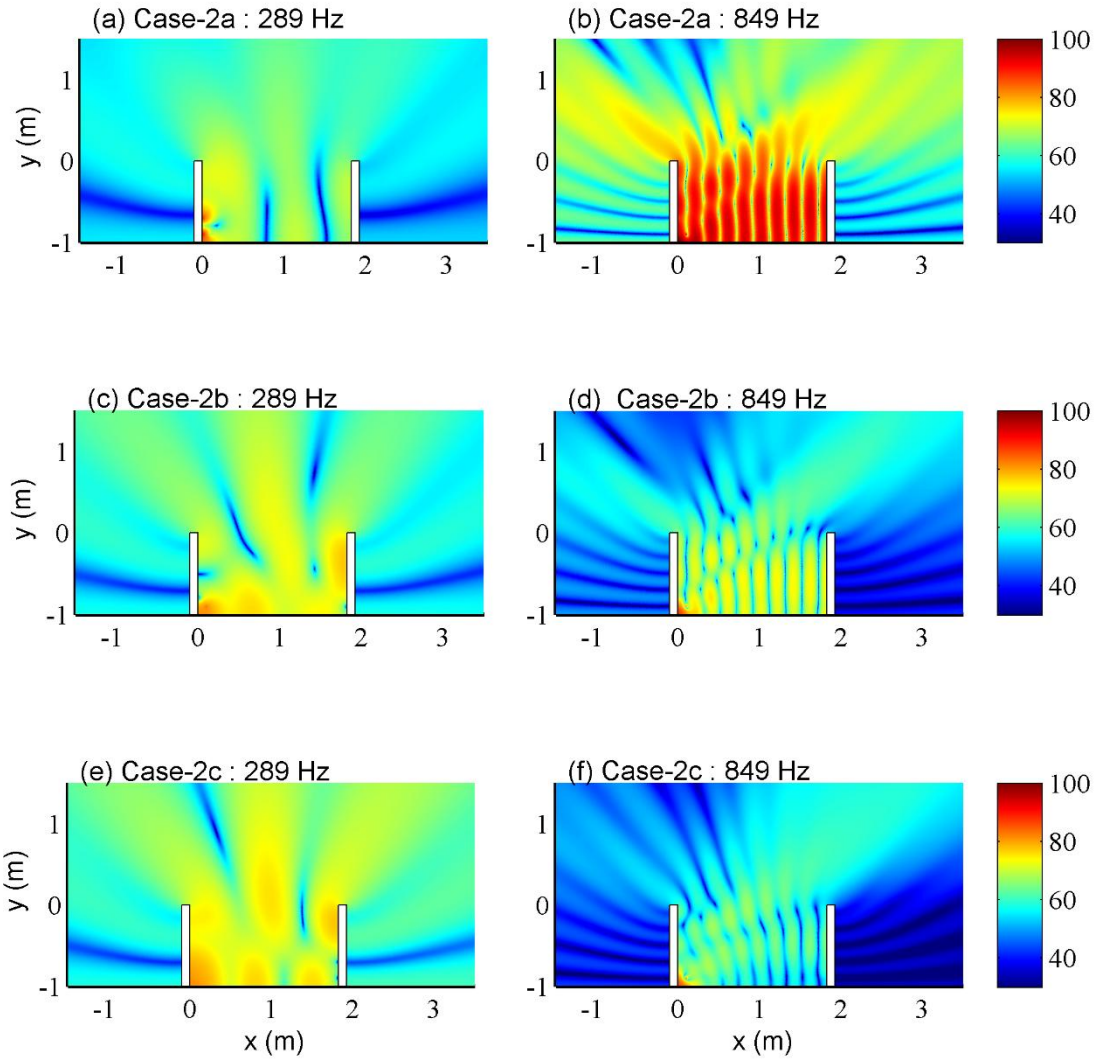

Fig 4.12: Sound pressure level distribution after installed with the resonators.

Finally, two resonators with different natural frequencies were installed on the barrier walls. Table 4.5 indicates the locations of these resonators. HR281 and HR468 resonators (named HR281-3 and HR468-1) were designed to study the combination of two resonators with different frequencies. The physical parameters for HR281 used these three cases are the same.

Table 4.5 Resonator locations for HR281 and HR468.

		Helmholtz resonator	Location	
			x	y
Different-Frequency	Case-3a	HR281-3 HR468-1	0 1.83	0.2-Ly 0.05-Ly
	Case-3b	HR281-3 HR468-1	1.83 1.83	0.2-Ly 0.05-Ly

Fig 4.13 shows that the use of two Helmholtz resonators tuned to different frequencies can result in a global noise reduction compared to the sound pressure level for a barrier in the absence of Helmholtz resonators. The natural frequencies of the two resonators are 281 and 468 Hz, respectively. These two resonators were both installed on the right side. The height for HR281 is 0.05 m and for HR468, the height is 0.2 m.

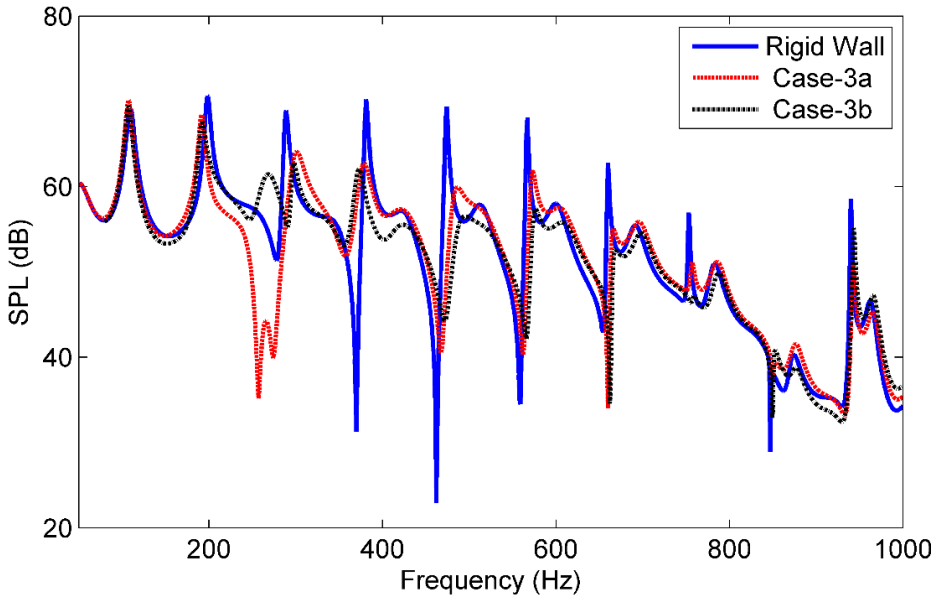

Fig 4.13: The SPL of the parallel barrier with the rigid wall compared to the Helmholtz resonator at 281 Hz.

It is clear from the above two figures, that after installing the resonator, the corresponding resonant peak was suppressed and the noise level was reduced. Following the radiation impedance results analysis, the nearby resonant peak also reduced because of the modal contribution from the suppressed mode. And the resonant frequency shift was also found. The SPL distribution of the parallel barriers integration

with two resonators at 289 Hz, 381 Hz, 474 Hz and 567 Hz is shown in Fig 4.14.

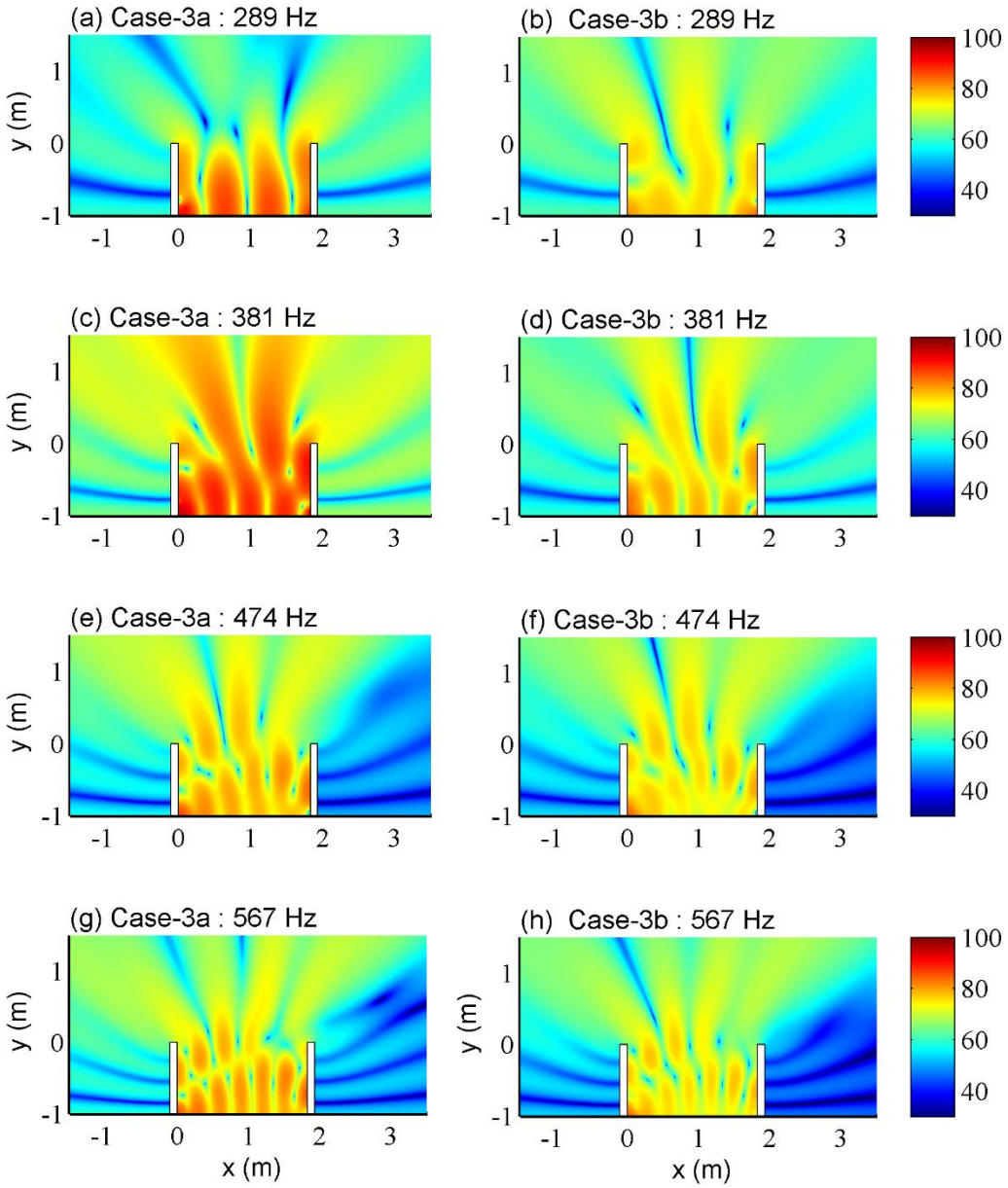

Fig 4.14: The SPL distribution of parallel barriers integration with HRF281 and HR468.

4.4.1 Sound Intensity

Attention was then paid to the sound intensity changes when the parallel barriers were integrated with HR281 and HR468.

By analogy with the reflection and transmission coefficients defined for reflecting and transmitting waves, a diffraction coefficient D is suggested in the GTD [24]. In this

definition, a diffraction field is determined by the acoustical property of the sound field at the diffracting point and the diffraction coefficient D.

$$p_d = Dp_i r^{-1/2} e^{jkr} \tag{4.24}$$

where p_d and p_i are the sound pressure at the receiving and diffracting points, and r is the distance from the diffracting point to the receiving point. Eq.(4.24) illustrates that: when a barrier is erected, the sound field behind the barrier is mainly contributed by the diffraction wave. The incident wave directly reaches the barrier top, then the sound field around the barrier top works as a secondary source and generates the diffracting waves. To this end, the sound pressure in the shadow zone has an inherent relationship with the sound pressure at the diffracting point. In addition, since the thickness of the barrier used in the current analysis is 0.1 m, which is much smaller than the wavelength of 1000 Hz, one could simply assume that the diffracting point is at the barrier top.

The diffraction coefficient D is determined by the directions of the incident and diffracting rays, the wavelength, and the geometrical and physical properties of the media at the point of diffraction. An asymptotical expanded form of the diffraction coefficient D is:

$$D = -\frac{e^{j\pi/4}}{2(2\pi k)^{1/2}}\left[\sec\left(\frac{\alpha-\theta}{2}\right)+\sec\left(\frac{\alpha+\theta}{2}\right)\right] \tag{4.25}$$

where α and θ are the angles of incidence and diffraction and can be found in [24]. As shown in Eq.(4.25), the diffraction coefficient is low for a high frequency. As a result, the sound pressure at the receiver has a descending trend with the increase of frequency. In addition, at the same frequency, the increase of incident angle α attains a bigger diffraction coefficient. That is to say, the sound wave is more effectively diffracted if the incident wave impinges normally to the barrier surface. In that case, the maximum diffraction coefficient is reached. If the incident wave is in parallel (at a

grazing angle) with the barrier surface, a minimum diffraction coefficient is obtained. It should be noted that, the scale factor of the sound intensity field in Fig 4.15 and Fig 4.16 is 100, while the scale factor in Fig 4.17 and Fig 4.18 is 1000, respectively. As shown in Fig 4.15 and Fig 4.17, the amplitude of sound intensity at 289 Hz after integration with two HRs is still less than that with rigid walls, though the scale factor is 1/10. That is to say, the sound pressure p_i at the diffraction point around the top of the right barrier is intensely reduced. When compared with the wave incident direction around the top edge, no obvious difference can be observed and hence the diffraction coefficient D undergoes little change. Combined with Eq.(4.24), the noise reduction can be achieved in the shadow zone.

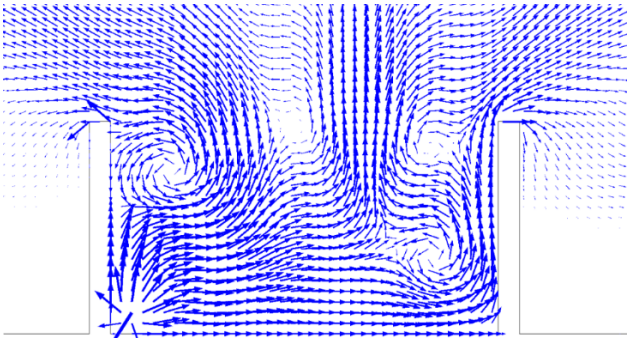

Fig 4.15： Sound intensity comparison of the parallel barrier without Helmholtz resonator at f=289 Hz, scale factor=100;

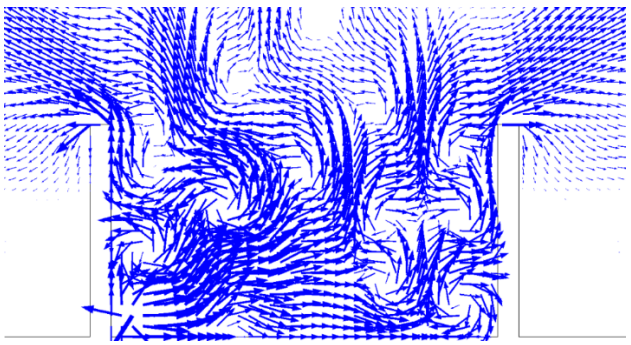

Fig 4.16: Sound intensity comparison of the parallel barrier without resonator at f=474 Hz, scale factor=100;

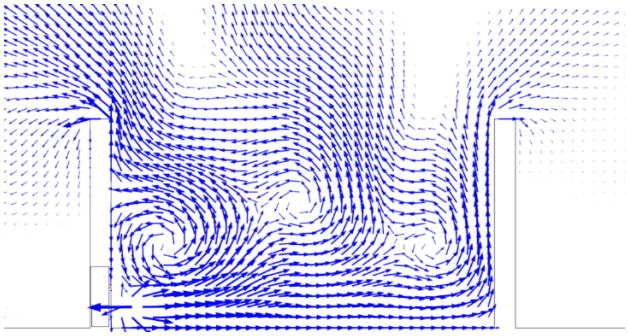

Fig 4.17: Sound intensity comparison of the parallel barrier with resonators in case-3a at f=289 Hz, scale factor=1000;

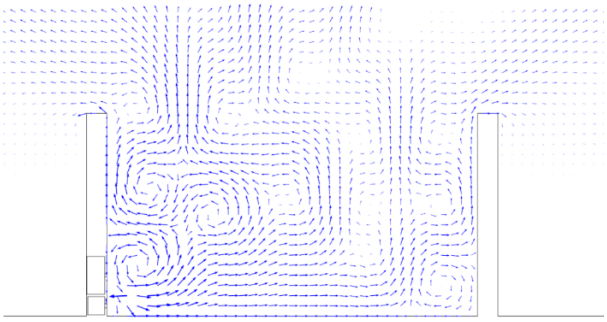

Fig 4.18： Sound intensity comparison of the parallel barrier with resonators in case-3a at f=474 Hz, scale factor=1000;

4.5 Experiment validation

4.5.1 Experimental set up

The experimental study was conducted in an anechoic chamber with the size 6m*6m*4m. The sketch for the parallel barriers is shown in Fig 4.19. Several pieces of wooden boards with a thickness of 18.5 mm were used to simulate the parallel barriers and the reflecting ground. Previous measurements have demonstrated that these wooden boards can be treated as acoustically rigid in the frequency range of interest [13]. The height of the parallel barriers is 1 m and the length of the barriers is 4.8 m. The distance between the two barriers was 1.83 m which was the same as that in the theoretical calculation.

In order to simulate a point source, a speaker is connected to a circular brass pipe. The length and the diameter of the brass pipe is l.5m and 25 mm. The directional feature of the point source was measured and showed that the deviation in the sound pressure level for all directions is within 1 dB for all the frequency range above 200 Hz.

During the measurements, the point source was fixed at (0.1, 0.1, 0) m as shown in Fig 4.19. in which the origin of the coordinate is located at the center of the left barrier and the ground plane. Four B&K microphones were supported by the tripod to measure the sound pressure behind the barrier located at the right side. The receivers are chosen at 1 m away from the right barrier and with heights of 0.2, 0.5, 0.7 and 1 m above the ground. The following Fig 4.19 illustrate the set up in the experiment.

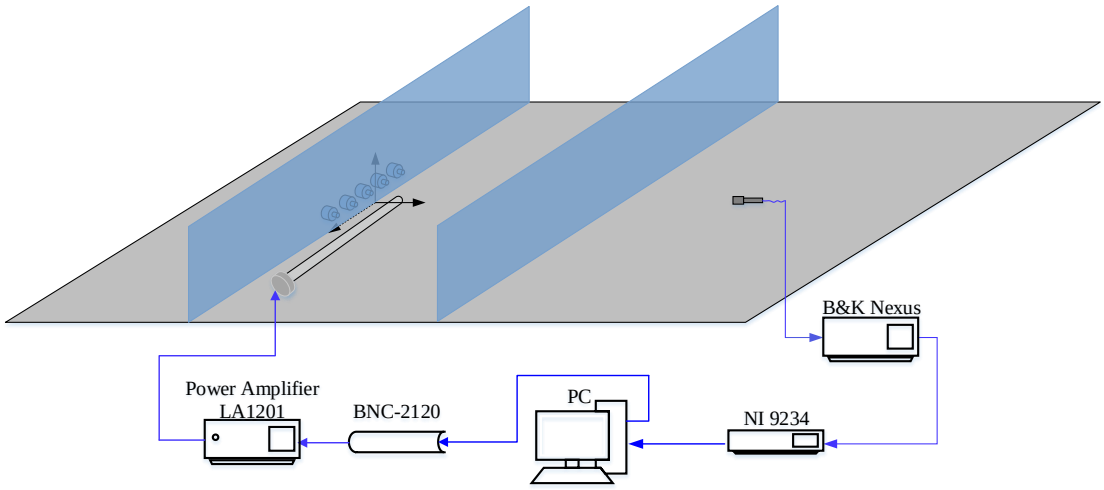

Fig 4.19: The sketch of the experimental study.

The resonator was made from circular cross sectional PVC tubes and rectangular cross sectional aluminum cavities. The physical dimensions of the resonators are listed in Table 4.6. Five identical resonators were fabricated. The natural frequency of these resonator were designed to 281 Hz and the measurement validated the design. These five resonators were mounted on the left barrier wall as shown in Fig 4.19. Their aperture center is 0.1 m above the ground.

Table 4.6 The geometric dimensions of the HRs and the measured resonance frequency.

Helmholtz Resonator	Neck diameter (mm)	Neck Length (mm)	Body Width (mm)	Body Length (mm)	Measured natural frequency (Hz)
HR281	21	30	49	124.6	281

A photo of the parallel barriers integrated with a resonator array can be found in Fig 4.20. The holes on the wooden panel is used to mount the resonators HR281.

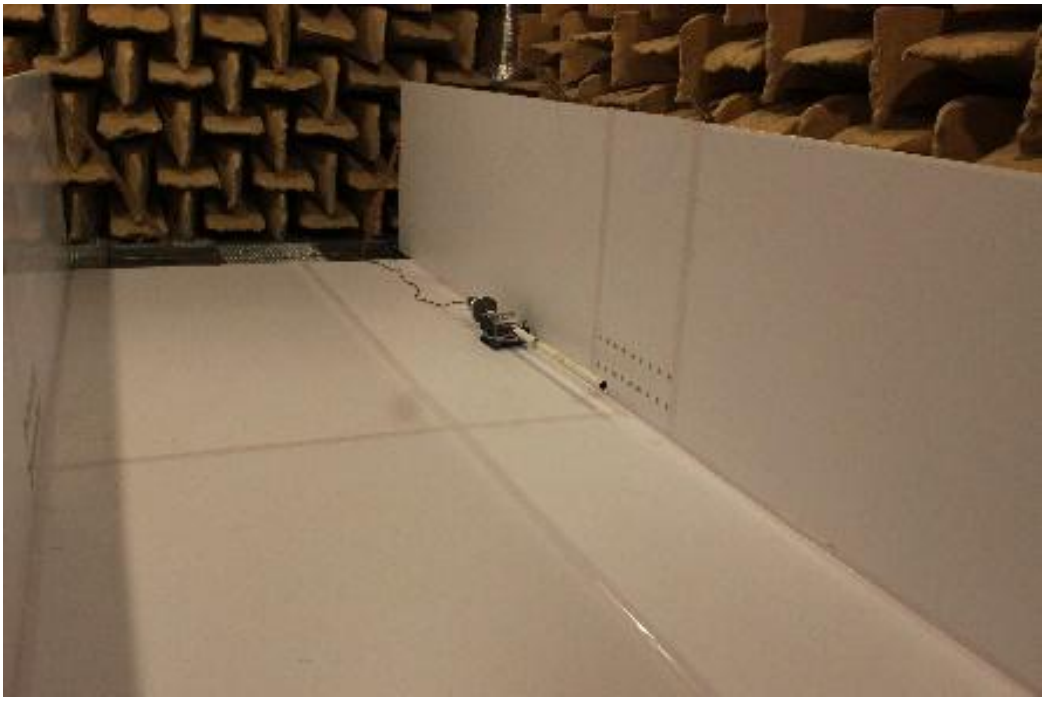

Fig 4.20: Experimental photo in the anechoic chamber.

The sound pressure level at the receivers for the parallel barriers with rigid wall condition was firstly measured. The resonator apertures were covered with stoppers made of aluminum which can be regarded as acoustically rigid.

Subsequently, the sound response at the same position after resonators were installed was investigated. As indicated from the Fig 4.21, after integrated with the resonator whose natural frequency is 281 Hz, the original sound peak at 289 Hz was suppressed. Different from the predictions in two dimensions, the SPL at higher frequencies were

not improved. It should be noted that, this experiment mainly aimed to examine the effectiveness of the resonator on noise control of parallel barriers, rather than validating the accuracy of the proposed theoretical model.

4.6 Numerical calculation by FMBEM

In this section, the developed FMBEM program is used to predict the sound field of the parallel barriers with a resonator array in three dimensions. The configurations used in the calculation are the same as that in the experiments in the anechoic chamber. The calculated frequency range is 200-1000 Hz, which is consistent with that in the experiment.

The parallel barriers and ground were treated as acoustically rigid surfaces. A point source fixed at the same position as in the experiment. Five same resonators were embedded in the left side of the parallel barriers. They are arranged horizontally and the distance between the resonators was identical, i.e. 0.1 m. The height of the resonator from the ground was the same as the sound source.

The maximum size of the boundary elements used to discretize the barriers is 0.025 m. with at least 12 elements per wavelength. When integrated with the resonators, the mesh for the resonator and around the aperture was refined. The maximum number of multipole and local expansion terms was set to 10 for this problem.

In Fig 4.21, the comparisons of the experimental measurements and numerical predictions at the receiver (1, 0.2) is presented. The solid and dashed lines without marks shows the results obtained from the FMBEM without and with five resonators. The solid and dashed lines with asterisk and circle are the results from the experiment. The tendency of the predictions consist with that of the experiment. Several sound peaks has emerged due to the multiple reflections generated by the two barrier walls. Noise reduction can be found around the target peak either in the experiment or the

experiment. It is likely that the discrepancies at high frequencies are due to some system errors in the measurement setup. The main source of these measurement errors was considered to be the directivity of the loudspeaker and the microphone. And also, it was difficult to make the panel stand vertically during the experimental setup.

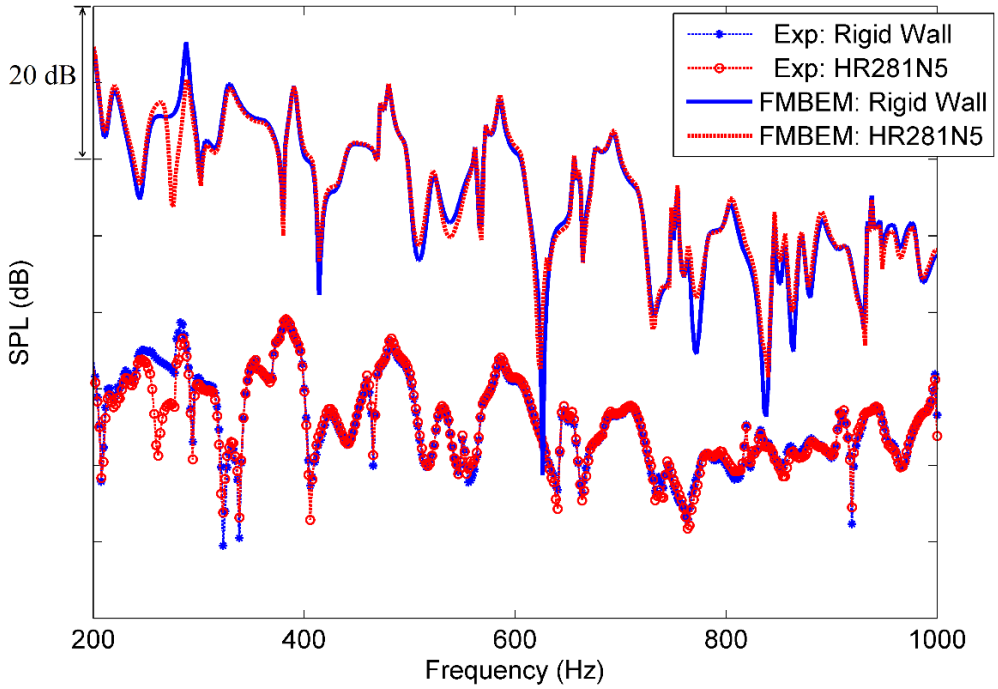

Fig 4.21: SPL comparison for parallel barriers with rigid wall and five resonators HR281.

Next, Fig 4.22 and Fig 4.23 present the contour plot of the SPL in dB on the parallel barriers and the near field without and with five same resonators of HR281. The color legend is shown at the right corner. As can be found in Fig 4.22, the contour indicates strong sound oscillation inside the bounded domain consist of the parallel barriers and the ground at 289 Hz. The sound leakage in the negative and positive direction on the z-axis weaken the oscillation. The sound leakage in the z-direction increase the noise level at the microphone locations but reduce the noise level at certain regions, as shown by the blue lines.

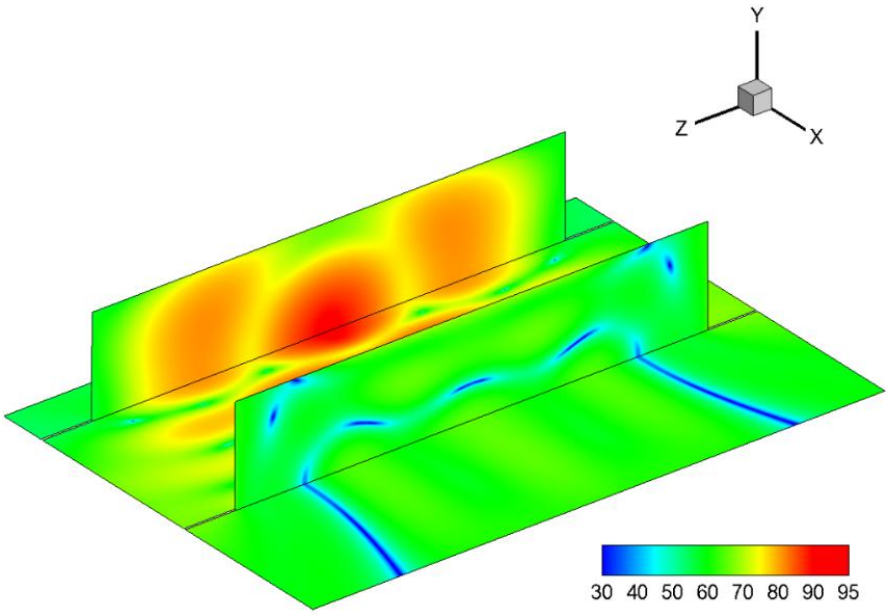

Fig 4.22: The sound field for the parallel barriers with rigid walls at 289 Hz.

As compared, the sound field after integration with the resonators is plotted in Fig 4.23. It is obvious that the resonators act as the secondary sound source and the sound response in the whole open space is suppressed at the target frequency.

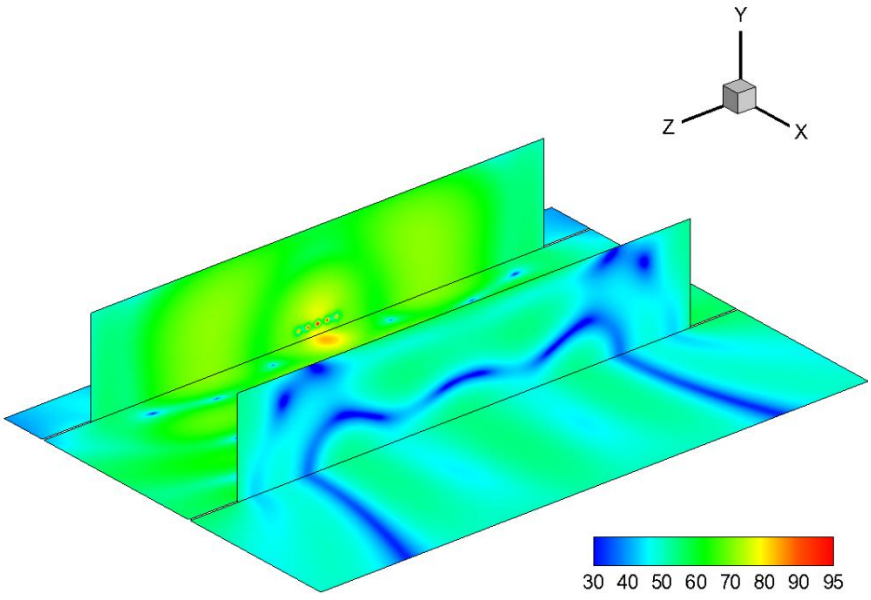

Fig 4.23: The sound field for the parallel barriers integrated with resonators at 289 Hz.

4.7 Summary

This chapter deals with the noise reduction degradation problem of parallel barriers used in traffic noise control. To understand the physics, the modal equation of the parallel barriers system is obtained. The eigenfunctions governing the sound field have been expressed as the finite sum of the coupled enclosure modes and the radiation modes. The radiation impedance matrix at the opening of the parallel barriers was obtained to specify the radiation characteristics of such barrier system.

Due to the difficulty in expressing the sound field analytically, a hybrid method based on the modal superposition method was developed first to obtain the sound field inside and outside the parallel barrier.

The mechanisms and the radiation impedance at the opening were investigated. The sound peaks at the receiver were dominated by the corresponding closed-cavity mode and contributed by the nearby modes.

The noise reduction inside and outside the bounded domain can be found obviously at the target frequency; however, the low noise response may be improved at the frequency which has not been excited well by the primary sound source. Through optimal design of the locations of the resonator, the deterioration can be suppressed and a broadband noise reduction can be obtained.

Finally, experiments were carried out to verify the noise performance prediction results by the proposed FMBEM. Generally speaking, the experimental results indicate an agreed tendency with the numerical results.

CHAPTER 5

NOISE SUPPRESSION BY PANELS INTEGRATED WITH PARALLEL BARRIERS VIA VIBROACOUSTIC COUPLING

5.1 Introduction

As shown in Chapters 3 and 4, the resonator array can be used to reduce the sound response at the low frequency range, however, the noise reduction band of the resonator is always narrow. Aiming to broader the noise reduction band at low frequency range, a flexible plate backed by a rectangular cavity is proposed to integrate with the parallel barriers. The backing cavity serves to one hand protect the sound wave radiated by the plate travelling to the receiver directly, on the other hand modify the plate vibration. Such a device is called the plate silencer, which is proposed by Huang [82] and applied such a device to attenuate the duct noise mainly at low frequency range. Through proper adjusting the plate property, the induced vibration of the plate radiates wave to the incident side. The noise reduction can be reached when the incoming and radiated wave interfere favorably. In order to implement conveniently in the compact duct system, Wang et al. [83] replace the plate end conditions to clamped-clamped instead of simply supported. The theoretical study examined the effectiveness of such a device and a broadband TL was obtained over low to medium frequency range. Wang also pointed out that the plate with soft ends can further improve the noise attenuation performance of the plate silencer.

In this chapter, in order to widen the noise reduction range and maintain the

effectiveness in the low frequencies, the plate cavity device is adapted to the parallel barriers. The light plate with high bending vibrates in response to the sound wave generated by the point source and reflected by the barrier walls and works as a wave reflector undergoing the sound cancelations at the downstream over a broad frequency band in the low frequencies. The goal of this chapter is to carry out a systematic analysis of the acoustics-structural interaction of the parallel barriers integrated with the plate cavity. To achieve this target, a theoretical model based on the modal coupling will be first established to reconstruct the acoustic-structure coupling behavior between the open enclosure and the vibrating panel backed with cavity. The influence of plate vibration on the sound field inside and outside the parallel barriers is then analyzed. Finally, the experimental measurements is carried out to validate the effectiveness of using the plate cavity to reduce the noise response of the parallel barriers in practical applications.

5.2 Theoretical formulations for acoustic-structure coupling

In this section, a theoretical model will be established to understand the underlying physics which includes the acoustic-structure coupling behavior and sound interference between the sound waves in the open space and the radiated waves from the vibrating panel backed with cavity. The sound pressure inside and outside the bounded domain of the parallel barriers can be solved using the procedure described in Chapters 3 and 4. In order to avoid unnecessary duplication, the whole procedure is presented briefly. However, the sound coupling between the plate cavity and the parallel barriers is critical to this study, so some essential expressions have been formulated in detail.

5.2.1 Descriptions of the coupling system

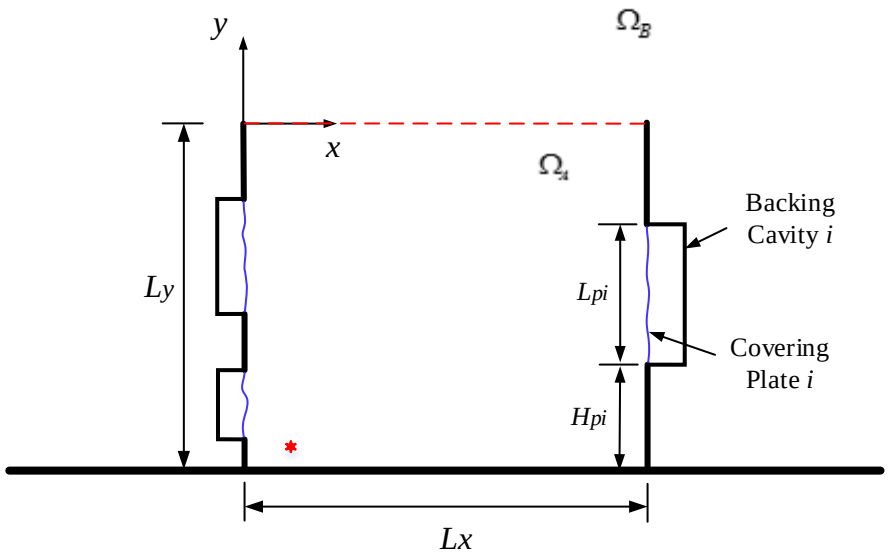

Fig 5.1: The sketch of the parallel barriers with multiple plate cavities.

The configuration is shown in Fig 5.1. The geometrical parameters of the parallel barriers are the same as that used in chapter 4. On the barrier walls facing the noise source is lined by flexible plate of length L_{pi} and a H_{pi} length of the lower end from the ground. The plate is clapmed at the two ends in y direction, and is enclosed by a rigid-walled cavity of depth $D_{cav,i}$ and length $L_{cav,i}$. Our interest here is in the acoustic interaction among the interior domain Ω_A, the exterior domain Ω_B and backing cavity domains $\Omega_{cav,i}$.

Assuming harmonic time dependence omitted, we can obtain the governing equations for the acoustic fields and the plate as:

$$\nabla^2 p_{A+B}(\vec{x}) + k^2 p_{A+B}(\vec{x}) = -Q_s \delta(\vec{x} - \vec{x}_s) \tag{5.1}$$

$$\nabla^2 p_{cav,i}(\vec{x}) + k^2 p_{cav,i}(\vec{x}) = 0 \tag{5.2}$$

$$\frac{B_{p,i}}{ikc}\frac{\partial^4 v_{p,i}}{\partial x^4} + m_{p,i} ikc v_{p,i} = p_{cav,i} - p_A \tag{5.3}$$

where $v_{p,i}$ is the vibration velocity of the plate i. $B_{p,i}$ and $m_{p,i}$ are the bending stiffness

and the mass per unit surface area of the plate i, respectively.

In the interior domain Ω_A, the governing equation and the boundary conditions are:

$$\nabla^2 p_A(\vec{x}) + k^2 p_A(\vec{x}) = -i\rho kcq_s \delta(\vec{x} - \vec{x}_s) \tag{5.4}$$

$$\left.\frac{\partial p_A}{\partial n}\right|_{y=0} = -j\rho kcv_n, \quad (0 < x < L_x) \tag{5.5}$$

$$\sum_{r=1}^{R} \left.\frac{\partial p_A}{\partial n}\right|_{x=0,L_x} = -j\rho kcv_p^r, \quad (H_{p,i} < y < H_{p,i} + L_{p,i}) \tag{5.6}$$

where, v_n is the particle velocity at the opening.

As described in chapter 3 and 4, the sound pressure $p_A(\vec{x})$ inside the domain A can be described by the undamped eigenmodes as:

$$p_A(\vec{x}) = \sum_{j=1}^{N} a_j \phi_j(\vec{x}) \tag{5.7}$$

where, a_j is the modal response of the j-th eigenmode $\phi_j(\vec{x})$. For the rectangular cavity, $\phi_j(\vec{x})$ is given in Chapter 3.

For the exterior domain Ω_B, the particle velocity v_n at the opening and the sound pressure p_B can be expressed as:

$$v_n(\vec{x}) = \sum_{m=1}^{M} b_m \psi_m(\vec{x}) \tag{5.8}$$

$$p_B(\vec{x}) = \sum_{m=1}^{M} b_m \varphi_m(\vec{x}) \tag{5.9}$$

where, b_m is the modal response of the mth mode $\varphi_m(\vec{x})$ and M is the maximum number of the truncated mode series. For the baffled open enclosure with the infinite baffled plane, $\varphi_m(\vec{x})$ can be expressed as:

$$\varphi_m(\vec{x}) = i\rho kc \int_{S_{op}} G(\vec{x}, \vec{x}_{op}) \cdot \psi_m(\vec{x}_{op}) dS_{op} \tag{5.10}$$

For the unbaffled open enclosure such as the outside domain Ω_B as in this chapter, $\varphi_m(\vec{x})$ can be obtained numerically by BEM or FEM. The details about obtaining $\varphi_m(\vec{x})$ numerically can be found in Chapter 4 and will not be discussed here.

Based on the pressure continuity at the opening,

$$p_A(\vec{x})\big|_{Sop} = p_B(\vec{x})\big|_{Sop} \tag{5.11}$$

Substituting Eqs. (5.7) and (5.9) into Eq.(5.11), we can obtain:

$$\sum_{j=1}^{N} a_j \phi_j(\vec{x}) = \sum_{m=1}^{M} b_m \varphi_m(\vec{x}) \tag{5.12}$$

Multiplying $\psi_{jx'}(x')$ at both sides of Eq.(5.12) and integrating over the opening leads to:

$$\sum_{j=1}^{N} a_j \delta_{jx,jx'} \psi_{jy}(0) = \sum_{m=1}^{M} b_m \int_{S_{op}} \left[\psi_\mu(x')\varphi_m(\vec{x}_{op})\right] dS_{op} \tag{5.13}$$

When defining $Z_{\mu,m} = \int_{S_{op}} \left[\psi_\mu(x') \cdot \varphi_m(\vec{x})\right] dS_{op}^{'}$, Eq.(5.13) can be rewritten as:

$$\sum_{j=1}^{N} a_j \delta_{jx,jx'} \psi_{jy}(0) = \sum_{m=1}^{M} b_m Z_{jx',m} \tag{5.14}$$

Applying the second Green identity to the interior domain Ω_A, one can obtain:

$$\begin{aligned} &a_i\left(k^2 - k_i^2\right) - i\rho kc \int_{S_{op}} \left(\phi_i v_n\right) ds_{op} \\ &-\sum_{i=1}^{R} i\rho kc \int_{s_p^r} \left(\phi_i v_{p,i}\right) ds_{p,i} = -i\rho kc q_s \phi_i(\vec{x}_s) \end{aligned} \tag{5.15}$$

The above equation indicates the effect of the multiple cavity on the modal response of the parallel barriers.

5.2.2 Parallel barriers coupled to single plate-cavity

The coupling of the parallel barriers and multiple plate cavities behaves like the acoustoelasticity model presented by Dowell et al. [48]. The discretized modal equations generally involve integral operations over the interface surface between the flexible plate and acoustic domain. As shown in the previous Chapter 4, the coupling between a single Helmholtz resonator and a multi-degree freedom open domain exhibits a very special feature. In fact, for a given plate cavity at one fixed location, dynamics of the panel and the sound field inside the backing cavity is critical for this research. Therefore, the problem of the parallel barriers interacts with only one plate cavity is studied first in the following part. After the mechanism study and a deep principle understanding, the theoretical model can be extended to consider more plate cavity with complicated configurations.

The dynamics of the plate described in Eq. (5.3) can be expanded as a series of *in vacuo* modes $\hbar_u(\vec{x})$ with their corresponding modal amplitude $V_{p,\mu}$. The solutions can be found in textbooks such as Ref. [127]; hence, only the final result is presented. In order to facilitate the formulation, the vibration mode shape $\hbar_u(\vec{x})$ is written using the local dimensionless variable $\xi = (y - H_p)/L_p$ as:

$$v_p(\vec{x}) = \sum_{u=1}^{U} V_{p,\mu} \hbar_\mu(\xi) \tag{5.16}$$

where

$$\hbar_\mu(\xi) = A_{1,\mu} e^{\lambda_\mu \xi} + A_{2,\mu} e^{-\lambda_\mu \xi} + A_{3,\mu} \sin(\lambda_\mu \xi) + A_{4,\mu} \cos(\lambda_\mu \xi) \tag{5.17}$$

with the $A_{i,\mu}$ and λ_μ can be obtained by

$$A_{1,\mu} = \frac{1}{2}(1 - \varepsilon_\mu),\ A_{2,\mu} = \frac{1}{2}(1 + \varepsilon_\mu),\ A_{3,\mu} = \varepsilon_\mu,\ A_{4,\mu} = -1 \tag{5.18}$$

$$\varepsilon_\mu = \frac{\cosh(\lambda_\mu) - \cos(\lambda_\mu)}{\sinh(\lambda_\mu) - \sin(\lambda_\mu)}, \quad \cos(\lambda_\mu)\cosh(\lambda_\mu) = 1 \tag{5.19}$$

Substituting Eq.(5.16) into Eq.(5.3) and then integrating over the plate, Eq.(5.3) can be transformed as:

$$L_\mu V_{p,\mu} = \int_0^1 \left(p_{cav} - p_A \right) \hbar_\mu \left(\xi \right) d\xi \tag{5.20}$$

where L_μ is the structural operator and can be defined as:

$$L_\mu = \frac{B_p}{ikc} \left(\frac{\lambda_\mu}{L_p} \right)^4 + m_p ikc \tag{5.21}$$

The acoustic pressure inside the backing cavity can be expressed based on the cavity modes [128]. For the rectangular cavity considered here, the acoustical pressure p_{cav} inside its backing cavity can be calculated from:

$$p_{cav}\left(\vec{x} \right) = ikc \sum\nolimits_{t=1}^{T} \frac{\phi_{cav,t}\left(\vec{x} \right)}{k^2 - \left(k_{cav,t} \right)^2} \int_0^1 \left[v_p\left(y' \right) \phi_{cav,t}\left(0, y' \right) \right] dy' \tag{5.22}$$

where $v_p\left(\xi \right)$ is the vibration velocity over the plate, $\phi_{cav,t}$ is the t^{th} acoustic cavity mode and $k_{cav,t}$ is the wave number of the corresponding cavity mode; $\phi_{cav,t}$ and $k_{cav,t}$ are given as,

$$\phi_{cav,t}\left(\vec{x} \right) = \sqrt{\frac{2 - \delta_{0,t_x}}{D_{cav}}} \cos\left(\frac{t_x \pi}{D_{cav}} x \right) \cdot \sqrt{\frac{2 - \delta_{0,t_y}}{L_{cav}}} \cos\left(\frac{t_y \pi}{L_{cav}} y \right) \tag{5.23}$$

$$\left(k_{cav,t}^2 \right)^2 = \left(\frac{t_x \pi}{D_{cav}} \right)^2 + \left(\frac{t_y \pi}{L_{cav}} \right)^2 \tag{5.24}$$

Substituting Eq.(5.16) into Eq.(5.22) and the sound pressure inside the backing cavity can be rewritten as:

$$p_{cav}\left(\vec{x} \right) = ikc \sum\nolimits_{u=1}^{U} V_{p,\mu} \sum\nolimits_{t=1}^{T} \frac{\phi_{cav,t}\left(\vec{x} \right)}{k^2 - \left(k_{cav,t} \right)^2} \int_0^1 \left[\hbar_\mu \left(\xi \right) \phi_{cav,t}\left(0, \xi \right) \right] d\xi \tag{5.25}$$

The above equation can be further rewritten as:

$$p_{cav}(\vec{x}) = \sum_{u=1}^{U} V_{p,\mu} p_{cav,\mu}(\vec{x}) \tag{5.26}$$

where, $p_{cav,\mu}(\vec{x})$ is the sound pressure inside the backing cavity caused by the μ-th modal vibration and is given as,

$$p_{cav,\mu}(\vec{x}) = ikc \sum_{t=1}^{T} \frac{\phi_{cav,t}(\vec{x})}{k^2 - \left(k_{cav,t}\right)^2} \int_0^1 \hbar_\mu(\xi') \phi_{cav,t}(0, y') d\xi' \tag{5.27}$$

Suppose $p_i(\vec{x})$ is the radiation pressure due to the modal vibration $\varphi_j(\xi)$. The modal impedance Z_{ij} can be given by

$$Z_{ij} = \int_0^1 p_i(\vec{x}) \varphi_j(\xi) d\xi \tag{5.28}$$

For the backing cavity, cavity impedance is the component of the modal impedance that is contributed by the acoustic pressure inside the cavity. In this regard, the cavity impedance, $Z_{cav,i\mu}$, is given as:

$$\begin{aligned} Z_{cav,i\mu} &= \int_0^1 \hbar_i(\xi)\, p_{cav,\mu}(\vec{x}) d\xi \\ &= ikc \int_0^1 \hbar_i(\xi) \left[\sum_{t=1}^{T} \frac{\left(2-\delta_{0,t_x}\right)\left(2-\delta_{0,t_y}\right)}{D_{cav} L_{cav}\left(k^2 - k_{cav,t}^2\right)} \cos\left(t_y \pi \xi\right) \int_0^1 \hbar_u(\xi') \cos\left(t_y \pi \xi'\right) d\xi' \right] d\xi \\ &= \sum_{t=1}^{T} \frac{ikc\left(2-\delta_{0,t_x}\right)\left(2-\delta_{0,t_y}\right)}{D_{cav} L_{cav}\left(k^2 - k_{cav,t}^2\right)} I_{t_y,i\mu} \end{aligned} \tag{5.29}$$

in which, $I_{t,iu}$ is defined as:

$$\begin{aligned} I_{t,i\mu} = &\int_0^1 \left[A_{1,i} e^{\lambda_i \xi} + A_{2,i} e^{-\lambda_i \xi} + A_{3,i} \sin\left(\lambda_i \xi\right) + A_{4,i} \cos\left(\lambda_i \xi\right) \right] \cos\left(t\pi\xi\right) d\xi \\ &\times \int_0^1 \left[A_{1,\mu} e^{\lambda_\mu \xi'} + A_{2,\mu} e^{-\lambda_\mu \xi'} + A_{3,\mu} \sin\left(\lambda_\mu \xi'\right) + A_{4,\mu} \cos\left(\lambda_\mu \xi'\right) \right] \cos\left(t\pi\xi'\right) d\xi' \end{aligned} \tag{5.30}$$

The calculation about $I_{t,i\mu}$ can be found in Appendix-A.

Therefore, the first item on the right side of Eq.(5.20) can be rewritten by the cavity

impedance and the modal coefficient of the plate vibration as

$$\int_0^1 p_{cav}\hbar_\mu d\xi = \sum_{l=1}^{U} V_{p,l}\int_0^1 p_{cav,l}\hbar_\mu d\xi = \sum_{l=1}^{U} V_{p,l}Z_{cav,l\mu} \tag{5.31}$$

The second item on the right side of Eq.(5.20) relates the plate vibration and the sound pressure inside the domain Ω_A.

$$\int_0^1 p_A\hbar_\mu(\xi)d\xi = \sum_{j=1}^{N} a_j\int_0^1 \phi_j(0,y)\hbar_\mu(\xi)d\xi = \sum_{j=1}^{N} a_j Z_{A,j\mu} \tag{5.32}$$

where $Z_{A,j\mu}=\int_0^1 \phi_j(0,y)\hbar_\mu(\xi)d\xi$.

Substituting Eqs.(5.31) and (5.32) into Eq.(5.20) yields:

$$\begin{aligned} L_\mu V_{p,\mu} &= \sum_{l=1}^{U} V_{p,l}Z_{cav,l\mu} - \sum_{j=1}^{N} a_j\int_0^1 \phi_j(\xi)\hbar_\mu(\xi)d\xi \\ &= \sum_{l=1}^{U} V_{p,l}Z_{cav,l\mu} - \sum_{j=1}^{N} a_j Z_{A,j\mu} \end{aligned} \tag{5.33}$$

For a single plate cavity integrated at the left inside walls of the parallel barriers, Eq. (5.15) can be simplified to

$$a_i\left(k^2-k_i^2\right) - i\rho kc\int_{S_{op}}\left(\phi_i v_n\right)ds_{op} - i\rho kc\int_{s_p}\left(\phi_i v_p\right)ds_p = -i\rho kcq_s\phi_i\left(\vec{x}_s\right) \tag{5.34}$$

Substituting the modal expressions for v_n and v_p into Eq. (5.34) yields:

$$\begin{aligned} &a_i\left(k^2-k_i^2\right) - i\rho kc\sum_{m=1}^{M} b_m\int_{S_{op}}\left(\phi_i\psi_m\right)ds_{op} \\ &-i\rho kc\sum_{u=1}^{U} V_{p,\mu}\int_{s_p}\left(\phi_i\hbar_\mu(\xi)\right)ds_p = -i\rho kcq_s\phi_i\left(\vec{x}_s\right) \end{aligned} \tag{5.35}$$

Setting $h_{i,\mu}=\int_{s_p}\left(\phi_i\hbar_\mu\left(\vec{x}_{s_p}\right)\right)ds_p$ and using the orthogonal property of the eigenmodes, Eq.(5.35) can be rewritten as

$$\begin{aligned} &a_i - \frac{i\rho kc}{\left(k^2-k_i^2\right)}\sum_{m=1}^{M} b_m\psi_{i_y}(0)\delta_{i_x,m} \\ &-\frac{i\rho kc}{\left(k^2-k_i^2\right)}\sum_{\mu=1}^{U} V_{p,\mu}h_{i,\mu} = -\frac{i\rho kcq_s}{\left(k^2-k_i^2\right)}\phi_i\left(\vec{x}_s\right) \end{aligned} \tag{5.36}$$

Combining Eqs. (5.14), (5.33) and (5.36) together, and setting

$$\mathbf{A}=\begin{Bmatrix}a_1\\a_2\\\vdots\\a_N\end{Bmatrix},\ \mathbf{B}=\begin{Bmatrix}b_1\\b_2\\\vdots\\b_M\end{Bmatrix},\ \mathbf{V}_{p,\mu}=\begin{Bmatrix}V_{p,1}\\V_{p,2}\\\vdots\\V_{p,U}\end{Bmatrix} \tag{5.37}$$

Eqs.(5.14), (5.33) and (5.36) can be written as:

$$\mathbf{A}+\mathbf{MB}+\mathbf{HV_p}=\mathbf{S} \tag{5.38}$$

$$\mathbf{\Phi A}=\mathbf{ZB} \tag{5.39}$$

$$\mathbf{LV_p}=\mathbf{Z_{cav}V_p}+\mathbf{Z_{enl}A} \tag{5.40}$$

The modal coefficients $\mathbf{A}$, $\mathbf{B}$ and $\mathbf{V_p}$ can be solved. With the theoretical model above, the sound field in and outside a baffled open cavity integrated with the plate-cavity can be calculated.

5.3 Numerical results and analysis

The geometrical parameters of the parallel barriers and the property of the air media are the same as that in Chapter 4. We will just list them in Table 5.1 and ignore the detailed descriptions. Besides, the external modal functions $\varphi_m(\vec{x})$ for the outside domain is obtained by COMSOL Multiphysics. The details about this step can be found in Chapter 4, too.

Table 5.1: Air property, parallel barriers size, sound source and receivers locations

Air property		Sound Source Locations	
Density: ρ_0	1.225	Location: (x_s,y_s) [m]	(0.1, -0.9)
Sound speed: c	340	Strength: Q_s	0.0001
Baffled Open Cavity		Receiver Locations	
Width: Lx [m]	1.83	R1	(1.82, -0.1)
Height: Ly [m]	1	R2	(5, -0.9)

Modal truncation needs to be implemented for Eqs. (5.7), (5.8) and (5.22). Convergence study for the SPL has been conducted as shown in Chapter 3 in the frequency range of [30, 1000] Hz. The steps can be found in the previous chapters and will not be discussed in detail. The results obtained by the proposed theoretical model based on the coupled mode theory agree well with those generated by the commercial software COMSOL. Therefore, in the following analysis, the comparison and analysis of the results are calculated by the proposed model.

5.3.1 The mechanism of plate cavity on noise control

The goal of the study in this chapter is to develop a broadband noise reduction device for the parallel barriers based on the acoustic-structure interaction. An investigation was conducted first to explain the physics mechanism of the plate on the noise reduction radiated from the opening. The range of interest is the low frequency regime. Following the studies for the plate silencer in the duct [83, 86], the light plate with high bending was used.

In order to facilitate the analysis and comparison with the previous results about plate silencer in Ref.[83] and Ref.[86], the mass ratio and the bending stiffness is defined as the dimensionless form in their studies,

$$m = \frac{m^*}{\rho_0^* h^*} \tag{5.41}$$

$$B = \frac{B^*}{\rho_0^* \left(h^*\right)^3 \left(c_0^*\right)^2} \tag{5.42}$$

The parameters with asterisk are referred to as the dimensional parameters and h^* equals 0.1 m.

The noise abatement by the plate cavity is subject to several design variables, for

instance, the backing cavity geometry, the plate property as well as their location. The effects of these parameters will be addressed in the next section. Consistent with the analysis in Chapters 3 and 4, the SPL at the outside receiver is compared with that of the rigid walls to validate the noise attenuation of the flexible plate on the parallel barriers. The sound spectrum at (5, -0.9) was chosen to represent the sound pattern at the far field. Fig 5.2 illustrates the sound spectrum comparison at receiver (5, -0.9) for the parallel barriers with rigid conditions and integrated with one plate cavity system. The design parameters for the plate cavity are given by:

$$L_p = 0.4\,m, \qquad H_p = 0.1\,m, \qquad D_p = 0.1\,m$$
$$m_p = 3, \qquad B_p = 0.045$$

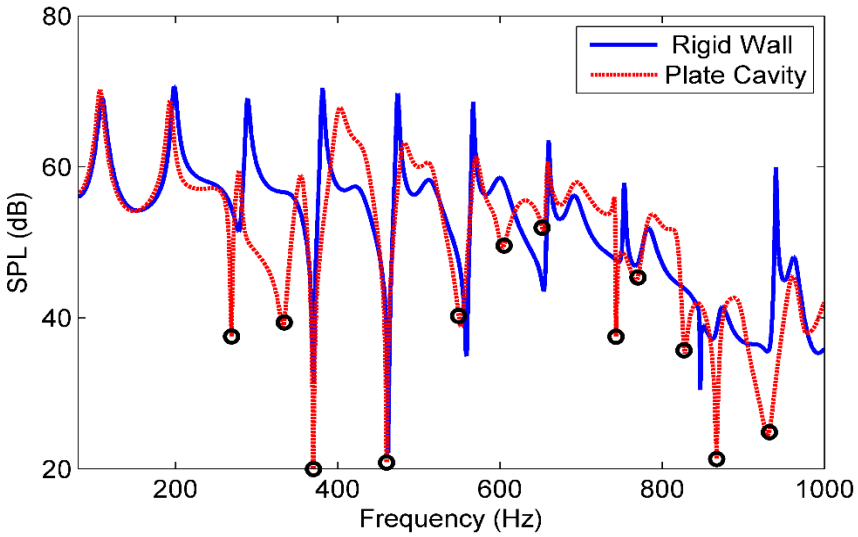

Fig 5.2: The sound spectrum at receiver for the parallel barriers with rigid wall and one plate cavity system.

As expected, the sound response is suppressed with properly tuned designs of the plate cavity. The sound pressure levels around the resonances of the enclosed cavity have been reduced. Obvious noise reduction can be found around the third peak for the rigid wall condition. A series of dips can be found, as indicated by open circles. SPL at these frequencies are suppressed well compared with vicinity frequencies.

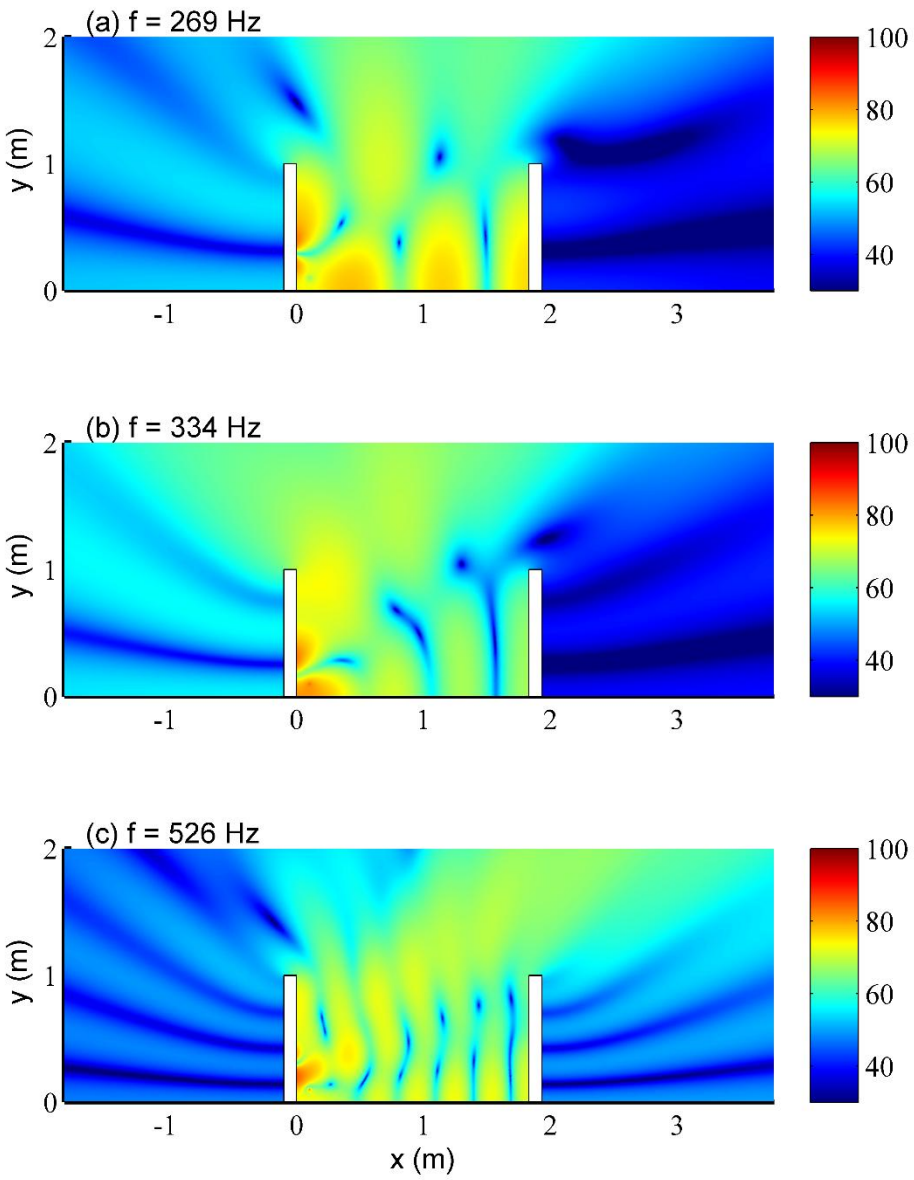

Fig 5.3: The SPL distribution of parallel barriers integrated with plate cavity at (a) 269 Hz; (b) 334 Hz and (c) 526 Hz.

To explain this phenomenon, it is proposed that the occurrence of the maximum sound suppression is related to the resonances of the plate or the resonances of the plate cavity system, just as the peak of a Helmholtz resonator appears at its resonance frequency. However, a preliminary investigation found that no coincidence can be observed between the resonant frequency of the plate cavity and the spectral dips in the SPL spectrum. This issue, the relationship of SPL dips and the resonances of the plate cavity system will be explored in the future work.

Fig 5.3 presents the SPL distribution of the parallel barriers integration with the plate cavity. Three frequencies corresponding to the dips in Fig 5.2 are chosen. As can be observed, the SPLs at these frequencies are suppressed inside and outside the bounded domain of the parallel barriers. Specially, the noise reduction for the right outside region at first two frequencies, 269 Hz and 334 Hz, is more obvious than that for the left region.

The first two vibration mode of the plate are shown in Fig 5.4, Fig 5.5 and Fig 5.6 in solid lines, together with the vibration response of the plate at the corresponding SPL dips for comparison (in dashed lines). When the frequency is extremely low, the cavity is compact and very stiff to the volume-displacing mode. As shown in Fig 5.4, the shape of plate vibration at 269 Hz looks rather like the second *in vacuo* mode which is almost not affected by the incompressibility of the air in the cavity.

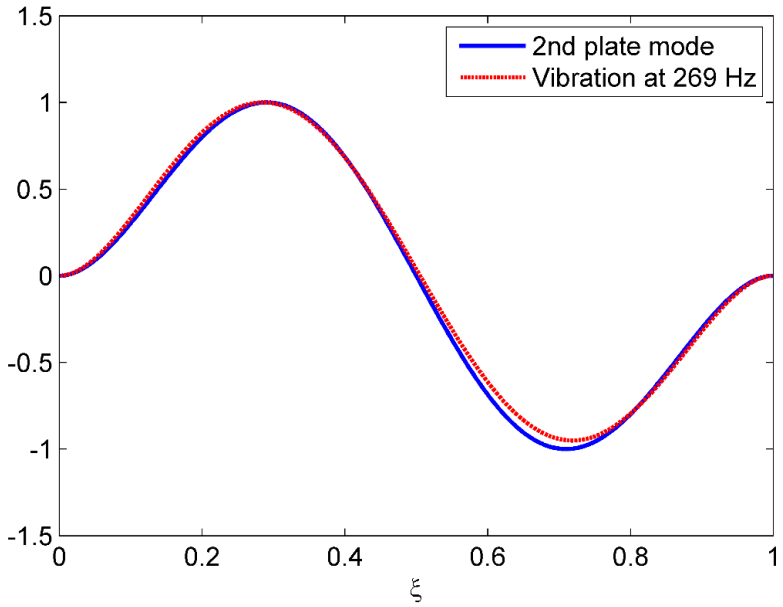

Fig 5.4: Comparison of the second plate mode and the plate response at 269 Hz.

However, at 334 Hz, the vibration of the plate is mainly dominated by the first mode. The possible explanation is that the cavity is compact and very stiff to the volume-displacing mode at this frequency. When observing the sound pressure distribution inside the cavity, a relatively uniform distribution can be observed at the plate side.

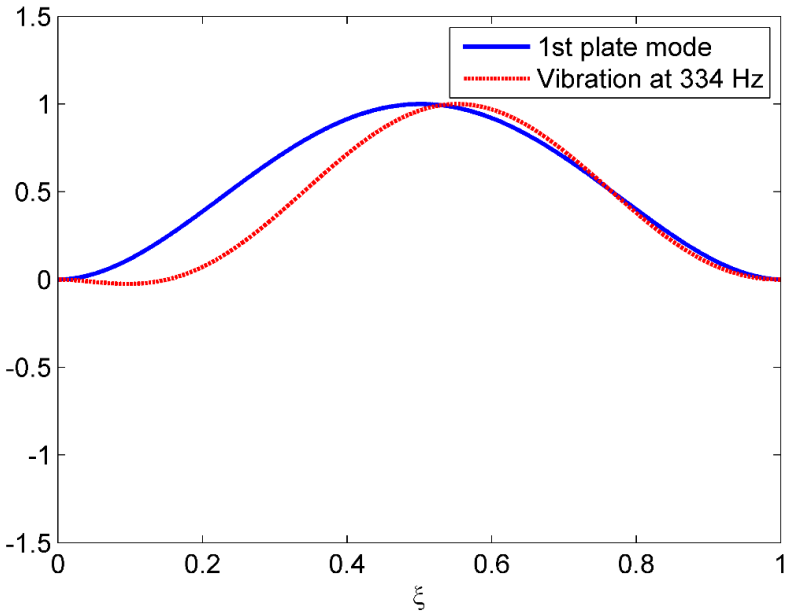

Fig 5.5: Comparison of the second plate mode and the plate response at 334 Hz.

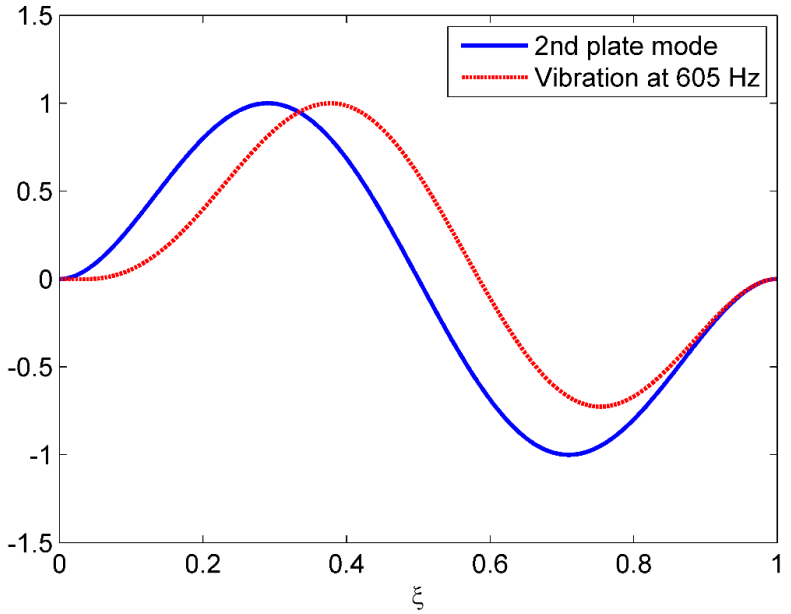

Fig 5.6: Comparison of the second plate mode and the plate response at 605 Hz.

The third response of plate vibration at 605 Hz shown in Fig 5.6 looks also like the second plate mode. On the whole, Fig 5.4-Fig 5.6 demonstrate remarkable similarity between the vibration modes of the plate cavity system and the plate vibration responses at the SPL dips, which suggests that the occurrence of the spectral dip of the noise reduction due to the plate cavity device is closely related to the resonances of such an

acoustic-structure system.

5.4 Properties of parameters

Compared with the tensioned membrane, the construction for plate cavity device is a very simple. However, a lot of variables can affect noise abatement performance greatly of this device. For instance, the cavity shape and location, the plate properties, and the installation method of the plate play important roles in determining the plate vibration. During the design of the plate cavity system, the effect of various design parameters are identified with other design parameters fixed.

The incident and reflected sound induce the dynamic motion of the plate, which is mainly determined by the mass and bending of the plate. The plate vibration in turn affects the impedance, sound reflection and ultimately the noise reduction performance of the plate cavity. Therefore, the variables analysis should be carried out to achieve the best noise reduction. These variables are basically divided into two categories: the first is geometrical variables such as the length, depth and location of the cavity or the plate; the second is related to structural properties, such as the mass and the bending of the plate.

5.4.1 Cavity shape and location

The backing cavity serves to prevent the noise transmission through the plate to the receivers. Meanwhile, it also introduces air stiffness to the system and modifies the resonances and vibration of the plate, especially at relatively low frequency. As claimed by Ref. [79] for rectangular duct, for given cavity volume, a shallower cavity with a longer plate has a wider TL spectrum. The noise reduction bandwidth increase while the peaks in amplitude fall. On the contrary, deeper and shorter cavity works like the

resonator and a better minimal TL can be obtained in a narrow frequency band. A primary study in this chapter has shown that broadband noise reduction can be obtained when setting the cavity length to 0.4 m, which is a little shorter than recommended by Ref.[79]. Another restriction of the cavity depth is the wall thickness of the barriers. Regarding the noise reduction performance and the space limitation of the barrier walls, the length and the depth of the cavity is 0.4 m and 0.1 m, respectively.

5.4.2 Structural properties

In this section, the structural properties of the plate on the noise abatement at the receiver is examined. The plate chosen was with light density and high tension.

5.4.2.1 Plate mass

The plate mass was first investigated by varying the mass ratio m_p while other parameters were fixed. For each mass ratio given, bending stiffness is consistent with the value of the PMI foam to search for the optimal noise reduction in the low frequency range.

The mass effect of the plate on the noise control for parallel barriers is shown in Fig 5.7 , in which the bending stiffness *B* equaling 0.045. The SPL after installing the plate silencer was compared with the rigid conditions. As shown in Fig 5.7 (a), an obvious noise reduction can be observed in the frequencies around the third SPL peak. As the mass increases, the spectra is shifted towards lower frequencies. For instance, the frequency of the first dip is 273 Hz for m_p =1, as compared, the frequency for the first dip is 237 Hz as shown in Fig 5.7 (c). Therefore, the noise reduction at lower frequencies can be obtained as increasing the mass of the plate. However, increasing the plate mass cannot improve the overall noise abatement, because the noise reduction

at high frequencies may be reduced. Shown by Fig 5.7 (c), the original fourth SPL peak is shifted and lifted. The SPL around this peak is larger than the original values. For the lighter plate, as shown by Fig 5.7 (a), the noise reduction can be obtained in the vicinity of this sound peak.

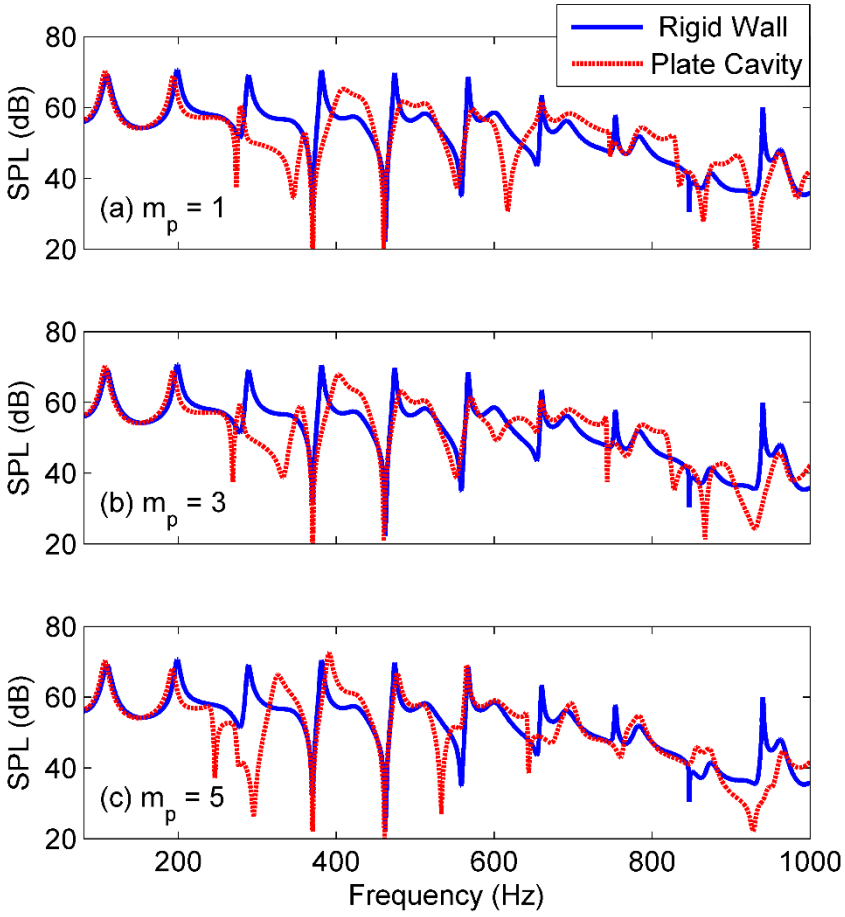

Fig 5.7: The SPL varies with the mass of the plate while the bending fixed at B=0.045: (a) m_p=1; (b) m_p=3 and (c) m_p=5.

As a summary, the mass effect is generally counterproductive. As the increase of plate mass, the noise reduction can be obtained at lower frequencies, while the sound response at higher frequencies is increased. Besides, for each mass ratio given, bending stiffness should be varied to search for the optimal noise reduction. The studies in this chapter mainly focus on exploring the acoustically coupling of the plate cavity and the parallel barriers. The performance optimization will be conducted in the future work.

5.4.2.2 Bending stiffness

Fig 5.8 displays the SPL spectra varying with different bending stiffness. The mass ration of the plate is fixed at m_p = 3, and the cavity is 0.1 m in depth and 0.4 m in length. Several SPL dips can be observed when varying the bending stiffness of the plate. The dip frequencies shift towards higher values as the increase of the bending stiffness. Shown in Fig 5.8 (a) is the SPL comparison when the bending stiffness is a small value, B_p = 0.03. The noise reduction can be obtained for the frequencies in the vicinity of 289 Hz. In the frequency range around 847 Hz, the low noise level from the rigid condition has been kept. When the bending stiffness increases, the dips are shifted to higher frequencies accordingly. However, when the bending stiffness is too high (B_p = 0.12) as shown in Fig 5.8 (d), the noise reduction can mainly be found at the original sound peaks. This is probably due to the high bending stiffness restricts the dynamic motion of the plate. Therefore, originally high sound oscillations between the rigid walls can induce the vibration of the plate and thereby the SPL peaks at these frequencies can be reduced obviously. The benefit of high bending can also be observed at higher frequencies, where the original low sound response is still reduced. In the previous work by Wang et al. [83], the bending stiffness should be high enough in order to achieve a broad stopband for duct noise control. However, in our work, the high bending stiffness does not always work well, especially at the high regime in the frequency range below 1000 Hz.

Combining Fig 5.7 and Fig 5.8, we can conclude that, with plate in light mass and high bending, the noise reduction can be achieved in the frequency range of 200 up to 1000 Hz. The sound levels at the multiple peaks have been reduced and the original low noise levels from the rigid wall condition have been maintained.

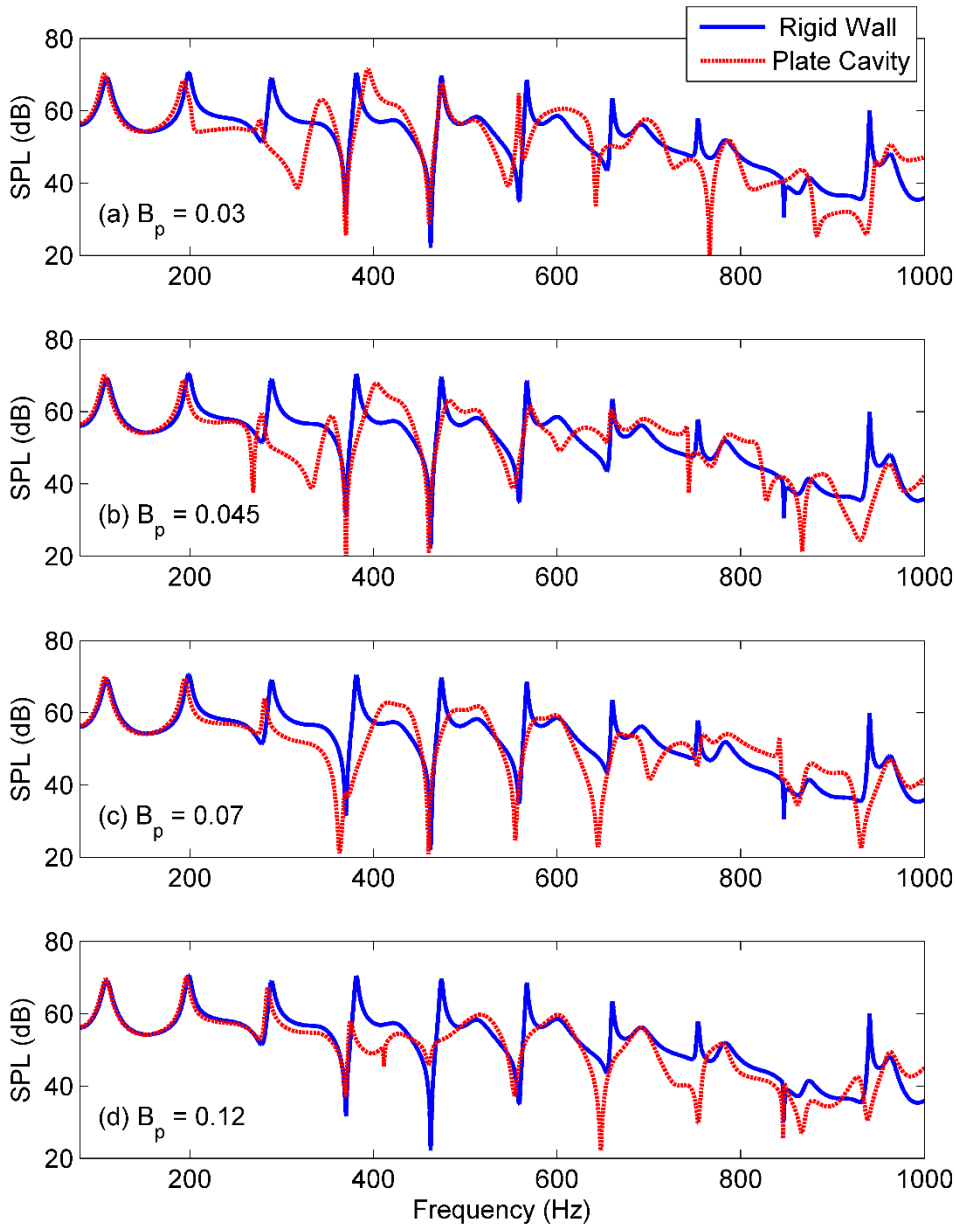

Fig 5.8: The SPL varies with the bending stiffness while the mass ratio fixed at m=3: (a) B_p=0.03; (b) B_p=0.045 ; (c) B_p=0.07 and (d) B_p=0.12.

5.5 Experimental validation

The experimental study was conducted in the anechoic chamber with the same setup as described in Chapter 4. The experimental diagram is shown in Fig 5.9. Details about the configuration of the parallel barriers and the measurement devices can be found in Chapter 4 and will be discussed here.

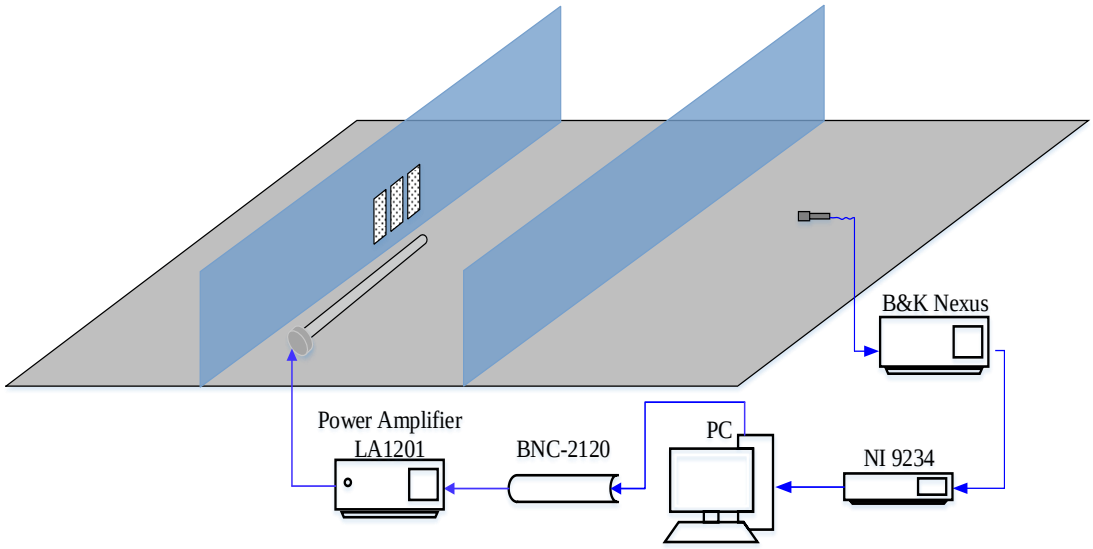

Fig 5.9: The sketch of the experimental setup.

The aim of this experiment was to validate the effectiveness of the plate cavity on the noise abatement of the parallel barriers. Three same backing cavities made of 18.5-mm-thick wood panel were installed on the left barrier which was near to the sound source, as indicated in Fig 5.10. The cross-section of the cavities was 100 mm x 100 mm and their lengths were consistent with the previous analysis.

As discussed in the above section, the plate should be light density while high tension. Therefore, PMI foam was chosen to fabricate the rectangular plate. The density of this material is 32 kg/m^3 and its Young's modulus is 0.036 Gpa. Three pieces of PMI foam were installed flush with the backing cavity.

The plate was a little larger than the opening of the backing cavity, measuring 420mm* 104mm*2mm, which are length, width and thickness. Two edges of the plates along the length direction were clamped and their effective length was 400 mm. A very small clearance existed between the plate lateral edges and the backing cavity wall such that the lateral edges could freely vibrate to simulate the two-dimensional behavior. The following photo illustrates the parallel barriers after installation with these three plate cavity systems.

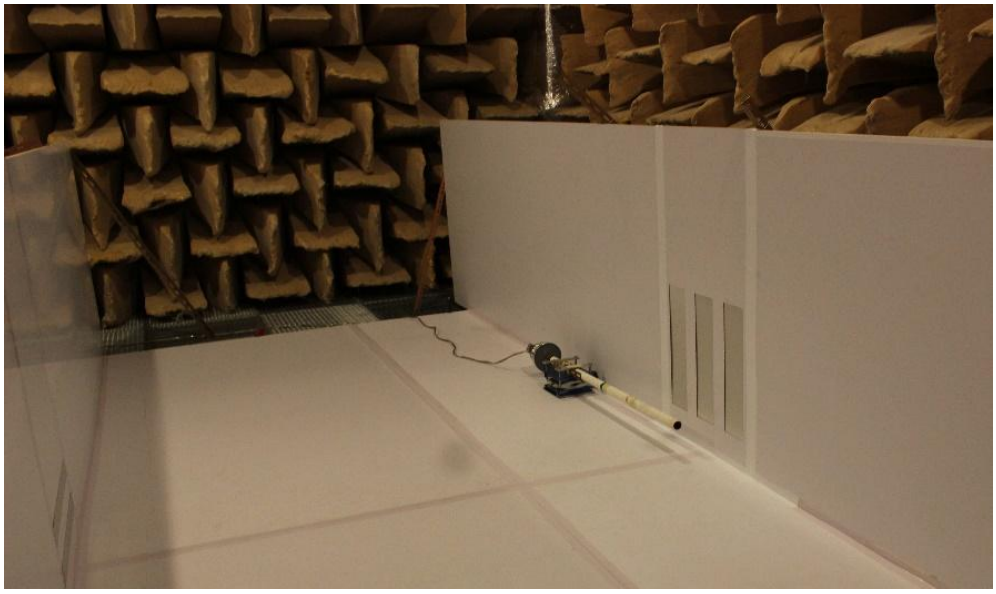

Fig 5.10: Image of the parallel barriers integrated with plate cavity.

Fig 5.11 presents the experimental results measured from the experiment. Dashed line with asterisk represents the SPL for the parallel barriers with rigid walls and the dashed line with open circles for the parallel barriers integrated with three plate cavity devices. It can be regarded that the SPL are suppressed in the frequency range of interest except that around the 800 Hz, where the increase can be observed.

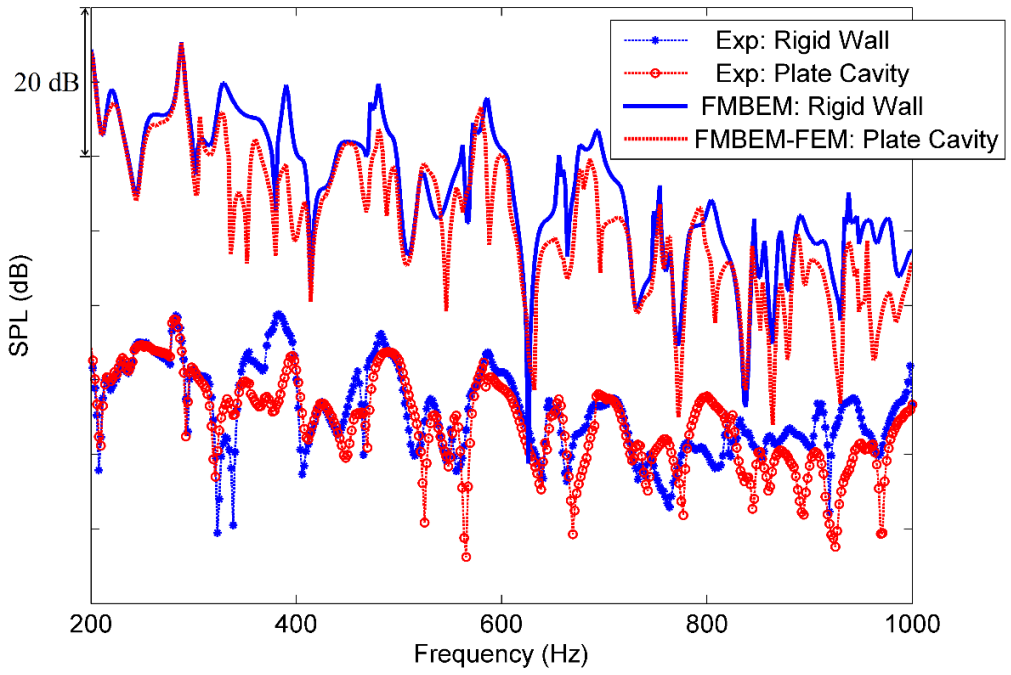

Fig 5.11: SPL Comparison for the parallel barriers with rigid walls and plate cavity.

5.6 Numerical calculation by fast multipole BEM

The FMBEM-FEM program was then used to predict the sound field of the parallel barriers integrated with the plate cavity system. The configurations used in the numerical calculations are the same as those in the experiment. The meshing and setup for the multipole expansions and truncations can be found in Chapter 4 and will not be discussed here. The constant triangle elements were used in the FMBEM and the number is 63402. The rectangular elements were used in the FEM and the number is 1200. The solid line in Fig 5.11 represents the SPL numerically calculated for the parallel barriers with rigid walls and the dashed line for the parallel barriers integrated with three plate cavity devices. An obvious noise reduction can be observed in the frequency range of interest after the frequency corresponding to the first peak. The main feature of the SPL outside the parallel barriers is similar with that in two dimensions. The difference is that the opening in z-direction decreases the noise response at higher frequencies. When comparing the results measured from the experiment and calculated by the FMBEM-FEM, the agreement in trend can be observed. The main difference is around 328 Hz, where the sound peak in the numerical result while the dip in the measurement. The explanation to this might be the weak response of the loud speaker and will be explored in the future work. The following two figures show the SPL comparison at 390 Hz for the parallel barriers with rigid walls and three plate cavity devices.

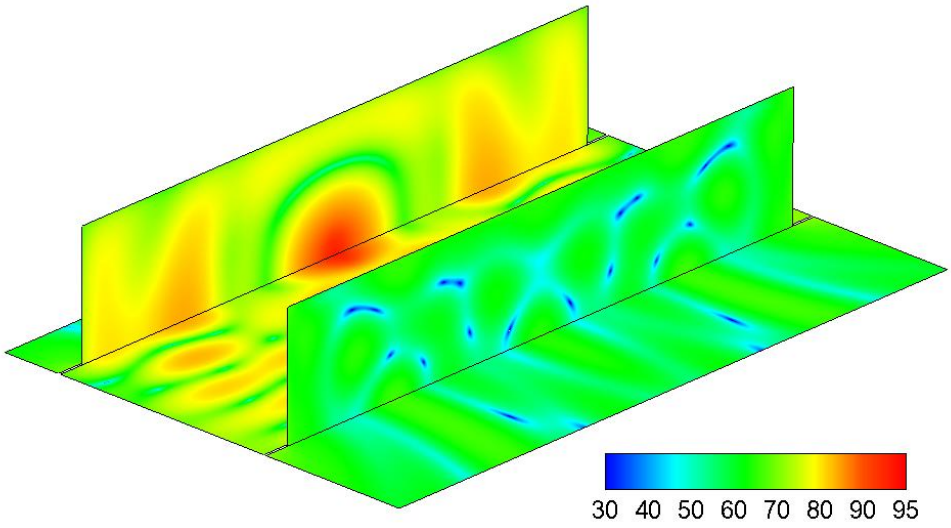

Fig 5.12：SPL distribution for parallel barriers with rigid walls.

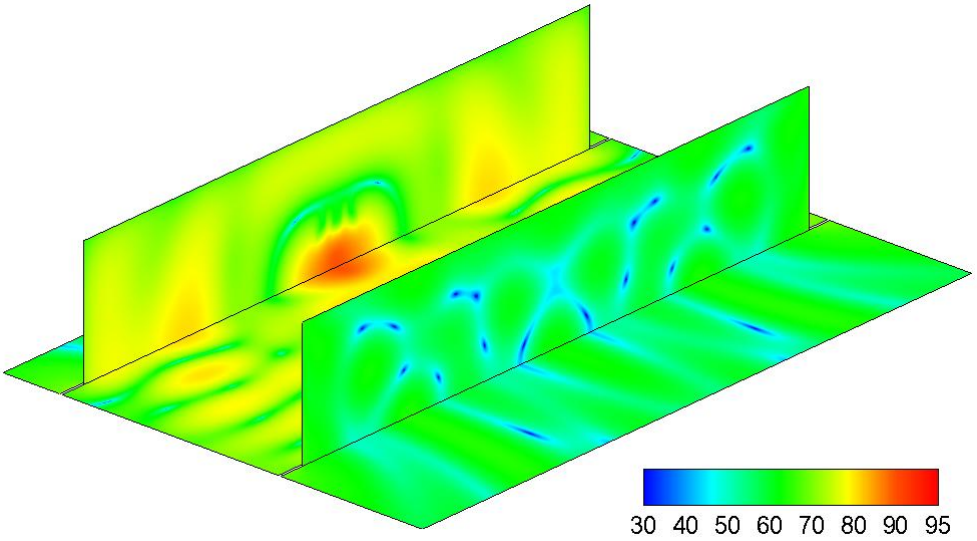

Fig 5.13: SPL distribution of parallel barriers with three plate cavity devices.

5.7 Summary

The systematic analysis of the acoustics-structural interaction of the parallel barriers integrated with the plate cavity was carried out. To achieve this target, a theoretical model was first established accounting for the acoustic-structure coupling behavior between the open enclosure and the vibrating panel backed with cavity. The influence of plate vibration induced by the sound source on the sound field inside and outside the parallel barriers was then analyzed. Moreover, the mass ratio and the bending stiffness

of the plate on the noise reduction of the parallel barriers was investigated. As the increase of the bending stiffness, the noise reduction in spectrum shifts to a higher frequency. As compared, the noise reduction shifts to a lower frequency as the increase of the plate mass. With a proper bending stiffness and mass ratio, broadband noise reduction can be obtained in the low frequency regime. Finally, the experimental validation in an anechoic chamber and numerical calculations by FMBEM-FEM in three dimensional were conducted. These results confirm the effectiveness of using the flexible panel to abate the noise of the parallel barriers.

CHAPTER 6

CONCLUSIONS AND RECOMMENDATIONS

6.1 Conclusions

The research in this thesis has been to solve the sound radiation and abatement from the open structures. The study was motivated by the degradation of the acoustic performance for parallel barriers and the inherent difficulties in controlling low frequency environmental noise. The theoretical and numerical model for the parallel barriers have been established and the Helmholtz resonators and plate cavity devices have been applied to improve the noise reduction of the parallel barriers in the present work.

Before developing the noise control device for the parallel barriers, the numerical method of FMBEM-FEM for the large scale acoustic-structural interaction in three dimensions has been established. In order to solve the non-unique solutions for exterior problem, the Burton-Miller formulation is used to modify the BEM. The fast multipole algorithm is then adopted to accelerate the computation of the BEM in large scale problem. The expansion and translation in the low-frequency regime is based on the partial wave expansion together with the rotation-coaxial translation method. In the high-frequency regime, the plane wave expansion and the interpolation/filtering method are used. These methods form the hybrid multipole expansion and translation in the wideband. To deal with the acoustic-structural interaction, the FEM is coupled to the FMBEM.

The acoustical coupling of the baffled open cavity and the Helmholtz resonators was then explored in three dimensions. The noise reduction by applying Helmholtz

resonator was investigated theoretically and experimentally. A theoretical model based on modal analysis was established to reconstruct the sound field inside and outside the cavity. The accuracy of the proposed method was validated by comparing with the numerical results obtained through the BEM programs. Combining the dominant equations of the sound fields inside and outside of the cavity, the characteristic matrix equation was produced and the eigenvalues of the open space were determined. It was found that the eigenfrequencies were complex and shifted to higher frequencies compared with their closed-cavity ones. For the convenience of the analysis, the resonator array was simplified to single one resonator, named HR381. Due to the acoustical coupling between the open cavity and the resonator, two new resonances emerge on each side of the targeted eigenfrequency. After inserting the HR381, noise reductions inside and outside the cavity was found at the target frequency. However, the noise levels in the vicinity of the target frequency have been increased. In order to achieve the noise reduction within a frequency band, the location, internal resistance and relative volume ratio of HR381 were explored. The theoretical analysis indicated that, the resonator should with a moderate internal resistance and large volume should be near to the primary sound source. Finally, the measurement for the baffled open cavity without and with one single resonator was conducted in the anechoic chamber, which also demonstrated the accuracy of the proposed theoretical model and the effectiveness of using the Helmholtz resonator to reduce the noise radiation level from the opening of the cavity. The proposed model provides a useful tool to analysis the noise reduction of sound radiation from the aperture of the baffled open cavity.

Afterwards, following the studies of the resonator on the baffled open cavity, the Helmholtz resonators were mounted on the barrier wall to reduce the noise level at the receivers far from the barrier. Due to the difficulty in expressing the Green’s function

for the unbaffled cavity analytically, a hybrid method was developed first to predict the sound field in and outside the parallel barrier. It was found that: (1) the degradations was caused by the resonances inside the bounded domain; (2) the sound peaks at the receiver inside the bounded domain were dominated by the corresponding closed-cavity modes and (3) the sound peaks at the receiver outside the bounded domain were dominated by the external modes. The resonator arrays were used to improve the noise reduction at these frequencies through suppressing the responses of their dominant modes. Comparison for the noise reduction by single HR281 at different location was carried out. When the single HR281 at (0, -0.9), a reduction in 17.14 dB was achieved at the target frequency. Besides, the noise level within the frequency range [198,381] Hz had also been reduced. However, the low noise response around 847 Hz was improved. The optimization location of the single HR281 should consider the balance between the noise reduction at the target peak and noise increase in the vicinity frequency. Two resonators with different natural frequencies, HR281 and HR468, were designed and mounted on the barriers. The deteriorations were suppressed and a broadband noise reduction was obtained in the frequency range from 200 to 1000 Hz. Finally, numerical calculations based on the developed FMBEM were carried out and compared with the experimental measurements. Roughly speaking, the good agreement could be found and validates the accuracy of the FMBEM in modeling the noise reduction of the parallel barriers integration with Helmholtz resonators.

As shown in Chapter 4, the resonator can reduce the noise level at the outside receivers. However, its drawback is that the reduction spectrum for single resonator is narrow. Array resonators combining several resonators at different natural frequencies can obtain a broadband noise abatement, while the compromise is that the acoustical coupling among the resonators and the parallel barriers deteriorates the noise reduction.

In Chapter 5, in order to broaden the noise reduction and maintain the effectiveness in low frequency range, the plate cavity device was adapted to the parallel barriers. The plate cavity system consists of the light plate with high stiffness and a rectangular backing cavity. A systematic analysis on the acoustics-structural interaction of the parallel barriers integrated with the plate cavity was carried out. The influence of plate vibration induced by the sound source on the sound field inside and outside the parallel barriers was then analyzed. The location and length of the plate cavity, the mass ratio and the bending stiffness of the plate on the noise reduction of the parallel barriers were investigated. As the increase of the plate cavity length, the noise reduction is shifted to lower frequencies. The noise abatement could only be found at the sound peaks as lifting the plate cavity location. When increasing the bending stiffness, the noise reduction in spectrum shifts to a higher frequency. As compared, the noise reduction shifts to a lower frequency as the increase of the plate mass. Finally, the experimental validation and numerical calculations by the proposed FMBEM-FEM were conducted for three-dimensional configuration. Good agreement can be found for the experimental measurements and the numerical calculations. These results confirm the effectiveness of using the flexible plate backed by rectangular cavity to improve the noise reduction of the parallel barriers.

6.2 Recommendations for future study

The studies in this thesis provide a theoretical, numerical and experimental analysis to improve the noise reduction of the parallel barriers by integration of Helmholtz resonators or plate cavity device. In order to enhance the understanding of the acoustical coupling of the open space as well as the noise control through structure-acoustics interaction, future work will be developed in the following areas.

The present study shows that the sound peaks at the receivers are dominated by the

resonances inside the bounded domain. A direct and effective way to reduce the noise level is to suppress these resonances. It is believed that a thorough understanding of the formation mechanism of the SPL spectral peaks not only can stimulate scholars' academic interest, but also can help to improve the resonator array or the plate cavity design as well as develop new applications. Although multi resonators are combined together and can obtain a broadband noise reduction enhancement in the low frequency range for parallel barriers. The parameters and optimization of the array resonators on the noise control still need further investigation.

In the derivation of the modal coupling for open domains (baffled open cavity and parallel barriers), the damping is not included. The experimental validation has demonstrated the importance of the damping on the sound levels at the resonances. Therefore, the damping will be considered in the future work.

A systematic study on the effect of multi plate cavity should be carried out. The acoustically rigid backing cavity used in this study is rectangular. It is necessary to identify the vibration of the plate backed by an irregular cavity. Also, it is of great help to fully understand the physics of the vibroacoustic on the sound radiation and abatement of open structures. Although attempts are made to explain the connection between the dip frequencies for the SPL spectrum and the plate vibration, there is not yet a clear explanation for the occurrence of the spectral peaks. Hence, further study should be conducted to investigate the formation mechanism of the spectral dips in the SPL spectrum.

APPENDIX-A

Coefficients in Eq.(5.30)

$$I_{t,i}^{1}=\int_0^1 e^{\lambda_i\xi}\cos\left(t\pi\xi\right)d\xi=\frac{\lambda_i\left[\cos\left(t\pi\right)e^{\lambda_i}-1\right]}{\lambda_i^2+\left(t\pi\right)^2} \tag{A.1}$$

$$I_{t,i}^{\ 2}=\int_0^1 e^{-\lambda_i\xi}\cos\left(t\pi\xi\right)d\xi=\frac{\lambda_i\left[1-\cos\left(t\pi\right)e^{\lambda_i}\right]}{\lambda_i^2+\left(t\pi\right)^2} \tag{A.2}$$

$$I_{t,i}^{\ 3}=\int_0^1 \sin\left(\lambda_i\xi\right)\cos\left(t\pi\xi\right)d\xi=\frac{\lambda_i\left[1-\cos\left(\lambda_i+t\pi\right)\right]}{\lambda_i^2-\left(t\pi\right)^2} \tag{A.3}$$

$$I_{t,i}^{\ 4}=\int_0^1 \cos\left(\lambda_i\xi\right)\cos\left(t\pi\xi\right)d\xi=\frac{\lambda_i\sin\left(\lambda_i+t\pi\right)}{\lambda_i^2-\left(t\pi\right)^2} \tag{A.4}$$

$$I_{t,\mu}^{1}=\int_0^1 e^{\lambda_\mu\xi}\cos\left(t\pi\xi\right)d\xi=\frac{\lambda_\mu\left[\cos\left(t\pi\right)e^{\lambda_\mu}-1\right]}{\lambda_\mu^2+\left(t\pi\right)^2} \tag{A.5}$$

$$I_{t,\mu}^{\ 2}=\int_0^1 e^{-\lambda_\mu\xi}\cos\left(t\pi\xi\right)d\xi=\frac{\lambda_\mu\left[1-\cos\left(t\pi\right)e^{\lambda_\mu}\right]}{\lambda_\mu^2+\left(t\pi\right)^2} \tag{A.6}$$

$$I_{t,\mu}^{\ 3}=\int_0^1 \sin\left(\lambda_\mu\xi\right)\cos\left(t\pi\xi\right)d\xi=\frac{\lambda_\mu\left[1-\cos\left(\lambda_\mu+t\pi\right)\right]}{\lambda_\mu^2-\left(t\pi\right)^2} \tag{A.7}$$

$$I_{t,\mu}^{\ 4}=\int_0^1 \cos\left(\lambda_\mu\xi\right)\cos\left(t\pi\xi\right)d\xi=\frac{\lambda_\mu\sin\left(\lambda_\mu+t\pi\right)}{\lambda_\mu^2-\left(t\pi\right)^2} \tag{A.8}$$

APPENDIX-B

The matrix in Eq.(5.38):

$$\mathbf{M} = -j\rho kc \begin{Bmatrix} \frac{\psi_{1y}(0)\delta_{1x,1}}{\left(k^2-k_1^2\right)}, \frac{\psi_{1y}(0)\delta_{1x,2}}{\left(k^2-k_1^2\right)}, \cdots, \frac{\psi_{1y}(0)\delta_{1x,M}}{\left(k^2-k_1^2\right)} \\ \frac{\psi_{2y}(0)\delta_{2x,1}}{\left(k^2-k_2^2\right)}, \frac{\psi_{2y}(0)\delta_{2x,2}}{\left(k^2-k_2^2\right)}, \cdots, \frac{\psi_{2y}(0)\delta_{2x,M}}{\left(k^2-k_2^2\right)} \\ \vdots \\ \frac{\psi_{Ny}(0)\delta_{Nx,1}}{\left(k^2-k_N^2\right)}, \frac{\psi_{Ny}(0)\delta_{Nx,2}}{\left(k^2-k_N^2\right)}, \cdots, \frac{\psi_{Ny}(0)\delta_{Nx,M}}{\left(k^2-k_N^2\right)} \end{Bmatrix} \tag{B.1}$$

$$\mathbf{H} = -j\rho kc \begin{Bmatrix} \frac{h_{1,1}}{\left(k^2-k_1^2\right)}, \frac{h_{1,2}}{\left(k^2-k_1^2\right)}, \cdots, \frac{h_{1,U}}{\left(k^2-k_1^2\right)} \\ \frac{h_{2,1}}{\left(k^2-k_2^2\right)}, \frac{h_{2,2}}{\left(k^2-k_2^2\right)}, \cdots, \frac{h_{2,U}}{\left(k^2-k_2^2\right)} \\ \vdots \\ \frac{h_{N,1}}{\left(k^2-k_N^2\right)}, \frac{h_{N,2}}{\left(k^2-k_N^2\right)}, \cdots, \frac{h_{N,U}}{\left(k^2-k_N^2\right)} \end{Bmatrix} \tag{B.2}$$

$$\mathbf{S} = -j\rho kcq_s \begin{Bmatrix} \frac{\phi_1(\vec{x}_s)}{\left(k^2-k_1^2\right)} \\ \frac{\phi_2(\vec{x}_s)}{\left(k^2-k_2^2\right)} \\ \vdots \\ \frac{\phi_N(\vec{x}_s)}{\left(k^2-k_N^2\right)} \end{Bmatrix} \tag{B.3}$$

$$\mathbf{\Phi} = \begin{bmatrix} \delta_{1x,1}\psi_{1y}(0), & \delta_{2x,1}\psi_{2y}(0), & \cdots, & \delta_{Nx,1}\psi_{Ny}(0) \\ \delta_{1x,2}\psi_{1y}(0), & \delta_{2x,2}\psi_{2y}(0), & \cdots, & \delta_{Nx,2}\psi_{Ny}(0) \\ & \vdots & & \\ \delta_{1x,NX}\psi_{1y}(0), & \delta_{2x,NX}\psi_{2y}(0), & \cdots, & \delta_{Nx,NX}\psi_{Ny}(0) \end{bmatrix} \tag{B.4}$$

$$Z_{\mu,m} = \int_S \int_S \left[\psi_\mu (x') \cdot \varphi_m (x) \right] dS dS'$$

$$\mathbf{Z} = \frac{1}{2} \rho kc \begin{bmatrix} Z_{1,1}, & Z_{1,2}, & \cdots, & Z_{1,M} \\ Z_{2,1}, & Z_{2,2}, & \cdots, & Z_{2,M} \\ & \vdots & & \\ Z_{NX,1}, & Z_{NX,2}, & \cdots, & Z_{NX,M} \end{bmatrix} \tag{B.5}$$

$$L_\mu = \frac{B_p}{jkc} \left(\frac{\lambda_\mu}{L_p} \right)^4 + m_p jkc; \ \mathbf{L} = \begin{Bmatrix} L_1, & 0, & \cdots & , 0 \\ 0, & L_2, & \cdots & , 0 \\ \vdots & & & \\ 0, & 0, & \cdots & , L_U \end{Bmatrix} \tag{B.6}$$

$$Z_{cav,i\mu} = \int_0^1 \hbar_i (\xi) \, p_{cav,\mu} (\xi) \, d\xi; \quad \mathbf{Z_{cav}} = \begin{Bmatrix} Z_{cav,11}, & Z_{cav,12}, & \cdots, & Z_{cav,1U} \\ Z_{cav,21}, & Z_{cav,22}, & \cdots, & Z_{cav,2U} \\ \vdots & & & \\ Z_{cav,U1}, & Z_{cav,U2}, & \cdots, & Z_{cav,UU} \end{Bmatrix} \tag{B.7}$$

$$Z_{enl,j\mu} = \int_0^1 \phi_j (\xi) \hbar_\mu (\xi) \, d\xi; \ \mathbf{Z}_{enl} = \begin{bmatrix} Z_{enl,11}, Z_{enl,12}, \cdots, Z_{enl,1N} \\ Z_{enl,21}, Z_{enl,22}, \cdots, Z_{enl,2N} \\ \vdots \\ Z_{enl,U1}, Z_{enl,U2}, \cdots, Z_{enl,UN} \end{bmatrix} \tag{B.8}$$

APPENDIX-C

The hypersingular integral arising in Eq.(2.17) can be written as

$$\begin{aligned} & F^1(\vec{x},\vec{y}) \\ & = \frac{\partial^2 G(\vec{x},\vec{y})}{\partial n(\vec{x})\partial n(\vec{y})} \\ & = \frac{e^{ikr}}{4\pi r^3}\left\{(1-ikr)n(\vec{x})\cdot n(\vec{x}) + \left[3(1-ikr)-k^2r^2\right]\frac{\partial r}{\partial n(\vec{x})}\frac{\partial r}{\partial n(\vec{y})}\right\} \end{aligned} \tag{C.1}$$

When $r \to 0$, the above equation can be changed to

$$F^1(\vec{x},\vec{y}) = \frac{\partial^2 G(\vec{x},\vec{y})}{\partial n(\vec{x})\partial n(\vec{y})} = \frac{e^{ikr}}{4\pi r^3}\left\{n(\vec{x})\cdot n(\vec{y}) + 3\frac{\partial r}{\partial n(\vec{x})}\frac{\partial r}{\partial n(\vec{y})}\right\} + O\left(\frac{1}{r}\right) \tag{C.2}$$

$F^1(\vec{x},\vec{y})$ is hyper singular and need special treat before using Gaussian integration. Firstly, the boundary can be treated as:

$$S = S - S_x + \lim_{\varepsilon\to 0}(S_x - e_\varepsilon + S_\varepsilon) \tag{C.3}$$

where S_x is the boundary including the point $\vec{x}$, S_ε is the hemisphere whose center is point $\vec{x}$ and radius is ε and e_ε is the surface encircled by S_ε on the boundary, the details can be found in the following Fig C.1.

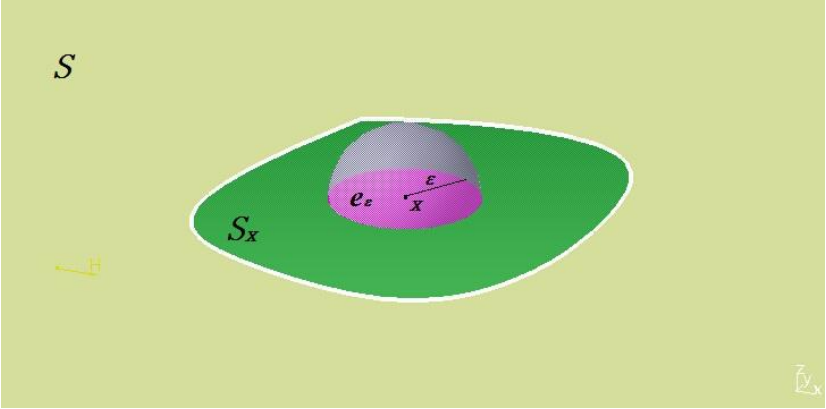

Fig C.1: The details of the singular point and the integral boundary surface.

$$\begin{aligned}
&\int_S F^1(\vec{x},\vec{y})\,p(\vec{y})\,dS(y)\\
&=\int_{S-S_x} F^1(\vec{x},\vec{y})\,p(\vec{y})\,dS(y)\\
&+\lim_{\varepsilon\to 0}\int_{S_x-S_\varepsilon} F^1(\vec{x},\vec{y})\,p(\vec{y})\,dS(y)\\
&+\lim_{\varepsilon\to 0}\int_{e_\varepsilon} F^1(\vec{x},\vec{y})\,p(\vec{y})\,dS(y)
\end{aligned} \tag{C.4}$$

On the other surface of the hemisphere S_ε,

$$\begin{aligned}
\frac{\partial r}{\partial n(\vec{y})} &= 1\\
\frac{\partial r}{\partial n(\vec{x})} &= -n_i(x)\,n_i(y)
\end{aligned} \tag{C.5}$$

Substituting Eq.(C.5) into the last part of Eq.(C.4), we can obtain:

$$\lim_{\varepsilon\to 0}\int_{S_\varepsilon} F^1(\vec{x},\vec{y})\,p(\vec{y})\,dS(y) = -\frac{1}{2\pi}\lim_{\varepsilon\to 0}\int_0^{\pi}\frac{n_i(x)\,n_i(y)}{\varepsilon}\,p(\vec{y})\,dS(y) \tag{C.6}$$

Then the second integral at the right side of Eq.(C.4) is

$$\begin{aligned}
&\lim_{\varepsilon\to 0}\int_{S_x-S_\varepsilon} F^1(\vec{x},\vec{y})\,p(\vec{y})\,dS(y)\\
&= p_i\lim_{\varepsilon\to 0}\int_{S_x-S_\varepsilon} F^1(\eta_x,\eta_y)\,\Phi^i(\eta_y)\,J(\eta_y)\,d\eta_1 d\eta_2\,p(\vec{y})
\end{aligned} \tag{C.7}$$

Neglecting the pi and changing the local coordinate to the polar coordinate, the above equation can be written as

$$\begin{aligned}&\lim_{\varepsilon\to 0}\int_{S_x-S_\varepsilon} F^1\left(\eta_x,\eta_y\right)\Phi^i\left(\eta_y\right)J\left(\eta_y\right)d\eta_1 d\eta_2 p\left(\vec{y}\right)\\&=\lim_{\varepsilon\to 0}\int_0^{2\pi}\int_{\rho_1}^{\rho_2} W\left(\rho,\theta\right)d\rho d\theta\end{aligned} \tag{C.8}$$

in which, the $W\left(\rho,\theta\right)$ is defined as

$$W\left(\rho,\theta\right)=F^1\left(\eta_x,\eta_y\right)\Phi^i\left(\eta_y\right)J\left(\eta_y\right)\rho \tag{C.9}$$

The expression of $n_i\left(x\right)n_i\left(y\right)/4\pi r^3$ can be changed to the following form in the polar coordinate,

$$f\left(\rho,\theta\right)=\frac{n_i\left(x\right)n_i\left(y\right)}{4\pi r^3}\Phi^i\left(\eta_y\right)J\left(\eta_y\right)\rho \tag{C.10}$$

When ρ is very small, $f\left(\rho,\theta\right)$ can be expanded based on its corresponding Laurent series in the folowing form,

$$f\left(\rho,\theta\right)=\frac{f_{-2}\left(\theta\right)}{\rho^2}+\frac{f_{-1}\left(\theta\right)}{\rho}+O\left(1\right) \tag{C.11}$$

Therefore, Eq.(C.8) can be written as

$$\begin{aligned}&I_0+I_{-1}+I_{-2}\\&=\lim_{\varepsilon\to 0}\left\{\int_0^{2\pi}\int_{\rho_1}^{\rho_2}\left[W\left(\rho,\theta\right)-\left(\frac{f_{-2}\left(\theta\right)}{\rho^2}+\frac{f_{-1}\left(\theta\right)}{\rho}\right)\right]d\rho d\theta\right\}\\&+\lim_{\varepsilon\to 0}\left\{\int_0^{2\pi}\int_{\rho_1}^{\rho_2}\left(\frac{f_{-1}\left(\theta\right)}{\rho}\right)d\rho d\theta\right\}+\lim_{\varepsilon\to 0}\left\{\int_0^{2\pi}\int_{\rho_1}^{\rho_2}\left(\frac{f_{-2}\left(\theta\right)}{\rho^2}\right)d\rho d\theta\right\}\end{aligned} \tag{C.12}$$

The three integral parts named I_0 , I_{-1} and I_{-2} , respectively.

I_0 can be calculated by the Gaussion method directly because the singularity has been removed from the integral.

$$I_0=\int_0^{2\pi}\int_0^{\rho_2}\left[W\left(\rho,\theta\right)-\left(\frac{f_{-2}\left(\theta\right)}{\rho^2}+\frac{f_{-1}\left(\theta\right)}{\rho}\right)\right]d\rho d\theta \tag{C.13}$$

Based on the Tylor series, we can obtain,

$$\rho = \varepsilon\beta(\theta) + \varepsilon^2\gamma(\theta) + O(\varepsilon^3) \tag{C.14}$$

Sustituting Eq.(C.14) into I_{-1} and integrating over ρ results in

$$I_{-1} = \int_0^{2\pi}\left[f_{-1}(\theta)\ln\left|\frac{\hat{\rho}(\theta)}{\beta(\theta)}\right|\right]d\theta - \lim_{\varepsilon\to 0}\left[\ln\varepsilon\int_0^{2\pi} f_{-1}(\theta)\,d\theta\right] \tag{C.15}$$

According to the Lipschitz condition in the sense of Cauchy principal value, the integral at the last term has to be identically zero, i.e., $\int_0^{2\pi} f_{-1}(\theta)\,d\theta = 0$. Therefore, the expression for I_{-1} becomes,

$$I_{-1} = \int_0^{2\pi} f_{-1}(\theta)\ln\left|\frac{\hat{\rho}(\theta)}{\beta(\theta)}\right|d\theta \tag{C.16}$$

Similarly, I_{-2} can be changed to

$$I_{-2} = \int_0^{2\pi} f_{-2}(\theta)\left[\frac{\gamma(\theta)}{\beta^2(\theta)} - \frac{1}{\hat{\rho}(\theta)}\right]d\theta + \lim_{\varepsilon\to 0}\left[\frac{1}{\varepsilon}\int_0^{2\pi}\frac{f_{-2}(\theta)}{\beta(\theta)}\,d\theta\right] \tag{C.17}$$

Combining the expressions of I_0 , I_{-1} and I_{-2} together, we can obtain,

$$\begin{aligned}&\int_0^{2\pi}\int_0^{\rho_2}\left[W(\rho,\theta) - \left(\frac{f_{-2}(\theta)}{\rho^2} + \frac{f_{-1}(\theta)}{\rho}\right)\right]d\rho\,d\theta + \int_0^{2\pi} f_{-1}(\theta)\ln\left|\frac{\hat{\rho}(\theta)}{\beta(\theta)}\right|d\theta \\ &+\int_0^{2\pi} f_{-2}(\theta)\left[\frac{\gamma(\theta)}{\beta^2(\theta)} - \frac{1}{\hat{\rho}(\theta)}\right]d\theta + \lim_{\varepsilon\to 0}\left[\frac{1}{\varepsilon}\int_0^{2\pi}\frac{f_{-2}(\theta)}{\beta(\theta)}\,d\theta\right]\end{aligned} \tag{C.18}$$

Therefore, the hypersingular integral of Eq.(C.1) can then be evaluated in the Hadamard finite part sense as

$$
\begin{aligned}
&\int_S F^1(\vec{x},\vec{y})\,p(\vec{y})\,dS(\vec{y}) \\
&= \int_{S-S_\varepsilon} F^1(\vec{x},\vec{y})\,p(\vec{y})\,dS(\vec{y}) \\
&+ p_i \int_0^{2\pi}\int_0^{\rho_2}\left[W(\rho,\theta)-\left(\frac{f_{-2}(\theta)}{\rho^2}+\frac{f_{-1}(\theta)}{\rho}\right)\right]d\rho\,d\theta \\
&+ p_i \int_0^{2\pi} f_{-1}(\theta)\ln\left|\frac{\hat{\rho}(\theta)}{\beta(\theta)}\right|d\theta \\
&+ p_i \int_0^{2\pi} f_{-2}(\theta)\left[\frac{\gamma(\theta)}{\beta^2(\theta)}-\frac{1}{\hat{\rho}(\theta)}\right]d\theta
\end{aligned}
\tag{C.19}
$$

The integrals at the right hand side of the above equation are in polar coordinates and can be calculated by the standard Gaussian method. While the functions about $f_{-1}(\theta)$, $f_{-2}(\theta)$, $\beta(\theta)$ and $\gamma(\theta)$ should be specified firstly. In polar coordinate defined by (ρ,θ) , the following relationship can be obtained,

$$
\begin{aligned}
y_i - x_i &= \rho\left[\cos(\theta)\left.\frac{\partial x_i}{\partial \eta_1}\right|_{\eta=\xi} + \sin(\theta)\left.\frac{\partial x_i}{\partial \eta_2}\right|_{\eta=\xi}\right] \\
&+ \rho^2\left[\frac{\cos^2(\theta)}{2}\left.\frac{\partial^2 x_i}{\partial \eta_1^2}\right|_{\eta=\xi} + \frac{\cos(\theta)\sin(\theta)}{2}\left.\frac{\partial^2 x_i}{\partial \eta_1 \partial \eta_2}\right|_{\eta=\xi} + \frac{\sin^2(\theta)}{2}\left.\frac{\partial^2 x_i}{\partial \eta_2^2}\right|_{\eta=\xi}\right] + O(\rho^3)
\end{aligned}
\tag{C.20}
$$

Or can be written as

$$
\begin{aligned}
&y_i - x_i = \rho A_i(\theta) + \rho^2 B_i(\theta) + O(\rho^3) \\
&A_i(\theta) = \cos(\theta)\left.\frac{\partial x_i}{\partial \eta_1}\right|_{\eta=\xi} + \sin(\theta)\left.\frac{\partial x_i}{\partial \eta_2}\right|_{\eta=\xi} \\
&B_i(\theta) = \frac{\cos^2(\theta)}{2}\left.\frac{\partial^2 x_i}{\partial \eta_1^2}\right|_{\eta=\xi} + \frac{\cos(\theta)\sin(\theta)}{2}\left.\frac{\partial^2 x_i}{\partial \eta_1 \partial \eta_2}\right|_{\eta=\xi} + \frac{\sin^2(\theta)}{2}\left.\frac{\partial^2 x_i}{\partial \eta_2^2}\right|_{\eta=\xi}
\end{aligned}
\tag{C.21}
$$

The expansion of $r = |y-\xi|$ at any order based on the Tylor expansion is

$$r^n = \rho^n A^n(\theta)\left[1+n\rho\frac{A_k(\theta)B_k(\theta)}{A^2(\theta)}\right]+O\left(\rho^{n+2}\right) \tag{C.22}$$

Then we can get the expansion of r^{-3}. The $A(\theta)$ and $B(\theta)$ in the above equation are defined as,

$$\begin{aligned} A(\theta) &= \left[A_1^2(\theta)+A_2^2(\theta)+A_3^2(\theta)\right]^{1/2} \\ B(\theta) &= \left[B_1^2(\theta)+B_2^2(\theta)+B_3^2(\theta)\right]^{1/2} \end{aligned} \tag{C.23}$$

Using the Eq. in the region near S_ε and let $n=1$ and $r=\varepsilon$, we can get the Tylor expansion of ε as following:

$$\varepsilon = \rho A(\theta)+\rho^2\frac{A_k(\theta)B_k(\theta)}{A(\theta)}+O\left(\rho^3\right) \tag{C.24}$$

Eq. (C.21) can be used to get the results of $A_i(\theta)$ and $B_i(\theta)$, then $\beta(\theta)$ and $\gamma(\theta)$ can be obtained through the above equation. Then the functions and can be calculated. From the Eq.(C.22), r^{-3} can be changed as,

$$\begin{aligned} r^{-3} &= \frac{S_{-3}(\theta)}{\rho^3}+\frac{S_{-2}(\theta)}{\rho^2}+O\left(\frac{1}{\rho}\right) \\ S_{-3}(\theta) &= \frac{1}{A^3(\theta)};\ S_{-2}(\theta) = -\frac{3A_k(\theta)B_k(\theta)}{A^5(\theta)}; \end{aligned} \tag{C.25}$$

Then the shape function $\Phi^n(\eta)$ is expanded in the region near S_ε as

$$\begin{aligned} \Phi^n(\eta) &= \Phi_0^n+\rho\Phi_1^n(\theta)+O\left(\rho^2\right) \\ \Phi_0^n &= \Phi^n(\xi) \\ \Phi_1^n(\theta) &= \cos(\theta)\left.\frac{\partial\Phi^n}{\partial\eta_1}\right|_{\eta=\xi}+\sin(\theta)\left.\frac{\partial\Phi^n}{\partial\eta_2}\right|_{\eta=\xi} \end{aligned} \tag{C.26}$$

Setting $J_i(\eta)=n_i(\eta)J(\eta)$ then the Jacbian matrix can be expanded as

$$J_i(\eta) = J_{i0} + \rho J_{i1}(\theta) + O(\rho^2)$$
$$J_{i0} = J_i(\xi); J_{i1}(\theta) = \cos(\theta)\left.\frac{\partial J_i}{\partial \eta_1}\right|_{\eta=\varepsilon} + \sin(\theta)\left.\frac{\partial J_i}{\partial \eta_2}\right|_{\eta=\varepsilon} \tag{C.27}$$

After this, the expansion forms of r^{-3} , $\Phi^n(\eta)$ and $n_i(\eta)n_i(\xi)J(\eta)$ have been obtained. Substituting these expressions into Eq.(C.10), the $f_{-1}(\theta)$ and $f_{-2}(\theta)$ are given by

$$f_{-1}(\theta) = \frac{1}{4\pi}\left[S_2(\theta)\Phi_0^n J_0 + S_3(\theta)\left(\Phi_1^n J_0 + \Phi_0^n n_i(\xi) J_{i1}(\theta)\right)\right]$$
$$f_{-2}(\theta) = \frac{1}{4\pi}\left[S_{-3}(\theta)\Phi_0^n J_0\right] \tag{C.28}$$

Till now, the expressions about $f_{-1}(\theta)$, $f_{-2}(\theta)$, $\beta(\theta)$ and $\gamma(\theta)$ have been derived. The Gaussian integration can be used to calculate the integral including the hyper-singular part and get an exact result.

REFERENCES

[1] J. Kang, Urban sound environment, CRC Press, 2006.

[2] A. Van Beek, M. Beuving, M. Dittrich, M. Beier, X. Zhang, H. Jonasson, F. Letourneaux, C. Talotte, M. Ringheim, Rail sources-state of the art, HARMONOISE report (HAR12TR-020118-SNCF10), European Commission, (2002).

[3] G. Watts, Acoustic performance of parallel traffic noise barriers, Applied Acoustics, 47 (1996) 95-119.

[4] J. Guo, J. Pan, Increasing the insertion loss of noise barriers using an active-control system, The Journal of the Acoustical Society of America, 104 (1998) 3408-3416.

[5] S. Wang, J. Tao, X. Qiu, Performance of a planar virtual sound barrier at the baffled opening of a rectangular cavity, The Journal of the Acoustical Society of America, 138 (2015) 2836-2847.

[6] N. Han, X. Qiu, A study of sound intensity control for active noise barriers, Applied Acoustics, 68 (2007) 1297-1306.

[7] D.N. May, N. Osman, Highway noise barriers: new shapes, Journal of Sound and Vibration, 71 (1980) 73-101.

[8] D. Hothersall, S. Chandler-Wilde, M. Hajmirzae, Efficiency of single noise barriers, Journal of Sound and Vibration, 146 (1991) 303-322.

[9] D. Crombie, D. Hothersall, S. Chandler-Wilde, Multiple-edge noise barriers, Applied acoustics, 44 (1995) 353-367.

[10] C. Yang, J. Pan, L. Cheng, A mechanism study of sound wave-trapping barriers, The Journal of the Acoustical Society of America, 134 (2013) 1960-1969.

[11] T. Wu, T. Cox, Y. Lam, From a profiled diffuser to an optimized absorber, The Journal of the Acoustical Society of America, 108 (2000) 643-650.

[12] D. Hothersall, D. Crombie, S. Chandler-Wilde, The performance of T-profile and associated noise barriers, Applied acoustics, 32 (1991) 269-287.

[13] K. Li, M. Law, M. Kwok, Absorbent parallel noise barriers in urban environments, Journal of Sound and Vibration, 315 (2008) 239-257.

[14] F. Asdrubali, G. Pispola, Properties of transparent sound-absorbing panels for use in noise barriers, The Journal of the Acoustical Society of America, 121 (2007) 214-221.

[15] T. Ishizuka, K. Fujiwara, Performance of noise barriers with various edge shapes and acoustical conditions, Applied Acoustics, 65 (2004) 125-141.

[16] D. Hutchins, D. Pitcarn, A laser study of multiple reflections within parallel noise barriers, The Journal of the Acoustical Society of America, 73 (1983) 2216-2218.

[17] G. Watts, N. Godfrey, Effects on roadside noise levels of sound absorptive materials in noise barriers, Applied Acoustics, 58 (1999) 385-402.

[18] M.R. Monazzam, S.M.B. Fard, Impacts of different median barrier shapes on a roadside environmental noise screen, Environmental Engineering Science, 28 (2011) 435-441.

[19] X. Wang, D. Mao, W. Yu, Z. Jiang, Sound barriers from materials of inhomogeneous impedance, The Journal of the Acoustical Society of America, 137 (2015) 3190-3197.

[20] A. Sommerfeld, Mathematische theorie der diffraction, Mathematische Annalen, 47 (1896) 317-374.

[21] I. Tolstoy, Exact, explicit solutions for diffraction by hard sound barriers and seamounts, The Journal of the Acoustical Society of America, 85 (1989) 661-669.

[22] W.J. Hadden Jr, A.D. Pierce, Sound diffraction around screens and wedges for arbitrary point source locations, The Journal of the Acoustical Society of America, 69 (1981) 1266-1276.

[23] A.D. Pierce, Diffraction of sound around corners and over wide barriers, The Journal of the Acoustical Society of America, 55 (1974) 941-955.

[24] J.B. Keller, Geometrical theory of diffraction, JOSA, 52 (1962) 116-130.

[25] W. Wei, T. Van Renterghem, D. Botteldooren, Simplified analytical model for sound level prediction at shielded urban locations involving multiple diffraction and reflections, The Journal of the Acoustical Society of America, 138 (2015) 2744-2758.

[26] K. Li, H. Wong, A review of commonly used analytical and empirical formulae for predicting sound diffracted by a thin screen, Applied Acoustics, 66 (2005) 45-76.

[27] S. Redfearn, XX. Some acoustical source-observer problems, The London, Edinburgh, and Dublin Philosophical Magazine and Journal of Science, 30 (1940) 223-236.

[28] Z. Maekawa, Noise reduction by screens, Applied Acoustics, 1 (1968) 157-173.

[29] U. Kurze, G. Anderson, Sound attenuation by barriers, Applied Acoustics, 4 (1971) 35-53.

[30] M. Delany, D. Harland, R. Hood, W. Scholes, The prediction of noise levels L10 due to road traffic, Journal of Sound and Vibration, 48 (1976) 305-325.

[31] S. Chandler-Wilde, D. Hothersall, The boundary integral equation method in outdoor sound propagation, Proceedings of the Institute of Acoustics, 9 (1987) 37-44.

[32] R. Seznec, Diffraction of sound around barriers: use of the boundary elements technique, Journal of Sound and Vibration, 73 (1980) 195-209.

[33] S.M. Fard, H. Peters, N. Kessissoglou, S. Marburg, Three-dimensional analysis of a noise barrier using a quasi-periodic boundary element method, The Journal of the Acoustical Society of America, 137 (2015) 3107-3114.

[34] P. Jean, C. Guigou, M. Villot, A 2.5 D BEM model for ground-structure interaction, Building acoustics, 11 (2004) 157-173.

[35] W. Hackbusch, Z.P. Nowak, On the fast matrix multiplication in the boundary element method by panel clustering, Numerische Mathematik, 54 (1989) 463-491.

[36] J.R. Phillips, J.K. White, A precorrected-FFT method for electrostatic analysis of complicated 3-D structures, Computer-Aided Design of Integrated Circuits and Systems, IEEE Transactions on, 16 (1997) 1059-1072.

[37] M. Bebendorf, Approximation of boundary element matrices, Numerische Mathematik, 86 (2000) 565-589.

[38] L. Greengard, V. Rokhlin, A fast algorithm for particle simulations, Journal of computational physics, 73 (1987) 325-348.

[39] N.A. Gumerov, R. Duraiswami, Fast multipole methods for the Helmholtz equation in three dimensions, Elsevier, 2005.

[40] M. Bapat, L. Shen, Y. Liu, Adaptive fast multipole boundary element method for three-dimensional half-space acoustic wave problems, Engineering Analysis with Boundary Elements, 33 (2009) 1113-1123.

[41] C.-J. Zheng, H.-B. Chen, L.-L. Chen, A wideband fast multipole boundary element method for half-space/plane-symmetric acoustic wave problems, Acta Mechanica Sinica, 29 (2013) 219-232.

[42] C.S. Pates, U.S. Shirahatti, C. Mei, Sound–structure interaction analysis of composite panels using coupled boundary and finite element methods, The Journal of the Acoustical Society of America, 98 (1995) 1216-1221.

[43] M. Fischer, L. Gaul, Fast BEM–FEM mortar coupling for acoustic–structure interaction, International Journal for Numerical Methods in Engineering, 62 (2005) 1677-1690.

[44] H. Isakari, T. Kondo, T. Takahashi, T. Matsumoto, A level-set-based topology optimisation for acoustic–elastic coupled problems with a fast BEM–FEM solver, Computer Methods in Applied Mechanics and Engineering, 315 (2017) 501-521.

[45] R. Panneton, A. L'Espérance, J. Nicolas, G.A. Daigle, Development and validation of a model predicting the performance of hard or absorbent parallel noise barriers, Journal of the Acoustical Society of Japan (E), 14 (1993) 251-258.

[46] Y. Miki, Acoustical properties of porous materials-Modifications of Delany-Bazley models, Journal of the Acoustical Society of Japan (E), 11 (1990) 19-24.

[47] K.M. Li, S.H. Tang, The predicted barrier effects in the proximity of tall buildings, The Journal of the Acoustical Society of America, 114 (2003) 821-832.

[48] E. Dowell, G. Gorman, D. Smith, Acoustoelasticity: general theory, acoustic natural modes and forced response to sinusoidal excitation, including comparisons with experiment, Journal of Sound and vibration, 52 (1977) 519-542.

[49] Y. Naka, A.A. Oberai, B.G. Shinn-Cunningham, Acoustic eigenvalues of rectangular rooms with arbitrary wall impedances using the interval Newton / generalized bisection method, The Journal of the Acoustical Society of America, 118 (2005) 3662-3671.

[50] S.R. Bistafa, J.W. Morrissey, Numerical solutions of the acoustic eigenvalue equation in the rectangular room with arbitrary (uniform) wall impedances, Journal of Sound and Vibration, 263 (2003) 205-218.

[51] C. Wang, L. Cheng, J. Pan, G. Yu, Sound absorption of a micro-perforated panel backed by an irregular-shaped cavity, The Journal of the Acoustical Society of America, 127 (2010) 238-246.

[52] B. Xu, S.D. Sommerfeldt, A hybrid modal analysis for enclosed sound fields, The Journal of the Acoustical Society of America, 128 (2010) 2857-2867.

[53] A. Snakowska, J. Jurkiewicz, Efficiency of energy radiation from an unflanged cylindrical duct in case of multimode excitation, Acta Acustica united with Acustica, 96 (2010) 416-424.

[54] J.-P. Berenger, A perfectly matched layer for the absorption of electromagnetic waves, Journal of computational physics, 114 (1994) 185-200.

[55] W. Koch, Acoustic resonances in rectangular open cavities, AIAA journal, 43 (2005) 2342-2349.

[56] S. Hein, W. Koch, Acoustic resonances and trapped modes in pipes and tunnels, Journal of Fluid Mechanics, 605 (2008) 401-428.

[57] S. Hein, W. Koch, L. Nannen, Trapped modes and Fano resonances in two-dimensional acoustical duct–cavity systems, Journal of fluid mechanics, 692 (2012) 257-287.

[58] S. Hein, W. Koch, L. Nannen, Fano resonances in acoustics, Journal of fluid mechanics, 664 (2010) 238-264.

[59] Y. Duan, W. Koch, C.M. Linton, M. McIVER, Complex resonances and trapped modes in ducted domains, Journal of Fluid Mechanics, 571 (2007) 119-147.

[60] A. Pelat, S. Félix, V. Pagneux, On the use of leaky modes in open waveguides for the sound propagation modeling in street canyons, The Journal of the Acoustical Society of America, 126 (2009) 2864-2872.

[61] P.J. Lee, J. Kang, Effect of height-to-width ratio on the sound propagation in urban streets, Acta Acustica united with Acustica, 101 (2015) 73-87.

[62] O. Richoux, C. Ayrault, A. Pelat, S. Félix, B. Lihoreau, Effect of the open roof on low frequency acoustic propagation in street canyons, Applied Acoustics, 71 (2010) 731-738.

[63] S. Kim, J. Pasciak, The computation of resonances in open systems using a perfectly matched layer, Mathematics of Computation, 78 (2009) 1375-1398.

[64] U. Fano, Effects of configuration interaction on intensities and phase shifts, Physical Review, 124 (1961) 1866.

[65] H. Feshbach, Unified theory of nuclear reactions, Annals of Physics, 5 (1958) 357-390.

[66] J. Okołowicz, M. Płoszajczak, I. Rotter, Dynamics of quantum systems embedded in a continuum, Physics Reports, 374 (2003) 271-383.

[67] D.N. Maksimov, A.F. Sadreev, A.A. Lyapina, A.S. Pilipchuk, Coupled mode theory for acoustic resonators, Wave Motion, 56 (2015) 52-66.

[68] A. Lyapina, D. Maksimov, A. Pilipchuk, A. Sadreev, Bound states in the continuum in open acoustic resonators, Journal of Fluid Mechanics, 780 (2015) 370-387.

[69] L. Xiong, W. Bi, Y. Aurégan, Fano resonance scatterings in waveguides with impedance boundary conditions, The Journal of the Acoustical Society of America, 139 (2016) 764-772.

[70] Y. Tong, Y. Kou, J. Pan, Forced acoustical response of a cavity coupled with a semi-infinite space using coupled mode theory, Wave Motion, (2017).

[71] A. Trochidis, Sound transmission in a duct with an array of lined resonators, J. Vib. Acoust, 113 (1991) 245-249.

[72] K. Chen, Y. Chen, K. Lin, C. Weng, The improvement on the transmission loss of a duct by adding Helmholtz resonators, Applied Acoustics, 54 (1998) 71-82.

[73] S.-H. Seo, Y.-H. Kim, Silencer design by using array resonators for low-frequency band noise reduction, The Journal of the Acoustical Society of America, 118 (2005) 2332-2338.

[74] B.S. Cazzolato, C.Q. Howard, C.H. Hansen, Finite element analysis of an industrial reactive silencer, in: ICSV5: Proceedings of the 5th International Congress of Sound and Vibration, 1997.

[75] S. Fard, H. Peters, S. Marburg, N. Kessissoglou, Acoustic Performance of a Barrier Embedded With Helmholtz Resonators Using a Quasi-Periodic Boundary Element Technique, Acta Acustica united with Acustica, 103 (2017) 444-450.

[76] B. Van der Aa, J. Forssén, Scattering by an array of perforated cylinders with a porous core, The Journal of the Acoustical Society of America, 136 (2014) 2370-2380.

[77] L. Huang, A theoretical study of duct noise control by flexible panels, the Journal of the Acoustical Society of America, 106 (1999) 1801-1809.

[78] L. Huang, Modal analysis of a drumlike silencer, the Journal of the Acoustical Society of America, 112 (2002) 2014-2025.

[79] L. Huang, Parametric study of a drum-like silencer, Journal of sound and vibration, 269 (2004) 467-488.

[80] Y. Choy, L. Huang, Experimental studies of a drumlike silencer, the Journal of the Acoustical Society of America, 112 (2002) 2026-2035.

[81] Y. Choy, L. Huang, Effect of flow on the drumlike silencer, The Journal of the Acoustical Society of America, 118 (2005) 3077-3085.

[82] L. Huang, Broadband sound reflection by plates covering side-branch cavities in a duct, the Journal of the Acoustical Society of America, 119 (2006) 2628-2638.

[83] C. Wang, J. Han, L. Huang, Optimization of a clamped plate silencer, the Journal of the Acoustical Society of America, 121 (2007) 949-960.

[84] C. Wang, L. Cheng, L. Huang, Realization of a broadband low-frequency plate silencer using sandwich plates, Journal of Sound and Vibration, 318 (2008) 792-808.

[85] Y. Choy, Y. Liu, H. Cheung, Q. Xi, K. Lau, Development of composite plate for compact silencer design, Journal of sound and vibration, 331 (2012) 2348-2364.

[86] X. Wang, Y. Choy, L. Cheng, Hybrid noise control in a duct using a light micro-perforated plate, The Journal of the Acoustical Society of America, 132 (2012) 3778-3787.

[87] J.B. Lawrie, I.M. Guled, On tuning a reactive silencer by varying the position of an internal membrane a, The Journal of the Acoustical Society of America, 120 (2006) 780-790.

[88] Y. Liu, Fast multipole boundary element method: theory and applications in engineering, Cambridge university press, 2009.

[89] H.A. Schenck, Improved integral formulation for acoustic radiation problems, The journal of the acoustical society of America, 44 (1968) 41-58.

[90] A. Burton, G. Miller, The application of integral equation methods to the numerical solution of some exterior boundary-value problems, Proceedings of the Royal Society of London. A. Mathematical and Physical Sciences, 323 (1971) 201-210.

[91] C. Zheng, T. Matsumoto, T. Takahashi, H. Chen, Explicit evaluation of hypersingular boundary integral equations for acoustic sensitivity analysis based on direct differentiation method, Engineering Analysis with Boundary Elements, 35 (2011) 1225-1235.

[92] J. do Rego Silva, Acoustic and elastic wave scattering using boundary elements, Computational mechanics, 1994.

[93] N. Nishimura, Fast multipole accelerated boundary integral equation methods, Applied Mechanics Reviews, 55 (2002) 299-324.

[94] S. Marburg, Six boundary elements per wavelength: Is that enough?, Journal of Computational Acoustics, 10 (2002) 25-51.

[95] N.A. Gumerov, R. Duraiswami, Recursions for the computation of multipole translation and rotation coefficients for the 3-D Helmholtz equation, SIAM Journal on Scientific Computing, 25 (2004) 1344-1381.

[96] H. Cheng, W.Y. Crutchfield, Z. Gimbutas, L.F. Greengard, J.F. Ethridge, J. Huang, V. Rokhlin, N. Yarvin, J. Zhao, A wideband fast multipole method for the Helmholtz equation in three dimensions, Journal of Computational Physics, 216 (2006) 300-325.

[97] R. Jakob-Chien, B.K. Alpert, A Fast Spherical Filter with Uniform Resolution, Journal of Computational Physics, 136 (1997) 580-584.

[98] K. Chen, P.J. Harris, Efficient preconditioners for iterative solution of the boundary element equations for the three-dimensional Helmholtz equation, Applied Numerical Mathematics, 36 (2001) 475-489.

[99] N.A. Gumerov, R. Duraiswami, A broadband fast multipole accelerated boundary element method for the three dimensional Helmholtz equation, J Acoust Soc Am, 125 (2009) 191-205.

[100] W. Wolf, S. Lele, Wideband fast multipole boundary element method: Application to acoustic scattering from aerodynamic bodies, International journal for numerical methods in fluids, 67 (2011) 2108-2129.

[101] L. Shen, Y. Liu, An adaptive fast multipole boundary element method for three-dimensional acoustic wave problems based on the Burton–Miller formulation, Computational Mechanics, 40 (2007) 461-472.

[102] H. Wu, Y. Liu, W. Jiang, W. Lu, A fast multipole boundary element method for three-dimensional half-space acoustic wave problems over an impedance plane, International Journal of Computational Methods, 12 (2015) 1350090.

[103] M. Ochmann, The complex equivalent source method for sound propagation over an impedance plane, The Journal of the Acoustical Society of America, 116 (2004) 3304-3311.

[104] F.J. Fahy, Sound and structural vibration: radiation, transmission and response, Academic press, 2012.

[105] Y. Lam, S. Roberts, A simple method for accurate prediction of finite barrier insertion loss, The Journal of the Acoustical Society of America, 93 (1993) 1445-1452.

[106] Q. Xi, Y. Choy, L. Cheng, S. Tang, Noise control of dipole source by using micro-perforated panel housing, Journal of Sound and Vibration, 362 (2016) 39-55.

[107] G. Emms, C. Fox, Control of sound transmission through an aperture using active sound absorption techniques: a theoretical investigation, Applied Acoustics, 62 (2001) 735-747.

[108] C. Field, F. Fricke, Theory and applications of quarter-wave resonators: A prelude to their use for attenuating noise entering buildings through ventilation openings, Applied Acoustics, 53 (1998) 117-132.

[109] J. Kang, M. Brocklesby, Feasibility of applying micro-perforated absorbers in acoustic window systems, Applied Acoustics, 66 (2005) 669-689.

[110] D. Li, L. Cheng, Acoustically coupled model of an enclosure and a Helmholtz resonator array, Journal of sound and vibration, 305 (2007) 272-288.

[111] D. Li, L. Cheng, G. Yu, J. Vipperman, Noise control in enclosures: Modeling and experiments with T-shaped acoustic resonators, the Journal of the Acoustical Society of America, 122 (2007) 2615-2625.

[112] G. Yu, L. Cheng, Location optimization of a long T-shaped acoustic resonator array in noise control of enclosures, Journal of Sound and Vibration, 328 (2009) 42-56.

[113] G. Yu, D. Li, L. Cheng, Effect of internal resistance of a Helmholtz resonator on acoustic energy reduction in enclosures, The Journal of the Acoustical Society of America, 124 (2008) 3534-3543.

[114] A. Selamet, V. Kothamasu, J. Novak, Insertion loss of a Helmholtz resonator in the intake system of internal combustion engines: an experimental and computational investigation, Applied Acoustics, 62 (2001) 381-409.

[115] S.J. Esteve, M.E. Johnson, Adaptive Helmholtz resonators and passive vibration absorbers for cylinder interior noise control, Journal of Sound and Vibration, 288 (2005) 1105-1130.

[116] S.J. Estéve, M.E. Johnson, Reduction of sound transmission into a circular cylindrical shell using distributed vibration absorbers and Helmholtz resonators, The Journal of the Acoustical Society of America, 112 (2002) 2840-2848.

[117] C.Q. Howard, C.H. Hansen, A. Zander, Vibro-acoustic noise control treatments for payload bays of launch vehicles: discrete to fuzzy solutions, Applied Acoustics, 66 (2005) 1235-1261.

[118] F.J. Fahy, Foundations of engineering acoustics, Academic press, 2000.

[119] R.D. Blevins, R. Plunkett, Formulas for natural frequency and mode shape, Journal of Applied Mechanics, 47 (1980) 461.

[120] F. Fahy, C. Schofield, A note on the interaction between a Helmholtz resonator and an acoustic mode of an enclosure, Journal of Sound and Vibration, 72 (1980) 365-378.

[121] L.E. Kinsler, A.R. Frey, A.B. Coppens, J.V. Sanders, Fundamentals of acoustics, Fundamentals of Acoustics, 4th Edition, by Lawrence E. Kinsler, Austin R. Frey, Alan B. Coppens, James V. Sanders, pp. 560. ISBN 0-471-84789-5. Wiley-VCH, December 1999., (1999) 560.

[122] S. Ortiz, L. Gonz á lez, C.G. D íaz, U. Svensson, P. Cobo, Acoustic resonances in a 3D open cavity with non-parallel walls, Journal of Sound and Vibration, 363 (2016) 181-198.

[123] D. Hutchins, H. Jones, B. Paterson, L. Russell, Studies of parallel barrier performance by acoustical modeling, The Journal of the Acoustical Society of America, 77 (1985) 536-546.

[124] Y. Tong, J. Pan, Modal analysis of the scattering coefficients of an open cavity in a waveguide, Wave Motion, 68 (2017) 242-252.

[125] D. Li, J.S. Vipperman, On the design of long T-shaped acoustic resonators, the Journal of the Acoustical Society of America, 116 (2004) 2785-2792.

[126] J. Pan, C. Hansen, D. Bies, Active control of noise transmission through a panel into a cavity: I. Analytical study, The Journal of the Acoustical Society of America, 87 (1990) 2098-2108.

[127] D.J. Inman, Engineering vibration, Prentice Hall New Jersey, 2008.

[128] H. Kuttruff, Room acoustics, Crc Press, 2016.